Chair of Simulation and Modelling of Metallurgical Processes

Doctoral Thesis

Observation of Flow Phenomena during Dendritic Solidification

November 2018

Mihaela Stefan-Kharicha, Inginer

Affidavit

I declare in lieu of oath, that I wrote this thesis and performed the associated research myself, using only literature cited in this volume.

Leoben 05.11.2018

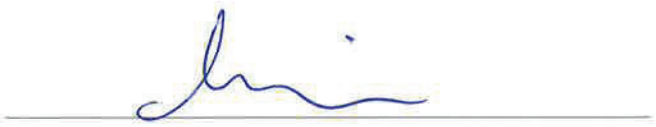

Mihaela, Stefan-Kharicha

Acknowledgement

No thesis manuscript would be complete without the acknowledgments words, because one thing is absolutely sure: I was not alone to realize this difficult WORK! Many people helped me, encouraged me and brought me to finish this thesis.

I will start by addressing my thankful gratitude to the person who actually gave me the great opportunity to write this thesis, my supervisor Prof. Andreas Ludwig. He always trusted me and encouraged me to continue this work. Thank you Andreas!

I thank respectfully Dr. Sven Eck who accompanied my work during the first three years and taught me the bases of the laser manipulation and PIV technique.

My thanks and appreciations go toward A. Ishmurzin, L. Könöszy, M. Ahmadein for their useful contribution and collaboration in the domain of numerical simulation, realized under the professional guidance of Dr. Wu.

I would like to extend my sincere thanks to all my colleagues during these more than 10 years, so they were a lot, for the lovely environment that they offered me! I would like to express my gratitude to the administrative staff (Jenny, Sabine, Claudia, Klaus) which was always so prompt in solving all kinds of problems. A special big thanks to Johann Mogeritsch who particularly helped me in the design of the experimental cells, with the laboratory work and gave me valuable advices in German!

Of course a kind and gentle hug to all my friends who were encouraging me and helped me by generously offering me some of their time, and especially a warm, big thank to my friend Helga!

And last but not least I have to thank my entire family: my husband Abdellah who was always beside me and gave me precious scientific help and moral support and of course my three kids which accompanied me with their laughs and love during this time. Without them, my lovely family, nothings of this work could have been done! I love you all!

Thank you to all that I forgot to mention here but who certainly contributed to the accomplishment of this work.

Preface

The present dissertation was prepared during my employment at the Chair of Simulation and Modelling of Metallurgical Processes (SMMP), Department of Metallurgy, Montanuniversitaet of Leoben (MUL), within the following two FWF projects: "Combined optical measurement techniques applied to convection processes during equiaxed solidification" (P 17619-N02) and "Investigations on the Interaction between Melt Flow and Solidification" (P22614-N22). The main results of my research activities were published in peered review papers. These publications are enumerated below:

Publication 1

S. Eck, M. Stefan Kharicha, A. Ishmurzin, A. Ludwig: Measurement and simulation of temperature and velocity fields during the cooling of water in a die casting model, Mat. Sci. Eng. A, 2005, vol. 413-414, pp. 79.

Publication 2

M. Stefan Kharicha, S. Eck, L. Könözsy, A. Kharicha and A. Ludwig: Experimental and numerical investigations of NH_4Cl solidification in a mould. Part 1: Experimental results, International Journal of Cast Metals Research, 2009, vol. 22, pp. 168.

Publication 3

A. Kharicha, M. Stefan-Kharicha, A. Ludwig and M. Wu: Simultaneous observation of melt flow and motion of equiaxed crystals during solidification using a dual phase particle image velocimetry technique. Part I: stage characterization of melt flow and equiaxed crystal motion, Metallurgical and Materials Transaction A, 2013, vol. 44A, pp. 650.

Publication 4

A. Kharicha, M. Stefan-Kharicha, A. Ludwig and M. Wu: Simultaneous observation of melt flow and motion of equiaxed crystals during solidification using a dual phase particle image velocimetry technique. Part II: relative velocities, Metallurgical and Materials Transaction A, 2013, vol. 44A, pp. 661.

Publication 5

M. Stefan-Kharicha, A. Kharicha, M. Wu and A. Ludwig: Observation of flow regimes and transitions during a columnar solidification experiment, Fluid Dyn. Res., 2014, vol. 46, pp. 21.

Publication 6

M. Stefan-Kharicha, A. Kharicha, M. Wu and A. Ludwig: On the coupling mechanism of equiaxed crystal generation with the liquid flow driven by natural convection during solidification, Metall. Mater. Trans. A, 2018, vol. 49A, pp. 1708.

Publication 7

A. Ludwig, M. Stefan-Kharicha, A. Kharicha and M. Wu: Massive formation of equiaxed crystals by avalanches of mushy zone segments, Metallurgical and Material Transaction A, 2017, vol. 48A, pp. 2927.

Publication 8

M. Stefan-Kharicha. A. Kharicha, J. Mogeritsch, M. Wu, A. Ludwig: Review of ammonium chloride-water solution properties, Journal of Chemical and Engineering Data, 2018, vol. 63, pp. 3170.

Publication 9

L. Könözsy, S. Eck, M. Stefan Kharicha, M. Wu and A. Ludwig: Experimental and numerical investigations of NH4Cl solidification in a mould. Part 2: numerical results, International Journal of Cast Metals Research, 2009, vol. 22, pp. 172.

Publication 10

L. Könözsy, M. Stefan Kharicha, S. Eck, M. Wu and A. Ludwig: Numerical and Experimental Investigation of NH4Cl Solidification, Materials Science Forum, 2010, vol. 649, pp. 367.

Publication 11

A. Kharicha, M. Stefan-Kharicha, A. Ludwig and M. Wu: Exploration of the double-diffusive convection during dendritic solidification with a combined volume-averaging and cellular-automaton model, Materials Science and Engineering, 2012, vol.33, pp. 012115.

Publication 12

M. Ahmadein, M. Wu, M. Stefan Kharicha, A. Kharicha, A. Ludwig.: Evaluation of a 5-phase mixed columnar-equiaxed solidification model with a benchmark solidification experiment of NH_4Cl-H_2O solution, Mater. Sci. Forum, 2014, vols. 790-791, pp. 247.

The most relevant publications to my dissertation (**Publications 1 to 8**) are enclosed at the end of the dissertation (Part D) and a comprehensive overview about these publications is given in Part C. The experimental work was entirely performed by me.

The experimental benchmark developed during this work was used to validate several solidification models presented in **Publications 9 to 12**. The numerical simulations were performed by L. Könözsy, A. Kharicha and respectively M. Ahmadein. Therefore these publications are not enclosed in this dissertation.

Furthermore participation at international conferences with oral presentations or posters is listed below:
“Measurement and Simulation of Temperature and Velocity Fields during the cooling of water in a Die Cast Model”, M. Stefan Kharicha, S. Eck, A. Ishmurzin, A. Ludwig, International Conference on Advances in Solidification Processes (ICASP-1), Stockholm, Sweden, June, 2005.

“Visualisation of a double flow during the solidification of NH_4Cl” M. Stefan Kharicha: presentation at the 5-th PIV user meeting, Hamburg, Germany, 2008,

"Experimental and Numerical Investigations of NH_4Cl Solidification in a Die Casting Mould. Part 1: Experimental Results", M. Stefan Kharicha, S. Eck, L. Könözsy, A. Ludwig, 2nd Int. Conf. Adv. in Solidification Processes (ICASP-2), Seggau, Austria, June 17-20, 2008.

“Particle Image Velocimetry (PIV) during the solidification of NH_4Cl in a Die Casting Model", M. Stefan Kharicha, A. Kharicha, L. Könözsy, S. Eck, A. Ludwig, Int. Conf. on "Solidification and Gravity” (SOLGRAV’ 08), Miskolc, Hungary, Sept. 1-4, 2008.

"Simultaneous observation of melt flow and motion of equiaxed crystals during solidification using a dual phase PIV technique"(Poster), MCWASP XIII (13th Modeling of Casting, Welding and Adv. Solidification Processes) Schladming, Austria, June 17-22, 2012.

"Evaluation of a 5-phase mixed columnar-equiaxed solidification model with a benchmark solidification experiment of NH_4 Cl-H_2 O solution" (Poster), 6th Int. Conf. on "Solidification and Gravity" (SOLGRAV’ 13), Miskolc, Hungary, Sept. 2-6, 2013.

Abstract

The current dissertation presents the “Observation of flow phenomena during dendritic solidification” of a hypereutectic ammonium chloride alloy, in a cast cell cooled homogeneously from the side and bottom walls. The main aim of this thesis work is to establish a valuable experimental benchmark with well controlled temperature boundaries for numerical simulations. The temperature was measured via thermocouples fixed in the mould and also temperature fields were extracted using Light Induced Fluorescence technique (LIF). A large interest was given to flow characterisation during solidification and especially its interaction with solidification. Additionally the measurements of the mushy zone thickness and estimation of total volume of mush developed in the cast cell during solidification was performed. The innovation brought in this work is the use of the dual Particle Image Velocimetry (PIV) technique to explore simultaneously the melt flow and the equiaxed crystals motion during the solidification of ammonium chloride. Different flow regimes were reported and flow velocities were extracted simultaneously with equiaxed crystals velocities. From the flow vectormaps the total flow kinetic energy (KE) was calculated and plotted versus time. At the beginning of the cooling process a steady convection pattern is formed, then solutal buoyancy together with falling crystals destabilize and break the steady convection flow into multiple chaotic cells, the flow transitioned from a 2D to a 3D turbulent regime. This regime is progressively replaced by a horizontal stratified flow, called meander flow. Several layers from the top to the bottom of the cell and from one side to the other side of the lateral columnar mushy zone were observed. The meander flow was found to be a new flow phenomena occurring when double diffusive convection is triggered by solidification. The solidification type observed in most experiments was mainly columnar. The reproducibility of these experimental data was very good and therefore they constitute an excellent benchmark for the validation of numerical models. However some experiments, under specific conditions, presented a rain fall of equiaxed crystals in the bulk melt and sometimes even freckles have been observed in the mushy region. In these cases the average melt flow velocity was related with the velocity of the columnar front and it was confirmed that for high velocity flow and high columnar front velocity, equiaxed crystal occurred. Furthermore a clear correlation between the strength of the flow and the occurrence of equiaxed crystals was observed: when equiaxed crystal occurred in large amount, a peak in

the flow KE was measured. The analysis of the results suggests strongly a fragmentation origin of the equiaxed crystals occurrence. A coupling mechanism between the hydrodynamics and the generation and growth of the equiaxed crystals was proposed. The transition from purely columnar growth to a strongly equiaxed rain (CET) was found to be initiated by the magnitude of the flow intensity driven by the equiaxed crystals, and the liberation and the transport of the fragments, by the same flow recirculating within the mushy zone. In these experiments where equiaxed crystals were observed, the relative velocity of a single crystal was extracted for different cases (falling down, moving up-ward) and plotted versus the crystals size (diameter). The results show an increase of the relative velocity with the measured size and a power law was found to fit these experimental data. The interaction between the fluid flow and the equiaxed crystal was found to be important in the area of high crystal number density; the two phases have often collinear velocity fields. In these regions, the liquid flow has shown smoother velocity variations than in the chaotic or the turbulent bulk. This observation is a proof that equiaxed crystals tend to damp a part of the liquid flow turbulence. Simultaneously, the velocities in the bulk flow were found to accelerate during the period of strong crystal fall near the vertical walls.

An inner equiaxed zone is often noticed in large industrial ingot castings. Observation of spectacular equiaxed avalanches in a large scale cast cell in laboratory, creating conspicuous equiaxed layers at the bottom of the cast cell, encourages us to believe that this phenomenon can be at the origin of the industrial one.

The experimental data presented in this work were used to validate several multi-phase solidification models. The solidification front and evolution of mushy zone thickness during solidification were calculated with reasonable accuracy using an Eulerian-Eulerian model. Furthermore a combined volume average method (for the inner dendrite) with cellular automaton model (for the envelope of the columnar grains) was developed. Evolution of the columnar dendrite envelope, the primary arm spacing and more complex flow phenomena such as the meandering flow were predicted by the numerical simulation.

CONTENTS

Part A: INTRODUCTION

1. Generalities on metals and alloys solidification

Part A is dedicated to the description of the formation of solidification structures. The occurrence of a specific structure is the result of the competition between different mechanisms: thermal, chemical and thermo-dynamical which take place at different time and space scales. The kinetic plays a particular role in the dynamic of the solidification. Solidification is often an out-equilibrium process, due to the fact that the cooling process can be faster than the actual mass and/or heat transport. Because the solute has a small diffusivity in the liquid and even smaller in the solid, the equilibrium is hard to achieve in a short cooling time. Also the latent heat released due to phase change needs time to be transferred. The system wants to reach equilibrium and the competition between these factors results in important differences in final structure and grain size.

The most important parameters which govern the structure type are:

cooling rate $\dot{T}$ [K/s],

temperature gradient near the columnar front G [K/m],

grain density N_0 [m^{-3}],

nucleation undercooling ΔT_n [K].

The ratio between the cooling rate and the temperature gradient represents the velocity of the isotherms, which has a very important influence on the microstructure.

1.1. Cooling curve of a binary alloy

For a pure material or alloy the measurement of the temperature in time will give the cooling curve. In Fig. A1a, which represents a schematic cooling curve for a pure metal, three zones are visible: first a decreasing, then a plateau and lastly a second decreasing. The plateau is even larger when the metal's latent heat is large and the cooling is slow. This plateau corresponds to the coexistence of the molten and solid metal, and defines the melting temperature T_m.

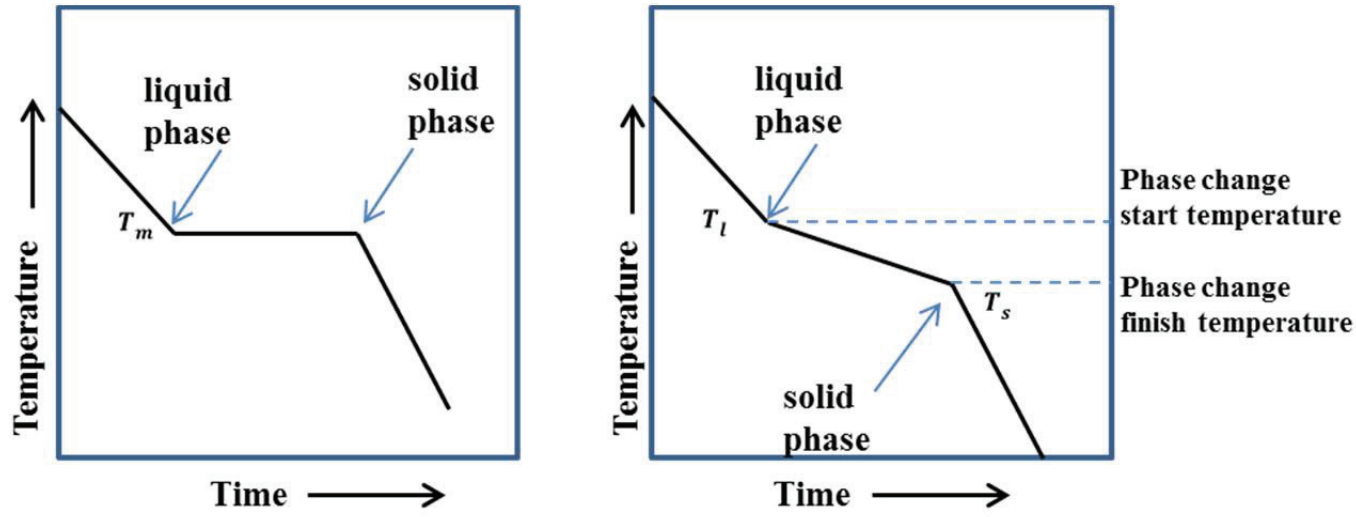

a) b)

Fig. A1: Schematic cooling curve of: a) a pure material and b) an alloy.

Nevertheless, for a binary alloy, the cooling curve is more complex, presenting different changes in slope, each corresponding to a phase change (Fig. A1b). The record of these specific temperatures permits us to determine the temperature intervals where the system has the same phases.

The most important temperatures are: that of the beginning of the solidification T_l, where the first solid crystals appear in the liquid melt, and that of the end of the solidification, which corresponds to the moment when the last liquid is solidified T_s. There is a corresponding cooling curve for any composition in the eutectic phase diagram. However, the interpretation of these cooling curves, in order to draw the equilibrium phase diagram, is difficult due to the following two reasons:

1. The start of the solidification is delayed compared to the liquidus temperature T_l. The solid is a very ordered phase compared to the liquid, the system needs in order to pass from liquid to solid to create the first solid embryo and thus to overpass the nucleation barrier. The first crystal is created at a lower temperature T_n and this difference $T_l - T_n$ is called nucleation undercooling ΔT_n and constitutes the driving force for solidification. After the undercooling takes place and the solidification starts, the temperature rises until the liquidus temperature is reached. This phenomenon is called recalescence and is due to the release of latent heat as the result of solidification. In Fig. A2b a schematic cooling curve with the occurrence of recalescence is shown and the liquidus temperature T_l is determined by extrapolation.

2. The temperature when the solidification ends is very hard to determine because of the non-homogeneities of the solid (the interdendritic liquid at eutectic composition).

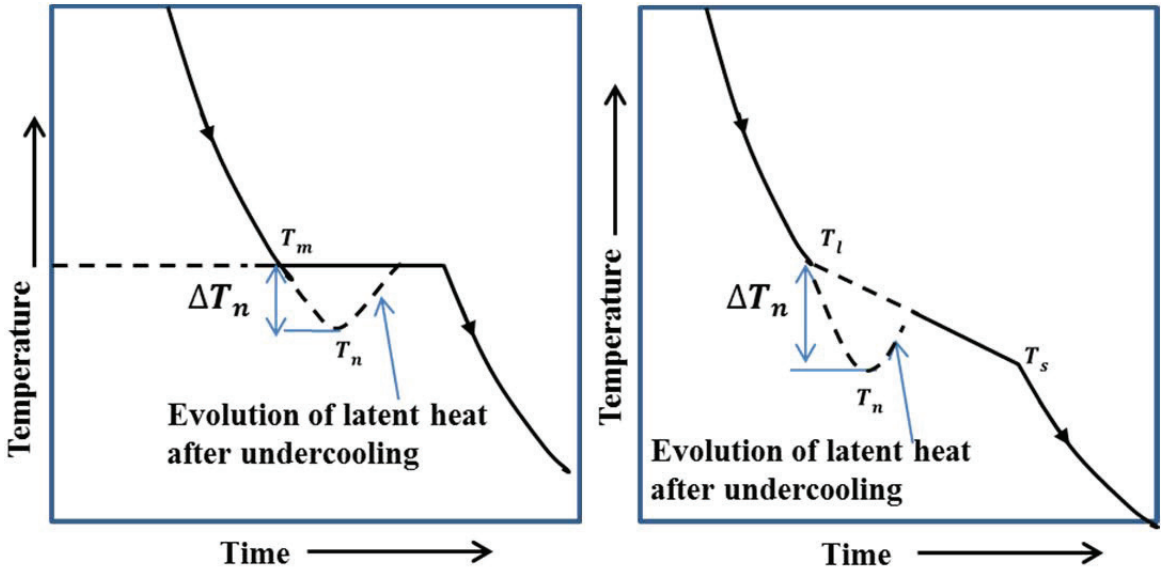

a) b)

Fig. A2: Schematic cooling curve with undercooling and recalescence: a) for a pure metal and b) for an alloy.

1.2. Solidification, binary phase diagram and segregation

During the solidification process at a local scale, the solid that forms has the concentration C_s^*, which is different from that of the liquid found at the solid-liquid interface, C_l^*. At the interface the solid concentration, C_s^* , is related to the liquid concentration C_l^* by the partition coefficient $k = C_s^*/C_l^*$ [Kurz and Fischer A1, Flemings A2, Lesoult A3]. If the melt is perfectly mixed during the solidification, the solid-liquid interface concentrations are those of equilibrium ($k = C_s^{eq}/C_l^{eq}$). In this case of thermo-dynamical equilibrium, the liquid concentration at a considered temperature is given by the phase diagram via the liquidus line and the solid concentration is given by the solidus line. This is only valid if the temperature, the liquid and solid concentrations are uniform in the whole system during the solidification process. In reality solidification never takes place under these conditions of perfect mixing at the system scale. But at local microscopic scale, equilibrium can be achieved. For a binary phase diagram at constant pressure (case treated all along this dissertation), the solid and liquid concentrations depend only on the temperature.

$$C_s^{eq} = C_s(T) \qquad \text{Eq. A1}$$

$$C_l^{eq} = C_l(T) \qquad \text{Eq. A2}$$

For simplicity the liquid and solid curves are replaced by lines and such a binary phase diagram is presented in Fig. A3, where the partition coefficient k is defined by a value smaller than 1.

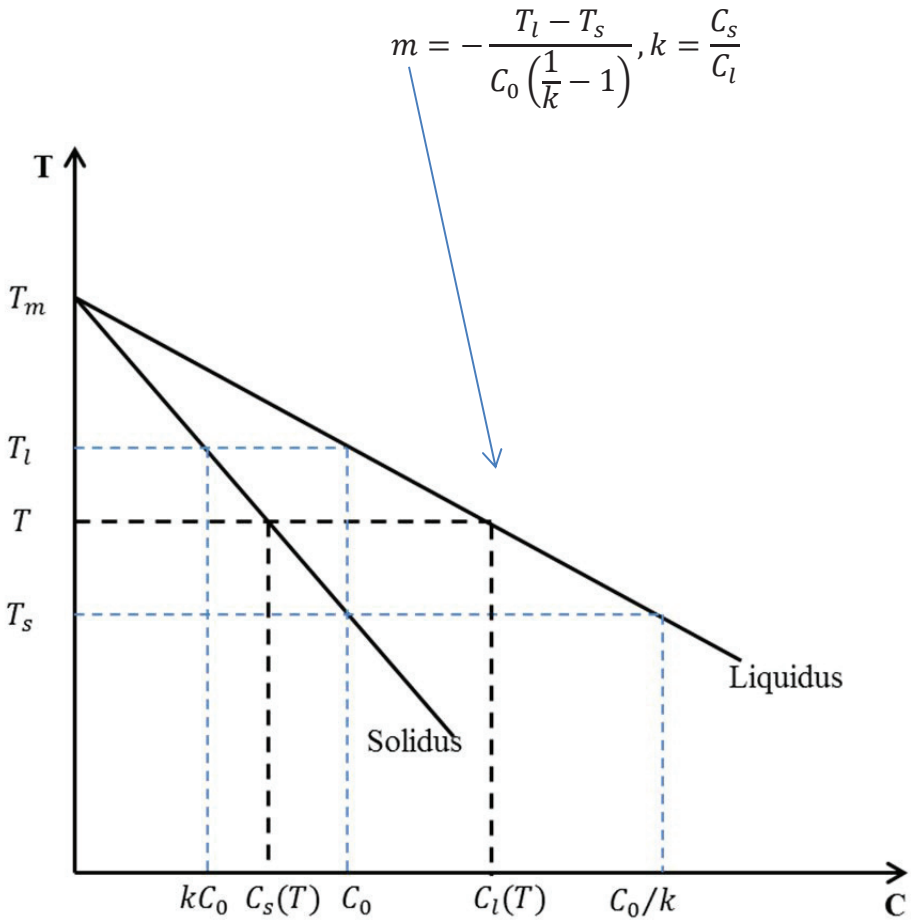

Fig. A3: Example of binary phase diagram with $k < 1$.

The partition coefficient k is constant if the solidus and liquidus curves are lines. The liquidus line is defined by the equation:

$$T_l = T_m + mC_l \qquad \text{Eq. A3}$$

where m is the liquidus slope, which is negative here.

In Fig. A3 the solidification interval at initial concentration C_0 is defined as:

$$\Delta T = T_l - T_s = mC_0\left(1 - \frac{1}{k}\right) \quad \text{Eq. A4}$$

If the assumption of perfect diffusion in the liquid and the solid is kept, the initial alloy concentration C_0 can be expressed as:

$$C_0 = f_l C_l + (1 - f_l)C_s \quad \text{Eq. A5}$$

From Eq. A5 a relation can be extracted which gives us the ration of the two phases (liquid and solid) found in equilibrium at each temperature:

$$f_l = \frac{C_0 - C_s}{C_l - C_s};\ f_s = \frac{C_l - C_0}{C_l - C_s} \quad \text{Eq. A6}$$

This relation is known as the lever rule. In the case of real solidification processes the relations A1 to A4, are applicable only at the solid-liquid interface where the equilibrium between C_s and C_l can be achieved. The solid concentration in reality is not homogeneous (perfect diffusion doesn't exist) and is very sensitive to the successive solid-liquid interface positions and also to the growing regimes of the solid front (planar, cellular or dendritic). The solid-liquid interface morphology is the result of solute and heat exchange optimisation at the interface. Three zones can be defined during the solidification of an alloy: a solid zone, a mushy zone and a liquid zone. A simplified scheme of the mushy zone is considered as a closed system in-between the dendrites branches, where solid and liquid coexist. If generally it is admitted that the liquid far from the solid-liquid interface is well mixed and has the same concentration everywhere, this is not the case in the mushy zone. At the solid–liquid interface the equilibrium presented by the phase diagram is accomplished. On the contrary, between two dendrites the solute concentration will vary [Flemings A2, Allen A4]. The concentration of the solute in-between the dendrites will be higher (conform the phase diagram presented in Fig. A3) than the concentration at the solid-liquid interface. The interdendritic liquid melt is undercooled (has a lower temperature than the T_l prescribed by the phase diagram), thus is very important to calculate this undercooling. Brody and Flemings [A5] advance the idea that the interdendritic space is adjusting in order to minimise the undercooling. In this way the undercooling would become negligible and the liquid would be "perfectly mixed", with the concentration given by the thermo-dynamical equilibrium. With this hypothesis, the liquid concentration in the mushy zone is directly controlled by temperature. Allen' s works [A4] confirm this hypothesis even if the undercooling is not always as low as affirmed by Flemings

[A2]. Theoretically solidification starts at the liquidus temperature and finishes at the solidus temperature. In reality solidification starts around the liquidus temperature (minus the undercooling) and very often ends at the eutectic temperature. This defines the interval of temperature and concentration, corresponding to the existence of the mushy zone.

If we consider (contrary to the diffusion hypothesis) that the solid forms layer by layer, each solid layer will have a different concentration. Considering the liquid fraction transformation $f_l \rightarrow f_l - df_l$, the Gulliver–Scheil law can be written in differential form:

$$(C_l - C_s)df_l = f_l dC_l = (1-k)C_l df_l \qquad \text{Eq. A7}$$

If $k > 1$ the solute solubility in the solid is greater than in the liquid, thus the solid will have at each layer a lower and lower solute concentration until only pure solvent is solidified. If $k < 1$ solute is rejected at the solid-liquid interface, thus solute redistribution will take place in the liquid ahead the interface. The solid is at each layer enriched until the equilibrium is reached. The solid alloy keeps the marks of major segregations. These segregations are in order of the interdendritic space size, it means of hundreds of micrometres, known as microsegregation. These concentration variations can be cancelled, when the diffusion is accelerated, by heat treatment. Nevertheless, in some alloys the composition can be very different at the ingot scale, this is known as macrosegregation. The Gulliver–Scheil law can be used to predict macrosegregation. In the case of the partition coefficient lower than 1, macrosegregation is due to the solute rejected during the solidification. Macrosegregation can take different forms [Lesoult A3]: segregated channels (also known as freckles or chimneys) which are strip-like shape with compositional variation, hot tears (crackings) (Fig. A4) [A6, A7]. The occurrence of these defects is directly related to the influence of convection on the mushy zone [Prescott and Incropera A8]. These channels or freckles are visible in the steel ingots with high content of C or other elements (S, Mg, Mo) [A2], on Al-Cu alloys [A2], on transparent alloys [A9] (Fig. A5) and on Pb-Sn alloys [Sarazin and Hellawell A10, Bergman et al. A11] (Fig. A6).

a) b)

Fig. A4: a) X-ray photography showing freckles in a Sn-3wt.% Pb ingot (10*6*1 cm) [A6]. b) Segregated channels in Ni supper-alloy (9 mm diameter) [A7].

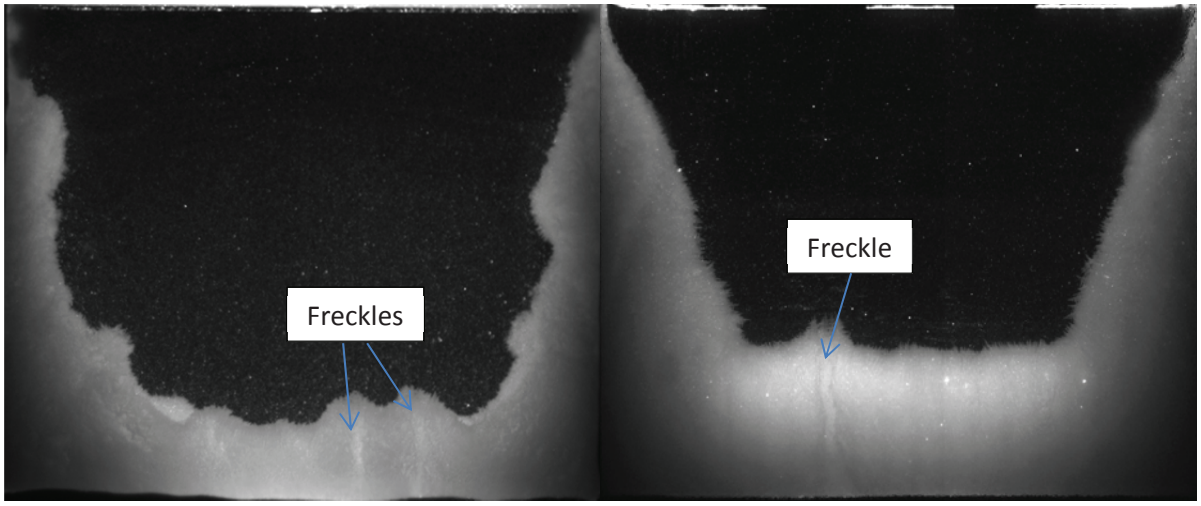

Fig. A5: Freckles in ammonium chloride-water mushy zone [A9].

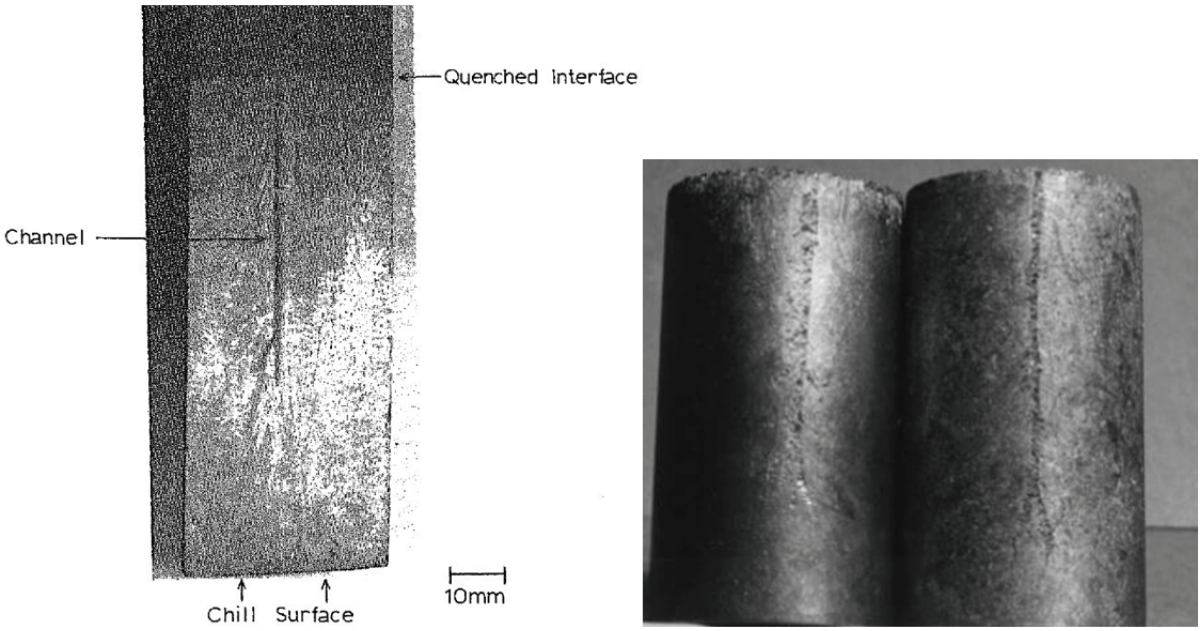

a) b)

Fig. A6: a) Longitudinal section of a quenched Pb-10 % Sn ingot showing a segregated channel [A10]; b) Freckle trails (segregated channels) on Pb-Sn ingots solidified at 0.25 K/min [A11].

1.3. Microsegregation and solid fraction

During the solidification of a binary alloy of nominal composition C_0, it was seen previously that solute will be rejected at the solid-liquid interface (for $k < 1$). In the case of thermo-dynamical equilibrium, infinite diffusion is considered in the liquid and in the solid. The first solid crystal appears at the temperature T_l and the last solid to solidify will happen at the temperature T_s. The liquid composition at the equilibrium is given by the lever rule:

$$C_l = \frac{C_0}{1-(1-k)f_s} \qquad \text{Eq. A8}$$

where f_s represents the solid fraction. The solid fraction is communally 1 when the system is entirely solid and 0 when is totally liquid. Using Eq. A3, $T_l = T_m + mC_l$ for $C_l = C_0$ the solid fraction can be expressed as function of temperature:

$$f_s = \left(\frac{1}{1-k}\right)\left(\frac{T_l - T}{T_m - T}\right) \qquad \text{Eq. A9}$$

where T_m is the melting temperature of the pure solvent. However in reality solidification is an out-equilibrium process, mostly due to chemical diffusion phenomena. Gulliver [A12] then Scheil [A13] proposed a model which takes into account the solute rejection in a simple

manner: it is assumed no diffusion in the solid and infinite diffusion in the liquid. The liquid concentration C_l and the solid fraction f_s become:

$$C_l = \frac{C_0}{(1-f_s)^{(1-k)}} \quad \text{Eq. A10}$$

$$f_s = 1 - \left(\frac{T_m - T}{T_m - T_l}\right)^{\left(\frac{1}{k-1}\right)} \quad \text{Eq. A11}$$

Moreover, it is well known that the solute diffusion in solid metals is not zero. Brody and Flemings [A5] in their model considered it, by introducing the Fourier number $\alpha = \frac{D_s t_s}{(\lambda_{2,f})^2}$, where D_s is the diffusion coefficient in the solid, t_s the solidification time and $\lambda_{2,f}$ the secondary dendrite arm spacing at the end of the solidification. This model was modified by Clyne and Kurz [A14]. They used a new coefficient α' because the Brody and Flemings model was invalid for too large solid diffusivity. Considering this new factor the liquid concentration and solid fraction can be written as follows:

$$\alpha' = \alpha[1 - \exp(-1)] - \frac{1}{2}\exp\left(-\frac{1}{2}\right) \quad \text{Eq. A12}$$

$$C_l = C_0[1 - f_s(1 - 2k\alpha')]^{\left(\frac{k-1}{1-2k\alpha'}\right)} \quad \text{Eq. A13}$$

$$f_s = \frac{1}{2k\alpha'}\left[1 - \left(\frac{T_m - T}{T_m - T_l}\right)^{\left(\frac{1-2k\alpha'}{k-1}\right)}\right] \quad \text{Eq. A14}$$

Using Eq. A12 – Eq. A14, for α'equal to 0 the Scheil model can be retrieved and for α'equal to 0.5 the lever rule case can be described. The exact solution of the Brody- Flemings model was found by Kobayashi [A15].

In the case of multicomponent alloys solidification, the models presented (lever rule, Scheil and Clyne-Kurz) can be adapted by taking into account the concentration of each element, considering $C_{l,i}$ the liquid concentration, $C_{0,i}$ the initial concentration and k_i the partition coefficient, for each alloy element i. Eq. A8, Eq. A10 and Eq. A13 become then:

$$C_{l,i} = \frac{C_{0,i}}{1-(1-k_i)f_s} \quad \text{Eq. A15}$$

$$C_{l,i} = \frac{C_{0,i}}{(1-f_s)^{(1-k_i)}} \quad \text{Eq. A16}$$

$$C_{l,i} = C_{0,i}[1 - f_s(1 - 2k_i\alpha')]^{\left(\frac{k_i - 1}{1 - 2k_i\alpha'}\right)} \quad \text{Eq. A17}$$

2. Solidification structure

2.1. Solid front morphology

The transition from liquid to solid state during metal alloys solidification is generally realised out of equilibrium. If the solid-liquid interface is closed to the thermo-dynamical equilibrium (defined by the phase diagram) thermal or solutal gradients will destabilise the interface. This destabilisation will induce different interface forms which will lead to the configuration of the solid, called microstructure. Three different classes of interface morphologies can be defined for a single, solid phase: planar front, cells and dendrites (Fig. A7a).

During metal alloys solidification, the obtained microstructure is generally columnar dendritic, the primary dendritic trunks are more or less oriented in the direction of the thermal gradient defined by the experimental conditions. Practically, the dendrites issued from different nuclei have different orientations. One grain contains dendrites resulted from the same nuclei and has the same crystallographic and morphological orientation. The grains are delimitated by zones corresponding to the change of dendrites orientation, called grain's boundaries (Fig. A7b). The structure and repartition of grains define the macrostructure of the sample.

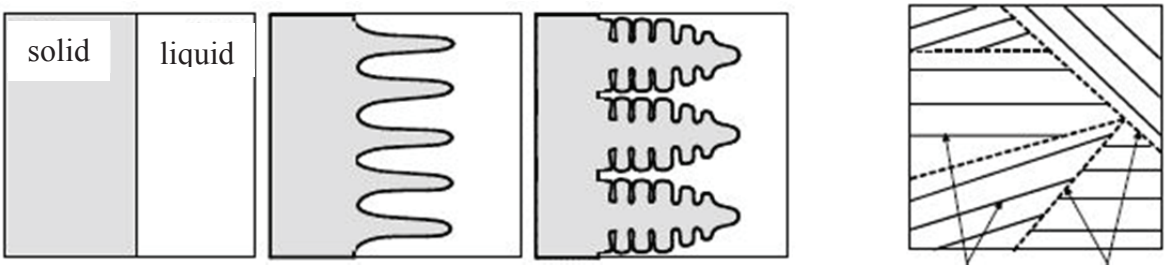

planar front cells dendrites grain's boundaries

a) b)

Fig. A7: a) Schema of different interface morphologies and resulting microstructures; b) Schematic view of a grain [A16].

Fig. A8 presents two example of microstructure resulted from the solidification of a SCN-3.6% acetone alloy and respectively pivalic acid at constant temperature gradient. These

organic alloys have the property to solidify by forming structures as metallic alloys. Because of their transparency, these alloys are often used to observe the dendritic growing structures.

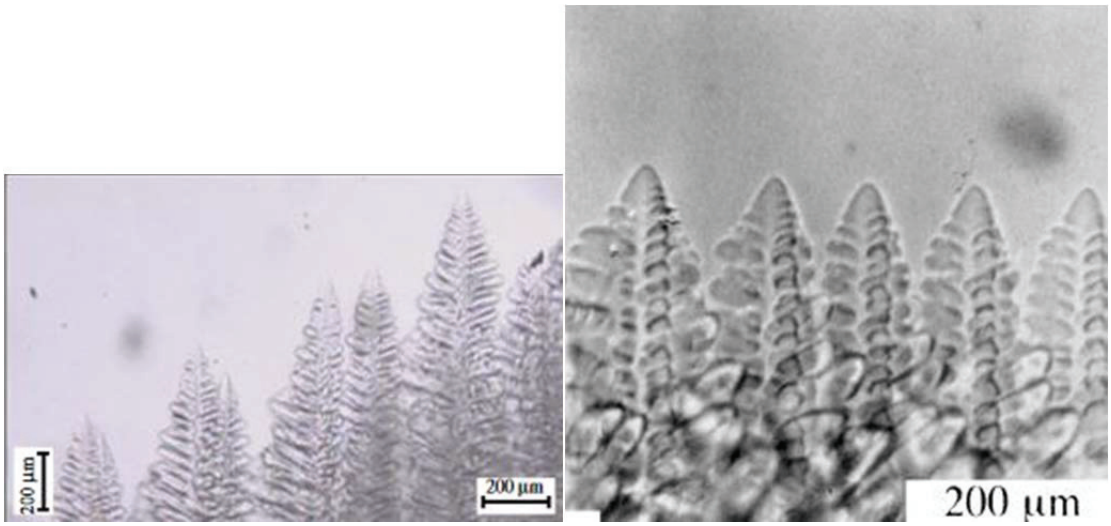

Fig. A8: Dendritic growth of a) SCN-3.6% acetone alloy [A17] for constant G (5.7Kmm^{-1}), V = 113 μm s^{-1}; b) pivalic acid [A18] for constant G (1.638Kmm^{-1}), V = 19.6 μm s^{-1}.

2.2. Solidified structures morphologies

If we look at the morphologies obtained after solidification, due to the different solid phases as illustrated in Fig. A9 a large variety of structures of different sizes can be observed:

- cells structure: elongated grains of column form, generally of same crystallographic orientation and limited by grains boundaries,
- dendritic structure: elongated grains with sharp edges and sidearms, generally of same crystallographic orientation and limited by grains boundaries,
- equiaxed structure: small grains of different crystallographic orientation,
- eutectic structure: lamellar or fibrous solid phases.

It is very important to notice that all these structures can be present in one single ingot. Their occurrence depends on the thermal history of the solidification and on the alloy composition.

a) b) c)

Fig. A9: Typical microstructure of a 10x6x1 cm^3 ingot of a Sn-3 wt.% Pb alloy cooled from the right wall [A10]: a) cooling rate 0.02 K/s, only columnar; b) cooling rate 0.023 K/s, columnar with equiaxed grains inside black oval; c) cooling rate 0.04 K/s, columnar with equiaxed grains inside black oval.

2.3. Solid-liquid interface and its stability

The metal solidification mechanism implies a thermo-dynamical phase change: from a disordered liquid state to an ordered solid crystal state. This state change requires a reorganisation at atomic level initiated by solid nuclei forming in the liquid. In order to create a solid nucleus, a solid-liquid interface needs to be created and its morphology depends on its stability during solidification.

2.3.1. Nucleation

Nucleation is a phenomenon out of equilibrium that needs an extra energy in order to build the solid-liquid interface. This energy barrier is overcome by undercooling, the liquid is at a temperature lower than the melting temperature. This temperature difference is called nucleation undercooling (ΔT_n). There are two nucleation types:

- Homogeneous nucleation: the nucleus is formed directly in the liquid without solid particle and solid contact (no mould contact). Even in a pure liquid, impurities are always present in a small percentage. Thus it is hard to speak about homogeneous nucleation in reality.
- Heterogeneous nucleation: solid particles already present in the liquid will reduce the nucleation energy barrier to be overcome the nucleation and the growth of a nucleus will be easier.

During solidification a nucleation rate is defined, that follows an Arrhenius type law [A19]:

$$I = I_0(N - N_0)\exp\left(-\frac{\Delta G_n}{k_B T}\right) \qquad \text{Eq. A18}$$

where I_0 is a constant (for metals is equal to 10^{20} s^{-1}), N_0 is the total number of nucleation sites per volume unit, N the number of activated sites, ΔG_n the activation energy, k_B the Boltzmann constant and T the temperature. Hunt [A19] in his heterogeneous model admitted that for small undercoolings ($\frac{\Delta G_n}{k_B T} \propto a/(\Delta T)^2$, where ΔT is the system imposed undercooling and a is a constant, $a = (\Delta T_n)^2 \ln(N_0 10^{20})$), the nucleation rate depends on the cooling conditions (number of activated sites, imposed undercooling) and on material properties (number of nucleation sites, nucleation undercooling).

2.3.2. Interface instability

Let us consider the case of a binary metal alloy of initial concentration C_0 of the alloy element, advancing with a planar front at a velocity V in a stationary regime. During the alloy solidification, the low solid solubility ($k < 1$) (Fig. A10) induces solute rejection in front of the interface. This solute rejection is limited to the boundary layer δ_c ($\delta_c = D_l/V$), characterised by the solute diffusion in the liquid D_l and interface velocity V. The resulting concentration profile is schematised on Fig. A11. The solute concentration in this boundary layer decreases exponentially with the distance x from C_0/k until C_0.

$$C(x) = C_0 + \left(\frac{C_0}{k} - C_0\right) exp\left(-\frac{V_x}{D_l}\right) \qquad \text{Eq. A19}$$

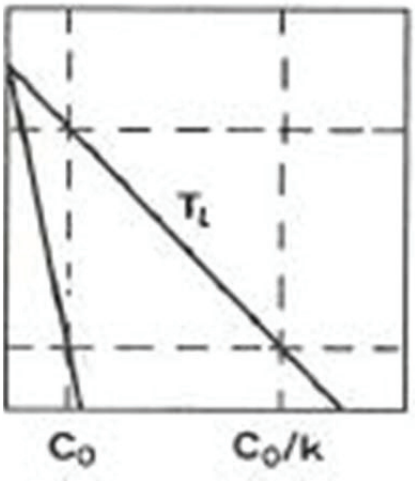

Fig. A10: Schema of a binary phase diagram with $k < 1$ [A1].

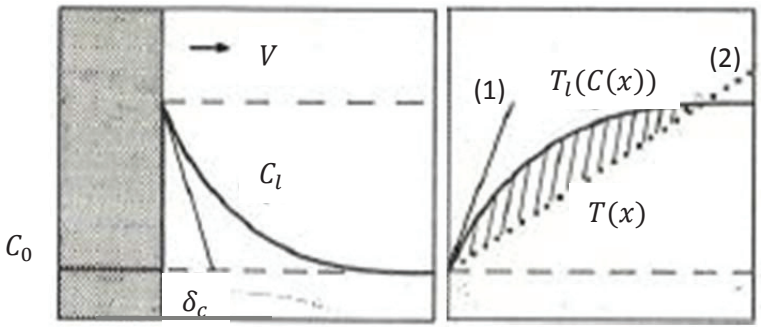

Fig. A11: Concentration a) and temperature b) profile at the solid-liquid interface. a) The solute rejection is localised in the liquid zone in front of the interface. b) The system can be stable (1) or under constitutional undercooling (2) (hashed part) [A1].

Considering the phase diagram from Fig. A10 the equilibrium temperature of the liquid can be described with the equation:

$$T_l\big(C(x)\big) = T_l + m(C(x) - C_0) \qquad \text{Eq. A20}$$

T_l and m are respectively the liquidus temperature and the liquidus slope.

The interface stability will then depend on the evolution on the temperature $T(x)$ imposed by the heat flux present during the solidification.

$$T(x) = T_m + m\frac{C_0}{k} + G(x) \qquad \text{Eq. A21}$$

Two cases can be distinguished (Fig. A11b):

(1) if $T(x)$ is larger than $T_l(C(x))$ locally, the system is stable, the solidification front stays planar.

(2) if $T(x)$ is lower than $T_l(C(x))$ locally, the system becomes unstable, the solid front destabilises. This instability condition is called constitutional undercooling because it depends only on the solute rejection in a given temperature gradient. More precisely a temperature gradient is defined at the interface: $G = \left(\frac{d}{dx}T(x)\right)_{x=0}$; in this manner the stability conditions can be determined and also the resulting interface morphology (Table A1). The interface instability results in the formation of cells or dendrites during solidification. Two growing classes can be defined:

- Constrained growth (directional solidification, G>0), corresponding to the unidirectional heat extraction. The dendrites grow generally under columnar form in the direction of the temperature gradient, following the isotherm advancement.
- Unconstrained growth (equiaxed solidification, G<0), corresponding to a radial heat extraction all around the crystal toward the undercooled liquid. The dendrite grows in an equiaxed manner until it reaches the next crystal. It should also be noticed that the equiaxed growth can take place in a positive temperature gradient, this is the case of the columnar to equiaxed transition (CET).

Thermal gradient	**Directional solidification** $G > 0$
$G > \frac{\Delta T_0}{D_l/V}$	Stable
$G < \frac{\Delta T_0}{D_l/V}$	Unstable

Table A1: Stability conditions for columnar dendritic solidification for the case of a binary alloy $\Delta T_0 = T_l - T_s = mC_0\left(1 - \frac{1}{k}\right)$.

2.4. Dendritic microstructure development

2.4.1. Kinetic growth

Kinetic growth is essentially dependent on phenomena happening around the dendrite tip. The dendrite tip undercooling ΔT^*, is defined for low velocities, as the sum of temperature undercooling ΔT_t, solute undercooling ΔT_c (solute and heat rejection) and curvature undercooling ΔT_r (Fig. A12):

$$\Delta T^* = \Delta T_t + \Delta T_c + \Delta T_r \qquad \text{Eq. A22}$$

The thermal undercooling is principally due to the latent heat release, when the temperature gradient in the liquid is negative (case of equiaxed solidification).

The solute undercooling corresponds to the constitutional undercooling (solute rejection in front of the interface):

$$\Delta T_c = m(C_0 - C_l^*) \qquad \text{Eq. A23}$$

where C_l^* is the interface concentration (the (*) is referring to the interface).

The curvature undercooling takes into account the surface tension phenomena existing at the interface:

$$\Delta T_r = \Gamma K_l \qquad \text{Eq. A24}$$

where Γ is the Gibbs Thomson coefficient ($\Gamma = \frac{\sigma}{\Delta S_f}$, σ is the surface tension of the solid-liquid interface and ΔS_f is the entropy of fusion) and K_l is the interface curvature.

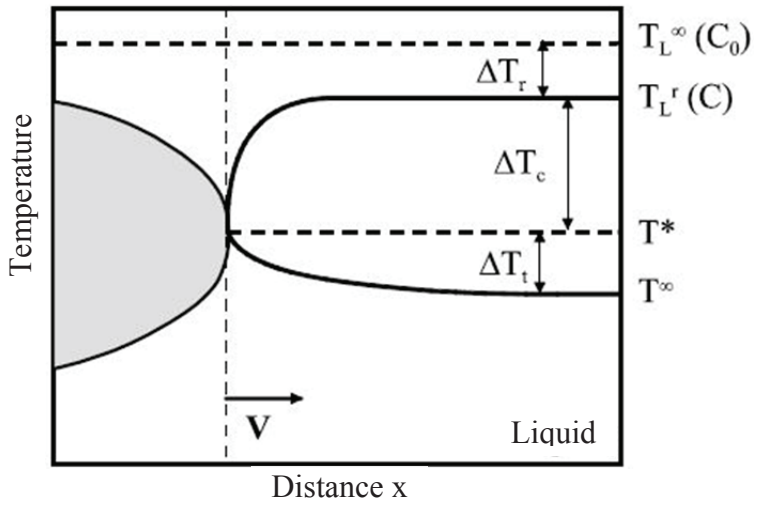

Fig. A12: Different contributions to the tip dendrite kinetic growth [Campanella A16].

For directional solidification ($G > 0$), the thermal undercooling can be neglected compared to the concentration undercooling for most of the metallic alloys, as the thermal diffusion is very large (~10^{-5} m^2/s) comparing to the solute diffusion (~10^{-9} m^2/s). The Eq. A22 can be then rewritten as follows:

$$\Delta T^* = \Delta T_c + \Delta T_r = T_l - T^* \qquad \text{Eq. A25}$$

T^* is the dendrite tip temperature. The effect of the solute rejection at the dendrite tip and the curvature effect on the growth morphology, must both be estimated.

In order to account for the dendrite tip diffusion (case of the stationary diffusion field), a number is defined as the ratio between the dendrite tip radius R and the boundary solute diffusion layer δ_c: $Pe = \frac{R}{\delta_c}$. This number is called the Peclet number and knowing that $\delta_c = 2D_l/V$ it can be also written as:

$$Pe = \frac{RV}{2D_l} \qquad \text{Eq. A26}$$

The mathematical solution of this diffusion field problem was elaborated by Ivantsov [A20] for the case of a paraboloid dendrite tip:

$$\Omega = I_v(Pe) \qquad \text{Eq. A27}$$

with the supersaturation $\Omega = \frac{C_l^* - C_0}{C_l^*(1-k)}$ and $I_v(Pe) = Pe * exp(Pe) * E_1(Pe)$, where

$I_v(x)$ is the Ivantsov function and $E_1(x)$ is the integral exponential function.

Langer and Müller-Krumbhaar [A21] introduced the marginal stability criterion, considering the curvature effect; they determined that the dendrite tip growths with a radius equivalent to the wave length of the marginal stability limit λ_i:

$$R = \lambda_i = 2\pi\sqrt{\frac{\Gamma}{G_c - G}} \qquad \text{Eq. A28}$$

where G_c is the solute gradient in the liquid at the dendrite tip: $D_l G_c = -V C_l^*(1-k)$. In this way it is possible to calculate R or T^* independently of V, using Eq. 26 and Eq. 28.

The KGT model [Kurz, Giovanola, Trivedi A22] combines the Ivantsov solution with the marginal stability criterion, for binary alloys, to determine the evolution of the dendrite tip radius, the temperature of the dendrite tip and the primary arm spacing with the growth velocity.

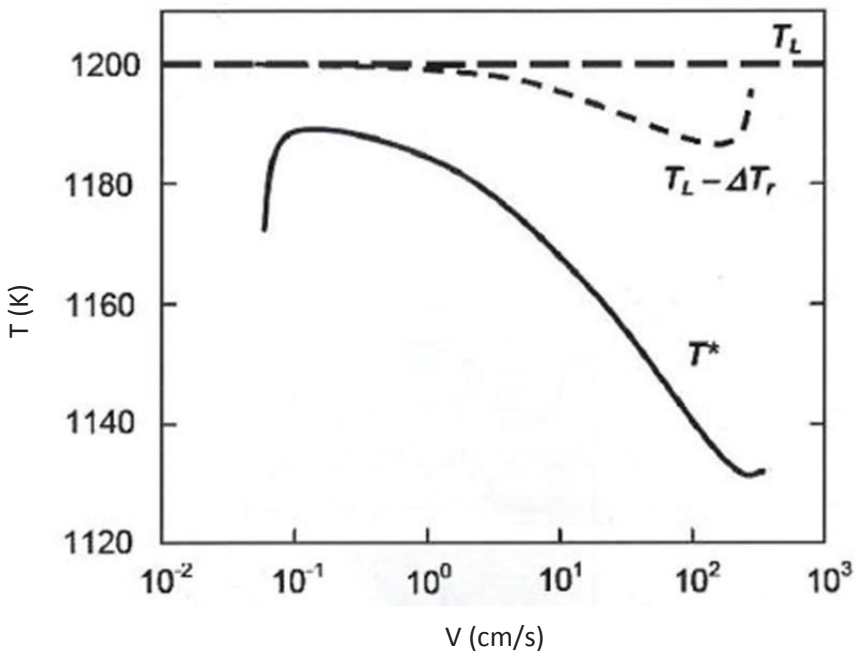

Fig. A13: Evolution of the dendrite tip temperature with the growth velocity for an Ag-5% Cu alloy [A22].

Fig. A13 shows the evolution of the dendrite tip temperature with the growth velocity and Fig. A14 presents the evolution curves of the dendrite tip radius and of the dendrite arm spacing with the velocity growth. Different microstructures can be distinguished, as illustrated in Fig. A14. At low velocity growth the planar front stays stable. At growth velocity corresponding to the constitutional undercooling the interface becomes unstable, first cells appear and then at higher growth velocities dendrites occur. At very high velocities the interface stabilises again and the absolute stability is reached [A1].

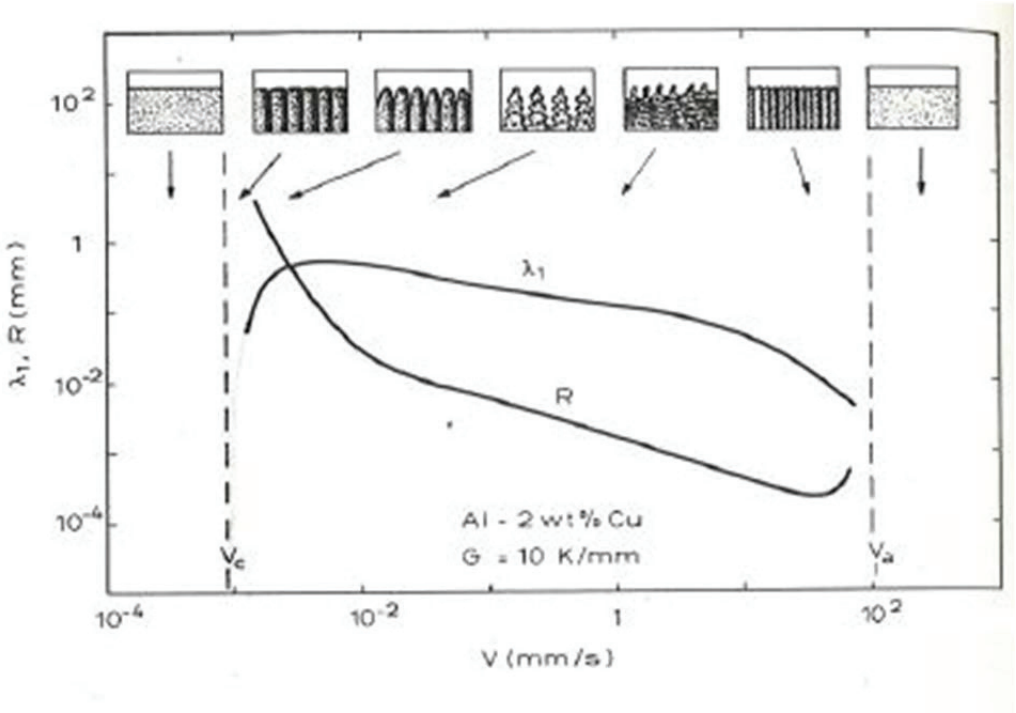

Fig. A14: Microstructure types assumed from the evolution curves of the dendrite tip radius and of the primary arm spacing λ_1 versus the velocity growth of a Al-2% Cu alloy [A1].

2.4.2. Primary and secondary dendrite arms spacing

Fig. A15 represents the major characteristics that define the dendritic microstructure: the dendrite tip radius R, the primary and secondary dendrite arms spacings λ_1 and λ_2. The microstructure, so the variation of these parameters, influences the material's properties (mechanical properties for example).

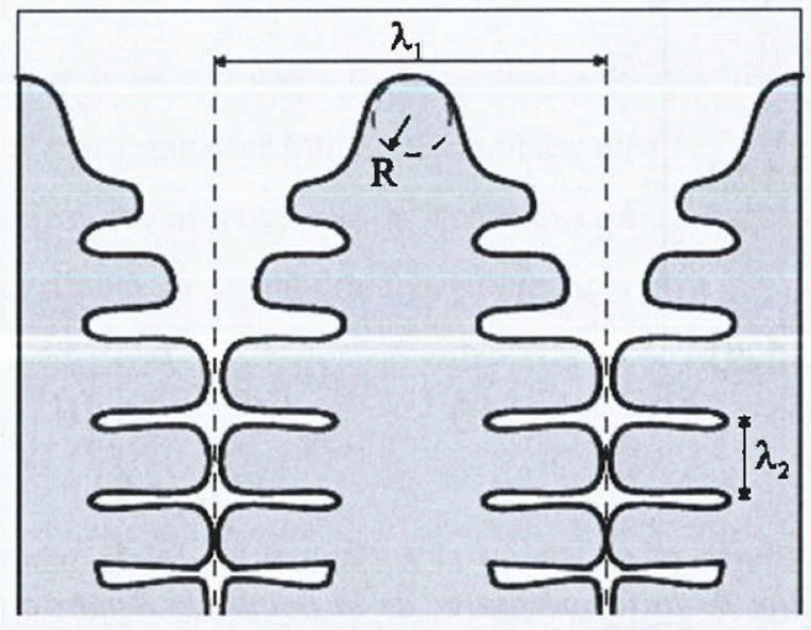

Fig. A15: Main characteristics of dendrites [Campanella A16].

The models to predict the primary dendrite arm spacing consider a relation, generally expressed as a function of the mushy zone thickness, the temperature gradient and the velocity growth. Eq. A29 shows an example of model [A23]:

$$\lambda_1 = 4.3\left(\frac{D_l \Gamma \Delta T_0}{m}\right)^{\frac{1}{4}} V^{-\frac{1}{4}} G^{-\frac{1}{2}} \qquad \text{Eq. A29}$$

Based on the work of Kattamis and Flemings [A24], Feurer and Wunderlin [A25] developed a model to calculate λ_2, taking into account the maturation phenomenon:

$$\lambda_2 = 5.5\left(M t_f\right)^{\frac{1}{3}} \qquad \text{Eq. A30}$$

with

$$M = \frac{\Gamma D_l ln\frac{C_l}{C_0}}{(1-m)(C_l - C_0)} \text{ and } t_f = \frac{\Delta T'}{|\dot{T}|} = \frac{\Delta T'}{|GV|} \qquad \text{Eq. A31}$$

where M is the maturation factor, t_f the solidification time, C_l is the final solute concentration in the liquid and $\Delta T'$ is the temperature difference between the dendrite tip and the solidus temperature. This can be approximated with ΔT_0.

3. Macrosegregation

Macrosegregation is the spatial variation of the concentration during the alloys solidification, on a scale starting from a few millimetres to centimetres, up to meters. These concentration variations have a negative impact on the alloys properties, leading even to the rejection of the solidified product. Macrosegregation happens in all the solidification processes: continuous casting, iron casting, aluminium and copper alloys mould casting, ingot casting in monocrystalline super alloys and in semi-conductors growth. Due to the low diffusivity of solutes in solid state and the large distances to cross, macrosegregation cannot be corrected by heat treatment, once the solidification is finished. The main cause for macrosegregation is the relative movement of the melt rich in solute and the solid phase. Most of the alloys elements have a lower solubility in the solid phase than in the liquid phase as illustrated in the phase diagram in Fig. A3. During the solidification process, the solute element is rejected from the solid into the liquid, thus the concentration of solute in the liquid phase is increasing continuously and is decreasing simultaneously in the solid. This segregation happens at the microstructure scale (which is often made by dendrites) and an inhomogeneity in the concentration distribution in the dendrites arms occurs, called microsegregation.

Ludwig et al. [A26] present the four mechanisms described by J.A. Dantzig and M. Rappaz [A27], responsible for macrosegregation, considering idealised scenarios. The macrosegregation is measured by means of mixture concentration, C_{mix}, as: $C_{mix} = \frac{f_l\rho_l\bar{C}_l+f_c\rho_c\bar{C}_c+f_e\rho_e\bar{C}_e}{f_l\rho_l+f_c\rho_c+f_e\rho_e}$, with f_l, f_c and $f_e$being the volume fractions of the liquid, columnar and equiaxed phases, ρ_l, ρ_c and ρ_e the corresponding densities, and $\bar{C}_l$, $\bar{C}_c$ and $\bar{C}_e$ the corresponding species concentrations averaged over the volume element. Note that volume fractions, densities and averaged concentrations are supposed to be constant in the volume element but may vary with time. The four mechanisms responsible for macrosegregation are associated with: i) melt flow; ii) moving crystals; iii) compact mush (a rigid solid skeleton that either consists of arrays of columnar dendrites or of globular/equiaxed crystals) and iv) phase transition. For each mechanism a Type$^+$ macrosegregation (corresponding to an increase of C_{mix}) and a Type$^-$ macrosegregation (corresponding to a decrease of C_{mix}) was described. Generally, any combination of the types of basic mechanisms might occur, thus they will be discussed intensively in the next sections.

Let us consider a small volume element inside the mushy region, which contains several dendrite arms separated by interdendritic liquid (Fig. A16).

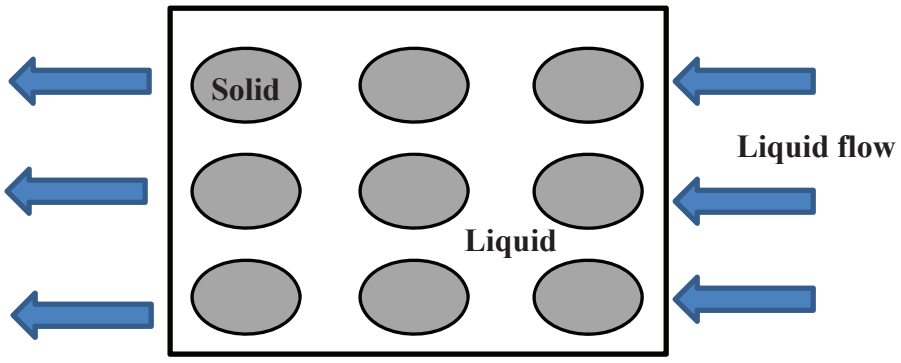

Fig A16: Schema of a small volume element inside the mushy region with dendrites arms (grey ovals represent their transversal sections) and interdendritic liquid circulating in-between.

In the case of no transport inside and outside this volume element, the average alloy composition inside the volume element stays constant and equal to the initial alloy composition C_0. If liquid or solid, with different solute concentration, enters this volume element, the average alloy composition in the volume element changes comparing to the initial alloy composition. These convections in the mushy region act over large distances and the consequence is the segregation on the macroscopic scale, known as macrosegregation. The macrosegregation can be positive or negative, by comparing the final concentration with the initial alloy concentration C_0.

The convection in the liquid can be generated by several mechanisms [Beckerman, A28]:

- variation of density caused by thermal or solutal gradients,
- flow induced by gas bubbles,
- forced convection due to electromagnetic stirring,
- movement of equiaxed crystals or dendrites fragments in the liquid,
- deformation of the solid in the mushy region due to mechanical or thermal constraints,
- liquid flow that feeds the solidification shrinkage.

3.1. Macrosegregation induced by liquid flow

The liquid flow through the mushy region, zone where the solid is supposed to grow as a rigid arrangement, is considered to be the main source for the macrosegregation phenomena. Macrosegregation in this case can be explained by the approach of Flemings et al. [A29]. They considered the local solute redistribution equations (LSRE), based on a local solute equilibrium on a small volume element inside the mushy zone, as illustrated in Fig. A16. As in a standard Scheil model the local solute diffusion in the solid phase is neglected, thus the

liquid composition in the mushy region, inside the volume element is supposed to be homogeneous and at the equilibrium. The solute concentration in the liquid C_l is controlled by the temperature and the liquidus slope given by the phase diagram. Considering the solute advection due to the liquid flow, inside and outside of the volume element and the different densities of the solid and liquid, Eq. A32 is obtained [Flemings A29]:

$$\frac{df_s}{dC_l} = \frac{(1-f_s)}{C_l}\frac{(1-\beta)}{(1-k)}\left(1-\frac{u_n}{v_T}\right) \qquad \text{Eq. A32}$$

where u_n is the liquid flow velocity in the direction normal to the isotherms, v_T is the isotherm velocity and β is the solidification shrinkage, expressed as the ration between the density difference (solid and liquid) and the solid density.

$$\beta = \frac{\rho_s-\rho_l}{\rho_s} \qquad \text{Eq. 33}$$

In one dimension the mass conservation equation shows that the liquid velocity, necessary to feed the solidification shrinkage, should be:

$$u_{n\backslash shrink} = v_T\left(1-\frac{\rho_s}{\rho_l}\right) = -v_T\left(\frac{\beta}{1-\beta}\right) \qquad \text{Eq. 34}$$

It must be noticed that the liquid flow due to solid shrinkage is opposite to the isotherm velocity, that is, in the same direction as the temperature decrease and the solid fraction increase. In Eq. A34, the liquid flow due to solid shrinkage $u_{n\backslash shrink}$ can have the same sign as v_T only if the alloy density decreases during the solidification ($\beta < 0$).

In Fig. A17 additional details about the liquid flow inside the mushy zone are given, making more clear the $u_{n\backslash shrink}$ and v_T terms. The solute concentration along the isotherms is constant, so the liquid flowing in or out the volume element along the isotherms has the same solute concentration and does not produce macrosegregation.

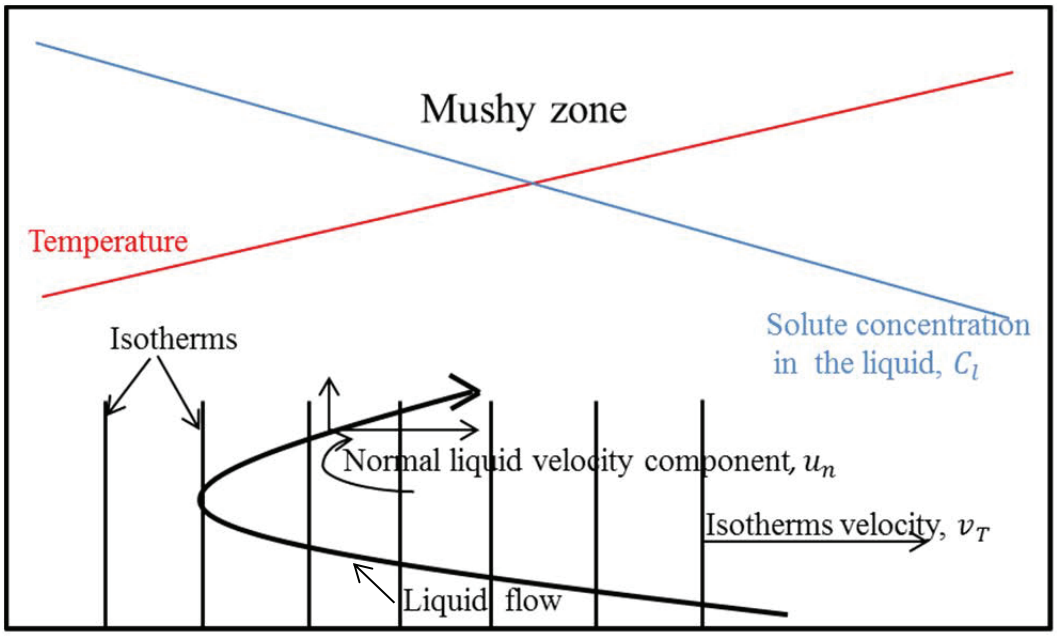

Fig. A17: Schema of liquid flow inside the mushy region.

Beckerman [A28] defined a flow factor ξ considering the liquid flow inside the volume element and the isotherms velocity, as follows:

$$\xi = (1-\beta)\left(1-\frac{u_n}{v_T}\right) \qquad \text{Eq. A35}$$

If ξ and k are assumed constant, Flemings's equation (Eq. A32) can be integrated and a modified Scheil equation can be obtained:

$$\frac{C_l}{C_0} = (1-f_s)^{\frac{k-1}{\xi}} \qquad \text{Eq. A36}$$

When $\xi = 1$ no macrosegregation occurs and Eq. A36 gives simply the Scheil classical equation.

There are two major cases when the macrosegregation phenomena do not occur ($\xi = 1$):

- If no shrinkage occurs ($\beta = 0$) and no liquid flow perpendicular to the isotherms exists ($u_n = 0$).
- If no liquid flow happens, except the flow needed to feed the solidification shrinkage in a given dimension:

$$u_n = -v_T \frac{\beta}{(1-\beta)} \text{ or } u_n = u_{n\backslash shrink}$$

When the flow factor ξ is different than 1 macrosegregation phenomena always happen, since the liquid concentration C_l varies in a different way than in the Scheil classical model. Using

the Scheil modified equation (Eq. A36), three different macrosegregation mechanisms can be described for $k < 1$.

3.2. Negative macrosegregation

This mechanism occurs when the flow coefficient is larger than 1, which means that the interdendritic liquid velocity in the direction of the temperature gradient (direction of the increase of the temperature and decrease of the solid fraction), is lower than the liquid velocity, necessary to feed the solid phase withdraw during the solidification ($u_n < u_{n\backslash shrink}$ or $\frac{u_n}{v_T} < -\frac{\beta}{(1-\beta)}$). It can be seen that for the same solid fraction f_s the liquid concentration C_l is lower compared to the case of $\xi = 1$, consequently a negative macrosegregation will take place.

In the case of $\beta \geq 0$, which means that the solid density increases during solidification compared to the liquid density, negative macrosegregation will take place only if the interdendritic liquid flows in the direction of the temperature decrease, towards a solid fraction increase and $|u_n| > u_{n\backslash shrink}$.

3.3. Positive macrosegregation

This macrosegregation type is characterised by a liquid concentration C_l higher than the case with $\xi = 1$, for the same solid fraction f_s. This mechanism will happen if the interdendritic liquid velocity in the direction of the temperature gradient (u_n) is higher than the shrinkage-driven flow velocity $u_{n\backslash shrink}$ and lower than the isotherms velocity ($v_T > u_n > u_{n\backslash shrink}$ or $\frac{u_n}{v_T} > -\frac{\beta}{(1-\beta)}$). This interval is defined by a flow coefficient with values in between 0 and 1.

The case $\beta = 0$, meaning that no solid shrinkage occurs during the solidification ($u_{n\backslash shrink} = 0$), is fulfilled when the liquid flows in the direction of the temperature increase, towards a decrease of solid fraction ($u_n > 0$), and has a velocity lower than the isotherms velocity ($u_n < v_T$).

The case $\beta > 0$ is often fulfilled when the liquid flows in the direction of the temperature decrease, towards regions of high solid fraction ($u_n < 0$), while $u_{n\backslash shrink} < 0$.

3.4. Remelting

This case will take place if the liquid circulates in the direction of temperature increase towards regions of low solid fraction, with a velocity higher than the isotherms velocity ($u_n > v_T$). This means that the flow coefficient is negative ($\xi < 0$).

Considering Flemings equation (Eq. A32) such flow will induce a decrease of solid fraction and of temperature. This means that remelting will be produced and segregated channels will form in the mushy zone. Once the solidification in this region is finished, a positive macrosegregation can be seen inside these channels.

The direction and the magnitude of the flow inside the mushy region depend on many factors. The permeability of the mushy zone is the most important parameter which can limit the flow inside the mush [A30]. Generally, the permeability decreases with the increase of solid fraction, thus small interdendritic spaces reduce the permeability.

The following examples illustrate more in detail the macrosegregation mechanisms described formerly.

3.5. Inverse segregation

Next to the cooled surfaces, a positive macrosegregation is often observed [Ohnaka and Matsumota A31]. This type of segregation is called inverse segregation (Fig. A18). J. S. Kirkaldy [A32] shows that it is a direct consequence of the second macrosegregation mechanism discussed previously. Actually next to the cooling surfaces (cooled walls) the liquid velocity is zero ($u_n = 0$), thus $u_{n\backslash shrink} < 0$. Consequently the condition $u_n > u_{n\backslash shrink}$ is always valid at the cooling surfaces and therefore a positive macrosegregation is produced.

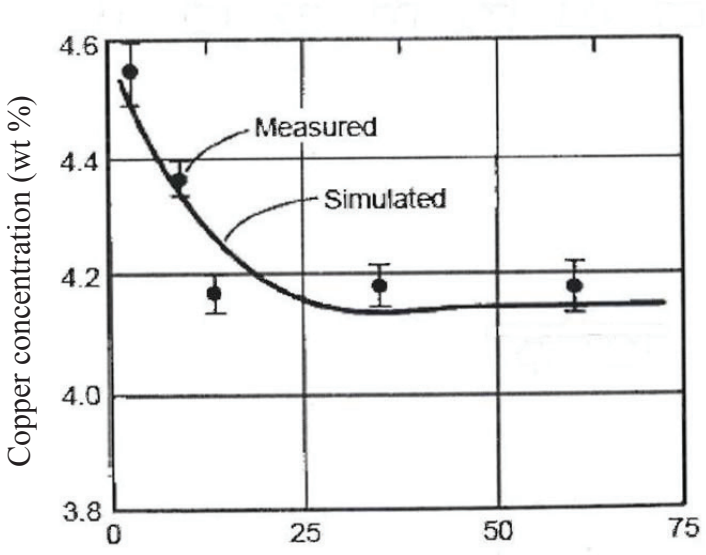

Fig. A18: Comparison of simulated and measured solute distribution during the unidirectional solidification of a Al-4.1 wt.% Cu ingot alloy [A31].

In the case when a gap exists between the cooling mould and the ingot to solidify, due to the metallostatic pressure the interdendritic liquid rich in solute is pressed into this gap. This phenomenon often occurs when positive macrosegregation is present at the chilled surface.

3.6. Macrosegregation due to the thermo-solutal convection flow

The first two macrosegregation mechanisms described previously, can be observed simultaneously if a convection flow exists in the mushy zone. This was demonstrated in the work of Ohnaka et al. [A31] on the Al-Cu alloy horizontal solidification. Fig. A19 presents a schema of the flow induced by themo-solutal convection with anti-clockwise circulating roll, in the bulk and also the liquid flow penetrating the mushy zone.

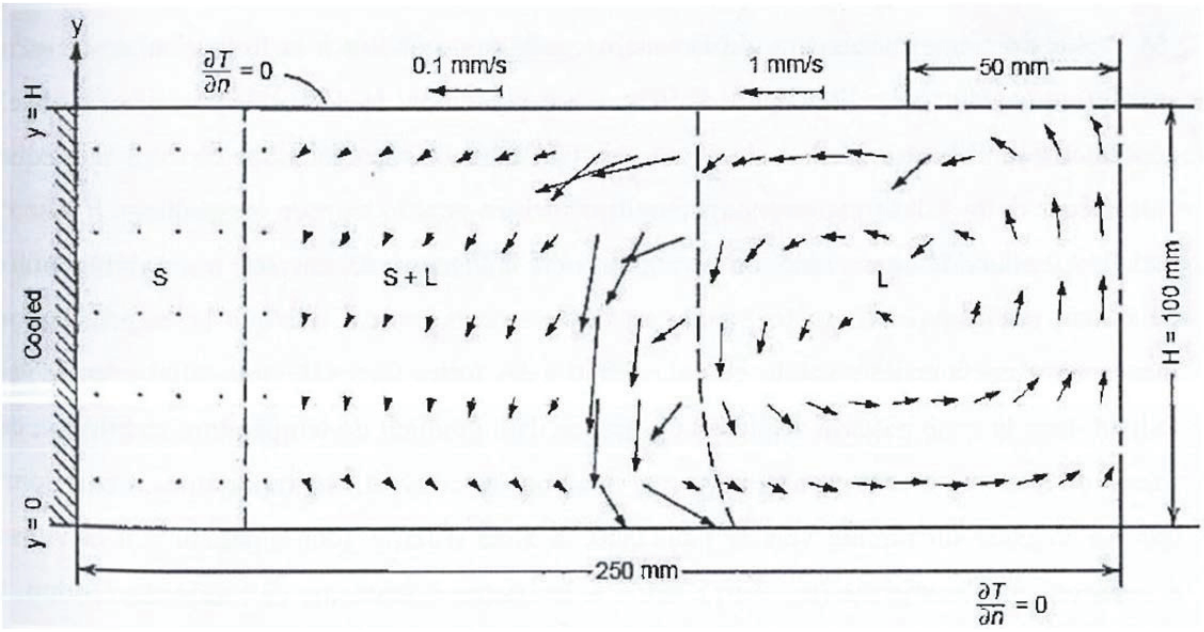

Fig. A19: Numerical simulation of the liquid flow (400 s after the cooling started) during the horizontal solidification of the Al-4.4 wt% Cu alloy [A31]

In the upper zone of the mushy region the flow is in the direction of the temperature decrease, $u_n < 0$. Considering the first macrosegregation mechanism a negative macrosegregation will occur in these conditions. The numerical simulations compared to the experimental results shown in Fig. A20, clearly confirm the occurrence of a negative macrosegregation in this upper region. Contrary in the lower part of the mushy region, the interdendritic liquid flows in the direction of the temperature increase $u_n > 0$ towards the bulk. This situation will produce a positive macrosegregation as explained in the second macrosegregation mechanism and firmly verified by results in Fig. A20.

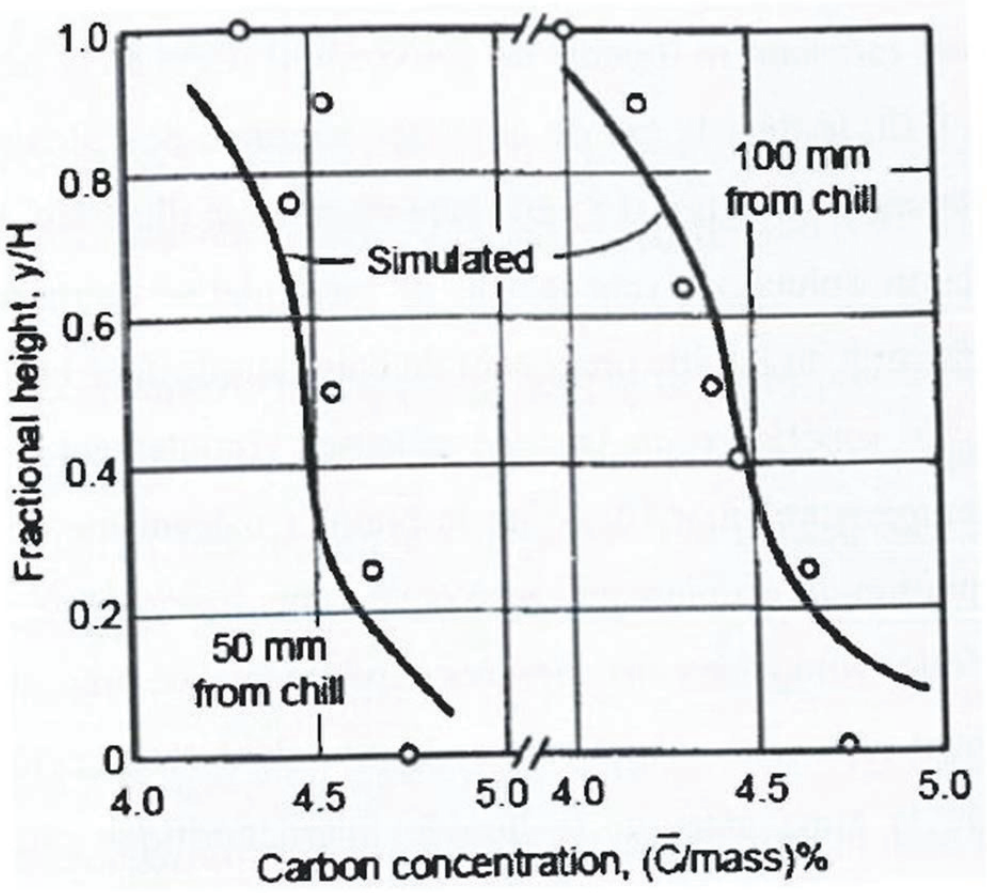

Fig. A20: Solute distribution in the ingot Al-4.4wt% Cu [A31]: negative macrosegregation at the top and positive at the bottom.

It is very interesting to notice that in the middle-high mushy region there is no macrosegregation, due to the flow parallel to the isotherm lines.

3.7. Segregated channels

The third macrosegregation mechanism brings the occurrence of channels. Fig. A21 shows this defect of segregation commonly called freckle. The segregated channels or freckles are often observed during the monocrystal directional solidification of Ni alloys, in the upper part. During this process a number of elements, as Al and Ti, are rejected in the liquid and at the same time heavy elements, as Tg, are incorporated in the solid. This situation is at the origin of a strong upper flow in the mushy zone. Even if a stable temperature gradient exits, convection rolls are so created, and considering that the liquid flow velocity is higher than the isotherms velocity, the solid fraction will decrease with the decrease of temperature (as described by the third mechanism). This phenomenon will create the conditions for the creation of channels in the mushy zone, where solute enriched liquid will flow out of the mush.

Fig. A21: Freckle of 2 mm diameter, observed in a Ni supper alloy [M. C. Schneider A33].

The numerical results presented in Fig. A22 show these flow configurations responsible for channels creation [A33]. In this case the size of the channel is a few millimetres thick and few cm high. During the solidification process these channels are filled with dendrites fragments, which can be seen in the final solidified alloy as equiaxed crystals. In this way the positive macrosegregation produced in these channels can then be seen in the numerical simulation results (Fig. A22).

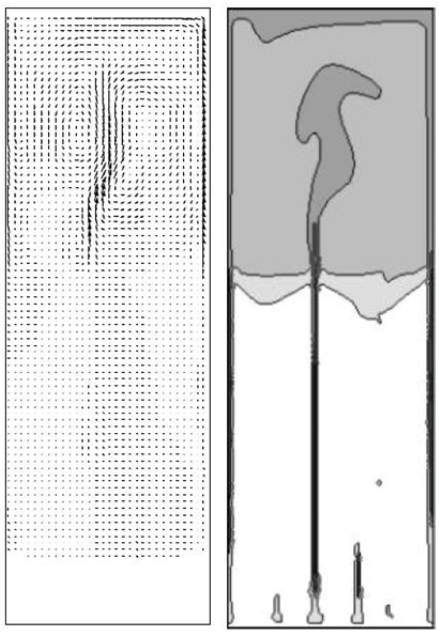

Fig. A22: Numerical simulation of segregated channels during the directional solidification of a Ni supperalloy [A33].

3.8. Macrosegregation produced by solid movement

Movement of solid during solidification can also produce macrosegregation in ingots, but no simple theory exists to clearly explain this phenomenon. Nevertheless few examples can be brought to illustrate these complex phenomena [Beckermann A34]. The most encountered form of solid movement is the sedimentation or the floating of small solid pieces at the beginning of solidification process. These can be constituted of dendrites fragments detached from the mushy zone or from equiaxed crystals already present in the liquid. These solid pieces can flow or fall down depending on their density compared with the liquid density. Generally these pieces have a different composition than the initial alloy composition and consequently their movement towards different parts of the ingot will produce macrosegregation. A well-known case is the example of the negative segregation cone observed in the bottom part of casting ingots (Fig. A23). This type of macrosegregation is limited to the equiaxed zones induced by dendrites sedimentation, which are poor in solute [Flemings A35, Lesoult A36].

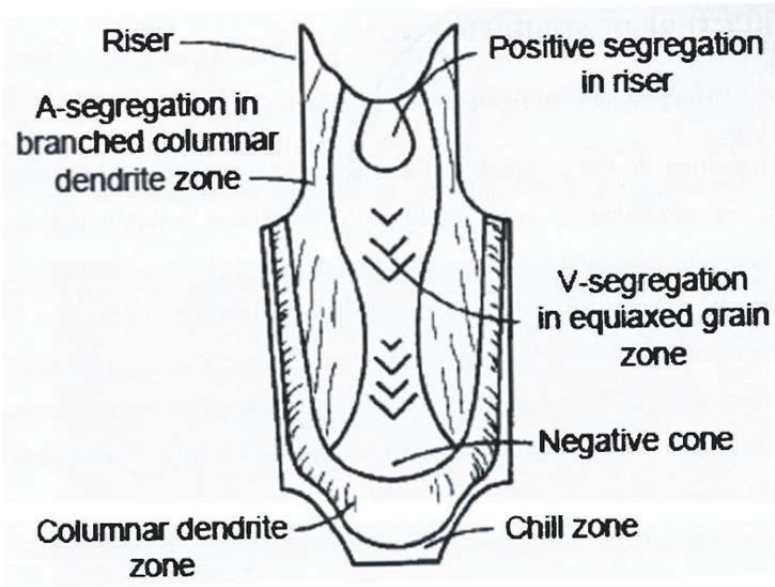

Fig. A23: Different types of macrosegregation observed in steel ingots [A34].

The flow entrained by the thermo-solutal forces also creates a negative macrosegregation in the lower part of the steel ingot but its effects are not so significant compared to the solid particles precipitation [Gu A37]. Similarly the negative axial macrosegregation in continuous casting by direct cooling is sometimes due to the sedimentation of solid fragments poor in solute. Reddy [A38] observed a comparable effect for an interdendritic flow due to the solid phase shrinkage, but these effects are still not very well understood.

Another example of macrosegregation generated by solid movement in the central zone of a steel ingot, characterized by equiaxed crystals is called V-type segregation (Fig. A23). This macrosegregation is composed of strips rich in solute appearing periodically along the median line. The V-type segregation is often produced by equiaxed crystals occurring in the centre of the ingot, forming a weak net that can be easily broken by the metallostatic forces [Flemings A35 and Lesoul A36].

4. Columnar to equiaxed transition

It has been seen previously that in dendritic growth two cases exist: columnar dendritic growth (directional constraint solidification) and equiaxed dendritic growth (non-constraint solidification). The transition between the two modes is possible and depends on the thermal and solutal conditions present during solidification. This transition called columnar to equiaxed transition (CET) has a major influence on the final material properties as the microstructure is completely different. The occurrence of equiaxed crystals during directional solidification is due to the fact that an undercooled liquid zone exists (comprised in between the tip dendrite temperature T^* and the liquidus temperature T_l). If solid nuclei are present in this zone they can grow and a growth competition between the equiaxed crystals and the columnar front starts and eventually leads to CET. The equiaxed crystals formation can have two origins:

- Fragmentation: the nuclei can be represented by dendrite's fragments detached from the mushy zone by local remelting and transported via convection flow in the undercooled liquid zone (Fig. A24). The fragmentation is a not very well understood phenomenon, but observation on organic alloys solidification have been made by C.J. Paradies [A37] and T. Sato [A38]. As Jackson [A39], Paradies [A37] and Sato [A38] related fragmentation to the local remelting of the finest dendrites arms at their neck. Liu [A40] concluded that the fragmentation is essentially due to the dissolution of dendrites arms because of solute variation in the mushy zone (solute variation caused by deceleration of the cooling velocity). Gu and Beckermann [A41] as Hellawell [A42] associated fragmentation to the solutal dissolution of dendrites arms in segregated channels. It should be noticed that Pilling's work [A43] states that interdendritic liquid flow causing mechanical deformation cannot be responsible for dendrites fragmentation.
- Inoculation: introducing seeding particles will constitute preferential growing sites (heterogeneous nucleation) for the further equiaxed crystals and consequently favours

CET even with a minimum undercooling. If the undercooling necessary to the heterogeneous nucleation is lower than the maximum undercooling existent in the liquid and if enough seeding particles are present then CET will be promoted.

4.1. CET blocking mechanism: mechanical

Considering a columnar dendritic front advancing at a velocity V in a thermal gradient G (Fig. A24), with the growing dendrite inducing an undercooled zone $\Delta T^* = T_l - T^*$ ahead of the columnar front, two cases can be distinguished:

- The undercooling ΔT^* is lower than the nucleation undercooling ΔT_n, the growth stays columnar.
- The undercooling ΔT^* is higher than the nucleation undercooling ΔT_n, the equiaxed crystals will grow ahead of the columnar front, in the undercooled zone (Fig. A24)

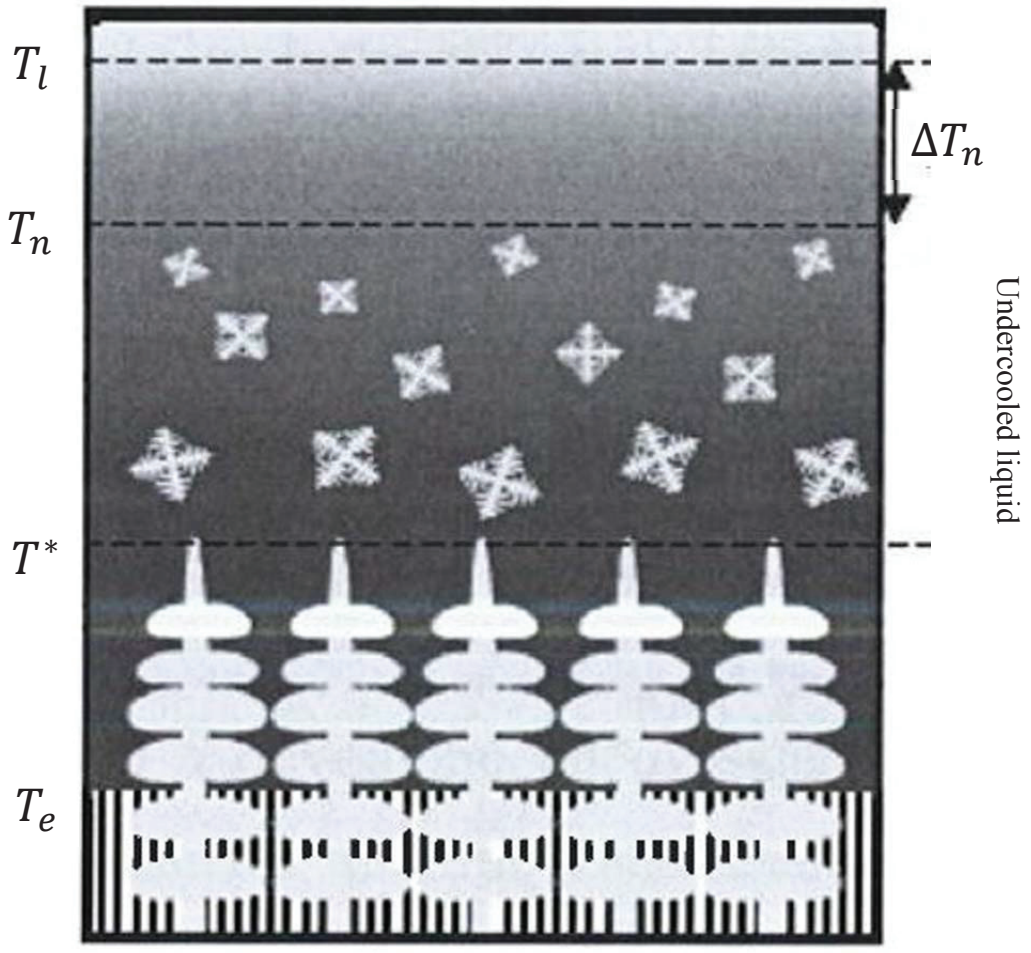

Fig. A24: Representation of CET, where T_l is the liquidus temperature, T_n the nucleation temperature, T^* the dendrite tip temperature, T_e the eutectic temperature and ΔT_n the nucleation undercooling [Reinhard A46].

In reality CET is a complex phenomenon, where many processes get involved: nucleation, growth kinetic (equiaxed and columnar), preferential growth directions, liquid flow convection and the resulting solute transport. Analytical and numerical qualitative approaches [A47] were developed to predict the CET, based on mixed models of heterogeneous nucleation and dendritic growth. Hunt [A19] established, based on thermal gradient at the interface, an analytical criterion of the columnar to equiaxed transition. He considered the number of the nucleation sites per volume, N_0, and the ratio between the nucleation undercooling and the constitutional undercooling. A growing criterion Φ_E was defined:

$$\Phi_E = \frac{4\pi r^3 N_0}{3} \qquad \text{Eq. A37}$$

where r is the radius of a equiaxed crystal equal to

$$r = \int_0^t V_e dt = \frac{A\left(\Delta T^3 - \Delta T_n^3\right)}{3VGC_0} \qquad \text{Eq. A38}$$

When $\Phi_E < 0.0066$ only columnar growth occurs and when $\Phi_E > 0.0066$ only equiaxed growth happens. In Eq. A38, V_e represents the growth velocity of an equiaxed crystal given by the dendrite tips, estimated using a KGT type model $V_e = A\Delta T^2/C_0$ (A is a growing constant depending on the material and ΔT the local undercooling). The cooling velocity is expressed as $\frac{dT}{dt} = -GV = \frac{d(\Delta T)}{dt}$ [A1]. Combining Eq. A37 and A38 for a columnar growth (the undercooling for the columnar growth is equal to $\Delta T_{col} = (VC_0/A)^{1/2}$), a criterion based on the thermal gradient is obtained. A columnar structure occurs if

$$G > 0.617(100N_0)^{1/3}\left(1 - \frac{\Delta T_n^3}{\Delta T_{col}^3}\right)\Delta T_{col} \qquad \text{Eq. A39}$$

and in the case of an equiaxed growth

$$G < 0.617(100N_0)^{1/3}\left(1 - \frac{\Delta T_n^3}{\Delta T_{col}^3}\right)\Delta T_{col} \qquad \text{Eq. A40}$$

These entire criterions are valid under certain hypothesis:

- The solute transport is done only by diffusion (without convection);
- The heterogeneous nucleation sites are randomly distributed and are active immediately, which makes the nucleation undercooling ΔT_n lower than the undercooling ahead of the solidification front;
- The growth of an equiaxed crystal is considered to be spherical;
- The temperature gradient is stable, thus the growth velocity of the columnar front and the temperature gradient are assumed to be constant.

Considering Eq. A39 and A40 a microstructure map can be drawn for any given system. Generally the equiaxed growth is favoured if the solid growth velocity, the alloy concentration and the nucleation sites are increasing and if the nucleation undercooling or the temperature gradient decreases and columnar growth occurs at low velocities and high gradients (Fig. A25).

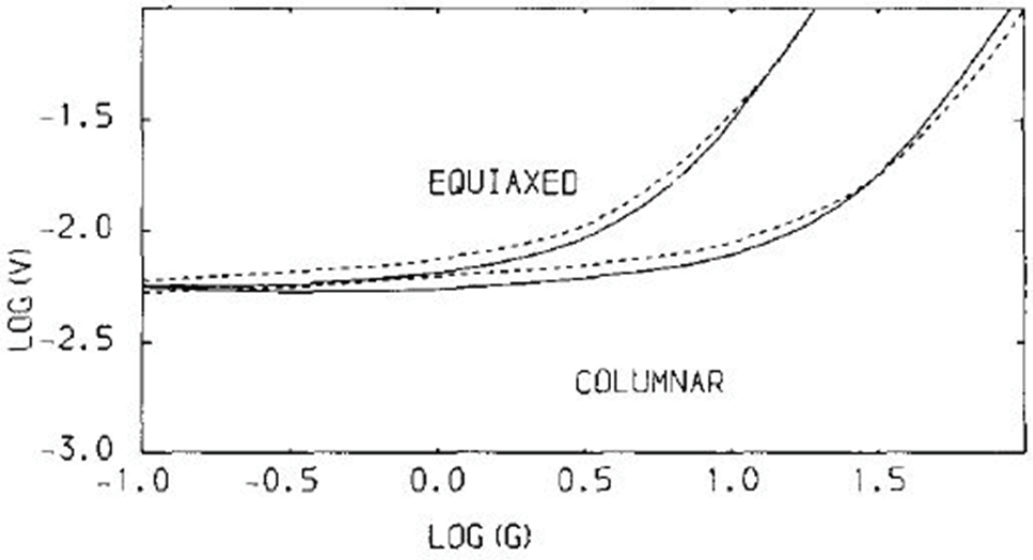

Fig. A25: Hunt diagram for Al-3wt.% Cu for a nucleation undercooling 0.75 K and N_0 = 1 mm^{-3}.

Later Flood [A48] developed a numerical model using a more complex description of the thermal exchanges between the growth and the solidification front advancement. Based on the Hunt model, Gäumann completed Flood's study by giving more importance to the nucleation [A49]. Wang considered a finite difference approach to solve the problem [A50]. All those models are valid only for a dendritic growth oriented parallel to the heat flux.

In order to account for super-alloy solidification, Gäumann [A51] adapted Hunt's model, considering the growth orientation. In the same way Gandin [A52] developed a cellular automata model to simulate growth competition among columnar grains, by taking into account the crystallographic orientation of the grains and the temperature evolution in the system. This model was then coupled with heat flux calculations, using finite elements method, resulting in a very important numerical tool of grain structure prediction in 2D and in 3D [A53].

The CET is of great importance for industry and it should be noticed that the complexity of this phenomenon is resulted from the large diversity of industrial casting conditions (particles seeding, cooling velocity, presence of natural convection or forced convection flow, etc.). The understanding of different phenomena occurring during CET will help to fully understand the microstructure obtained in castings.

4.2. CET blocking mechanism: solutal

This mechanism is based on solutal interactions due to the solute rejection during equiaxed growth. The equations are issued from Wang and Beckerman model [A50]. Both convection flow and movement of free equiaxed crystals are not taken into account (grains sedimentation due to gravity is also neglected). Martorano et al. [A54] define three phases inside a volume element:

- A solid volume fraction ε_s,
- A liquid interdendritic fraction ε_d,
- A liquid extradendritic fraction ε_l,

and $\varepsilon_s + \varepsilon_d + \varepsilon_l = 1$.

The grain volume fraction is expressed by $\varepsilon_g = \varepsilon_s + \varepsilon_d$. In another way the inter- and extra-dendritic liquids are separated by an invisible envelope all around the grain (Fig. A26).

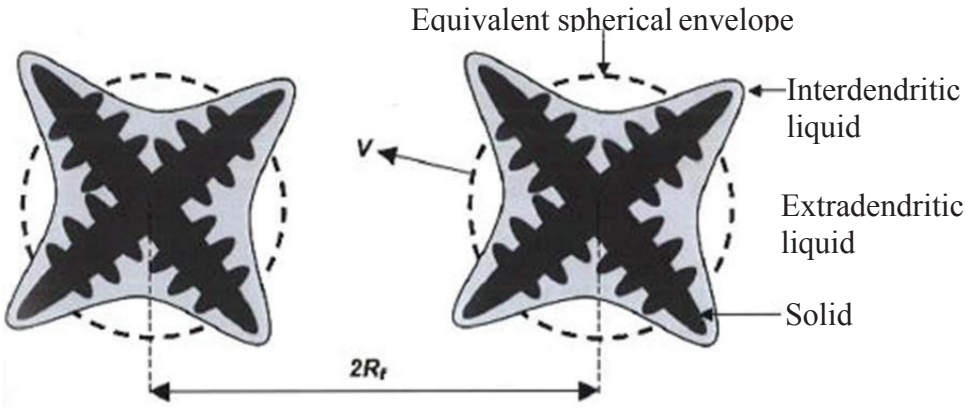

Fig. A26: Schema of the envelope around the equiaxed grain delimitating the inter- and extra-dendritic liquids [A54].

Using these notations, Hunt's criterion of columnar to equiaxed transition becomes: $\varepsilon_g = 0.49$. To model the equiaxed grain, with its dendritic branches, a sphere of equivalent surface S_e is defined (as shown on Fig. A26), the distance between two grains is $2R_f$, where R_f represents the final grain radius. The grain growth velocity, which is determined by the

kinetic of free tip growth (Lipton, [A47]), is added to the energy and solute conservation equations.

$$V = \frac{4\sigma^* D_l m_l (k-1) C_l^*}{\Gamma} (Iv^{-1}(\Omega))^2 \text{ with } Iv^{-1}(\Omega) = 0.4567 \left(\frac{\Omega}{1-\Omega}\right)^{1.195} \quad \text{Eq. A41}$$

where $\sigma^* \approx 1/(4\pi^2)$ is the stability constant, Γ is the Gibbs-Thomson coefficient, Iv^{-1} is the inverse of the Ivantsov function and Ω is the supersaturation, defined as $\Omega = \frac{C_l^* - C_l}{C_l^*(1-k)}$.

Hunt's model considers C_l constant and equal to C_0, while Martorano's model considers variation of C_l during equiaxed growth (but not during columnar growth). Phenomena playing a role in the solutal interactions, like the solutal blocking due to solute rejection by the equiaxed grains during their solidification, are therefore considered. The solute rejected enriches the inter-dendritic liquid (Fig. A27) and consequently the gradient concentration, which is the driving force, will decrease progressively. The grains growth will then slow down until it stops (the grains do not come in direct contact).

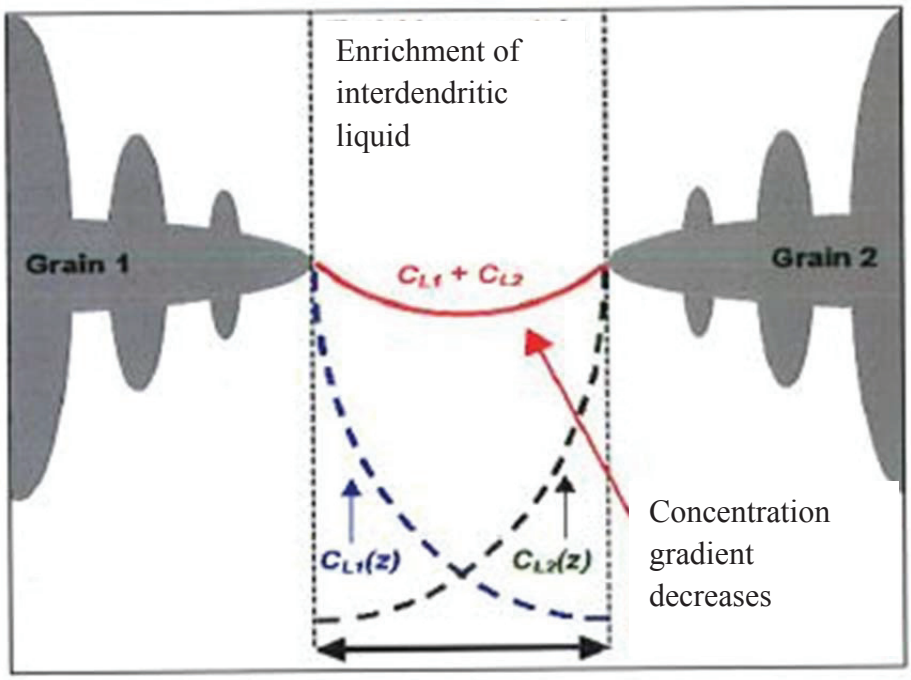

Fig. A27: Concentration profile between two equiaxed grains during solutal blocking [A46].

Martorano's model puts in evidence two limiting cases for CET, represented on Fig. A28. In the first case the equiaxed grains density is relatively large (as in the case when an inoculant is introduced) thus the grains remain practically spherical. A large number of globular grains reject a great quantity of solute in the surrounding liquid, causing a drastic decrease of the

solutal undercooling ahead of the columnar front. The CET takes then place for volume fraction values lower than 0.49 (Hunt's criterion). In the second case the grain density is relatively lower but the grain size is larger (R_f increases). The equiaxed grains become strongly dendritic, hence for large R_f values, the liquid concentration C_l stays for a while close to the initial concentration C_0 and afterwards tends to C_l^*. During this period of time the equiaxed grains continue to grow and the CET takes place for volume fraction larger than 49% as predicted by Hunt's criterion.

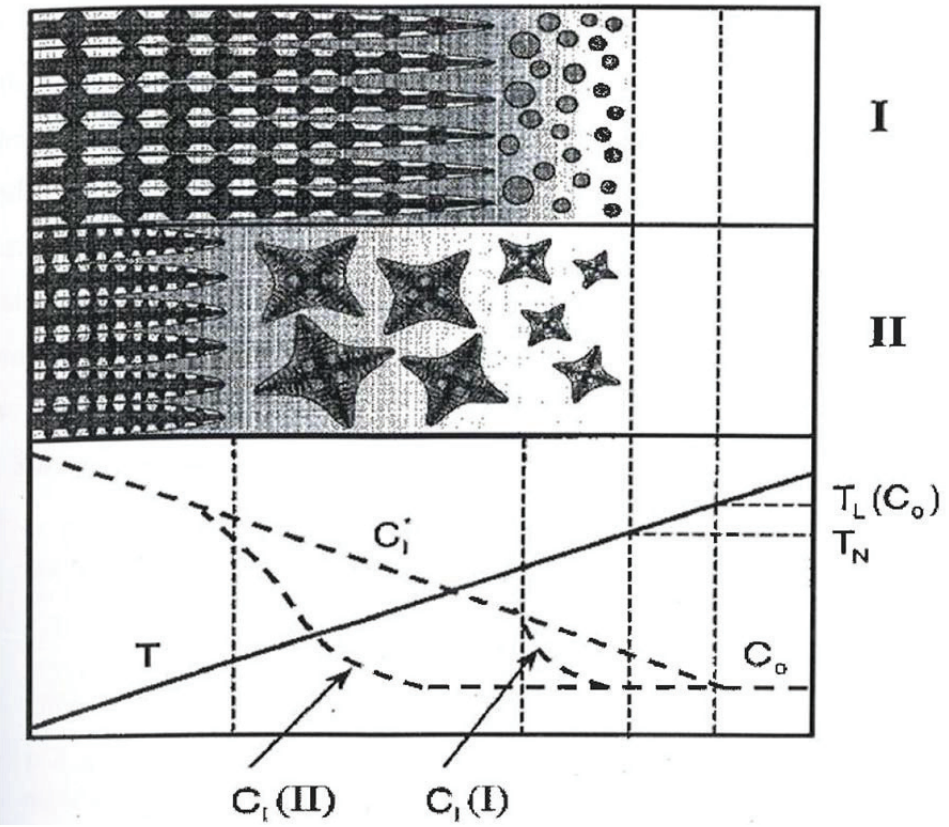

Fig. A28: Solutal interaction between columnar and equiaxed grains [A54]. Case I: solutal interactions in the presence of a large density grain. Case II: solutal interactions in the presence of a lower density grain.

The comparison of Martorano's model [A54] with the two models of Gandin results in a satisfactory concordance for CET. Recently Badillo and Beckermann [A55] developed a CET model employing the phase field method. They consider the elongation of the equiaxed grain in the direction of the temperature gradient during their growth, the existence of a mixed growing regime columnar–equiaxed for large velocity growth and also the particle deactivation potential for nucleation via solutal interactions.

A three phase Eulerian approach was developed by Ludwig and Wu [A56, A57] to model the columnar to equiaxed transition. The three phases defined during the mixed solidification are: the parent melt, the columnar dendrites and the equiaxed crystals. A binary "steel" (Fe–0.34 wt.% C) ingot casting was used as benchmark for simulation, in ordered to demonstrate the ability of the model. This model was modified and a five phase regions resulted: extradendritic melt, interdendritic melt and solid dendrites in equiaxed grains, interdendritic melt and solid dendrites in columnar arrays of dendrites [A58].

All the classical CET models don't consider the natural convection flow nor the forced convection flow, which has a major influence (fragments movement, equiaxed grains movement, particle movement, solute repartition, etc.) and neither the gravity effects (particles and grains sedimentation, etc.). We will propose a new CET mechanism resulting from a coupling between equiaxed crystals production and hydrodynamics (see Publication 6: "*On the coupling mechanism of equiaxed crystal generation with the liquid flow driven by natural convection during solidification"*).

The theoretical and bibliographic study presented in this chapter is based on fundamental notions of the binary metallic alloys solidification process. The works realised by Kurz and Fisher [A1], Flemnings [A2], Rappaz et al. [A27], Hunt [A19] represent the base of the solidification knowledge. These fundamentals of solidification will help to understand the problems developed later, but also permit us to have an overview of the solidification topic: equations' models, analytical and experimental studies, which are supported by experimental benchmark.

References Part A

[A1] W. Kurz and D.J. Fisher: *"Fundamentals of solidification"*, fourth revised ed., Trans. Tech. Publication ltd., 1998.

[A2] M. C. Flemings: *"Solidification processing"*, McGraw-Hill, INC., 1974.

[A3] L. G. Lesoult: *"Solidification, cristallisation et microstructures"*, Techniques de l'ingénieur, M58, pp. 1-26.

[A4] D. J. Allen and J. D. Hunt: *"Discussion of the nucleation and solidification of Al-Ti alloys"*, Met. Trans. A, 1979, vol. 10A, pp. 1389.

[A5] H. D. Brody and M. C. Flemings: *"Solute redistribution in dendritic solidification"*, TMS of AIME, 1966, vol. 236, pp. 615.

[A6] L. Hachani, B. Saadi, X. D. Wang, A. Nouri, K. Zaidat, A. Belgacem-Bouzida, L. Ayouni-Derouiche, G. Raimondi, Y. Fautrelle: *"Experimental analysis of the solidification of Sn-3wt.%Pb alloy under natural convection"*, Int. J. Heat and Mass Transfer, 2012, vol.55, pp. 1986.

[A7] A. F. Giamei and B. H. Kear: *"On the nature of freckles in nickel base superalloys"*, Metall. Trans., 1970, vol.1, pp. 2185.

[A8] P. Prescot and F. Incropera: *"Convection heat and mass transfer in alloy solidification"*, Advances in heat transfer, 1996, vol. 28, pp. 231.

[A9] A. Kharicha, M. Stefan-Kharicha, A. Ludwig and M. Wu: *"Simultaneous observation of melt flow and motion of equiaxed crystals during solidification using a dual phase particle image velocimetry technique. Part 1: stages characterization of melt flow and equiaxed crystals motion"*, Metall. Mater. Trans. A, 2013, vol. 44, pp. 661.

[A10] J. R. Sarazin and A. Hellawell: *"Channel formation in Pb-Sn, Pb-Sb and Pd-Sn-Pb alloy ingots and comparison with the system"*, Met. Trans. A, 1988, vol. 19A, pp. 1861.

[A11] M. I. Bergman, D. R. Fearn, J. Bloxham, and M. C. Shannon: *Convection and Channel Formation in Solidifying Pb-Sn Alloys"*, Met. Trans. A, 1997, vol. 28A, pp. 859.

[A12] G. H. Gulliver: *"Metallic alloys: their structure and constitution"*, London, Griffin, 1922.

[A13] E. Scheil: *"Bemerkungen zur schichtkristallbildung"*, Z. Metallforschung, 1942, vol. 34, pp. 70.

[A14] T. W. Clyne and W. Kurz: *"Solute redistribution during solidification with rapid solid state diffusion"*, Met. Trans., 1981, vol. 12A, pp. 965.

[A15] S. Kobayashi: *"Solute redistribution during solidification with diffusion in solid phase: a theoretical analysis",* J. Crystal Growth, 1988, vol. 88, pp. 87.

[A16] Th. Campanella, PhD, École Polytechnique Federale de Lausanne, 2003.

[A17] E. Üstün, E. Cadırlı and H. Kaya: *"Dendritic solidification and characterization of a succinonitrile–acetone alloy"*, J. Phys.: Condens. Matter, 2006, vol. 18, pp. 7825.

[A18] E. Cadirly, N. Marasli, B. Bayender, M. Gündüz: *"Investigation of the structure parameters according to the solidification parameters for pivalic acid"*, J. Mat.Sci. 1999, vol.34 pp. 5533.

[A19] J. D. H unt: *"Steady-state columnar and equiaxed growth of dendrites and eutectics",* Mater. Sci. Eng. V, 1984, vol. 65, pp. 75.

[A20] G. P. Ivantsov, *Doklady Akademii Nauk SSSR.,* 1947, vol. 58, pp. 567.

[A21] J. S. Langerand H. Muller-Krumbhaar: *"Theory of dendritic growth I. //. and I/1*", Acta Met., 1978, vol. 26, pp. 1681.

[A22] W. Kurz, B. Giovanola and R. Trivedi: *"Theory of microstructural development during rapid solidification",* Acta Met., 1986, vol. 34, p p . 823.

[A23] W. Kurz and D. J. Fisher: *"Dendrite growth at the limit of stability: tip radius and spacing",* Acta Met., 1986, vol. 29, pp. 11.

[A24] T. Z. Kattamis and M. C. Fleming: *"Dendrite morphology, microsegregation and homogenization of 4340 low-alloy steel",* Trans. TMS-AIME, vol. 233, 1965, pp. 992.

[A25] U. Feurer and R. Wunderlin: *"Fundamentals of solidification",* Trans. Tech. Publication LTD. Aedermannsdorf, Switzerland, 1986.

[A26] A. Ludwig, M. Wu and A. Kharicha: "*On macrosegregation*", Metall. Mater. Trans. A, 2015, vol. 46, pp. 4854.

[A27] J. A. Dantzig and M. Rappaz: "*Solidification"*, EPFL, London, 2009.

[A28] C. Beckermann: *"Macrosegregation"*, ASM Handbook, 2008, vol. 15, pp. 348.

[A29] M. C. Flemings and G. E. Nereo: *"Macrosegregation: part 1"*, Trans. Met. Soc. AIME, 1967, vol. 239, pp. 1449.

[A30] D. R. Poirier: *"Permeability for flow of interdendritic liquid in columnar-dendritic alloys"*, Metall. Trans. B, 1987, vol. 18, pp. 245.

[A31] I. Ohnaka and M. Matsumoto: *"Computer simulation of macrosegregation in ingots"*, J. Iron Steel Inst. Jpn., 1987, vol. 73, pp. 1698.

[A32] J. S. Kirkaldy and W. V. Youdelis: *"Contribution to the theory of inverse segregation"*, TMS AIME, 1958, vol. 212, pp. 833.

[A33] M. C. Schneider, J. P. Gu, C. Beckermann, W. J. Boettinger and U. R. Kattner: *"Modelling of micro and macrosegregation and freckles formation in single-crystal nickel-base superalloy directional solidification"*, Metall. Mater. Trans. A, 1997, vol. 28, pp. 1517.

[A34] C. Beckermann: *"Modelling of macrosegregation: Applications and future needs",* Int. Mater. Rev., 2002, vol. 47, pp. 243-261.

[A35] M. C. Flemings: *"Principles of Control of soundness and homogeneity of large ingots",* Scand. J. Metall., 1976, vol. 5, pp. 1-15.

[A36] G. Lesoult: *"Macrosegregation in steel strands and ingots: characterization, formation and consequences",* Mater. Sci. Eng. A, 2005, vol. 413-414, pp. 19-29.

[A37] J. P. Gu and C. Beckermann: *"Simulation of convection and macrosegregation in a large steel ingot",* Metall. Mater. Trans. A, 1999, vol. 30, pp. 1357-1366.

[A38] A. V. Reddy and C. Beckermann: *"Modelling of macrosegregation due to thermo-solutal convection and contraction driven flow in direct chili continuous casting of an Al-Cu round ingot",* Metall. Mater. Trans. B, 1997, vol. 28, pp. 479-489.

[A39] C. J. Paradies, R. N. Smith and M. E. Glicksman: *"The influence of convection during solidification on fragmentation of the mushy zone of a model alloy"*, Metall. Mater. Trans. A., 1997, vol. 28, pp. 875.

[A40] T. Sato, W. Kurz and K. Ikawa: *"Experiments on dendrite branch detachment in the succinonitrile-camphor alloy",* Trans. of the Japan institute of metals, 1987, vol. 28, pp. 1012.

[A41] K. A. Jackson, J. D. Hunt, D. R. Uhlmann and T. P. Seward: *"On the origin of the equiaxed zone in castings",* TMS AlME, 1966, vol. 236, pp. 149.

[A42] S. Liu, S.-Z. Lu and A. Hellawell: *"Dendritic array growth in the system NH_4Cl-H_20 and $[CH_2CNh$-$H_20]$: The detachment of dendrite side arms induced by deceleration",* J. Crystal Growth, 2002, vol. 234, pp. 740.

[A43] J. P. Gu, C. Beckermann and A. F. Giarnei: *"Motion and remelting of dendrite fragments during directional solidification of a Nickel-base superalloy",* Metall. Mater. Trans. A, 1997, vol. 28, pp. 1533.

[A44] A. Hellawell, J. R. Sarazin and R. S. Steube: *"Channel convection in partly solidified systems",* Phil. Trans. R. Soc. Lond. A, 1993, vol. 345, pp. 507.

[A45] J. Pilling and A. Hellawell: *"Mechanical deformation of dendrites by fluid flow",* Metal. Mater. Trans. A, 1996, vol. 27, pp. 229.

[A46] Guillaume Reinhard, PhD, Université Paul Cezanne Aix-Marseille III 2006.

[A47] J. Lipton, W. Reinemann and W. Kurz: *"Columnar to equiaxed transition (CET) in castings-part I: Determination of the CET from cooling curves",* Arch. Eisenhunttenwes, 1984, vol. 55, pp. 195.

[A48] S. C. Flood and J. D. Hunt: *"Columnar and equiaxed growth II. Equiaxed growth ahead of a columnar front",* J. Crystal Growth, 1987, vol. 82, pp. 552.

[A49] M. Gäumann, R. Trivedi and W. Kurz: *"Nucleation ahead of the advancing interface in directional solidification",* Mater. Sci. Eng., 1997, vol. A226-228, p p. 763.

[A50] C. Y. Wang and C. Beckermann: *"A multiphase solute diffusion model for dendritic alloy solidification",* Met. Trans. A, 1993, vol. 24, pp. 2787.

[A51] M. Gäumann, C. Bezenvon, P. Canalis and W. Kurz: *"Single-crystal laser deposition of superalloys: Processing-microstructure maps",* Acta Mater., 2001, vol. 49, pp. 1051.

[A52] Ch.-A. Gandin and M. Rappaz: *"A coupled finite element-cellular automaton model for the prediction of dendritic grain structures in solidification processes",* Acta Metall. Mater., 1994, vol. 42, pp. 2233.

[A53] Ch.-A. Gandin, J.-L. Desbiolles, M. Rappaz and Ph. Thevoz: *"A three-dimensional cellular automata-finite element model for the prediction of solidification grain structures",* Metall. Mater. Trans. A, 1999, vol. 30A, pp. 3153.

[A54] M. A. Martorano, C. Beckermann, Ch.-A Gandin: *"A solutale interaction mechanism for the columnar to equiaxed transition in alloy solidification* ", Metall. Mater. Trans. A, 2003, vol. 25, pp. 1657.

[A55] A. Badillo, C. Beckermann: *"Phase-field simulation of the columnar-to-equiaxed transition in alloy solidification",* Acta Mater. 2006, vol. 54, pp. 2015-2026.

[A56] A. Ludwig and M. Wu: *"Modelling the columnar-to-equiaxed transition with a three-phase Eulerian approach"*, Mat. Sci. and Eng., 2005, vol. A 413–414, pp. 109.

[A57] M. Wu and A. Ludwig: "*A 3-phase model for mixed columnar-equiaxed solidification*", Metall. Mater. Trans. A, 2006, vol. 37, pp. 1613.

[A58] M. Wu and A. Ludwig: "*An idea to treat the dendritic morphology in the mixed columnar-equiaxed solidification*", Int. J. Cast Metals Research, 2009, vol. 22, pp. 323.

Part B: PRESENTATION OF EXISTING BENCHMARKS IN SOLIDIFICATION

During last years a lot of important experimental work on solidification was performed by many scientists and an exhaustive list is too long to be given here. In PART B of this dissertation only well controlled experiments relating flow phenomena with solidification will be presented.

One of the first experiments using ammonium chloride to study the influence of the liquid flow through the mushy region on the macrosegregation was performed by Hunt et al. [B1]. In his benchmark experiment fluid flow occurred because of the density difference between the liquid ahead of the dendrites and that of the interdendritic liquid (Fig. B1). Evidence was obtained that A- and V-segregated channels occur (Fig. B1), similar to those obtained in cast steel, as direct result of the fluid motion trough the mushy region. Hunt determined certain conditions which influence A-segregated channels and one of them was the alloy composition. New experiments were performed [B2] to demonstrate that by adjusting the density difference to a minimum the A segregated channels were eliminated. These new experiments on ammonium chloride solidification demonstrated again the importance of the interdendritic fluid motion for understanding some of the mechanisms behind the phenomena of macrosegregation.

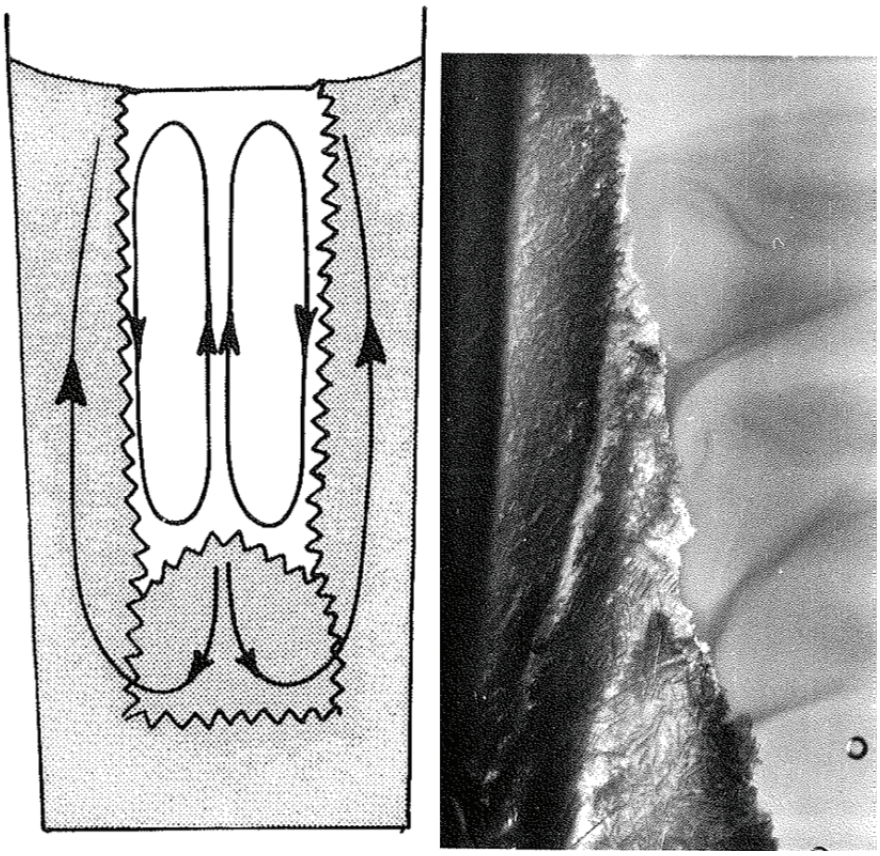

a) b)

Fig. B1: a) Expected convection pattern during solidification where the density of the rejected solute is lighter than the melt; b) Segregated channels in ammonium chloride solidification, similar to those obtained in steel castings [B1].

Ohno's experiments on ammonium chloride solidification [B3] demonstrated again the importance of ammonium chloride alloy for modelling of metallic solidification, due to its transparency and solidification structures which are similar to those in metals. During solidification of a 38 wt.% NH_4Cl aqueous solution poured at 110°C, three stages were identified: an early stage, when lighter solute is rejected at the solid-liquid interface and fine crystals are observed either floating or falling to the bottom; a middle stage, when a nucleation zone forms beyond the diluted solution zone and dendrites breaking is observed (mainly due to the movement of solution in front of the solid shell); and a final stage during which crystals precipitation proceeds and an A-segregated zone forms at the bottom (Fig. B2a). Observation of the solidification of the same concentration alloy poured at 90°C made him suggested some conditions which should be accomplished in order to avoid inverse segregated zones in steel ingot casting (Fig. B2b).

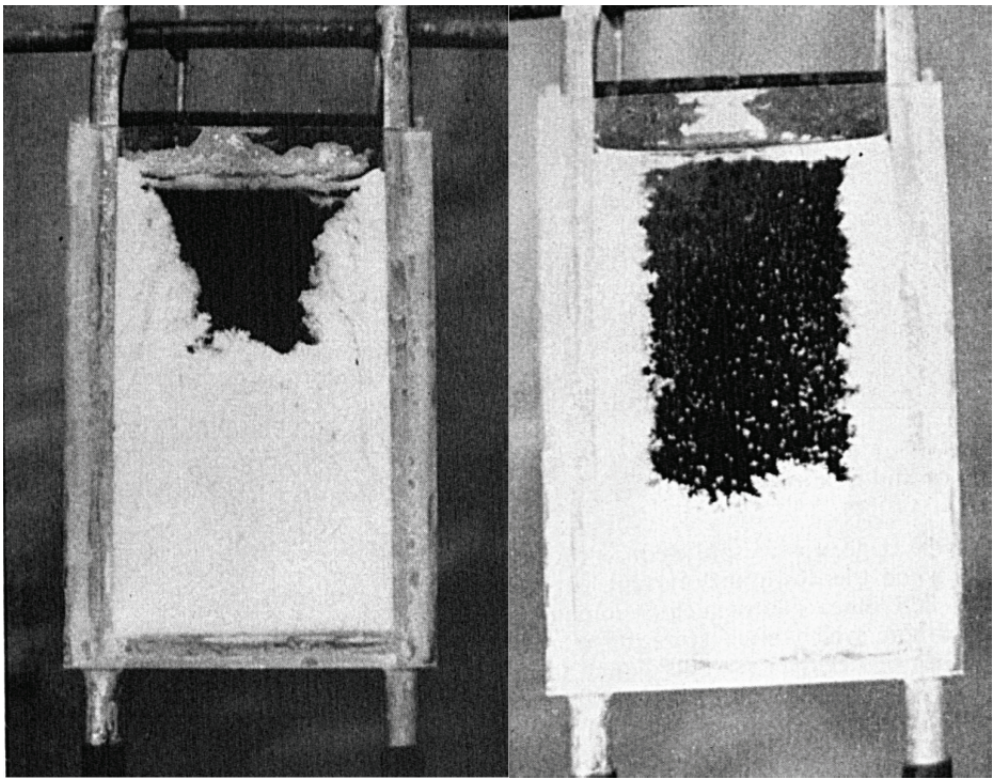

a) 300 s b) 130 s

Fig. B2: a) A segregated channels during ammonium chloride solidification, melt poured at 110°C; b) No segregated channels during ammonium chloride solidification, melt poured at 90°C [B3].

Many experimental studies [B4-B7] have been done to investigate the development of the thermo-solutal convection during solidification, also known as double-diffusive convection. As a transparent analogue for metallic alloys, the NH_4Cl-H_2O solution has proven its convenience to study thermo-solutal convection during columnar solidification. Nishimura and Imoto [B4] studied experimentally the influence of the double diffusive convection on solidification of NH_4Cl-H_2O in a confined cavity cooled laterally. Temperature and concentration at several points were simultaneously measured. Temperatures were visualized using encapsulated liquid crystals suspended in solution, together with thermocouples readings. For concentration measurements sample extraction method using microsyringes was used, via eight holes at the back of the test cell. The refractive index of the aqueous solution extracted by the syringe was read through a refractometer at 25°C. This procedure was repeated three times at a position and each refractive index was averaged. Since the needle was inserted slowly and normal to the flow, the disturbance of the flow was negligible. They presented the structure of time dependent horizontally-stacked flow convection cells due to

double diffusivity (Fig. B3). The thickness of each convection cell increases with the advancement of solidification while the concentration in each convection cell stays constant. Convection in each cell is mainly controlled by temperature, but diffusion is dominant at the thin interface between cells. The fluid in the interface diffusive layer is initially stagnant and begins to rotate when the diffusion at the interface diffusive layer reaches a certain value. A criterion for convection cell generation was found to be related to the solutal buoyancy and the Rayleigh number in the diffusive layer (Ra~10^4).

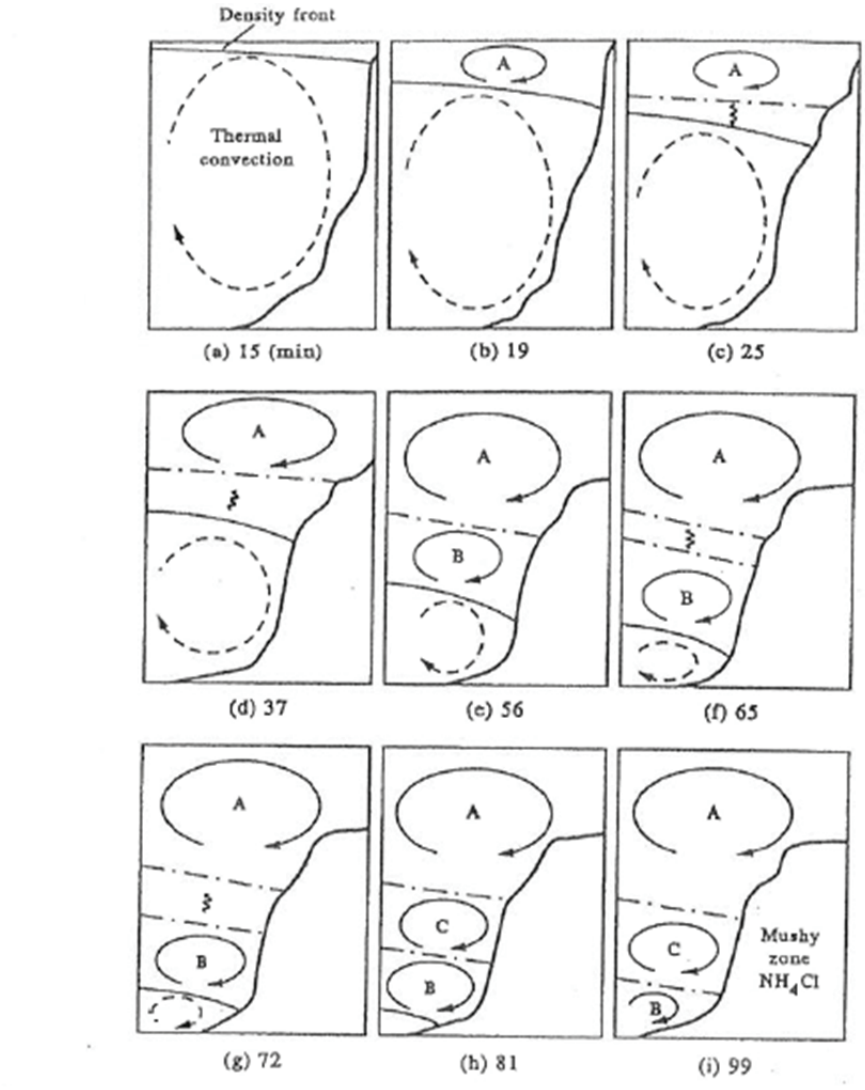

Fig. B3: Time evolution of solidification morphology and flow patterns with developing convection cells during solidification of 25 wt.% NH_4Cl.

Kumar et al. [B5, B6] studied the Rayleigh- Bernard convection phenomena during solidification of hypo and hyper-eutectic concentrations of NH_4Cl, directionally solidified from the top. Two different types of flow pattern were observed consequently for each concentration. For hypoeutectic liquid, solidification presents a mushy zone region and the

solutal buoyancy effects aid the thermal buoyancy forces. If the initial concentration is hypereutectic then the solutal effects oppose the thermal buoyancy forces. The crystals created at the top surface fall down and settle at the bottom of the cavity. As well at the top, a eutectic front is observed to progress vertically until meeting the crystals accumulated at the bottom. The flow visualisation was compared (only for the hypoeutectic case) with the numerical results and the agreement was good.

Christerson and Incropera [B7] compared the experimental results with numerical simulation using the newly developed continuum model [B8]. They considered for the experiments a rectangular cavity with one hot wall (40°C) and one cold wall (-30°C) and an initial NH_4Cl concentration of 30 wt.%. Because of the uncertainties in the measurement of the initial solution concentration, the simulation considered two sets of data of 30 wt.% and 31 wt.% NH_4Cl, in order to examine the effect of this uncertainty. The comparison between experimental and predicted data has been made in terms of solidification morphology, liquid mass fraction and temperatures. Qualitatively the model predicts several important features of the solidification process like the irregularities of the liquidus front. Moreover the retardation of the front growth is predicted at the top of the cavity, due to remelting and impingement of thermally driven flow. Furthermore the channelling in the mushy region is estimated, due to the flow of water-rich interdendritic fluid. Quantitatively discrepancies were found in the prediction of solidus and liquidus front (under predicted by the model, especially for later times), occurrence of steady state conditions (20 min predicted numerically and 56 min observed experimentally), under prediction of the solidification by approximately 60% for the solid region and respectively 25% for the mushy region. However a much better agreement of the liquidus front at later times was obtained when the simulations were based on the 31wt.% NH_4Cl. Differences between experimental and numerical simulations are attributed to weakness in the model assumption, to the mushy zone anisotropies and to the inaccuracy in the used properties values.

Furthermore, there exist some complementary studies (physical model, numerical simulations and experiments) of equiaxed solidification using hypereutectic NH_4Cl-H_2O presented by Beckermann's group [B9-B11]. Beckermann and Wang applied the shadowgraph technique to the solidification of NH_4Cl 30 wt.% in an evenly cooled square cavity [B9] and compared these results with multiphase model simulations [B10]. Although Beckermann used the shadowgraph images only for a qualitative comparison, a carefully applied analysis of shadowgraph images could as well provide information about the distribution and sizes of

grains in the liquid melt at least for small fractions of solid. The limit of the shadowgraph method is that it doesn't allow velocity measurements. The numerical simulations based on the multiphase model reproduced with reasonably good agreement the experimental results in terms of grain growth in the presence of grain movement, recalescence and the rate of formation of the crystal sediment bed. A much better agreement seems likely to be obtained, if dendrites fragmentation would have been accounted for. Moreover the effect of convection on free dendritic growth and the highly transient and three dimensional thermo-solutal convection flow in the liquid were not considered in the numerical simulations. These publications [B7-B11] proved the powerful means of combined experimental measurements and numerical simulations in the understanding of phenomena involved during solidification.

F. Chen [B12] also performed experimental and numerical work on the double-diffusive layer (DDL) during the directional solidification of a 28 wt.% NH_4Cl alloy, and measured the position of the melt/mush interface, the height of the eutectic solid, the number of plumes, the height of the salt fingers and the position of each interface between the double diffusive layers. The growth of the mush is influenced by the temperature of the bottom plate (T_B), the mush is growing faster when T_B is closer to the eutectic temperature. The time to reach the maximum plumes number is also depending on T_B; the time is shorter for lower T_B. DDL will occur when the maximum number of plumes will occur, thus the time onset of DDL is accordingly shorter for lower T_B. The height of the liquid in the test box influences the occurrence of DDL by the stability of the plume which vanishes at H = 20 cm; the thickness of the DDL was not found to be depending on the T_B.

C.F. Chen and F. Chen [B13] presented an overview on channel and freckle formation, focussing on directional solidification of NH_4Cl- H_2O alloys. They studied (by shadowgraph), the occurrence of plumes in the fluid region just above the mushy zone when the temperature gradient is large. They estimated the porosity across the mushy zone (using Computed Tomography), the solute Rayleigh number, the inner diameter of the channel, the average size of the dendrites and the average flow velocity deep down in the mushy zone.

First quantitative measurements in differentially heated cavities were obtained by S.Y. Wang [B14, B15], C. Ghenai [B16], P. V Skudarnov [B17] and Y.-C. Shih [B18] by using PIV techniques. S.Y. Wang et al. employed a PIV technique to measure the velocity field in a cavity subjected to cooling from two vertical walls and the bottom wall, for very low concentration (4 wt.% NH_4Cl) [B14] without any solidification phenomena. For hypereutectic solution (22 wt.% NH_4Cl) a complex flow pattern, because of the existence of equiaxed grains

and broken dendrites in the bulk melt, was observed by S. Y. Wang et al. [B15]. Thus the velocity field obtained from the pictures is based on a mixture of equiaxed crystals and particles seeds movement. It is known that equiaxed crystals flow can develop a relatively large settling or drift velocity [B19, B20].

C. Ghenai et al. [B16] also studied the solidification of binary NH_4Cl-H_2O alloys in a rectangular cavity cooled at one vertical wall (-20°C), using PIV. The convection flow pattern, the solid layer thickness and the temperature distribution were obtained for different initial concentrations. They determined that the initial concentration (0-20 wt. % NH_4Cl) influences the solidification process in terms of evolution of the convection flow patterns, the thickness of the solid layer and the solidification growth rate. The flow patterns due to normal convection were different: at low concentration (5 wt.%) only one clockwise circulation region was present in the upper part, but at high concentration (20 wt.%) two clockwise circulation regions were noticed in the upper part. It was observed that the solidification process was slower with the increase in initial concentration of the binary solution. The thickness of the frozen layer is almost double at the bottom of the cavity compared to the middle or top of the cooled lateral wall.

Skudarnov [B17] investigated the effect of the initial solute concentration (10, 15, 22 wt.% NH_4Cl) on the evolution of the convection pattern during its solidification. The observed vortexes were described as the result of a double-diffusive convection which was found to be a time-transient phenomenon. In the first stage, the velocity field showed a major circulation loop, later many small eddies appeared, and finally several layers of circulation flows were observed. The convection pattern was characterised by a pair of convective cells for the 10 wt.% NH_4Cl concentration. For the 22 wt.% NH_4Cl solution the convection pattern was characterised by vertically stacked layers of double-diffusive convective cells. The magnitude of the velocity flow seemed to decrease as solidification proceeded. Almost all pictures presented in [B10, B15, B18] showed strong presence of equiaxed crystals, at the vicinity of the solidification front but also in the bulk flow.

The recent work of Shih [B18] also considered solidification of hypereutectic solutions of NH_4Cl in a rectangular cell cooled only from one side. From the vector fields presented we can see clearly that in some regions of the flow the liquid and equiaxed are caught together, but it was not possible to differentiate between them (Fig. B4a). A multiple layer flow was observed (Fig. B4b), phenomenon which will be further explored in this dissertation.

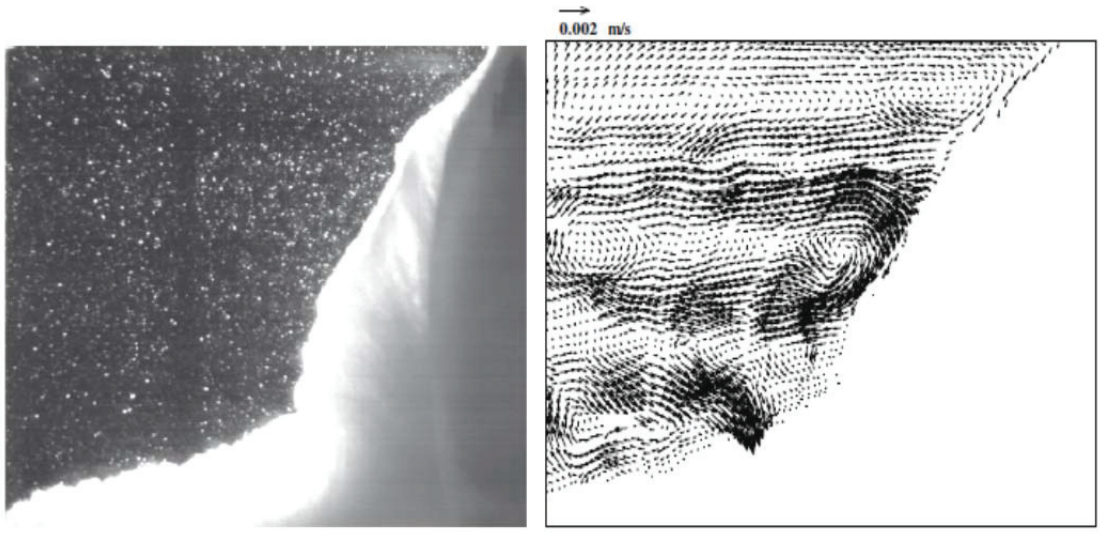

a) b)

Fig. B4: a) Solidification image (180 min.) and b) vector map (180 min.) obtained during the solidification of an 28 wt.% NH_4Cl alloy.

F. L. Tan [B21] also used NH_4Cl to study the solidification from bottom (upward solidification) or from top (downward solidification). He varied as well the initial concentrations of ammonium chloride as follows: 8%, 16%, 24% and 32 %. He discussed the formation, evolution of the mushy zone and the interaction at the solid liquid interface. The dynamics of the fluid flow and equiaxed crystals movement were less explored.

Another method than the PIV to measure velocity vectors is the so called Molecular Tagging Velocimetry (MTV). Lum et al. successfully applied this laser-based optical method to measure velocity fields in the complex thermo-solutal flows associated with solidification in the presence of significant buoyancy [B22]. A 26 wt.% ammonium chloride-water alloy was directionally solidified. Plumes were randomly observed and in order to obtain the chimneys at given positions, 11 nucleators were fixed on the cooling base plate in a regular manner. The mushy zone was plotted with respect to time and a similar evolution was found as in our studies [B23]. The velocity vectors were measured during different stages of solidification. At an early stage (~3 min) of solidification convective flow patterns were observed (1mm/s). Later (~100 min) in a well-developed plume far from the solidification front, the velocities measured were on the order of 2-3 mm/s. The last results were a bit lower than those reported by Liu et al. [B24] maybe because the area of maximum velocity within the plume was outside the tagging plane.

In a more recent work, Lum et al. [B25] applied the Light Induced Fluorescence (LIF) to the study of bottom chilled unidirectional solidification of ammonium chloride, in order to measure the temperature and concentration fields in complex flow features as plumes. The same experimental setup was used previously in Lum et al. [B22]. It was found that temperature within the plumes is around 2 degrees lower than in the surroundings.

A snowing phenomenon was observed by Saffie, Tan and Tso [B26] during the directional solidification (bottom cooled) of a hypereutectic ammonium chloride-water alloy. Different concentrations and bottom temperatures were studied. During the snowing phenomenon ammonium chloride crystals (fragments) are ejected out through the mush via convective plumes, and then they fall down just like atmospheric snow occurring in nature. Ink injection tests and analyses showed an initial convective flow in one direction when thermal buoyancy dominates temporarily and as solidification progresses, the double-diffusive convective flow takes over and reverses the direction of flow. This double-diffusive convective flow is similar to observations made by Tan [B21]. However it seems that the flow is not strong enough to carry these ejected crystals far into the bulk. The increase in concentration decreases the time for the onset of snowing, but increases the size of the ejected crystal fragments, which increase the mush fraction (Fig. B5a). The mush fraction and solid fraction are defined as the ratio of mush volume to the total volume of the solution
inside the test cell and the ratio of solid volume to the total volume, respectively. At a lower temperature the mush growths faster and thus the onset of snowing occurs at a higher mush fraction, but temperature does not significantly change the time of onset of snowing. The time of ending of snowing phenomena is delayed, inducing an increase in mush fraction. The Rayleigh number was calculated for different, concentrations, temperatures and volumes but no critical Rayleigh number was detected for the onset of the snowing phenomenon. However an increase in the global Rayleigh number was observed at the end of the snowing phenomenon comparing with the start. As well the Rayleigh number at the beginning of the snowing phenomenon increases with the increase of temperature. The start of the snowing could not be associated with any parameter. However the onset of equiaxed crystals happened for all experiments, around 0.05 mush fraction. The end of the snowing phenomenon was more related to the solid fraction as it always finished around 1.5-0.2 solid fraction (Fig. B5b).

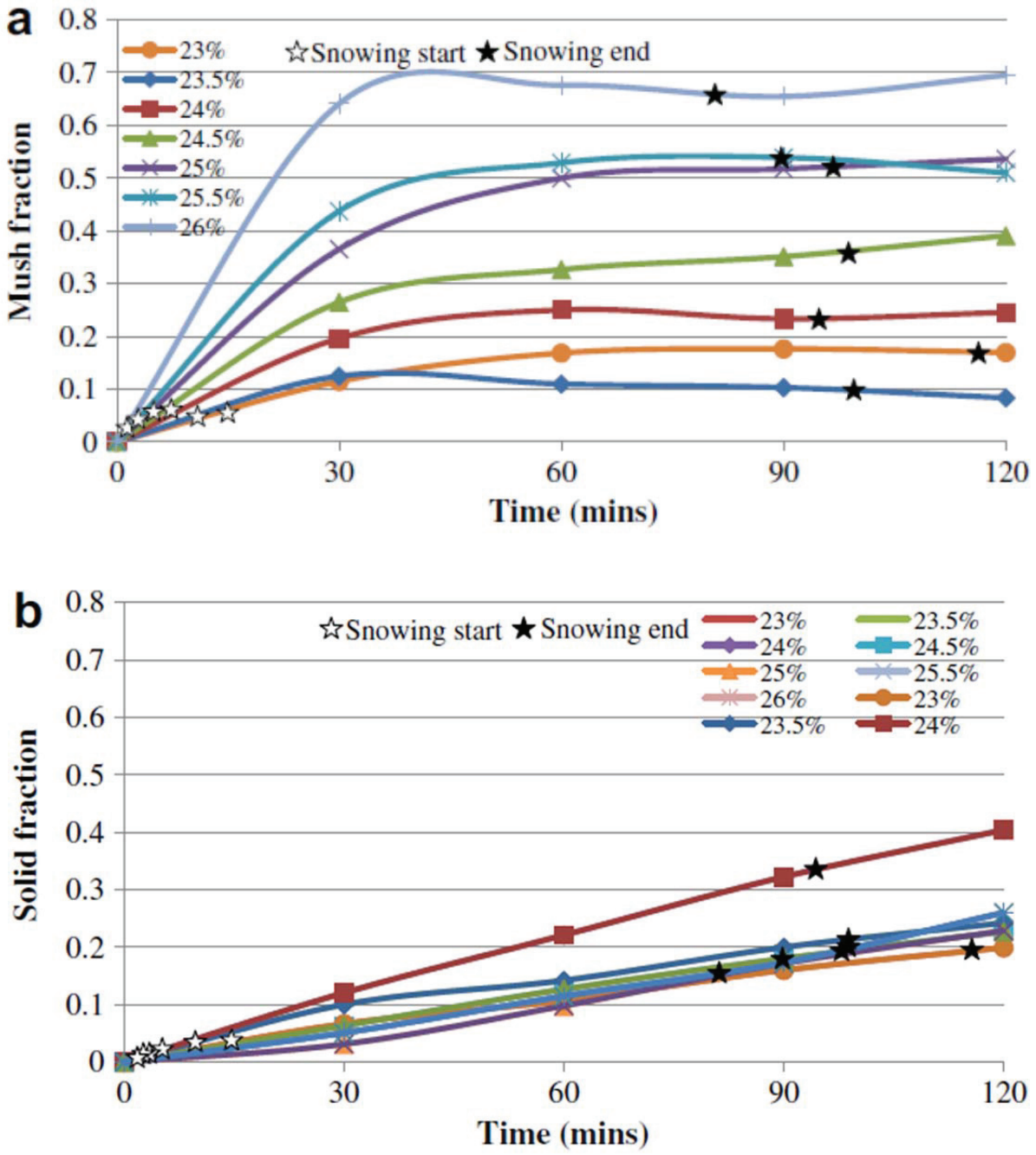

Fig. B5: a) Mush fraction b) solid fraction versus time for different concentrations [B25].

Dendrite fragmentation could occur from different causes and in many circumstances. Paradies et al. [B26] performed experiments under forced flow convection (around 10 cm/s) in superheated SCN - acetone melt. Cooling rates (0.1 to 0.6 K/min), chill melt temperature difference (8 to 18 K), melt flow rate (1.8 to 11.9 cm/s) and acetone concentrations (1.3 and 6.1 wt.%) were varied for the solidification runs. The fragmentation rate (number of fragments counted per mm^2 and per second) was correlated with a higher velocity melt near the mushy zone (Fig. B6). Small fragments less than 0.2 mm were used to follow and measure

the velocity melt near the mushy region (0.2 mm beyond the longest dendrite and 0.4 mm into the mushy region). The crystals created from the fragmentation were observed to fall in the region closed to the mush, while the forced flow was upward far from the mush. The increase in fragmentation rate was correlated to the direction of the flow near the mushy zone, it was observed that it increased less for downward flow that for upward flow near the mushy region. A simple explanation could be that the downward flow melt is cooler than the surrounding melt and does not accelerate the local remelting as quickly as the warmer upward melt flow. However it was not possible to extract a clear relation between the observed fragmentation rate and the controlling parameters of the system, which includes the temperature differences between the chill walls, the cooling rate, and flow magnitude. Nevertheless the velocity of the melt near the mushy region should be related to the mixed convection flow due to the forced flow and the solutal forces acting at the mushy interface. The fragmentation mechanism was unclear, but it was assumed to be rather remelting or capillary pinching than mechanical shear, even if hydrodynamic shear could not be totally excluded.

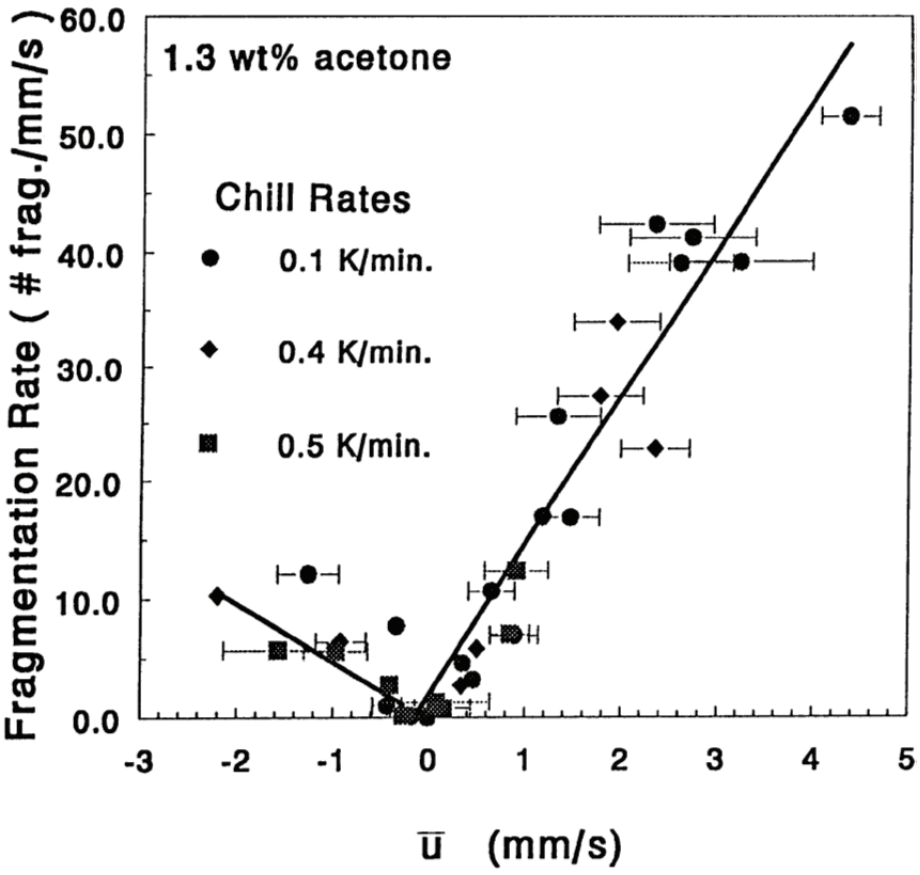

Fig. B6: Correlation of fragmentation rates with the average velocity of particles near the mushy zone–melt interface (SCN-1.3 wt. % acetone) [B26].

In situ observations were performed with X-ray microscopy [B27] on the dendrite fragmentation in Al-Cu, initiated by different mechanisms. Not all the mechanism have the same potential to induced CET, it depends on the mush depth where the fragmentation takes place. Also the gravity is of great importance. It was experimentally observed that detachment always occurs on the tertiary branches first and sometimes a secondary-arm fragmentation can happen as the consequence of the first one (Fig. B7). They proved that high-order side-branch remelting is prone to produce dendrite fragmentation than coarser parent branches. It was concluded that fragmentation rate depends on the degree of network branching and that the transport of fragments out of the mush is done by the buoyant flow. The average eutectic front velocity and dendrite tip velocity was extracted from recorded images and could be compared with numerical calculations.

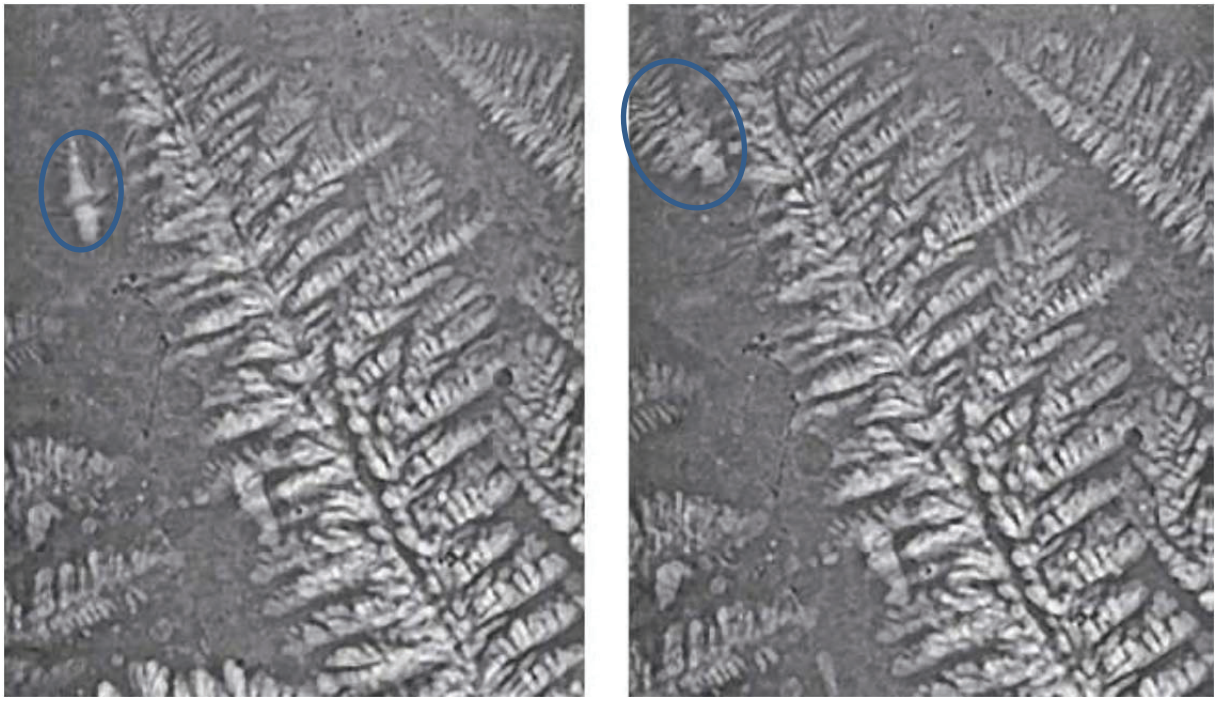

Fig. B7: Dendrite fragmentation from deep inside the mush in Al-20 wt.% Cu alloy [B27].

The influence of the natural and forced convection on the solidification of Sn and Sn-Pb alloy was studied using X-ray by Hachani et al. [B28-B30]. A large zone of segregated melt was put in evidence at the base of the ingot in the case of natural convection. A tendency to developed segregated channel was noticed next to the lateral walls of the ingot. In the case of forced convection three cases were investigated: electromagnetic stirring in the same direction that the natural convection, electromagnetic stirring in the opposite direction to the natural convection and alternative electromagnetic stirring. The first case showed that the segregated channel can be promoted by forced convection. The second case created mainly an equiaxed

structure but didn't suppress the segregated channels. The third case had the same effect as the second case. This experimental study clearly demonstrated that the final morphology is the result of the flow in the mushy region.

In [B29] Hachani et al. solidified eight identical rectangular ingots of Sn-3wt.% Pb alloy. During solidification the temperature was monitored via 30 thermocouples. This allows us to estimate the time evolution of the temperatures due to natural convection and assess the velocity field, the solidification macrostructure and the segregation behaviour. X-ray radiography and induction coupled plasma analysis was performed afterwards and results show that the main features of solidification were reproducible.

Ramani and Beckermann [B31] performed experiments on the dendrite tip growth velocities of settling ammonium chloride crystals in a supercooled aqueous solution of ammonium chloride. The measured dendrite tip growth velocity was plotted versus the relative velocity between the crystal and the solution for different supercoolings. The tip velocities are two orders of magnitude larger than those found in a purely diffusive environment. Preliminary comparisons with Stoke solution of Ananth and Gill for a single dendrite tip growing in a uniform flow show approximately good approximation, however uncertainties concerning the Gibbs-Thomson coefficient of NH_4Cl are large. Appolaire [B19, B20] also studied the fall of a single NH_4Cl crystal in an undercooled ammonium chloride melt. A power law or an exponential tendency can be noticed when the relative crystal velocity is plotted versus the crystal size. This tendency is similar to findings presented in current dissertation work and it can be attributed to the increase in size of the crystal while falling. The equiaxed crystals surrounded by undercooled liquid will grow, while those which meet low concentrated liquid could experience melting.

The innovation in the current work consists in the employment of the dual PIV technique during solidification in order to explore the melt flow and the equiaxed crystals motion simultaneously. Amongst other phenomena simultaneous liquid and solid flow is an important phenomenon in solidification. Solidification takes place either in the form of a growing columnar front and/or in the form of an equiaxed crystal fall. Convection in the liquid melt is caused by both thermal and solutal buoyancy forces. In many cases the flow is turbulent or at least unstable. In the case when columnar growth is present, there exists a mushy region where both solid and liquid phases are present. When equiaxed solidification is present, the phases (liquid melt and equiaxed crystals) interact with each other through momentum and energy exchange. The resulting solid-liquid multiphase flow pattern strongly depends on the

microstructure of the equiaxed crystals, which in turn is governed by grain nucleation and growth mechanisms. Because the coupled liquid-solid-flow causes structural and chemical inhomogeneities in the final solidified products, a fundamental understanding of the multiphase transport phenomena coupled with the grain nucleation and growth mechanisms is required. However, there is a lack of consistent experimental data to support the numerous theories for flow-particle interaction that have been developed in recent years. Either only a qualitative observation of the flow was performed (fingers-plumes and chimneys observation by shadowgraph) [B9, B12, B13], or/and a quantitative flow investigation (flow vector maps showing convention flow, vortexes, etc.) was accomplished [B14-B18]. In cases were equiaxed grains occurred the flow vector maps are actually a mixture of flow and grains movement, as it was not possible to distinguish between them [B15-B18]. The solid structure was observed in terms of equiaxed crystals fall (measurement of crystal settling velocity) [B19, B20, B31] or columnar solid growth (measurement of columnar thickness) [B21-B25]. There exists no investigation concerning simultaneously melt flow, mushy zone growth and equiaxed crystals nucleation; such study will allow inquiring over the flow-grains interaction. To explore this two phase flow, liquid and solid, we need to distinguish between the melt flow and solid crystals (equiaxed crystal and broken off dendrites) instantaneously and simultaneously. The ammonium chloride-water alloy solidification permits the instantaneous observation (as the alloy is transparent) and the double PIV technique (2 CCD cameras together with a special fluorescent tracer particles for the flow) used in the work presented in this dissertation, is offering the possibility to explore simultaneously the melt flow and the solid growth (either columnar or equiaxed crystals).

References Part B

[B1] R. J. McDonald and J. D. Hunt: *"Fluid motion through the partially solid regions of a casting and its importance in understanding A type segregation"*, MS AIME, 1969, vol. 245, pp. 1993.

[B2] R. J. McDonald and J. D. Hunt: *"Convective fluid motion within the interdendritic liquid of a casting"*, Metall. Trans., 1970, vol. 1, pp. 1787.

[B3] A. Ohno: *"Compositional depression of undercooling and formation of segregation between columnar and equiaxed zones"*, Proc. of Solidification of Met. The Iron and Steel Institute, London, 1968, pp. 349.

[B4] T. Nishimura, T. Imoto: *"Occurrence and development of double diffusive convection during solidification of a binary system"*, Int. J. Heat Mass Transfer, 1994, vol. 37, pp. 1455-1464.

[B5] P. Kumar, S. Chakraborty, K. Srinivasan, P. Dutta: *"Studies on transport phenomena during directional solidification of a noneutectic binary solution cooled from the top"*, Metall. and Mat. Trans. B, 2003, vol. 34, pp. 899-909.

[B6] P. Kumar, K. Srinivasan, P. Dutta: *"Visualization of convection loops due to Rayleigh-Bernard convection during solidification"*, Mech. Res. Comm., 2006, vol. 33, pp. 593-600.

[B7] M. S. Christerson, F. P. Incropera: *"Solidification of an aqueous ammonium chloride solution in rectangular cavity-I. Experimental study"*, Int. J. of Heat and Mass Transfer, 1989, vol. 32, pp. 47-68.

[B8] M. S. Christenson, F. P. Incropera: *"Solidification of an aqueous ammonium chloride solution in rectangular cavity-II. Comparison of predicted measured results"*, Int. J. of Heat and Mass Transfer, 1989, vol. 32, pp. 69-79.

[B9] C. Beckermann, C. Y. Wang: *"Equiaxed dendritic solidification with convection: part III. Comparisons with NH_4Cl-H_2O experiments"*, Metall. and Mat. Trans. A, 1996, vol. 27A, pp. 2784-2795.

[B10] C. Beckermann, C. Y. Wang: *"Equiaxed dendritic solidification with convection: part II. Numerical procedure"*, Metall. and Mat. Trans. A, 1996, vol. 27A, pp. 2765-2783.

[B11] C. Beckermann, C. Y. Wang: *"Multiscale phase model part I"*, Metall. Mater. Trans. A, 1996, vol. 27A, pp. 2754-2764.

[B12] F. Chen: *"Formation of double-diffusive layers in the directional solidification of binary solution"*, J. of Crystal growth, 1997, vol. 179, pp. 277- 286.

[B13] C. F. Chen and F. Chen*: "Experimental study of directional solidification of aqueous ammonium chloride solution"*, J. Fluid Mech., 1991, vol. 227, pp. 567- 586.

[B14] S. Y. Wang, C.X. Lin, M. A. Ebadian: *"Vortex flow of low concentration NH_4Cl-H_2O solution during the solidification process"*, Int. J. of Heat and Mass Transfer, 1999, vol. 42, pp. 4153-4163.

[B15] S. Y. Wang, C. X. Lin, M. A. Ebadian: *"Study of double-diffusive velocity during the solidification process using particle image velocimetry"*, Int. J. of Heat and Mass Transfer, 1999, vol. 42, pp. 4427-4445.

[B16] C. Ghenai, A. Mudunuri, C. X. Lin, M. A. Ebadian: *"Double diffusive convection during solidification of a metal analog system (NH_4Cl-H_2O) in a differentially heated cavity"*, Exp. Therm. and Fluid Sci., 2003, vol. 28, pp. 23-35.

[B17] P. V. Skudarnov, C. X. Lin, M. H. Wang, N. Pradeep, M. A. Ebadian: *"Evolution of convection pattern during the solidification process of a binary mixture: effect of initial solutal concentration"*, Int. J. of Heat and Mass Transfer, 2002, vol. 45, pp. 5191-5200.

[B18] Y.-C. Shih, S.-M. Tu: *"PIV study on the development of double diffusive convection during the solidification effected by lateral cooling for a super-eutectic binary solution"*, Appl. Therm. Eng., 2009, vol. 29, pp. 2773-2782.

[B19] B. Appolaire, V. Albert, H. Combeau, G. Lesoult: *"Experimental study of free growth of equiaxed NH_4Cl crystals settling in undercooled NH_4Cl-H_2O melts"*, ISIJ International, 1999, vol.39, pp. 263-270.

[B20] B. Appolaire, Ph.D., INPL, 1999.

[B21] F. L. Tan: *"Upward or downward solidification of a binary alloy inside a rectangular enclosure"*, Appl. Therm. Eng., 2008, vol.28, pp. 1962-1973.

[B22] C. L. Lum, M. M. Koochesfahani, J. J. McGrath: *"Measurement of the velocity field with MTV during the solidification of an alloy analog with mushy region"*, Proc. of ASME IMECE, New York, USA, Nov. 11-16, 2001.

[B23] M. Stefan Kharicha, S. Eck, L. Könözsy, A. Kharicha and A. Ludwig: *"Experimental and numerical investigations of NH_4Cl solidification in a mould. Part 1: experimental results"*, Int. J. of Cast Met. Research, 2009, vol. 22, pp. 168.

[B23] S. Liu, A. Hellawell: *"Experiments with constrained chimney- plume flows in the system ammonium chloride-water: comparison with unconstrained case"*, J. Fluid Mech., 1999, vol.388, pp. 21-48.

[B24] M. B. Shafii, C. L. Lum and M. M. Koochesfahani: *"In situ LIF temperature measurements in aqueous ammonium chloride solution during uni-directional solidification"*, Exp. in Fluids Experim. Meth. and their Appl. to Fluid Flow, 2009, published on line.

[B25] M. G. M Saffie, F. L. Tan and C. P. Tso: *"A study on the snowing phenomenon in binary alloy solidification"*, Appl. Therm. Eng., 2013, vol. 50, pp. 562–71.

[B26] C. J. Paradies, R. N. Smith, M. E. Glicksmann: *"The influence of convection during solidification on fragmentation of the mushy zone of a model alloy"*, Metall. Mater. Trans. A, 1997, vol. 28, pp. 875-883.

[B27] R. H. Mathiesen, L. Arberg, P. Bleuet, A. Somogyi: *"Crystal fragmentation and columnar-to-equiaxed transitions in Al-Cu studied by synchrotron x-ray video microscopy",* Metall. Mater. Trans. A, 2006, vol. 37, pp. 2515-2524.

[B28] L. Hachani, PhD, Universite de Grenoble, 2006.

[B29] L. Hachani, K. Zaidat, Y. Fautrelle: *"Multiscale statistical analysis of the tin-lead alloy solidification process"*, Int. J. of Thermal Sciences, 2016, vol. 110, pp. 186-205.

[B30] L. Hachani, K. Zaidat, Y. Fautrelle: *"Experimental study of the solidification of Sn–10 wt.%Pb alloy under different forced convection in benchmark experiment"*, Int. J. of Heat and Mass Transfer, 2015, vol.85, pp. 438–454.

[B31] A. Ramani and C. Beckermann: *"Dendrite tip growth velocities of settling NH_4Cl equaixed crystals"*, Scripta Materialia, 1997, vol. 36, pp. 633.

Part C: PRESENTATION OF OWN BENCHMARK EXPERIMENTS AND CORRESPONDING RESULTS

The work presented in this thesis was realised at the Chair of Simulation and Modelling of Metallurgical Processes in the Metallurgy Department of the Montanuniversitaet Leoben during two FWF Projects (P 17619-N02 and P 22614-N22). As the name indicates, the chair's main topic is to simulate numerically solidification phenomena. But a numerical model needs experimental benchmark in order to be verified. The present thesis constitutes such experimental benchmarks, where a hypereutectic ammonium chloride alloy was solidified in different die cast cells with a U-shape made of brass and the front and back sides made of transparent glass. Different initial alloy concentrations were tested but finally the concentration of 29.6 wt.% NH_4Cl was chosen in order to perform our investigations during solidification. In the following chapter (**Part D: Publications)**, the different experimental results on flow velocity measurements, total flow kinetic energy calculations, crystal velocity measurements, columnar solid front growth velocity calculations, total mushy zone evolution, occurrence of equiaxed crystals, interaction between flow and equiaxed crystals, will be presented. All the experimental work was performed by me solely, which includes the measurements and the calculations to extract the information necessary to interpret the results. The interpretation of the results was done in collaboration with other scientists.

First investigations (**Publication 1**) consisted in measuring simultaneously the temperature and velocity fields in a copper cast cell (10*10*3 cm^3) only filled with water. The cell's walls were cooled homogeneously from 41°C to 6°C. During cooling down two symmetric rolls which formed due to natural convection were observed. Flow velocities were measured using the Particle Image Velocimetry (PIV) technique. The temperature field measurement was obtained by applying the Laser Induced Florescence (LIF) technique. In addition 2D and 3D axis symmetrical simulations were performed by A. Ishmurzin using the commercial software Fluent. The results in terms of velocity and temperature fields were compared with the experimental results and good agreement was found. In the numerical simulations a heat transfer coefficient of 100 W/m^2K was applied at the free surface between water and air. Further examinations were completed in order to determine more realistic heat transfer coefficient (h). Heat can be lost or gained from ambient air through the top free surface and through the two glasses (front and back). We tried to extract the heat transfer coefficient via the top free surface and the heat transfer coefficient via the front glass. Two cases were

considered: in the first, the cell's glass walls (front and back) were insulated and cooling was done only through the top free surface; in the second case the top free surface was insulated together with the back glass wall and cooling was done only via the front glass. The temperature was measured in the two cases via thermocouples: the first in the air (T_{air}), second in the water (T_{water}) and third in the copper wall. Using Eq. C1 the heat transfer coefficient between the water and air, considering the heat loss via the front glass or via the top water surface, was calculated:

$$h = \frac{S(T_{water} - T_{air})}{\rho c_p V \frac{\partial T_{water}}{\partial t}} \qquad \text{Eq. C1}$$

where ρ is the water density, c_p the water heat capacity, V and S the volume and respectively the surface over which the heat is exchanged.

The values of the heat transfer coefficient were found to be lower than the estimated ones and to decrease in time (Fig. C1).

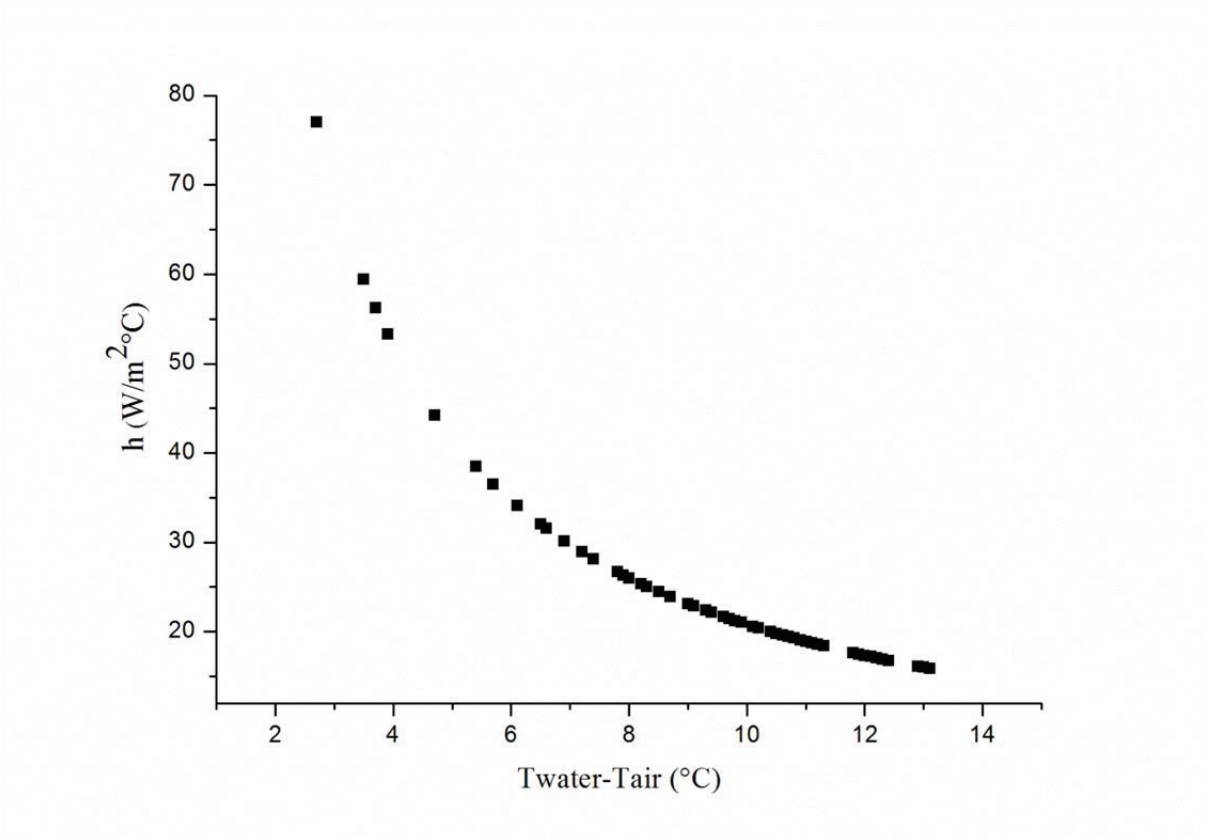

Fig. C1: Heat transfer coefficient (h) calculated using Eq. C1, when heat was lost only via the front glass.

The next step in this study was the solidification of NH_4Cl-H_2O alloy. Experiments were performed first in a thick brass cell (10*10*3 cm^3) but lately a thinner cell was designed (10*10*1 cm^3), considered more suitable for comparison with 2D numerical simulations. For the first experimental benchmark a 29.6 wt.% NH_4Cl was cooled from 41°C to 26°C in the thin cell. The mushy zone thickness was measured at the bottom wall at three different positions (**Publication 2**). The time evolution of the mushy zone thickness at these points were plotted and fitted with a function following the square root of time law and the reproducibility of the implemented α factor was demonstrated. The average values for the α factor show little variation and are therefore suitable as parameter to validate numerical simulations.

Publication 3 gives a presentation of the double PIV technique, employed to record simultaneously the melt flow and equiaxed crystal motion during solidification. After the formation of a steady convection pattern, solutal buoyancy together with falling crystals destabilize and break the steady convection flow into multiple chaotic cells. At the beginning of the solidification process, the flow transitioned from 2D to a 3D turbulent regime. Five different flow regimes were detected and a detailed description was given for each of it. The last flow regime, when the forces involved in the double diffusive phenomenon become equivalent, is shown in Fig. C2. This flow regime was called Meander Flow (MF) and to our knowledge was never observed before.

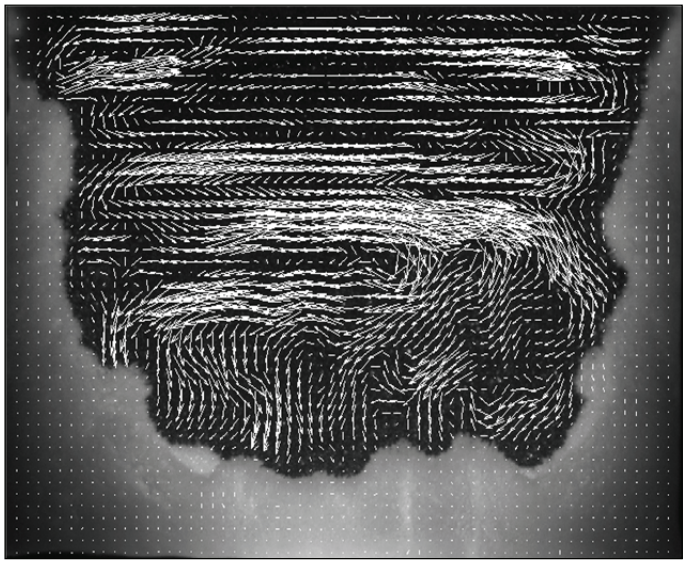

Fig. C2: Melt velocities observed during the Meander Flow regime (MF).

The total flow kinetic energy was extracted from the velocity fields calculated using PIV during solidification and a characteristic peak was found at the time corresponding to the occurrence of massive amount of equiaxed crystals (Fig. C3).

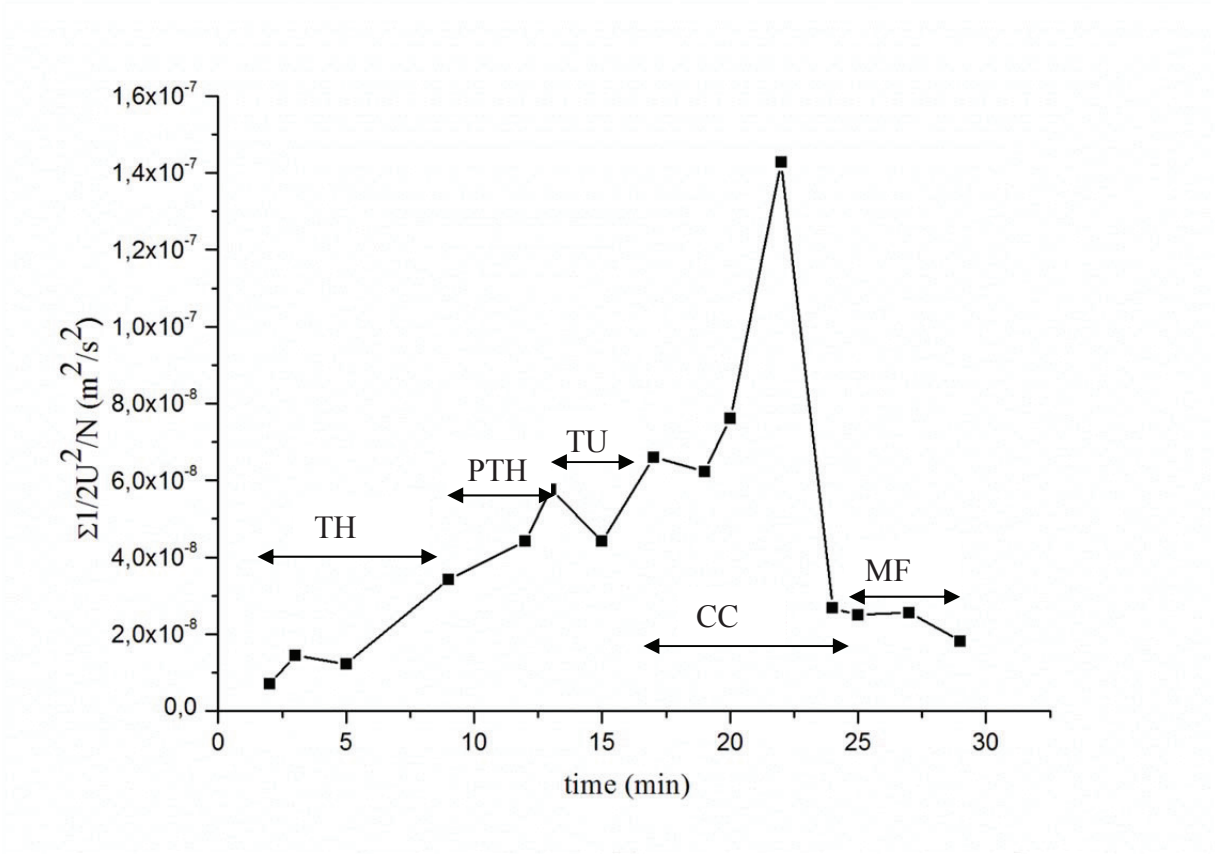

Fig. C3: Evolution of the flow kinetic energy (KE) contained in the liquid region. The different flow regimes are indicated: (TH) thermal stage, (PTH) perturbed thermal buoyancy by the start of solidification, (TU) turbulent flow, (CC) coherent chaotic state, (MF) meandering and stratified flow.

In **Publication 4** (continuation of Publication 3) the relative velocity of the equiaxed crystal was estimated as the difference between of the single equiaxed crystal velocity and the flow velocity (Fig. C4). Using the same dual PIV technique described in Publication 3 it was possible to separate the melt flow velocity from the equiaxed crystals velocity.

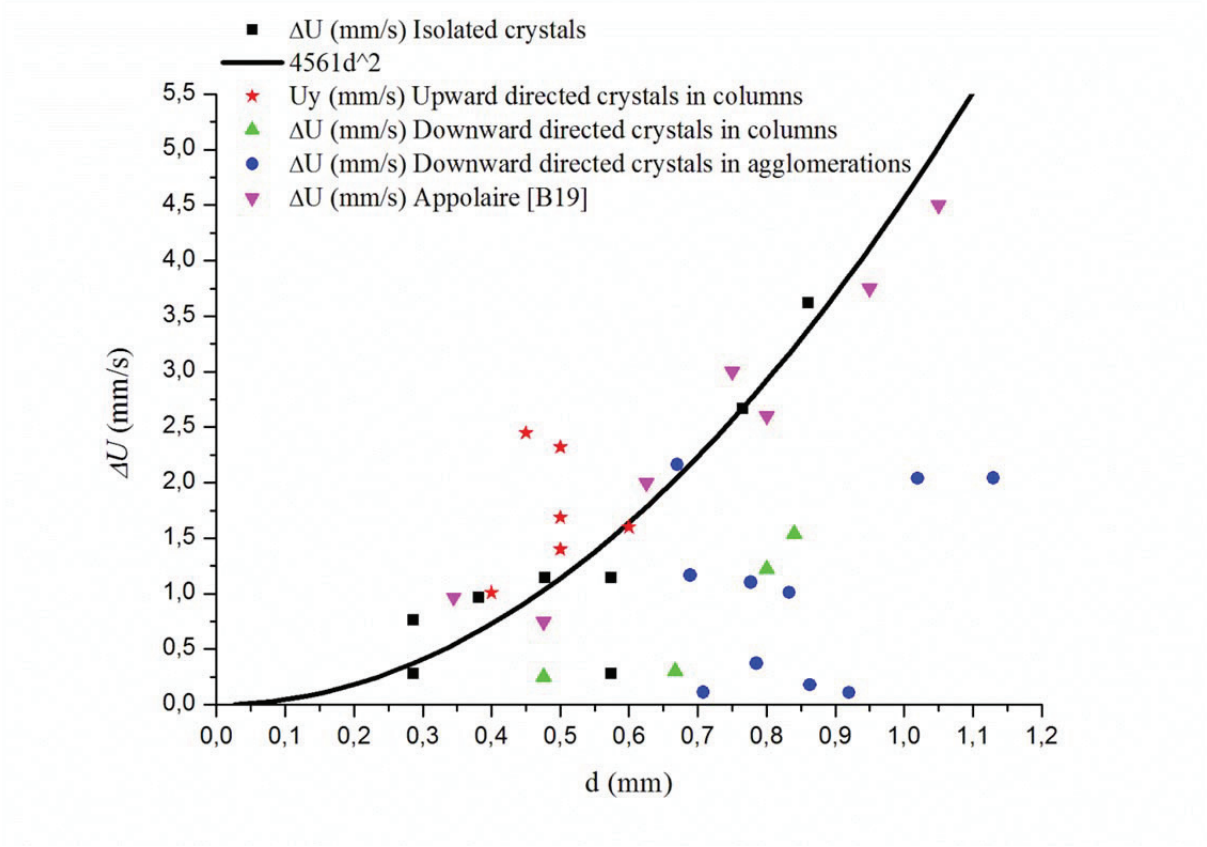

Fig. C4: Relative velocity ΔU for single crystals versus the crystal size (d), and comparison between rising (red) and falling (green) velocity magnitude in chimneys.

Differences in the settling velocities were observed, between the case of a single crystal and a crystal found in a column or agglomeration. For the case of a single crystal an increase of the relative velocity was observed with the crystal size diameter (d). The values are in good agreement with the results obtained by Appolaire [B19] and a power tendency law was found, approximating the equiaxed crystals to spheres of equivalent size (using Stokes law). The coupling between the fluid flow and the equiaxed crystals was found to be important in areas of high crystal density. Chaotic and turbulent behaviours are found to be damped in regions of high equiaxed crystal density.

Publication 5 studies the hydrodynamics during the columnar solidification of a hypereutectic ammonium chloride alloy (29.6 wt.%). Four sets of experiments were performed with each having as starting temperature (same temperature for cell's walls and liquid alloy) 5, 10, 15 and respectively 20 °C more than the equilibrium liquidus temperature (37°C). The different flow regimes were described and the average flow kinetic energy was extracted. In the beginning of the solidification the solutal buoyancy generates a turbulent flow, which is progressively replaced by the development of stratification from the top of the

cell. Later, the stratification leads to the development of a long lasting meandering flow, which filled almost all the liquid region. The average flow kinetic energy (KE) was found to decrease in time. The starting KE value (at the beginning of the cooling process) was found to increase with the increase of the pouring temperature. Concerning the solid (mushy zone) formed during solidification no difference was found between the different experimental sets: the solidification front was always smooth and no freckles appeared in the mushy zone. After one hour of cooling the cell was filled at approximately 50% with mush. As these experiments showed a good reproducibility (each experiment was done two times) they represent an excellent benchmark for validation of the numerical models that target the simultaneous prediction of flow dynamics and solidification.

Publication 6 gathers experiments performed at 9.5 cm liquid height in the cell. In all previously presented experiments (Publication 1 to 5) the liquid alloy was filled in until 8 cm height. The aim of these new experiments was to investigate the influence of the flow behaviour on the solidification type. It was expected that the higher liquid height will induce a stronger flow and therefore the creation of equiaxed crystals will be enhanced. All those experiments have shown significant occurrence of equiaxed crystals everywhere in the bulk melt. The flow kinetic energy and the total solid mushy zone evolution during solidification were extracted. A geometrical solidification model was developed and the growth velocity of the solid columnar front was calculated. The evolution of the flow kinetic energy presented a peak and this was related to the occurrence of equiaxed crystals. Generally a clear correlation between the strength of the flow and the occurrence of equiaxed crystals was observed. The analysis of the results suggests strongly a fragmentation origin of the equiaxed crystals occurrence (mechanism of equiaxed crystal formation including flow and fragmentation is described in Fig. C5). The transition from purely columnar growth to a strongly equiaxed rain (CET) was found to be triggered by the intensity of the coupling between the magnitude of the flow velocity driven by the equiaxed crystals, and the liberation and the transport of the fragments, by the same flow recirculating within the mushy zone. The occurrence of equiaxed grains increases the flow intensity and a stronger flow can induce more equiaxed grains and consequently CET.

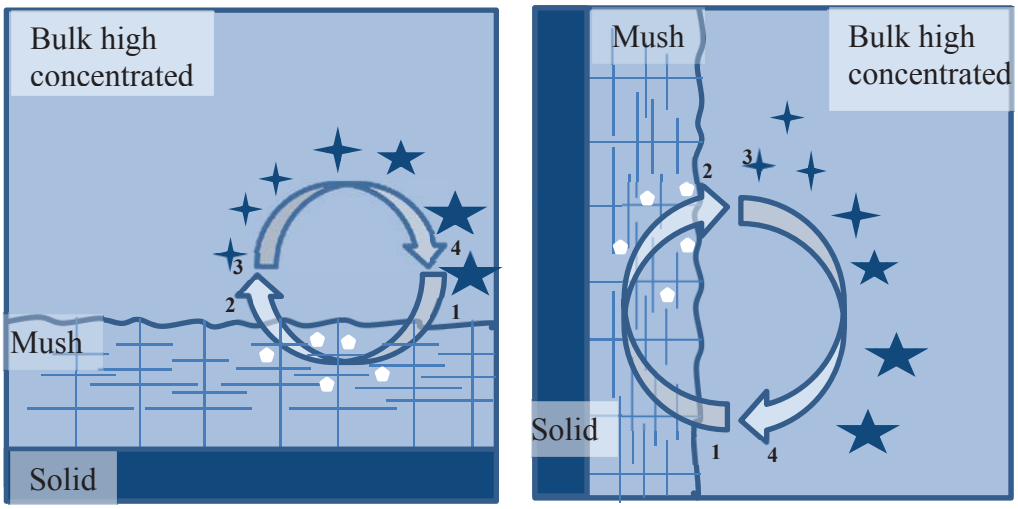

Fig C5: Coupling mechanism at the origin of CET: 1 - 2 strong flow running through the mushy zone transporting eventually dendrite's fragments out; 3 - 4 equiaxed growth and drag of the flow downward.

Publication 7 brings an evidence of a phenomenon, which especially as it happened repeatedly, may significantly contribute to the formation of the inner equiaxed zone in castings: sliding down of large areas of lateral mushy region and formation of spectacular crystals (dendrites fragments) avalanches. These avalanches happen in alloys where a solutal buoyant up flow exists in the interdendritic mush. Those dendrites fragments continue to grow as equiaxed crystals forming equiaxed layers clearly visible in the lower part of the casting (Fig. C6).

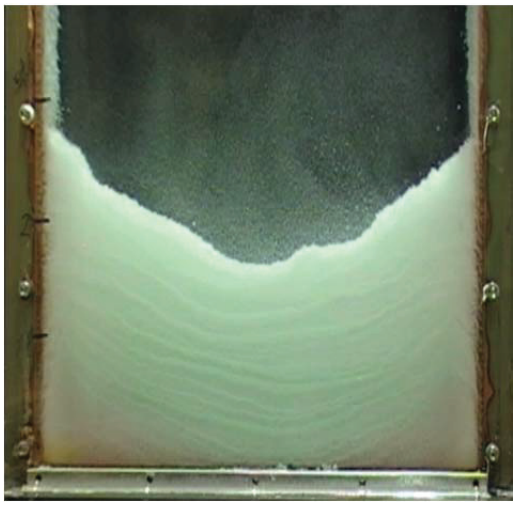

Fig. C6: Sedimented equiaxed crystals at the bottom of the containment with around 15 traces of massive equiaxed formation due to repeating occurrence of massive avalanches.

In order to have a complete characterisation of solidification, complementary work should be done. Investigation of the temperature and concentration fields during solidification would be of great importance. Light Induced Fluorescence (LIF) is a good technique to be employed in temperature field calculation. This technique was employed in the current study but only for water experiments and could be in the future extended to ammonium chloride solidification experiments. Even more important is the concentration field measurements during the PIV experiments. Some investigations to estimate the concentration field were already performed by Beckermann [B9] using shadowgraph and thus could be used in further experiments. Measurements of in-situ flow in the mushy zone would be a great advancement in the field of solidification and especially on the understanding of dendrite fragmentation during solidification. However a technique able to observe the flow through the mushy zone needs still to be developed.

Ammonium chloride is a transparent analogue of metals, which means that this inorganic substance solidifies like metals. For these reasons was often used to create an experimental benchmark, useful to model/simulate solidification. Accurate thermo-physical properties are very important in order to perform realistic numerical calculations. **Publication 8** gives an overview of the most important properties measured and/or calculated: density, viscosity, thermal conductivity, diffusivity, Gibbs Thomson coefficient and different phase diagrams. Furthermore analyse and comparison of these properties are given in the paper.

Publications 9 to 12 correspond to results obtained by numerical simulations of the afore mentioned experimental benchmarks. The numerical simulations were performed by L. Könözsy, A. Kharicha and respectively M. Ahmadein. Therefore these publications are not enclosed in this dissertation and only a short description is given below.

Publication 9 and **Publication 10** are both presenting numerical solidification calculations of the experimental benchmark shown in Publication 2. The mathematical model using an Eulerian-Eulerian volume averaging approach is described in those two publications. The temperature fields during solidification, the final shape of the mushy zone and respectively the thickness of the mushy zone in the centre of the bottom wall were compared with the experimental results and satisfactory agreements were found.

Publication 11 explores the double diffusive convection due to thermo-solutal phenomena observed during solidification of ammonium chloride-water alloy. A two-dimensional model is built to simulate directly the envelope of the columnar dendrites with a cellular automaton

model. The mushy interior of the dendrite is modelled with a volume averaging method. The occurrence of several flow regimes during solidification is predicted, such as turbulent, stratified and meandering flows. During the two dimensional meandering flow, the concentration field is organised in horizontal layers of quasi-uniform concentration. Those layers are separated by very thin boundary layers so that the concentration varies vertically in staircases.

Publication 12 presents the results of a 5-phase mixed columnar-equiaxed solidification model. The flow behavior and the solidification structure of NH_4Cl-70 wt.% H_2O solution are reproduced qualitatively. Three flow regimes can be numerically distinguished: an initial laminar symmetric flow, then a chaotic unsteady flow, formed after solidification began, and lastly a meandering flow. Solutal plumes at the bottom columnar tip front can also be predicted. The calculated liquid velocity and volume fraction of mush also agree with the experiments. The calculated mush thickness at the bottom and corners deviates slightly from the experiment. Further parameter study and grid verification are suggested to improve the quantitative results of the simulation.

Part D: PUBLICATIONS

ELSEVIER

Materials Science and Engineering A 413–414 (2005) 79–84

MATERIALS SCIENCE & ENGINEERING A

www.elsevier.com/locate/msea

Measurement and simulation of temperature and velocity fields during the cooling of water in a die casting model

S. Eck *, M. Stefan Kharicha, A. Ishmurzin, A. Ludwig

University of Leoben, Department of Metallurgy, Franz-Josef Str. 18, 8700 Leoben, Austria

Abstract

Simultaneous measurements of temperature and velocity fields have been performed by applying combined laser induced fluorescence (LIF) and particle image velocimetry (PIV) techniques to natural convection in a die cast model. A 10 cm × 10 cm × 3 cm U-shape rectangular die casting model has been filled with pure water and the cell walls have been continuously cooled between 41 and 6 °C. The resulting natural convection pattern and temperature field have been measured with PIV and LIF. Furthermore, the convection pattern has been simulated in 2D and 3D using the commercial CFD software FLUENT. The comparison of the experimental and numerical results given in this work shows good agreement both qualitatively and quantitatively.

Keywords: Convection; Water; Die casting model; Particle image velocimetry (PIV); Laser induced fluorescence (LIF); CFD calculation

1. Introduction

The two phase model proposed by Ludwig et al. [1–4] has been successfully applied to globular equiaxed solidification. The model considers nucleation and growth of equiaxed grains, motion and sedimentation of grains, feeding flow and solute transport by diffusion and convection. It allows the prediction of macrosegregations and the distribution of grain size. Whether the Eulerian multiphase model can be successfully applied to the solidification and phase separation processes is strongly dependent on the definition and implementation (through user defined subroutines) of source terms, interaction terms, and other auxiliary terms into the conservation equations. Thus, experiments with the same boundary conditions are essential to verify the numerical predictions. In a recent publication, we presented an experimental observation study of convection during equiaxed solidification of transparent alloys [5]. There, 3D samples of NH_4Cl–H_2O solutions were solidified under defined experimental conditions. The occurring melt convection had been investigated by particle image velocimetry (PIV). Fig. 1 shows PIV results measured during the early stage of the solidification process when the formation of crystals was observed at the cell walls, forming a columnar zone. The convectional field in the measurement cell at this stage showed two major vortices with downward streaming at the cold walls and upward streaming in the centre of the measurement cell. The occurrence of NH_4Cl crystals was observed optically and first attempts were made to quantitatively measure their number density, size distribution and sedimentation rate by PIV and particle tracking (PT). The aforementioned study demonstrated the applicability of particle image velocimetry and particle tracking in a solidification experiment. It illustrated that the convectional flow field, particle numbers and sizes can be quantified with these techniques. The aim of the experiments which we present in the present paper is to further investigate the temperature and velocity fields of the stable convection rolls that had been observed prior to solidification. A quantification of the temperature and the occurring velocities in the convection rolls should be compared with CFD calculations of the same system. The combination of experimental and numerical results will lead to a better understanding of the process as well as improvements to our numerical model. Since the influence of Rhodamine on the NH_4Cl–water solidification has not yet been explored, we started with PIV and LIF investigations of pure water, where the same convection rolls have been observed as in the early stage of NH_4Cl–H_2O solidification.

2. Experimental techniques and setup

Particle image velocimetry (PIV) is a whole-flow-field technique providing instantaneous velocity vector measurements in a cross-section of a flow. The use of modern CCD cameras

* Corresponding author. Tel.: +43 38424 022 223.
E-mail address: sven.eck@unileoben.ac.at (S. Eck).

0921-5093/$ – see front matter © 2005 Elsevier B.V. All rights reserved.
doi:10.1016/j.msea.2005.09.071

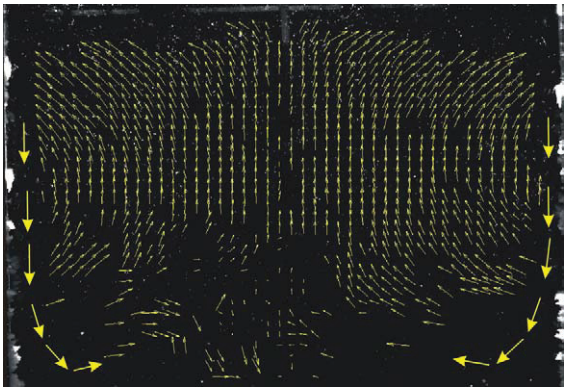

Fig. 1. PIV results measured during the early NH_4Cl–H_2O solidification process, see Ref. [5].

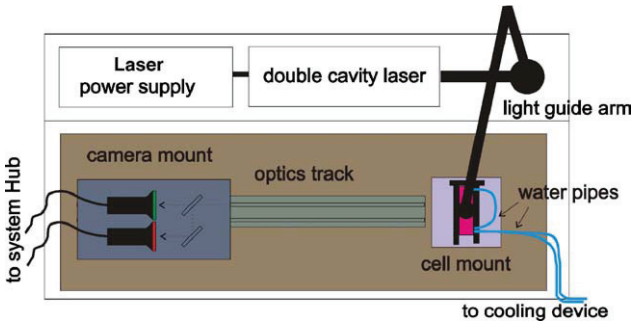

Fig. 3. Sketch of the combined PIV–LIF setup.

and dedicated computing hardware results in real-time velocity maps. The measurement principle of PIV has been presented in a former publication [5]. Planar laser induced fluorescence (P-LIF) is an image acquisition method which enables visualization and quantitative measurements of concentration or temperature fields. In our experiments, we took advantage of the temperature dependence of the fluorescence intensity of Rhodamine B. The experimental procedure will be described in the following section. For the PIV and LIF experiments presented in this study we used a double cavity Nd-YAG Laser (frequency doubled, $\lambda = 532$ nm). The data analysis for PIV was performed using the commercial software package "FlowManager", provided by DANTEC dynamics [6]; the data analysis for P-LIF was performed via a self-developed image processing script written in MATLAB. A square measurement cell with 10 cm × 10 cm × 3 cm inner diameter was designed with three copper walls and two transparent sides made of glass. Front and top view of the measurement cell are shown in Fig. 2 together with a sketch of the setup for stereoscopic PIV/LIF. The three copper walls of this measurement cell can be cooled and heated separately or together in a controlled manner. The coolant used consisted of a mixture of water and automotive anti-freeze. It could be heated/refrigerated between +150 and −35 °C and pumped by an external bath (HAAKE C30P) through silicone tubes into the cell walls. Inside the copper walls the coolant followed a meander path which led to a uniform temperature at the inside of the cell walls. The temperature of the cell walls and for some checking experiments inside the measurement cell were measured and recorded via a 16 channel thermocouple reader (Stanford SR 630) equipped with NiCr-Ni (type K) thermocouples. For the experiments presented in this work, two identical cameras were mounted on a 50% beam splitter with the optical axis perpendicular to the glass plates of the measurement cell (Fig. 3). The camera lens of the PIV camera was covered by a band pass filter around $\lambda = 532/533$ nm, the camera lens of the LIF camera was covered by a high pass filter $\lambda = 570$ nm. In this way, the PIV camera only recorded direct or scattered light from the laser source, whereas the LIF camera only recorded the fluorescence of Rhodamine B.

2.1. Temperature field measurement (LIF)

Temperature levels are deduced from the local fluorescence re-emitted by the temperature sensitive marker Rhodamine B which is excited by a laser ($\lambda = 532$ nm, $P_0 = 1$–100 mW). The local fluorescence level depends on the Rhodamine concentration as well as on the exciting laser power. For a set of experiments, we therefore kept the laser power and the experiment geometry (camera setup and focus position) fixed. Preliminary experiments showed that the temperature field in the measurement cell within 1 min can be considered as constant. The LIF images shown in this work represent the calculated mean pixel value images of 50 sequential images, i.e. averaged over 50 s. This procedure was applied for both the LIF calibration and evaluation. For a medium laser power ($P_0 = 20$–50 mW), the fluorescence increased linearly for small concentrations but reached a saturation at higher concentrations. For our combined PIV–LIF

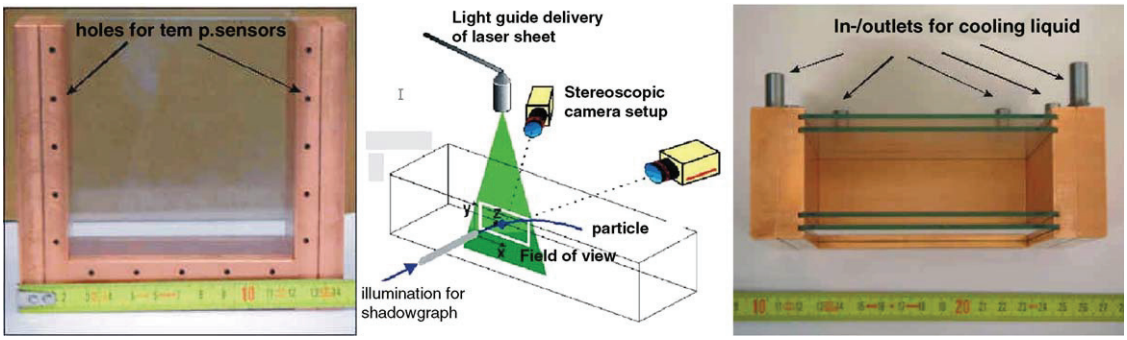

Fig. 2. Front and top views of the measurement cell and sketch of a stereoscopic PIV setup.

measurement, we chose a concentration of 90 μg/l to avoid the saturation regime.

2.2. Velocity measurements (PIV)

In the present study, polyamide particles of 20 μm diameter were used for the velocity measurements. The average flow velocity during the convection experiments in our setup was in the order of 10^{-3} m/s. These seeding particles were chosen because the flow velocity was considerably higher than the particle settling velocity (for water in the order of 10^{-6} m/s as given in [7]). For PIV, the time between pulses was set to 1 s. The processing technique used in this study was Dantecs' "adaptive correlation", a cross-correlation method described in [6]. The interrogation area was 32 × 32 pixels, i.e. 1.5 mm × 1.5 mm, using three refinement steps, starting at 256 × 256 pixels. The overlaps of the interrogation area in the horizontal and vertical directions were 25 and 50%, respectively. Furthermore, a filter was applied, which filters out vector maps by arithmetic averaging over vector neighbors; an averaging area of 3 × 3 was used. This filter removed outliers due to false correlations resulting from reflections at the cell walls.

2.3. Measurement procedure

In agreement with the NH_4Cl–H_2O solidification experiments the temperature range of interest was 5–45 °C. For our PIV/LIF investigations we filled the measurement cell with 200 ml of distilled water and added 90 μg/l Rhodamine B. The LIF calibration was done by a self-developed MATLAB script. In brief, the fluorescence intensity was plotted versus the corresponding temperature for three different temperatures: 5, 15, and 45 °C. The script correlated the fluorescence intensity to the temperature at each pixel of the image via a linear fit. This correlation was stored and applied to LIF images taken with the same setup, i.e. the same Rhodamine concentration, camera setup and laser intensity. For the convection experiments, the water was left for several minutes at 41 °C until the movements from the stirring had settled. When the PIV showed a random but low velocity distribution, the cooling of the cell walls was started. When setting the cooling water reservoir from 42 to 5 °C at maximum flow rate and cooling power, the coolant cooled the copper cell walls almost linearly from 40.7 to 6 °C within 1500 s and stayed at 6 °C for the rest of the experiment. The slope of the cell wall temperature was fit by a line with the simple equation $T(t)$ (°C) = 40.29 (°C) − 0.020 (K/s) × t (s). The result of the temperature measurement at the cell walls and a linear fit for the first 1500 s are shown in Fig. 4. Due to the good thermal conductivity of copper the walls the temperature differences along the cell walls were ≤0.2 K, as revealed by thermocouple measurements. As soon as the cooling of the wall had been started, PIV and LIF images were recorded.

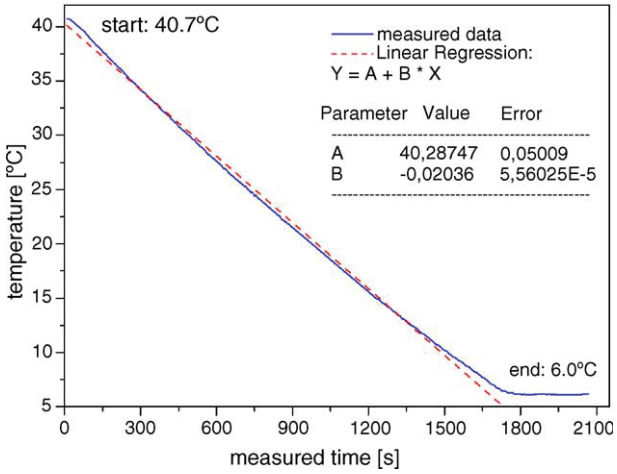

Fig. 4. Measured and approximated cell wall temperature.

3. Numerical simulation setup

The numerical simulation of natural convection of water in the die casting model was performed using the commercial CFD software FLUENT [8]. The density of water was taken as piecewise-linear temperature dependent [9]. The flow was calculated both in 2D and 3D and assumed to be laminar. The results of 2D and 3D calculations were found to be equivalent. Since the temperature field of the cavity was axis symmetric, the numerical simulation was chosen to compute only half the experimental cell, i.e. a 50 mm × 65 mm rectangle represented the 2D computational domain. The computational grid was structured quadrilaterally, accordingly refined near the top, left, and the bottom walls, in order to resolve sharp temperature gradients at these borders. On the side and bottom planes of the cell, the temperature for each time step was assumed to be constant. At the upper surface of the cell, convective heat transfer between air and water was assumed, with a heat transfer coefficient of 100 W/(m^2 K), the temperature of the free air was taken as 20 °C (RT), and the free slip condition was taken for the velocity at this interface. As the initial condition, the temperature of water within the computational domain was set to 40.3 °C, whereas velocities were set to zero. The time dependent boundary condition for the wall temperature given in Fig. 4 has been implemented in the FLUENT calculation via a user defined subroutine (UDF) [8].

4. Experimental results

In Fig. 5, we present the results of PIV velocity field and LIF temperature field measurements from 600 and 1500 s after the cooling of the cell walls began. The measured velocity vectors in Fig. 5(a, b, and e) are displayed in a rainbow color scheme where red corresponds to the highest and blue to the lowest velocity. A more quantitative description of the velocity field will be given in the comparison with the numerical results. The measured LIF temperature fields given in Fig. 5(c and d) are displayed with their corresponding color bar, where red corresponds to high and blue to low temperatures. The initial state PIV, i.e. 1–100 s after the start of the cooling showed a random distribution of velocity vectors in the order of 0.1 mm/s and a uniform temperature field of 40.7 °C (not shown). A visual

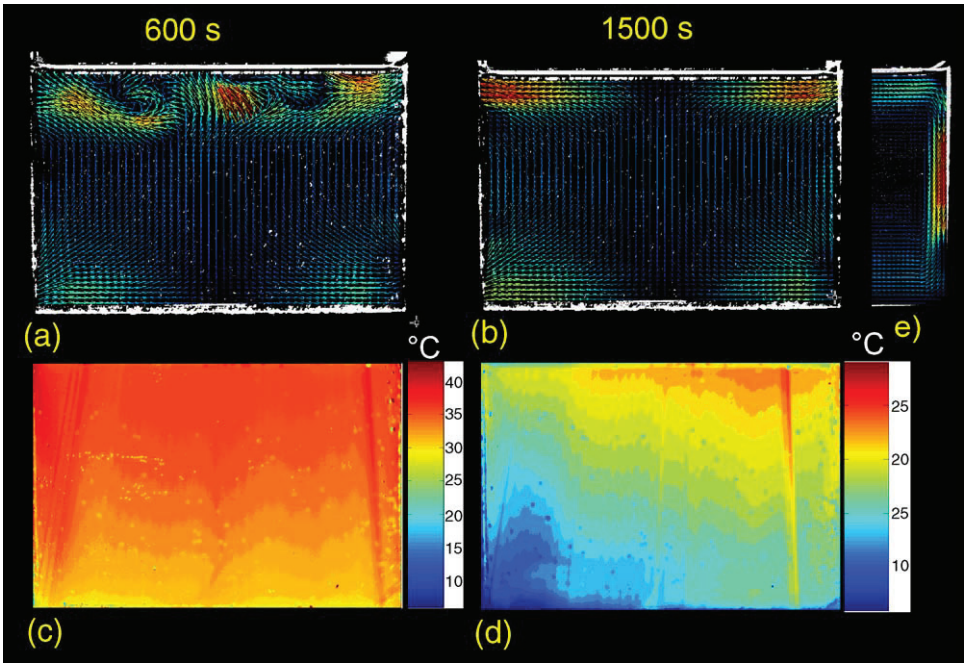

Fig. 5. PIV (a, b, e) and LIF (c and d) results of natural convection of water, details in the text.

observation of the particle flow showed the development of two convection rolls after 300–600 s. The established temperature gradient led to small changes of density which, in turn, created buoyancy forces that drive the flow of the liquid. At this stage the two clearly distinguishable convection rolls appeared in the instantaneous PIV measurements together with an unstable velocity region near the liquid–air interface at the top of the measurement cell (Fig. 5a). The LIF temperature field of this stage is given in Fig. 5c). The temperature field gradually changed from 30 °C at the bottom to 40 °C at the top with horizontal isolines in the centre and decreasing temperature close to the cooled side walls of the cell. The vertical lines visible as fan with darker rays in Fig. 5(c and d) are artefacts due to shadowing from particles floating at the liquid–air interface. A 1500 s after the start of the cell cooling, the visual observation and PIV showed two stable and axis symmetric convection rolls forming a centre region of low velocity in the order of 0.1 mm/s, accompanied by higher velocity regions (0.5–1 mm/s) in the corners of the measurement cell (Fig. 5b). The LIF taken at this stage is given in Fig. 5(d); the temperatures in the water at this stage ranged from 15 to 30 °C, the observed unsymmetry between the right and the left side of the cell are considered as an artefact due to an uneven illumination, however a tendency to horizontal isolines is still visible. In the visual observation of the process the convection rolls clearly reveal a down-flow near the cell walls and an up-flow in the centre of the measurement cell. When dividing the images into 32 × 32 pixel regions, the interrogation areas for the actual PIV correlation led to correlation problems near the cell walls which rendered the down-flow occurring close to the wall invisible. After ∼60 min, i.e. when a steady-state temperature was reached, the down-flow near the cell side wall was wide enough to be measured with PIV as shown in Fig. 5(e).

5. Comparison of experimental and simulation results

In Fig. 6, we present the results of the numerical simulation, where Fig. 6(a and b) show the velocity and Fig. 6(c and d) the temperature fields at 600 and 1500 s, respectively. Comparison of Figs. 5 and 6 shows a good qualitative agreement of the measured and calculated velocity fields and temperature intervals within the cell. The best agreement was achieved 1500 s after the start of the cooling when a stable state was obtained in the experiment. To judge the agreement more quantitatively, velocity profiles have been extracted from the experimental and numerical results. In Fig. 7, we present velocity profiles displaying the length of the measured velocities along five vertical lines at 1–5 cm distance from the right cell wall. The 5 cm line profile thus represents velocities measured on the vertical center line of our measurement cell, i.e. the symmetry line of the numerical setup. The experimental and numerical results are displayed in Fig. 7(a and b), respectively. On the centre line the measured velocities ranged from 0 to 0.1 mm/s with a maximum in the centre and minima on the top and the bottom. Going from the centre towards the wall the line profiles show a constant value around 0.1 mm/s as minimum in the centre and maxima up to 0.8 mm/s near the top and 0.4 mm/s in the bottom region. The fact that the two top corners showed velocities which were by a factor of ∼2 higher than the bottom corners is attributed to the different interface conditions. At the top, the liquid air friction facilitates the flow as compared to the liquid-wall friction at the bottom and the side walls. In the numerical simulation this behavior was taken into account by assuming a non-slip condition at the cell walls and a slip condition at the top in the simulation setup. The fact that the experimental velocity curves show kinks at the top and bottom interface is attributed to PIV correlation problems

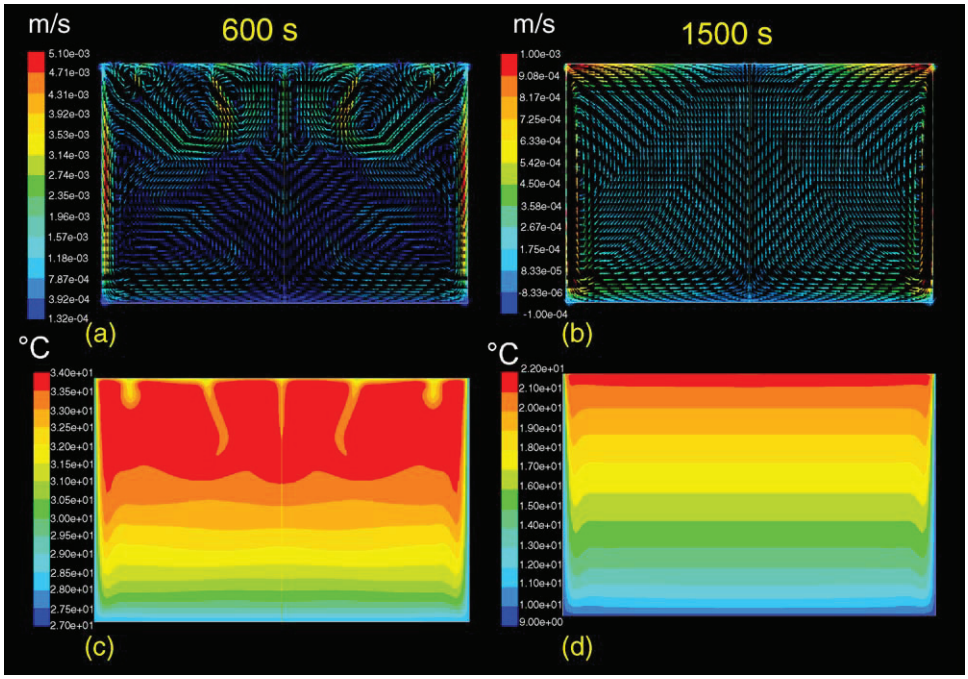

Fig. 6. CFD calculated velocity and temperature fields in water after 600 s (a and c) and 1500 s (b and d).

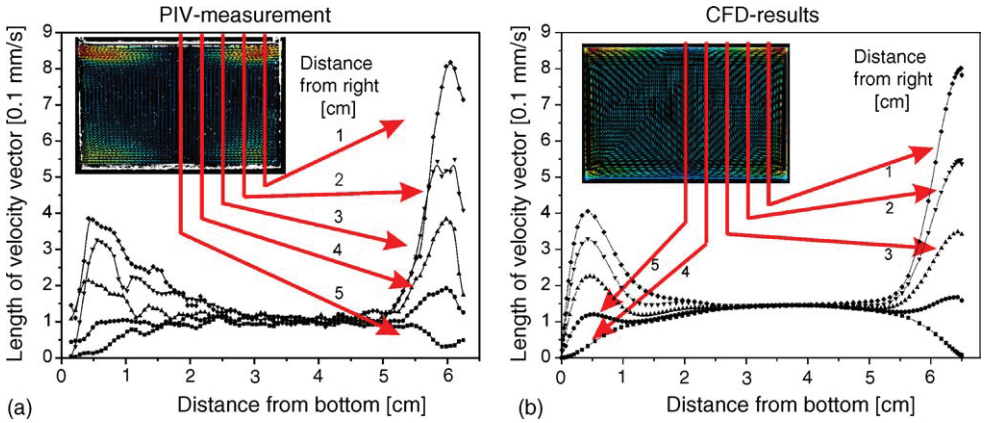

Fig. 7. Velocity distribution along vertical lines at the given distances from the right cell wall.

which arise due to reflections at the cell wall and the liquid–air interface.

6. Summary and outline

Simultaneous measurements of temperature and velocity fields have been performed applying a combined laser induced fluorescence (LIF) and particle image velocimetry (PIV) setup to natural convection in a die casting model. Furthermore, the natural convection has been modeled numerically using a single phase model. The work illustrated the difficulties to get reasonable experimental results on one hand and to choose proper boundary conditions and material properties for numerical simulations on the other hand. The achieved agreement between numerical prediction and experimental results confirms the applicability of the reported setups as starting points for both experimental and numerical investigations of the convection during hypereutectic NH_4Cl–H_2O solidification in our die casting model.

Acknowledgements

This work has been funded by the Austrian Science Funds (FWF) [10] and was supported by the Austrian Christian Doppler (CD) Research Association in the frame of the CD Laboratory "Multiphase Simulation of Metallurgical Processes".

References

[1] A. Ludwig, M. Wu, Metall. Mater. Trans. A 33 (2002) 3673–3683.
[2] M. Wu, A. Ludwig, A. Bührig-Polaczek, Solidification and Crystallization, in: D. Herlach (Ed.), 2004, pp. 204–212.
[3] M. Wu, A. Ludwig, Adv. Eng. Mater. 5 (2003) 62–66.
[4] M. Wu, A. Ludwig, A. Bührig-Polaczek, P.R. Sahm, Inter. J. Heat Mass Transfer 46 (15) (2003) 2819–2832.

[5] S. Eck, J. Mogeritsch, A. Ludwig, Mater. Sci. Forum 508 (2005) 157–162.
[6] FlowManager software and Introduction to PIV Instrumentation, Dantec Dynamics GmbH, Publ. No.: 9040U3625, 2000.
[7] C. Ghenai, A. Mudunuri, C.X. Lin, M.A. Ebadian, Exp. Therm. Fluid Sci. 28 (1) (2003) 23–35.
[8] FLUENT 6.2 UDF Manual, Fluent Inc., 2005.
[9] J.A. Dean, Lange's Handbook of Chemistry, McGraw-Hill Inc., 1999.
[10] Fonds zur Förderung der wissenschaftlichen Forschung (FWF), Projekt 17619, http://www.fwf.ac.at.

Experimental and numerical investigations of NH_4Cl solidification in a mould

Part 1: Experimental results

M. Stefan Kharicha*[1], S. Eck[1], L. Könözsy[2], A. Kharicha[2] and A. Ludwig[1]

This work represents a benchmark experiment to test numerical solidification codes dealing with combined columnar and equiaxed growth. The solidification of a hyper-eutectic NH_4Cl–H_2O solution has been investigated in a $100 \times 80 \times 10$ mm^3 brass cell cooled on three sides from 41°C down to 26°C. The cell was illuminated by a laser generated light sheet and images were recorded throughout the whole solidification process. Both columnar and equiaxed growth of NH_4Cl was observed. The freckle formation observed during preceding experiments in a $100 \times 100 \times 30$ mm^3 brass cell was not present in this thinner cell which made the cell more suitable for comparison with numerical predictions. Numerical simulations of the same solidification process were performed using an Eulerian-Eulerian multiphase approach and its details will be presented in Part 2.

Keywords: NH_4Cl solidification, multiphase flow, convection, numerical simulation

Introduction

Amongst other phenomena, simultaneous liquid flow and solid movement is an important phenomenon in solidification.[1] Convection in the liquid melt is mainly caused by thermo-solutal buoyancy forces, while the movement of free solid crystals is due to the density difference of solid and liquid under the influence of gravity.

The two phase model proposed by Ludwig *et al.* has been thought to be able to describe globular equiaxed solidification and the Columnar-to-Exquiaxed Transition (CET).[2–8] Whether such an Eulerian multiphase model will describe solidification and phase separation processes properly, is strongly dependent on the definition and implementation of source terms, interaction terms, and other auxiliary terms for the corresponding conservation equations. Thus, experiments with well defined boundary conditions are essential to verify such numerical predictions.

An important contribution to this field was done by Beckermann *et al.*[9–11] where both numerical and experimental results for NH_4Cl solidification proved the suitability and limits of the applied numerical solidification model. The aim of the present investigation is to create benchmark experiments which can be used to validate numerical models for both columnar and equiaxed solidification. In a previous investigation,[12] the authors presented results by using Particle Image Velocimetry (PIV) in order to measure the natural convection of water in a die cast model. In this work the same technique is used to visualize the solidification process.

Experimental technique and setup

The experimental cell is a square cavity with $10 \times 10 \times 1$ cm^3. The two side walls and the bottom are made from brass and the front and back sides are made from glass plates.[12] A meander path for the cooling liquid through the bronze walls generated a homogeneous cooling. The cooling was done with a HAAKE C30P bath linked through silicone tubes to the cell walls. The coolant liquid was a mixture of water and ethanol, which can be used as coolant down to −35°C. The temperature in the cell walls was monitored via thermocouples. NiCr-Ni thermocouples (accuracy +/−0·1°C) were connected to a thermocouple reader (Stanford SR 630), which continuously recorded the temperature during the experiment and linked the image acquisition with the temperature through a trigger signal. A double cavity Nd-YAG laser (frequency doubled, $\lambda = 532$ nm) was used as a light source. In contrast to the shadowgraph technique applied by Beckermann *et al.*[9–11] the presented PIV setup generated a 2 mm wide light sheet that illuminated the cell from the top. Thus, the PIV setup results represent a quasi two dimensional cross section of the solidification process, whereas the shadowgraph technique generated volume averaged results. The image acquisition was performed with a CCD camera mounted perpendicularly to the cell. Pictures were evaluated using the

[1]Chair of Modelling and Simulation of Metallurgical Processes, Dept. Metallurgy, University of Leoben, Franz Josef Str. 18, A-8700 Leoben, Austria
[2]Christian Doppler Laboratory for Multiphase Modelling of Metallurgical Processes, University of Leoben, Franz-Josef Str. 18, A-8700 Leoben, Austria

*Corresponding author, email mihaela.kharicha@mu-leoben.at

Received 17 June 2008; accepted 12 September 2008
DOI 10.1179/136404609X368000

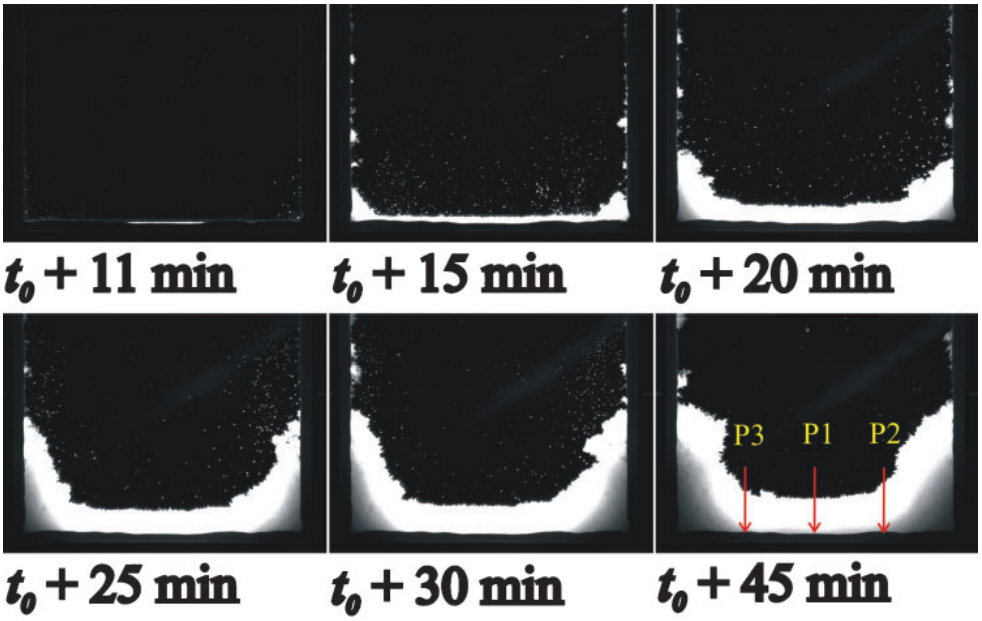

1 Sequential images of the 29·5 wt-% NH_4Cl-H_20 solidification process in a 10 cm wide mould

commercial software 'Flow Manager', developed by Dantec Dynamics.[13] The camera lens was covered with a band pass filter $\lambda = 532 \pm 3$ nm, to ensure that the CCD camera only recorded direct or scattered light from the laser source and excluded background light.

Measurement procedure

In the present experiments a hypereutectic alloy of 29·5 wt-% NH_4Cl was solidified. According to the phase diagram published in ref,[1] the liquidus temperature for this concentration is 36°C. The solution was prepared at 41°C and then poured into the cell that had been preheated at 41°C. The height of the solution in the cell is 8 cm. Next, the solution rested for 15 minutes. After this holding time, the cooling of the cell walls was started at time t_{initial} by setting the bath to 26°C. The temperature was recorded by the thermocouples fixed in the cell walls. The resulting temperature profile was similar to the one published elsewhere,[12] i.e. a linear cooling rate of 1·2 °C min^{-1} was observed for the first 826 sec until the set temperature was reached and then the temperature stayed at $26^\circ \pm 0{\cdot}1$°C for the rest of the process. Note that this temperature is only sufficient to solidify around 20% of the sample. The recording of the images started simultaneously with the cooling of the cell walls at $t_{initial}$; images were taken every 10 seconds until the solidification was complete, i.e. ~45 minutes after $t_{initial}$.

Results and discussion

Figure 1 shows sequential images of the solidification process together with the time at which the images were taken. In the first stage of the solidification process (image not shown) a convection of the melt was observed with a downward flow near the cell walls and an upward flow in the centre. This can be understood as the thermal convection, caused by the temperature dependent density of the melt. In the second stage of the solidification process, columnar dendrites were observed growing from the sidewalls approx. 11 minutes (700s) after t_{initial}. In the third stage a large number of equiaxed grains appeared in the lower part of mould where according to previously published measurements[1] the temperature had dropped below the liquidus temperature. Notice that according to additional experiments intended to capture both the crystal movement and the movement of the melt (not shown) the thermal convection pattern at this stage of solidification was replaced by an unsteady flow pattern. This can be explained by the increasing influence of solutal convection that opposes the thermal convection at this stage. In the following stages of the solidification process, the equiaxed grains followed the convectional flow and some of them interacted with columnar crystals at the side walls where they were captured. These captured grains grew together with the columnar dendrites towards to the melt. Other equiaxed grains were rejected from the sidewalls into the bulk melt by the thermal and solutal convection driven flow. These crystals continuously grew until they reached a size where gravity dominated over the other forces, thus they settled to the bottom of the mould. The solidification process ended 34 min after the first crystals had appeared, i.e. 45 minutes after t_{initial}. At the end of the process around 35% of the cavity is covered with mush.

A measurement of the mushy zone thickness at the vertical walls was hindered by the fact that it was frequently observed that the mixed equiaxed/columnar NH_4Cl growing horizontally from the side walls broke due to gravity and the strong flow along the walls. The first breaks of the horizontally growing crystals were usually observed 25 minutes after t_{initial}. On the other hand the horizontal solid layer at the bottom grew homogeneously throughout the process. To monitor the growth of the mushy zone, its thickness was therefore measured at three different positions perpendicular to the bottom cell wall. The three positions are indicated in the last image in Figure 1.

Figure 2 shows a plot of the mushy zone thickness versus the solidification time at these three different positions. The jumps in the measured thickness at P2 and P3, i.e. the two positions at 2·5 cm distance from the cell walls, indicate that crystals had broken off the

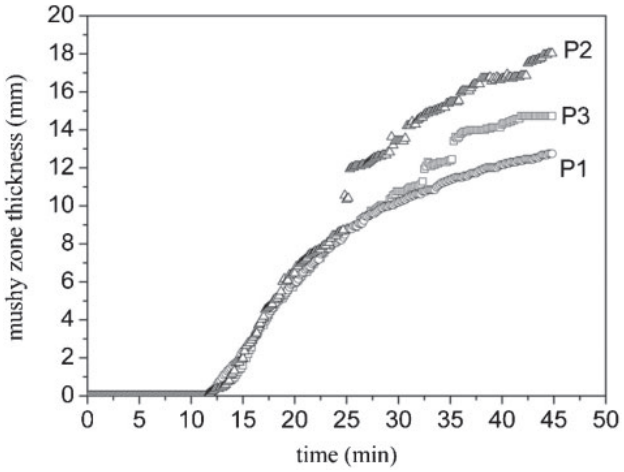

2 Measured thickness of the columnar zone at three positions on the bottom wall as indicated in the last image of Fig. 1

vertical walls and settled on top of the solid layer growing from the bottom. However, the thickness measured in the centre of the cell, i.e. at P1, showed a

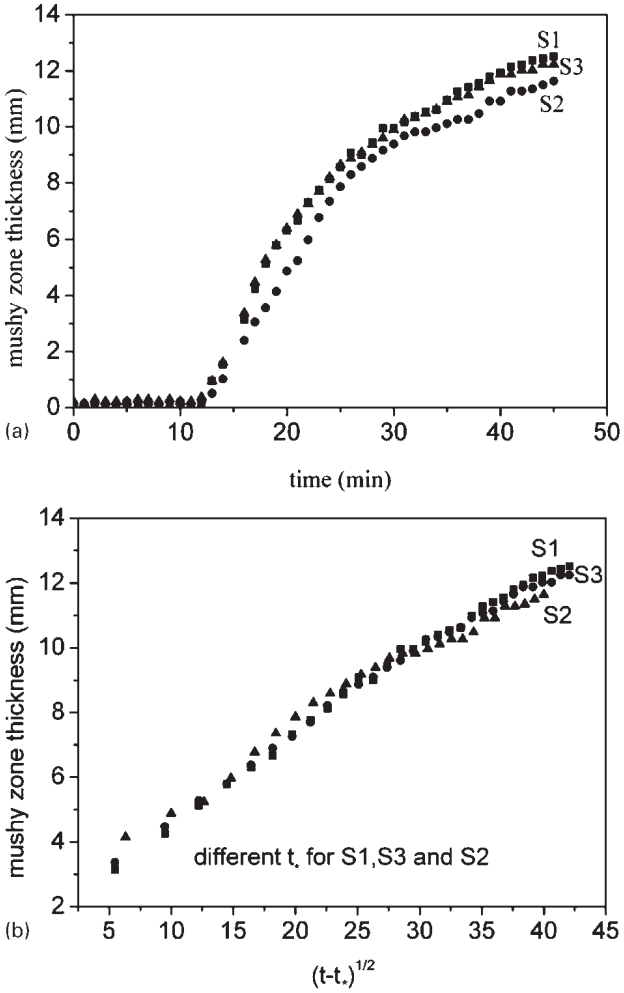

3 *a* Measured thickness of the columnar zone in the centre of the bottom wall versus time for three different experiments with the same initial concentration (29·5 wt-% NH_4Cl) and cooling rate; *b* Measured thickness of the columnar zone in the centre of the bottom wall versus $\sqrt{t-t_*}$ for three different experiments with the same initial concentration (29·5 wt-% NH_4Cl) and cooling rate

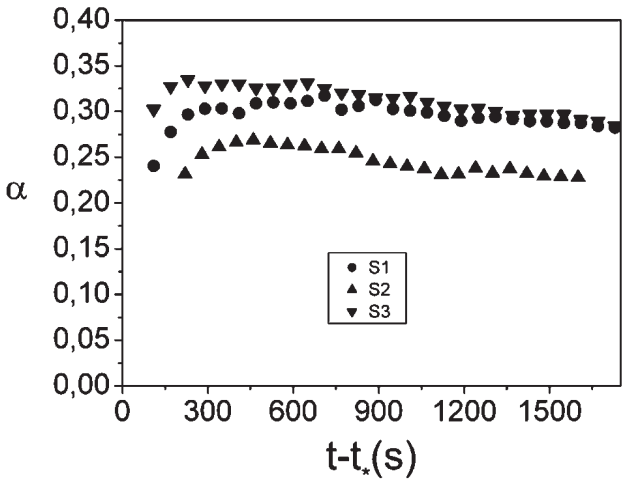

4 Evolution of $\alpha_{\sqrt{t}}$ (definition given in the text) for the three experiments presented in Fig. 3

continuously increasing layer. Figure 3a shows the corresponding centre position measurements for 3 different experiments with the same initial concentration and the same cooling rate. The plot indicates that t_0 (the time when solidification started) and the thickness of the mushy zone at P1 at certain times of the solidification process were reproducible within 10% of the measured thickness. Figure 3b shows the mushy zone thickness measured at P1 plotted versus $\sqrt{t-t_*}$.

On these plots of mushy zone thickness versus time, two growth regimes were observed. Initially the amount solidified increases linearly with time, later the amount solidified increases linearly with the square root of time[14] as shown in Figure 3b. The square root of time growth regime can be described by the following equation:

$$d=\alpha\sqrt{(t-t_*)}+\beta \quad (1)$$

where d is the thickness of the mushy zone; t the solidification time, t_* the time when the square root of time growth period starts and β the thickness of the mushy zone at t_*.

α was calculated for each point in the linear and in the square root of time regime, as $\alpha_{\text{lin}}=\dfrac{d}{t-t_0}$ and $\alpha_{\sqrt{t}}=\dfrac{d-\beta}{\sqrt{(t-t_*)}}$, respectively. Figure 4 shows plots of $\alpha_{\sqrt{t}}$ versus the solidification time. At the beginning of 'the square root of t' growth regime, $\alpha_{\sqrt{t}}$ is not constant but after a very short time becomes approximately constant. Nevertheless, a little decrease in $\alpha_{\sqrt{t}}$ was noticed. The magnitude of the $\alpha_{\sqrt{t}}$ factor is related to the local thermal and solutal gradient at the solidification front. The observed decrease of $\alpha_{\sqrt{t}}$ can therefore be attributed to the fact that both gradients decrease with solidification time. Table 1 shows the calculated average α factors for the three experiments presented in

Table 1 Average α-factors for the three experiments presented in Fig. 3

	α_{lin}	$\alpha_{\sqrt{t}}$
S1	0·01096	0·29
S2	0·01071	0·23
S3	0·01039	0·30

Fig. 3. The average values of the α-factors show only small variations between the different experiments and are therefore considered suitable as a parameter to validate the numerical calculations of the solidification process.

Summary

This work represents benchmark experiments with NH_4Cl–H_2O solutions designed to test numerical solidification codes dealing with combined columnar and equiaxed growth. It has been shown that several experiments with a fixed geometry, initial concentration and cooling rate generated reproducible results. Furthermore the various stages of the solidification process that have to be reproduced by numerical models were shown. For a quantitative comparison with numerical results, the thickness of the mushy zone at certain positions in the setup was monitored versus the solidification time. The resulting plot was fitted with a function following the square root of time law and the reproducibility of the implemented α-factor was demonstrated. In the second part of this work[6] the presented experimental results are compared with numerical simulation predictions gained by a sophisticated Eulerian-Eulerian multiphase approach.

Acknowledgements

This work was funded by the Austrian science funds FWF (Fonds zur Förderung der wissenschaftlichen Forschung) by means of the Project 17619-N02 'Measurement of flow fields during equiaxed solidification'.

References

1. S. Eck, J. Mogeritsch and A. Ludwig: *Mater. Sci. Forum*, 2006, **508**, 157–162.
2. A. Ludwig and M. Wu, Metall: *Mater. Trans. A*, 2002, **33A**, 3673–3683.
3. M. Wu, A. Ludwig and A. Bührig-Polaczek, Special Issue of Adv. Eng. Mat., ed. D. Herlach, 2004, pp. 204–212.
4. M. Wu, A. Ludwig: *Adv. Eng. Mat.*, 2003, **5**, (1), 62–66.
5. M. Wu, A. Ludwig, A. Bührig-Polaczek and P.R. Sahm: *Inter. J. Heat and Mass Transfer*, 2003, **46**, (15), 2819–2832.
6. L. Könözsy, S. Eck, M. Stefan Kharicha, M. Wu and A. Ludwig, Second International Conference on Advances in Solidification Processes (ICASP-2), June 2008, Seggau, Austria, accepted for publication in IJCMR.
7. M. Wu and A. Ludwig: *Metall Mater. Trans.*, 2006, **37A**, 1613–1631.
8. M. Wu and A. Ludwig: *Metall Mater. Trans.*, 2007, **38A**, 1465–1475.
9. C. Y. Wang and C. Beckermann: *Metall. Mater. Trans. A*, 1996, **27A**, 2754–2764.
10. C. Y. Wang and C. Beckermann: *Metall. Mater. Trans. A*, 1996, **27A**, 2765–2783.
11. C. Beckermann and C. Y. Wang: *Metall. Mater. Trans. A*, 1996, **27A**, 2784–2795.
12. S. Eck, M. Stefan Kharicha, A. Ishmurzin and A. Ludwig: *Mat. Sci. Eng. A*, 2005, **413–414**, 79–84.
13. Dantec Dynamics GmbH, Wetterkreutz 5, D-91058 Erlangen, Germany.
14. M. C. Flemings 'Solidification Processing', Mcgraw-Hill College (1974).

Simultaneous Observation of Melt Flow and Motion of Equiaxed Crystals During Solidification Using a Dual Phase Particle Image Velocimetry Technique. Part I: Stage Characterization of Melt Flow and Equiaxed Crystal Motion

ABDELLAH KHARICHA, MIHAELA STEFAN-KHARICHA, ANDREAS LUDWIG, and MENGHUAI WU

A dual phase particle image velocimetry technique is applied to study the flow pattern during a combined equiaxed-columnar solidification process. This technique is able to measure simultaneously the liquid and the equiaxed grain velocity pattern within an academic Ammonium Chloride water ingot. After the formation of a steady convection pattern, solutal buoyancy together with falling crystals destabilize and break the steady convection flow into multiple chaotic cells. In the beginning of the solidification process, the flow transitioned from 2D to a 3D turbulent regime. The kinetic energy for the flow was calculated during the solidification process.

DOI: 10.1007/s11661-012-1414-z

I. INTRODUCTION

MODELING of metallurgical processes is a rapidly expanding field and the research activities in the last decades cover a wide range of areas including melt pretreatment, solidification, and subsequent manufacturing routes. Among those activities, solidification stands in the central position because the primary structure of the materials, and even many defects such as porosity, (macro or micro) segregation, and hot tears, forms during solidification. Those primarily formed structures or defects once existing are difficult to remove or modify by the subsequent material processing.

The more realistic models for describing industry-relevant manufacturing processes, with involvement of solidification, are based on the solution of the macroscopic transport equations (mass, momentum, enthalpy, and species) at the system length scale. Microscopic phenomena such as nucleation, crystal growth kinetics, and thermodynamic equilibria at liquid-solid interfaces are considered with simplified models, which are coupled with the macroscopic transport equations.[1,2]

An important phenomenon in solidification is the simultaneous occurrence of melt flow and crystal motion. Solidification takes place either by a growing columnar front and/or by the growth of equiaxed crystals. Columnar growth happens in the form of cells or dendrites from the mold walls into the bulk melt due to heat extraction from outside. In equiaxed solidification, globular or dendritic crystals form by nucleation or fragmentation and subsequent growth into the surrounding melt. Convection in the melt might have different reasons. Most often, thermal and/or solutal buoyancy together with external body forces occurs. In most of the cases, the flow is unstable and even turbulent. In the case when columnar growth is present, there exists a mushy region where both solid and liquid phases are present. When equiaxed solidification is present, the phases (liquid and equiaxed crystals) interact with each other through momentum and energy exchange. The resulting solid-liquid multiphase flow pattern strongly depends on the microstructure of the equiaxed crystals, which in turn is governed by grain nucleation and growth mechanisms. Because the coupled liquid-solid flow causes structural and chemical inhomogeneities in the final solidified products, a fundamental understanding of the multiphase transport phenomena coupled with the grain nucleation and growth mechanisms is required. The occurrence of dispersed two-phase flows in nature and industrial applications is abundant. The current paper presents some similarity with processes in which dispersed solid particles interact with a carrier flow. However, there is a lack of consistent data to support the numerous theories for flow-particle interaction that have been developed in recent years.[3–8]

In the past, many experimental studies[1–5,9] have been done to investigate the development of the thermo-solutal, also known as double-diffusive, convection during solidification. As a transparent analog for metallic alloys, the NH_4Cl-H_2O solution has proved its convenience to study thermo-solutal convection during columnar solidification. Furthermore, there exist some experimental studies of equiaxed solidification using hypereutectic H_2O-NH_4Cl, mainly presented by Beckermann's group.[10–12] They used the aqueous solution to combine quantitative measurements with visualization of

ABDELLAH KHARICHA, Research Team Leader, MIHAELA STEFAN-KHARICHA, Ph.D. Student, ANDREAS LUDWIG, Professor, and MENGHUAI WU, Associate Professor, are with the Department of Metallurgy University of Leoben, Leoben, Austria. Contact e-mail: abdellah.Kharicha@notes.unileoben.ac.at

Manuscript submitted March 23, 2012.
Article published online September 19, 2012

two-dimensional equiaxed dendritic solidification. These publications[10–12] proved the powerful means of combined experimental measurements and numerical simulations. In a recent work, Lum *et al.*[13] successfully applied a laser-based optical method, called molecular tagging velocimetry (MTV), to measure velocity fields in the complex thermo-solutal flows associated with solidification in the presence of significant buoyancy. On the other hand, Beckermann and Wang[10] applied the shadowgraph technique to compare qualitatively the numerically achieved model with experimental results.

Quantitative measurements in differentially heated cavities with solidification were obtained by Wang *et al.*,[14,15] Ghenai *et al.*,[16] Skudarnov *et al.*,[17] and Shih and Tu[18] by means of recent particle image velocimetry (PIV) techniques. Wang *et al.*[14] employed an advanced PIV technique to measure the velocity field in a cavity subjected to cooling from two vertical walls and the bottom wall. Low concentration solutions were used. Skudarnov *et al.*[17] and Shih and Tu[18] investigated the effect of the initial solute concentration on the evolution of the convection pattern during solidification. The observed vortexes were described as the result of a double-diffusive convection. In the first stage, the velocity field showed a major circulation loop. Later, many small eddies appeared, and finally several layers of circulation flows were observed. The magnitude of the velocity flow seemed to decrease as solidification proceeded. Almost all pictures presented in the previous works[10,15,18] showed a strong presence of equiaxed crystals not only at the vicinity of the solidification front, but also in the bulk region. Thus, the velocity field obtained from the pictures is based on a mixture of equiaxed crystal and particle seed movements. It is known that equiaxed crystals can develop a relatively large settling or drift velocity.[19,20] The purpose of the present study is to present the results of a new PIV technique that is able to separate the liquid and equiaxed flow.[21–24] This technique is able to measure simultaneously the liquid and the equiaxed velocity magnitude and pattern. It was utilized to measure the complete velocity field during a solidification process in a small cavity cooled from the bottom and two lateral sides.

The PIV technique was introduced elsewhere.[25–28] This technique can measure the whole two-dimensional or three-dimensional flow field simultaneously without disturbing the flow field.[29] To measure the velocity of the fluid, the flow is seeded with small tracer particles with a density similar to the fluid density. A plane of the flow is illuminated by a thin sheet of light. The images of the tracer particles within the plane are recorded twice with a very small time delay of Δt onto a high speed camera. Then, the velocity vectors of the flow are calculated by means of adaptive- or cross correlation of the two subsequent images. The highest peak in the resulting correlation surface indicates the relative displacement for which the best fit between image patterns was obtained and is assumed to represent the real displacement. Errors and limitations that are intrinsic to this technique have been clearly identified by Westerweel.[30]

II. EXPERIMENTAL PROCEDURE

For our quantitative study of the interaction between melt flow and solidification, we have chosen the relatively thin rectangular cavity shown in Figure 1, which was cooled from three sides with a predefined cooling rate. A hypereutectic 29.5 wt pct H_2O-NH_4Cl solution was solidified under controlled conditions. The process was monitored with a two-camera PIV device, whereby a 1-mm-thick cross section in the middle of the test cell was illuminated from the top by Nd-YAG laser pulses.

The cell was made of brass with 1-mm-thick glass plates in the front and at the back. Inside the brass walls, cooling channels which follow a meandering path were designed to achieve a homogeneous temperature. The cooling was controlled by pumping water with a given temperature through the cooling channels.

The H_2O-NH_4Cl solution was prepared by mixing NH_4Cl powder with distillate water and heating to 318.15 K (45 °C) until the powder had completely dissolved. According to the H_2O-NH_4Cl phase diagram, the liquidus temperature of an alloy containing 29.57 wt pct NH_4Cl is 310.15 K (37 °C). Then, fluorescent tracer particles (polyamide particle colored with the Rhodamine B) were added, whereby the solution was intensively stirred. The average diameter of the particles is around 10 μm and their material density is around 1.05 g/cm^3. The density of a 29.5 wt pct NH_4Cl solution at liquidus is about 1.078 g/cm^3 and that of a eutectic NH_4Cl solution is 1.076 g/cm^3. Thus, tracer particles and solution have a similar density (difference 2.7 pct for a 29.5 wt pct NH_4Cl solution and 2.5 pct for the eutectic alloy), and it is reasonable to assume that the particles follow correctly the flow of the solution.

After having added the particles, the solution H_2O-NH_4Cl is poured into the preheated die at 317.15 K (44 °C). This was done slowly in order to prevent capturing of air bubbles. Nevertheless, if air bubbles

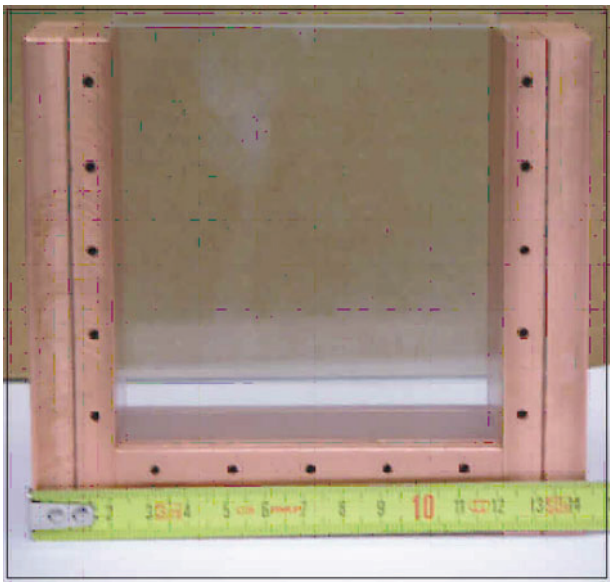

Fig. 1—Rectangular cavity used for the controlled solidification experiments. The inner dimensions are 10 × 10 × 1 cm^3.

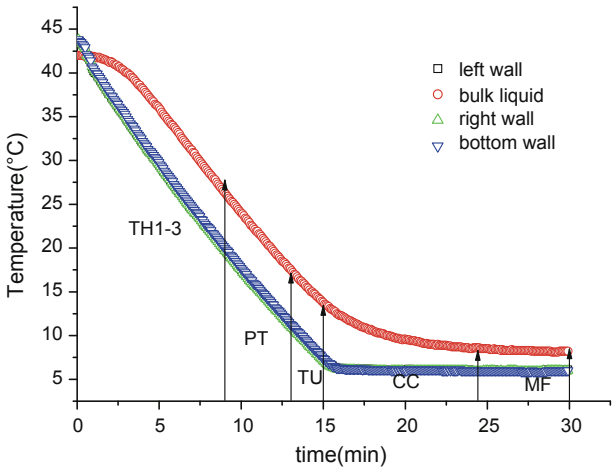

Fig. 2—Evolution of the wall temperatures and the temperature in the upper middle of the liquid solution.

stacked to the cell walls, they were mechanically removed carefully. The filling height was kept at 8 cm. After filling, we waited typically 1 hour to equilibrate the temperature field before we started cooling. In this time, the small, but continuous, heat loss through the front and back window resulted in a steady and symmetric thermal buoyancy flow which was used as the reproducible initial stage for the different experimental runs. Then, the brass cell walls were cooled by 1.2 K (1.2 °C)/min (Figure 2), while the temperature of the brass walls and at the top middle position in the solution was recorded every 5 seconds. In order to avoid condensation of humidity on the glass plates, we stopped cooling when 278.15 K (5 °C) was reached. According to the H_2O-NH_4Cl phase diagram, this corresponds to a solid fraction of 30 pct. Thus, the solidification process terminated with a partly solidified cell.

A. *Storage Data and Image Processing Tools*

The two-color PIV system adopted in this study comprised a pulsed laser system for illumination, two high speed cameras for image acquisition, a synchronization unit, and a software packet for image and data processing. The laser was a double-pulsed solid-state Nd-YAG and had an output power of 120 mJ with a maximum pulse rate of 21 Hz. The pictures taken by the cameras were in the resolution of 1600 × 1186 pixels.

Perpendicular to the casting cell, the two CCD cameras were mounted in parallel. The PIV camera mount has a common housing with a shared observation window for the two cameras. This insures straightforward imaging of the same area of the flowing media, while allowing flexible camera positioning. To distinguish the liquid flow from the crystals, a green filter was mounted on one CCD camera (band pass filter of 532 ± 2 nm through which only laser light passes, which was scattered by the equiaxed crystals) and an orange filter on the other camera (high pass filter of 570 ± 2 nm through which only the light passes, which was reemitted by the fluorescent dye (Rhodamine B)). In this way, the cameras captured images without "interphase" noise, which could then have been processed without any further treatment to obtain the two velocity fields. A set of 20 images was taken every 60 seconds and stored on a PC. The time separating two images was 0.25 seconds which was small enough to catch the time variation of any motion.

Numerous sources of uncertainty exist in such a complex measurement. The positioning of the measurement plane formed by the laser sheet was set as accurate as possible. Nevertheless, an error generated by the laser alignment with respect to the measurement cell of 0.5 pct was unavoidable. The uncertainty related to the PIV technique will be discussed in the next section. The type T thermocouple used had an accuracy of ±0.1 K (0.1 °C).

B. *The Adaptive Correlation and the Particle Tracking Methods*

The processing technique used in this study was an adaptive correlation method. Two sequential image maps were subsampled in interrogation areas of 16 × 16 or 32 × 32 pixels to obtain the velocity vectors. As usual, the size of the interrogation area depends on the space resolution needed. An overlap of the initial interrogation areas of 50 pct in a horizontal and vertical direction was set. Overlapping of the interrogation areas increases the chance that all particle movements are contained within at least one interrogation area. In numerical practice, the cross correlation of corresponding areas of each image in the image pair is performed, using an FFT-based algorithm, to find the relative displacement that provides the best fit between both particle image patterns. This displacement was taken as the estimation of the mean displacement in the considered area. The theoretic foundations of this technique have been clearly summarized by Westerweel[30] (a more detailed presentation is given in the literature[31]).

An adaptive algorithm for PIV image analyzing may be defined as an algorithm that is able to use the information obtained from the image to further enhance the information recovery and validation process. The aim of the adaptive method is to overcome some of the limitations of the classical standard correlation algorithms.[31,32] Better results were obtained by successively performing the interrogation of the image pair, each time with smaller interrogation areas and using the previously obtained estimation of the displacement field to determine the optimum offset at each location. In this way, the probability that particle images in both frames correspond to the same set of particles does not decay as the size of the interrogation area is reduced. In addition, the signal-to-noise ratio was improved for the correlation obtained with the present method.[31,32]

Correlations are by far the most common approach when dealing with high density seeding images. However, in the present work, the density of equiaxed crystal within an interrogation area could not be guaranteed. When crystal rain occurs, the adaptive correlation technique gives excellent results. However, in areas with

a very low number of equiaxed particles, another method, the particle image tracking, was preferred. The use of this method is valid when the mean distance between particle images is large compared to the particle image diameter or the pixel size. It consists of tracking individual particle images to find the correspondent displacements. The high density limit has been defined by Adrian[25] as the seeding condition for which particle displacements are of the same order of magnitude as the mean spacing between particle images.

C. *Validation of the Velocity Vector Field*

All the considered interrogation techniques will deliver some small percentage of erroneous velocity vectors. The reasons for the occurrence of these spurious vectors may be found in the limitations of each technique and in the quality of the images. Therefore, special care was given to the recording of the images in order to limit certain amount of noise, owing to ambient light, bad focusing, misalignment, etc. that may deteriorate the signal-to-noise ratio in parts of the image. In addition, a quality control for the obtained vector field as classified by Nogueira *et al.*[33] was performed in order to discriminate between correct measurements and spurious vectors. The first criterion used to eliminate an unreliable vector is the ratio of the largest to the second largest peak in the cross correlation. If a ratio exceeds the threshold (83 pct) value, then there are two probable values for velocity. In an area with some presence of equiaxed crystals, the second pick in the flow correlation map was clearly identified as the pick corresponding to the equiaxed crystals. The origin of this contamination was due to some diffraction of the light scattered by the tracer particle. Some shadow of crystal can be detected within the flow pictures. For the same reason, it is not possible to follow the flow within the mushy zone. If the second pick was clearly identified as a result of the other phase, the velocity vector was automatically validated even if the threshold for the pick ratio was not reached. For other cases, if a bad result was detected in a single interrogation area, we replaced it by interpolation from the valid neighbors. In case several neighbor interrogations areas did not pass the pick ratio criteria, we chose to delete and not replace the bad vectors. This situation was encountered near the cooling walls where a fast and thin downward jet was present due to the strong thermal buoyancy at the beginning of the experiments.

III. RESULTS

Figure 2 shows the cooling curves of the experiment discussed in the present paper. First, it is obvious that the left, right, and bottom walls reveal the same temperatures. As defined from the circulating coolant, the temperature of the walls dropped by 1.2 K (1.2 °C)/min until the lower temperature limit of 278.15 K (5 °C) was reached. The temperature measured at the top middle position in the solution (labeled in Figure 2 with "bulk liquid") revealed some delay. After about 4 minutes and until 13 minutes, the bulk temperature followed the same linear variation as the wall temperatures, but at 7 K (7 °C) higher. While the wall temperature reached the lower temperature limit, the difference between wall and bulk liquid temperatures decreased in a Gaussian form.

As mentioned in the previous section, the cell was heated to 317.15 K (44 °C) prior to cooling. Due to a small heat loss *via* the front and back windows and the constant heating from the brass walls, the temperature measured at the top middle position in the solution cooled down from the pouring temperature of 317.15 K (44 °C) to around 315.15 K (42 °C). Thus, the liquid along the heated brass walls is slightly hotter than in the bulk, and so a typical thermal convection pattern appeared with an upward flow along the vertical walls and a downward flow in the center. This convection pattern was steady and reproducible and canceled any residual motion from pouring. It was thus taken as a well-defined initial condition for the solidification experiments.

As outlined in the following, the process proceeded by passing seven different stages. The first three stages (labeled by TH1, TH2, and TH3) involved only liquid, whereas the last four (labeled by PTH, TU, CC, and MF) involved solidification as well.

A. *Thermal Stage 1 (TH1): Initial Thermal Buoyancy*

As mentioned before, the experiment started with a steady thermal convection pattern which is shown in Figure 3.

Due to the fact that the temperature measured at the top middle position in the solution turned out to be two degrees below the predefined cell temperature, the liquid in contact with the vertical walls had a tendency to rise by thermal buoyancy. This is at the origin of the symmetric flow pattern shown in Figure 3. The direction of the flow was upward near the vertical walls and downward at the center. As we found that this pattern is

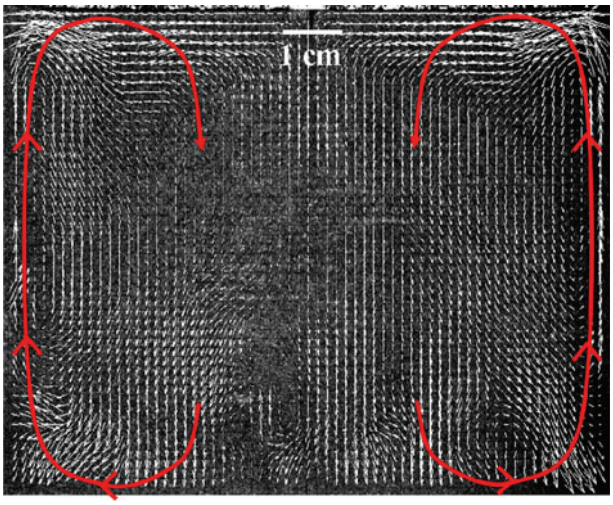

Fig. 3—Melt convection prior to the start of active cooling (thermal stage 1: TH1) measured with PIV. As the slightly hotter walls heated the liquid nearby, it flows upward. The velocity vectors are scaled linearly between v_{min} = 0.185 mm/s and v_{max} = 2.215 mm/s.

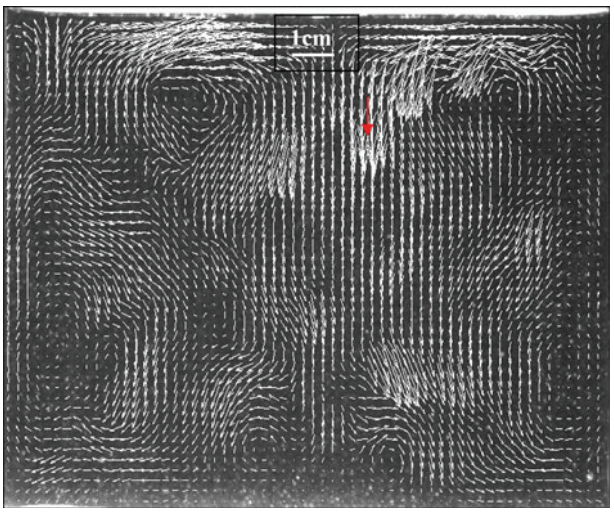

Fig. 4—After the walls' cooling was switched on, the walls' temperature dropped below the temperature of the solution, and thus the upward flow tendency along the vertical walls turned into a downward one. This unstable situation defines the unstable transition stage (thermal stage 2: TH2). The PIV measurement was done $t = 2$ min after the active cooling was started. The velocity vectors are scaled linearly between $v_{min} = 0.03$ mm/s and $v_{max} = 0.37$ mm/s.

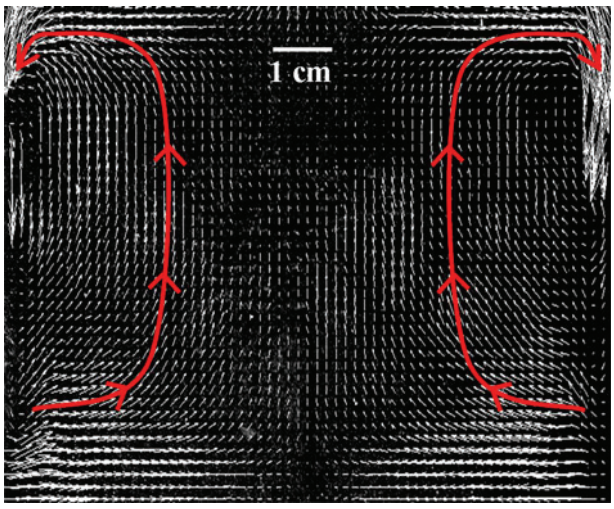

Fig. 5—With time, the downward flow near the vertical walls led again to a stable thermal buoyancy pattern (thermal stage 3: TH3). The PIV results shown were taken $t = 8$ min after switching on the cooling. The velocity vectors are linearly scaled between $v_{min} = 0.08$ mm/s and $v_{max} = 1.12$ mm/s.

almost steady, we took it as the initial condition for the experiment.

B. *Thermal Stage 2 (TH2): Unstable Transition Stage*

We took the moment at which the wall cooling actively started as zero point in time. As now the wall temperature decreases below the temperature of the solution, the former steady convection pattern becomes unstable (Figure 4) and small eddies were emitted from the vertical walls. This stage took typically around 7 to 8 minutes before a new stable flow pattern appeared again.

C. *Thermal Stage 3 (TH3): Stable Thermal Buoyancy*

When the wall temperature decreases below the temperature of the solution, the liquid close to the vertical walls has a tendency to sink by thermal buoyancy. However, in the experiment, it took 8 minutes until a stable convection pattern established again (Figure 5). This time, the direction of the flow was downward near the walls and upward at the center. As cooling became stronger and stronger, the magnitude of downward flow velocity slightly increased with time. It is clear that the hydrodynamic pattern of this stage was found to be more stable and symmetric than that of stage TH1. Stage TH3 lasted only around 1 to 2 minutes before evidence for solidification appeared. Note that due to the bad correlation, the velocity vectors directly along the vertical walls are not shown in Figure 5.

D. *Perturbation of the Thermal State (PTH): Solidification Perturbed Thermal State*

Visible solidification, mainly columnar, started at about 9 to 10 minutes after beginning of the cooling. It did not appear uniformly all over the wall surfaces, but rather in islands of columnar dendritic crystals (Figures 6(a) and (b)). In the vicinity of each columnar island, the flow is immediately disturbed by the presence of one or two small eddies (Figure 6(a)). However, during about the first 3 to 4 minutes of visible solidification, the main pattern of the flow (symmetry, magnitude, main direction) is not changed. Sometimes, the strong downward jet is able to detach columnar structures of up to 5 mm in size from the cooling wall. This phenomenon happens mainly at this stage, rarely in later stages. Few equiaxed crystals were also occasionally observed at the vicinity of the vertical walls (Figure 6(a)). This stage lasted around 3 to 4 minutes.

E. *Turbulent Flow State (TU)*

As the solidification proceeded, the number of equiaxed crystals increased, and perturbations of the main flow increased in magnitude. A new flow regime with a large number of small eddies appeared (Figures 7(a) and (b)). Now, solidification totally covered the walls and filled about 5 pct of the domain (at the end, ~30 pct is reached). The lake of coherence of the observed eddies, and the presence of strong velocity gradients even far from the walls, is a strong indication of the three-dimensional and turbulent character of this regime. In this stage, large visible equiaxed crystals appeared only near the walls. However, the movement of the small crystals could be evaluated by correlation. This stage lasted around 2 minutes.

F. *Coherent Chaotic Flow State (CC)*

Out of the turbulent flow stage, a regime where the flow map is coherent, but still chaotic, appeared (Figure 8(a)). The characteristic eddy size was of about 1.5 to 2 cm, and thus larger than the distance between

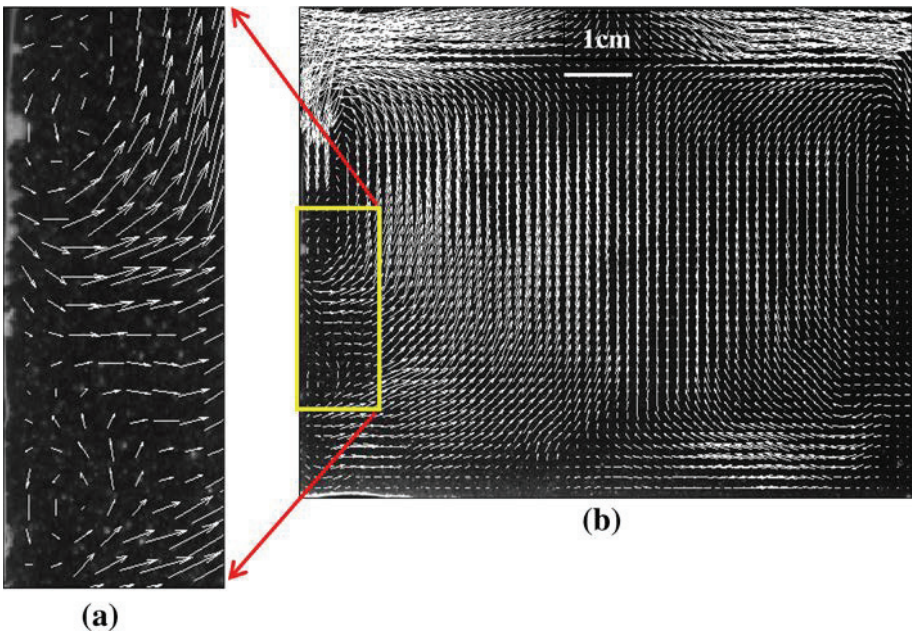

Fig. 6—Measured flow field just after solidification became visible. Due to the formation of dendrites at the walls, eddies were generated close by (*a*) and thus the stable thermal buoyancy stage got more and more disturbed (*b*). Thus, we call this stage of the solidification the perturbed thermal stage (PTH). The measurement was taken $t = 9$ min after switching on the cooling. The velocity vectors were scaled between $v_{min} = 0.169$ mm/s and $v_{max} = 0.57$ mm/s for (a) and between $v_{min} = 0.052$ mm/s and $v_{max} = 0.73$ mm/s for (b). Note that in the zoom (a), some equiaxed crystals are already visible.

the two glass plates. The equiaxed crystallization was very strong (Figure 8(b)), and it represented the leading solidification mechanism. The velocity magnitude was at its maximum. Large crystals appeared even in the bulk far from the vertical walls, and often fell, grouped in columns or in agglomeration. Note that during this stage, most of the solidification process happened. This included the initiation and growth of freckles (flow channels in the mush) where traces can be seen in Figure 9(a). At the end of this stage, the solidification front had almost reached its final position. Stage CC lasted around 10 minutes.

G. *Meandering Flow State (MF): Quasi-Steady Meandering Flow Occurs*

The small eddies disappeared progressively and gave place to a meandering flow traveling from the top to the bottom (Figure 9(a)). The flow is stratified into 5 to 7 circulation layers. It is possible to follow the flow streamlines from the top to the bottom of the cell. The number density of equiaxed crystals decreased in the vicinity of the vertical solidification front and increased in the bulk in the form of a relatively large crystal column or in agglomeration (Figure 9(b)). But, globally equiaxed falls were not as strong as in the previous CC regime. The meander flow seems to penetrate the bottom mushy zone. In this regime, the number of equiaxed crystals and the magnitude of the flow velocity were continuously decreasing in time until extinction. Finally, about 30 pct of the cell volume is filled with solid. Stage MF lasted around 5 to 10 minutes until the typical meandering flow disappeared.

IV. ANALYSIS AND DISCUSSION

The key mechanisms that control the melt flow in the test cell are thermal and solutal convection and drag by columnar and equiaxed crystals. In order to identify the different flow regime that we could encounter, it is useful to compute the global Rayleigh number

$$Ra = \frac{g\beta_T \Delta T \cdot H^3}{\alpha v} + \frac{g\beta_C \Delta C \cdot H^3}{Dv}, \qquad [1]$$

with β_T and β_C being the thermal and solutal expansion coefficients, α the heat conductivity, v the kinematic viscosity, D the diffusion coefficient in the liquid, and g the gravity constant. H is the typical length at which thermal and solutal buoyancy occurs. We have taken the height of the liquid in the test cell as H. ΔT is the temperature difference responsible for thermal buoyancy and ΔC is the concentration difference responsible for solutal buoyancy.

In the present experiment, the highest melt temperature existed at the top middle position in the bulk T_{bulk} and the lowest in the liquid right at the cooled walls, which can be approximated by T_{wall}. We thus took

$$\Delta T = T_{bulk} - T_{wall}. \qquad [2]$$

As for a hypereutectic H_2O-NH_4Cl solution, the solute redistribution coefficient is larger than one ($k > 1$), the formation of NH_4Cl crystals lead to a reduction in melt concentration. Thus, the initial concentration is the highest and the lowest melt concentration occurs right at the cooled walls where solidification has just started. We thus took

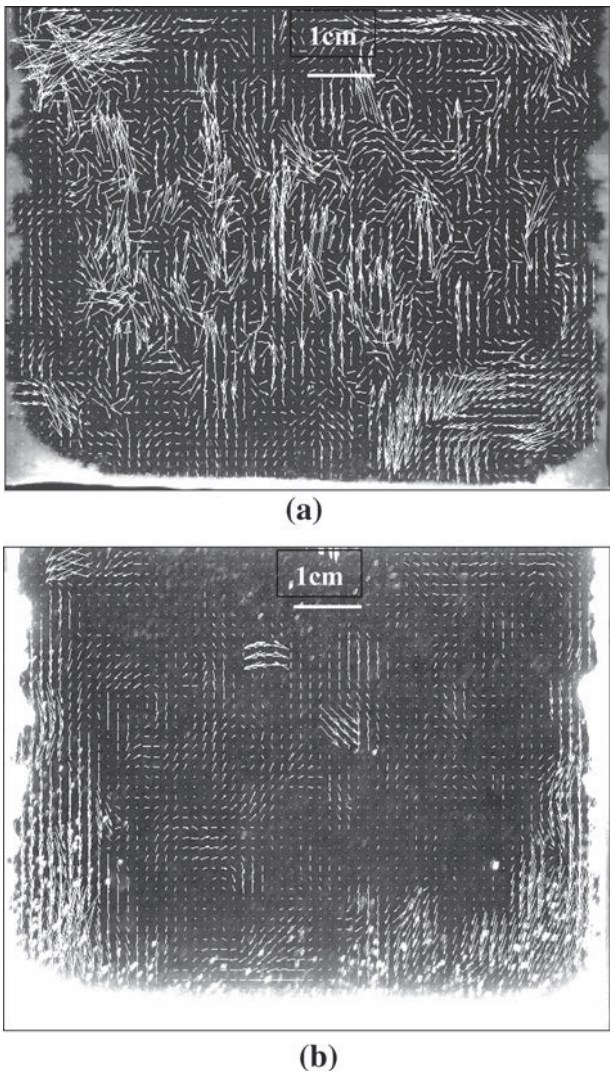

Fig. 7—When solidification further proceeded, a new flow regime with a large number of small eddies appeared. As described in the text, this regime turned out to be turbulent, and thus we call it the turbulent regime (TU). At this stage, the large number of equiaxed crystals was allowed to measure both the liquid velocity shown in (*a*) and the velocity of the equiaxed crystals shown in (*b*). The two-camera PIV measurement was done at $t = 13$ min. The velocity vectors are scaled between $v_{min} = 0.051$ mm/s and $v_{max} = 0.709$ mm/s for the liquid (a) and between $v_{min} = 0.252$ mm/s and $v_{max} = 3.52$ mm/s for the equiaxed crystals (b). Note that the crystals are one order of magnitude faster.

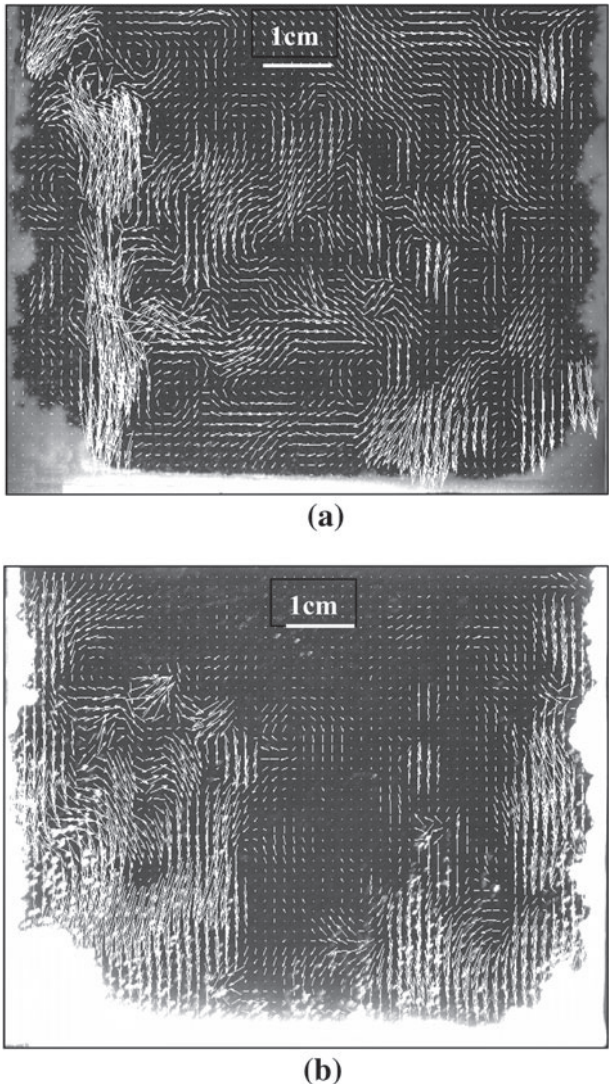

Fig. 8—Examples showing the melt velocities (*a*) and the equiaxed crystals' velocities (*b*) for the so-called coherent CC. The two-camera PIV measurement was done at $t = 15$ min. The velocity vectors are scaled between $v_{min} = 0.111$ mm/s and $v_{max} = 1.56$ mm/s for the liquid (a) and between $v_{min} = 0.278$ mm/s and $v_{max} = 3.87$ mm/s for the equiaxed crystals (b).

$$\Delta C = C_0 - C(T_{wall}), \qquad [3]$$

with $C(T_{wall}) = C_{eutetctic} + m(T_{wall} - T_{eutetctic})$ being the equilibrium concentration at T_{wall} and m the slope of the liquidus temperature being positive for hypereutectic H_2O-NH_4Cl. In the present process, since the temperature and the concentration field are continuously evolving, the magnitude of the global Rayleigh number is consequently changing. To evaluate the Rayleigh number, the main difficulty remains in a good estimation of the magnitude and the time variation of ΔT and ΔC.

In the thermal buoyancy stages (TH1, TH2, TH3), ΔT never exceeds 7 K (7 °C), which is also true during solidification. Thus, the thermal Rayleigh number does not exceed 10^8. This is one order of magnitude smaller than the critical number for the occurrence of turbulence. Nevertheless, with the time the wall temperature changes, it is possible to promote unstable behaviors such as those observed at stage TH2. Note that the material properties used to calculate the Rayleigh number are given in Table I.

When the wall temperature reached the liquidus temperature of hypereutectic H_2O-NH_4Cl solution, solidification created ammonium crystals and lower concentrated liquid. This lower concentrated liquid led to a tendency for upward buoyancy and thus contributed to the instabilities observed in the stage PTH. However, the interaction between the flow at the wall and the columnar crystals can also generate eddies. In Figure 6(a), the generation of vortices at the vicinity of few columnar dendrites can be seen. Therefore, it is

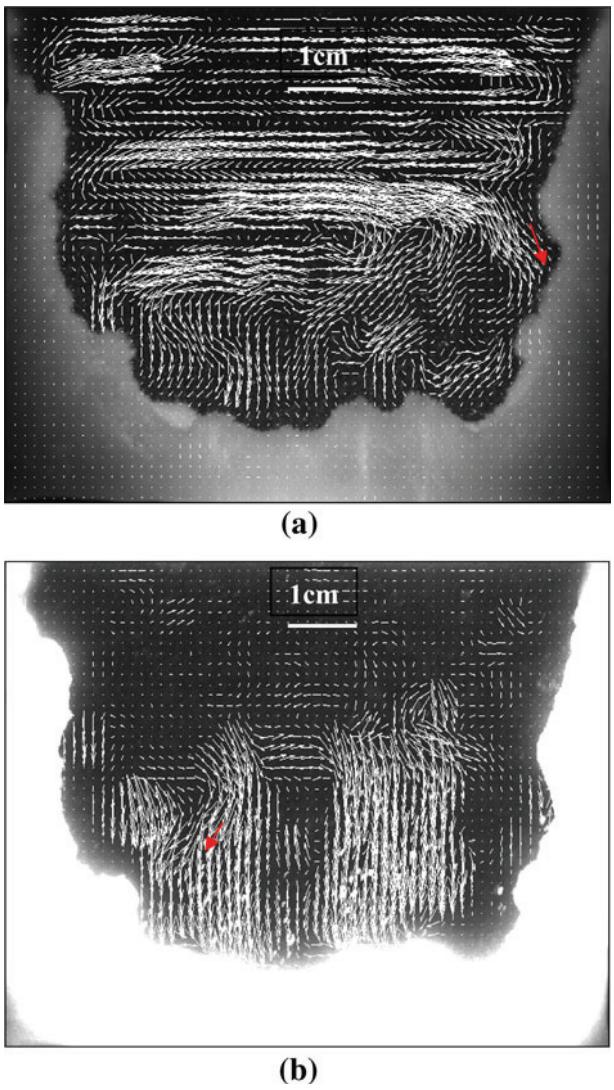

Fig. 9—Examples showing the melt velocities (*a*) and the equiaxed crystals' velocities (*b*) for the meandering flow regime (MF). The two-camera PIV measurement was done at $t = 30$ min. The velocity vectors are scaled between $v_{min} = 0.067$ mm/s and $v_{max} = 0.466$ mm/s for the liquid (a) and between $v_{min} = 0.155$ mm/s and $v_{max} = 2.17$ mm/s for the equiaxed crystals (b).

obvious that these perturbations are due to the presence of columnar crystals and not due to the solutal convection. At this stage, the thermal downward jet is strong enough to wash out the low concentration solute rejected during the solidification.

However, with proceeding solidification, solutal convection plays a more important role. Phenomena such as plume dynamics, chaos, or turbulence can appear.[34–36] For a vertical wall, the transition to turbulence occurs at $Ra = 10^9$.[37] With the material properties given in Table I, the solutal Rayleigh number becomes $Ra = 2.2 \times 10^{11} \cdot \Delta C$. Therefore, the critical concentration difference that can lead to the occurrence of turbulence can be estimated to be $\Delta C_{crit} = 0.45$ wt pct which easily occurs during solidification by interdendritic segregation. This means that right from the start of solidification, the flow regime might become turbulent.

Table I. Material Properties of the H_2O-NH_4Cl Solution

Property	Symbol	Value
Density of the liquid	ρ_W	1078 kg/m^3
Density of solid ammonium chloride	ρ_A	1527.4 kg/m^3
Thermal conductivity of the liquid	k_l	0.468 W/m/K
Liquid specific heat	c_{pl}	3249 J/kg/K
Liquid diffusion coefficient	D	4.8×10^{-9} m^2/s
Dynamic viscosity of the liquid	μ	1.3×10^{-3} kg/m/s
Thermal expansion coefficient	β_T	3.832×10^{-4} K^{-1}
Solutal expansion coefficient	β_c	0.257
Eutectic composition	$C_{eutectic}$	19.7 pct NH_4Cl
Eutectic temperature	$T_{eutectic}$	257.75 K

During the first 5 minutes of solidification, the concentration in the bulk can be approximated with the original concentration C_0. At the wall, the rejected solute has a concentration C (T_{wall}). At 4 minutes from the start of the solidification (at 13 minutes in Figure 2), the wall temperature reaches 284.15 K (11 °C). Then, $\Delta C \sim 10^{-1}$ and the corresponding Rayleigh number is probably at its maximum and reaches the value of 10^9. This could explain why the measured flow map in stage TU shows such chaotic and incoherent structures, a clear indication of the presence of turbulence. A flow is defined as coherent when the vector field shows clearly its main velocity structure. It must be emphasized that the given Rayleigh number is only an estimated value, it is calculated based on constant physical values found in the literature. Real physical values might be temperature and concentration dependent, which then modify the actual value of the Rayleigh number. But, the order of magnitude found indicates that turbulence in the present solidification process can be generated through solutal buoyancy. Nevertheless, by comparing Figures 7(a) and (b), we can notice that areas where a large number of equiaxed crystals exist are less subject to incoherence. The flow in these regions is well structured in clear streamlines or in large eddies. Obviously, the presence of floating crystals damps the turbulence eddies of the melt flow. Later, with the extension of areas of floating crystals (Figure 8(b)) and the decrease of ΔC, a laminarization of the entire domain occurs.

The evolution in time of the total kinetic energy of the liquid flow calculated with the measured velocity magnitude U as

$$KE = \sum_N \frac{1}{2} U^2 / N \qquad [4]$$

is presented in Figure 10. N is the total number of vectors. In the mushy zone, the velocity vectors are zero. Although there is the presence of some instabilities, no large change in the kinetic energy is observed before the start of solidification. Even if we would have taken the large velocity jets along the walls—which are not completely resolved—into account, the kinetic energy would not change dramatically.

The kinetic energy increased continuously during the perturbed thermal and turbulent regimes. The maximum is reached close to the end of the coherent chaotic regime

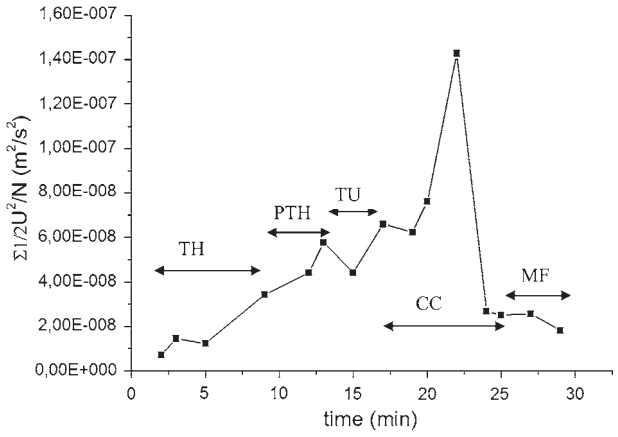

Fig. 10—Evolution of the apparent liquid kinetic energy. The different flow regimes are indicated: TH, thermal stages; PTH, perturbed thermal buoyancy by the start of solidification; TU, turbulent flow; CC, coherent chaotic state; MF, meandering and stratified flow.

(CC) at about $t = 22$ minutes. Later, in the stratified regime (MF), the kinetic energy decreases to levels similar to those of the thermal buoyancy states. This evolution of KE does not correspond to what is reported by Skudarnov *et al.*,[17] where the velocity decreases in magnitude all along with time. The reason for that might be the fact that in our experiment, we end up in a partly solidified sample where all dynamics fade out with time.

At around 25 minutes, the lower number of equiaxed crystals promotes a steadier and slower melt flow structure (Figure 9(b)). However, the flow path seems to be controlled by the local curves of the dendrite tip envelop. It is probable that the meandering flow regime is created by an auto-organization of the solutal convection in curved constrained geometry (from top to bottom). The concentration differences are small since the evolution of the dendrite tip envelop front is nearly stopped, but large enough to generate a flow KE similar to that of the thermal states.

Since the two vertical glass plates are only 1 cm apart, the flow will have a natural tendency to develop a 2D structure. In PIV analysis found in the literature, the flow was also generally believed to be 2D.[10,16,19–24] If the measurements allow the possibility to follow the flow path, then the flow can be qualitatively considered as two dimensional. Then, the streamlines can be closed, and the life of the eddies can be followed from appearance to dissipation. For our experiment, this was the case for all stages except the turbulent regime where coherence of the flow was totally lost. In the CC, the flow field revealed a clear 2D regime. In addition, the areas around strong chimney jets might also be subject to some turbulence or at least 3D effects.

A. *Equiaxed Motion and Interaction with Melt Flow*

Another source of energy is the fall of larger equiaxed crystals, which accelerates the melt flow in the vertical direction. A large number of equiaxed crystals can generate large melt flow velocities in some regions. In the present investigation, it was not possible to count the number of crystals. However, it was possible to estimate the part of the laser sheet that was occupied by large crystals just by looking at the area where the adaptive correlation was successful. At the coherent chaotic state, it became obvious that areas where the melt flow is the most intense correspond to areas where equiaxed crystals occupied large areas of the laser sheet. Thus, it can be concluded that the strong increase of KE between 15 and 23 minutes (Figure 10) is generated by the strong equiaxed crystal motion.

At the end of the experiment, the mushy zone represents 28 pct of the cell volume. According to the phase diagram, only 8 pct of the NH_4Cl mass will solidify. If the entire concentration solidifies in a packed form, it can fill only 6 pct of the cell volume. A simple calculation gives that in average, the mushy zone contains about 25 pct of solid and 75 pct of liquid. However, this is only an average value, the real solid fraction might be much higher at the vicinity of the cold wall and much lower near the solidification front. While the flow enters openly within the bottom mushy zone, it is deviated and curved by the solidification front surface. The vertical mushy regions act almost as nonpermeable media. Perhaps the fact that the vertical mushy regions are built with a succession of equiaxed and columnar layers might explain the difference with the bottom mushy layer. In addition, the sizes of equiaxed crystals that participate in the growth of the vertical walls are smaller than the ones reaching the bottom regions. Using a similarity between packed crystals and packed spheres, the Black-Kozeny law[38–40] predicts that the permeability increases with the crystals' size. These considerations, together with the flow observation, confirm that a strong variation in effective permeability (and porosity) might exist specially all over the surface of the solidification front.

B. *Topography of Stationary Mushy Regions*

In the presented experiment, solidification is never totally symmetric. This is specially the case at the vertical walls where the topography of the stationary mush possessed an irregular wavy shape. The characteristic size of these waves is 2 to 5 cm in length and 1 to 4 cm in depth (Figure 11). The bottom surface is also subject to variation mainly due to the occurrence of flow chimneys. Irregular columnar growth can be produced by turbulent thermal and solutal fields. The flow vector map suggests that such strong variations exist all along the process. Variation in solutal concentration might produce local remelting of the newly built structure. However, from our experimental observation, it becomes obvious that the main origin of these irregularities is the instability generated from the competition between equiaxed and columnar solidification. For a wavy vertical front, due to the presence of the sedimentation of equiaxed crystals, the wave will develop differently on its upward- and downward-oriented side. This seems to be the case during the regime CC where the sedimentation of equiaxed crystals is particularly strong (Figure 11). Thus, the topography of the mushy zone might develop with a mechanism of crystals

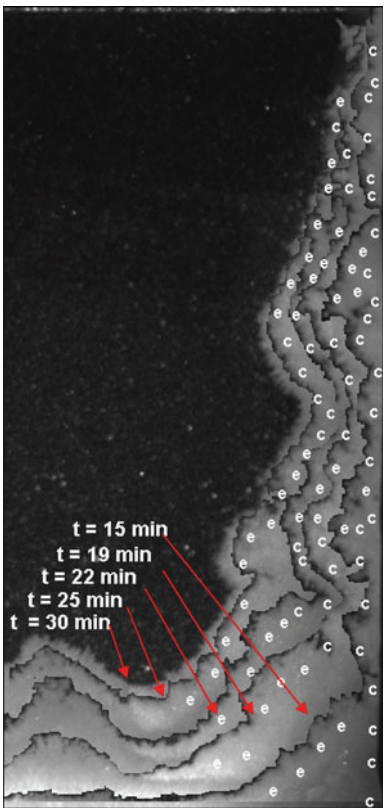

Fig. 11—Nonuniform columnar-equiaxed distribution at the solidification front. (c) indicates a nearly pure columnar dendritic growth front, whereas on the surface (e), equiaxed crystals have sedimented.

clogging on its upward- or vertical-oriented surface, while its downward-oriented surface can only develop through further columnar growth. On the picture, it is possible to observe columnar tips, rarely present on upward-oriented surfaces. In later regimes, as the equiaxed solidification decreases in intensity, the topography of the mushy zone become more and more uniform. At the end of solidification, several layers of equiaxed crystals inclined in the "A" form can be seen.

V. CONCLUSIONS

A special PIV was used to measure the velocity field during a columnar/equiaxed solidification process. The single-phase measurement technique developed for PIV has been extended to cope with liquid-equiaxed flows. It was applied to H_2O-NH_4Cl solidification in a die cast cell of $10 \times 10 \times 1$ cm^3 in which both the liquid velocity and the crystal velocity maps could be extracted. The separation between the two velocity fields could be obtained with the use of fluorescent particles' tracers that emit different waves when excited with the laser wavelength. Two pictures were taken simultaneously with two different cameras; the first one recorded only the laser light through a green filter, while the second one used an orange filter to record only waves emitted by the fluorescent particles. Thus, the first camera could follow only the crystals' paths, while the second camera recorded the liquid velocity field.

During the cooling, different regimes were observed. Before solidification, the flow is controlled by only thermal buoyancy. As soon as the solidification starts, turbulence and chaos are generated in the liquid by a solutal buoyancy mechanism. At the same time, strong equiaxed crystal rains occur at the vicinity of the solidification fronts. At the end of the process, the flow becomes more steady and auto-organizes in a meandering and stratified structure.

A coupling between the fluid flow and the equiaxed crystal was found. In areas with a high crystal density, the turbulence of the flow seems to be damped. The flow in these regions has either large eddies or clear streamlines. However, in the present configuration, it is not yet clear how much is the contribution of the equiaxed rains to the generation of chaos with respect to the solutal buoyancy. Spatio-temporal behavior of the liquid and crystal flow suggested the presence of instabilities and auto-organization often observed in the field of nonlinear systems and chaos. Complex behavior can be expected from the interaction of the flow and equiaxed crystals in larger systems.

ACKNOWLEDGMENTS

We kindly acknowledge the FWF (Austrian Science Fund, grant number P17619-N02 and P22614-N22) which paid the PhD scholarship for Mrs. Stefan-Kharicha who performed the experiences, measurements, and calculations.

REFERENCES

1. FLUENT 6.3: *User's Guide*, Fluent. Inc., Lebanon, NH, 2006.
2. A. Ludwig and M. Wu: *Metall. Mater. Trans. A*, 2002, vol. 33A, pp. 3673–83.
3. R.A. Gore and C.T. Crowe: *J. Fluid Eng. T. ASME*, 1991, vol. 113, pp. 304–07.
4. G. Hetsroni: *Int. J. Multiphase Flow*, 1989, vol. 15, pp. 735–46.
5. D.A. Kalitov and E.K. Longmire: *Exp. Fluids*, 2002, vol. 32, pp. 252–68.
6. A. Kitagawa, Y. Hagiwara, and T. Kouda: *Exp. Fluids*, 2007, vol. 42, pp. 871–80.
7. G. Montante and F. Magelli: *Ind. Eng. Chem. Res.*, 2007, vol. 46, pp. 2885–91.
8. T. Virdung and A. Rasmuson: *Proceedings of the 11th European Conference on Mixing*, VDI-GVC, Bamberg, Germany, 2003, pp. 129–36.
9. C. Beckermann and R. Viskanta: *Appl. Mech. Rev.*, 1993, vol. 46, pp. 1–27.
10. C. Beckermann and C.Y. Wang: *Metall. Mater. Trans. A*, 1996, vol. 27A, pp. 2784–95.
11. C.Y. Wang and C. Beckermann: *Metall. Mater. Trans. A*, 1996, vol. 27A, pp. 2754–64.
12. C.Y. Wang and C. Beckermann: *Metall. Mater. Trans. A*, 1996, vol. 27A, pp. 2765–83.
13. C.L. Lum, M.M. Koochesfahani, and J.J. McGrath: *ASME IMECE*, New York, 2001, pp. 1–7.
14. S.Y. Wang, C.X. Lin, and M.A. Ebadian: *Int. J. Heat Mass Transf.*, 1999, vol. 42, pp. 4153–63.
15. S.Y. Wang, C.X. Lin, and M.A. Ebadian: *Int. J. Heat Mass Transf.*, 1999, vol. 42, pp. 4427–45.
16. C. Ghenai, A. Mudunuri, C.X. Lin, and M.A. Ebadian: *Exp. Therm. Fluid Sci.*, 2003, vol. 28, pp. 23–35.
17. P.V. Skudarnov, C.X. Lin, M.H. Wang, N. Pradeep, and M.A. Ebadian: *Int. J. Heat Mass Transf.*, 2002, vol. 45, pp. 5191–5200.

18. Y.-C. Shih and S.-M. Tu: *Appl. Therm. Eng.*, 2009, vol. 29, pp. 2773–82.
19. B. Appolaire, V. Albert, H. Combeau, and G. Lesoult: *ISIJ Int.*, 1999, vol. 39, pp. 263–70.
20. B. Appolaire: Ph.D., INPL, 1999.
21. S. Eck, J. Mogeritsch, and A. Ludwig: *J. Mater. Sci. Forum*, 2006, vol. 508, pp. 157–62.
22. S. Eck, M. Stefan Kharicha, A. Ishmurzin, and A. Ludwig: *Mater. Sci. Eng. A*, 2005, vols. 413–414, pp. 79–84.
23. M. Stefan Kharicha, S. Eck, L. Könöszy, A. Kharicha, and A. Ludwig: *Int. J. Cast Met. Res.*, 2009, vol. 22, pp. 1–4.
24. L. Könözsy, M. Stefan Kharicha, S. Eck, M. Wu, and A. Ludwig: *Mater. Sci. Forum*, 2010, vol. 649, pp. 367–72.
25. R.J. Adrian: *Annu. Rev. Fluid Mech.*, 1991, vol. 23, pp. 261–304.
26. Z.-C. Liu, C.C. Landreth, R.J. Adrian, and T.J. Hanratty: *Exp. Fluids*, 1991, vol. 10, pp. 301–12.
27. C. Willert, B. Stasicki, M. Raffel, and J. Kompenhans: *SPIE Proc.*, 1995, vols. 2546–2519, pp. 32–39.
28. K. Okamoto and M. Oki: *International Conference on Advanced Optical Diagnostics in Fluids, Solids and Combustion*, Tokyo, Japan, 2004, pp. 1–5.
29. Y.A. Hassan: *Ann. N. Y. Acad. Sci.*, 2002, vol. 972, pp. 223–28.
30. J. Westerweel: *Meas.-Sci. Technol.*, 1997, vol. 8, pp. 1379–92.
31. J. Westerweel: Ph.D., Technical University of Delft, 1993.
32. S. Kumar and S. Banerjee: *Phys. Fluids*, 1998, vol. 10, pp. 160–77.
33. J. Nogueira, A. Lecuona, and P.A. Rodriguez: *Meas. Sci. Technol.*, 1997, vol. 8, pp. 1493–501.
34. C. Beckermann, C. Fan, and J. Mihailovic: *Int. Video J. Eng. Res.*, 1991, vol. 1, pp. 71–82.
35. C. Bizon, J. Werne, A.A. Predtechensky, K. Julien, W.D. McCormick, J.B. Swift, and H.L. Swinney: *Chaos*, 1997, vol. 7, pp. 107–24.
36. S. Schoofs and F.J. Spera: *Transp. Porous Med.*, 2003, vol. 50, pp. 179–95.
37. A. Bejan: *Heat Transfer*, Wiley, New York, 1993.
38. N. Zabaras and D. Samanta: *Int. J. Numer. Methods Eng.*, 2004, vol. 60, pp. 1103–38.
39. C.Y. Wang, S. Ahula, C. Beckermann, and H.C. de Groh, III: *Metall. Mater. Trans. B*, 1995, vol. 26B, pp. 111–19.
40. A. Badillo, D. Ceynar, and C. Beckermann: *J. Cryst. Growth*, 2007, vol. 309, pp. 197–215.

Simultaneous Observation of Melt Flow and Motion of Equiaxed Crystals During Solidification Using a Dual Phase Particle Image Velocimetry Technique. Part II: Relative Velocities

ABDELLAH KHARICHA, MIHAELA STEFAN-KHARICHA, ANDREAS LUDWIG, and MENGHUAI WU

A two-camera Particle Image Velocimetry (PIV) technique is applied to study the flow pattern and the equiaxed crystal motion during an equiaxed/columnar solidification process of Ammonium Chloride in a die cast cell. This technique is able to measure simultaneously the liquid and the equiaxed grain velocity pattern as already shown in Part I of this paper. The interaction between the equiaxed grains and the melt flow was explored by means of relative velocities. In single isolated configurations, the settling velocity of equiaxed crystal was found to be 41 times smaller than spheres of equivalent size. The coupling between the fluid flow and the equiaxed crystals was found to be important in areas of high crystal density. Chaotic and turbulent behaviors are found to be damped in regions of high equiaxed crystal density.

DOI: 10.1007/s11661-012-1415-y

I. INTRODUCTION

SOLIDIFICATION is a multidisciplinary field involving thermodynamics, fluid dynamics and solid mechanics, heat and mass transfer, and other disciplines.[1–3] One of the most challenging problems in solidification modeling is the complex interactions between physical phenomena occurring at different length scales ranging from atomic rearrangement over single crystal-melt interactions to heat extraction, momentum and species transport at the system level.

An important phenomenon in solidification is the simultaneous occurrence of melt flow and crystal motion. Solidification takes place either by a growing columnar front and/or by the growth of equiaxed crystals. Columnar growth happens in the form of cells or dendrites from the mold walls into the bulk melt due to heat extraction from outside. In equiaxed solidification, globular or dendritic crystals form by nucleation or fragmentation and subsequent growth into the surrounding melt. When equiaxed solidification is present, the phases (liquid and equiaxed crystal) interact with each other through momentum and energy exchange. The resulting solid–liquid multiphase flow pattern strongly depends on the microstructure of the equiaxed crystals, which in turn is governed by grain nucleation and growth mechanisms. Because the coupled liquid–solid flow causes structural and chemical heterogeneities in the final solidified products, a fundamental understanding of the multiphase transport phenomena coupled with the grain nucleation and growth mechanisms is required. The occurrence of dispersed two-phase flows in nature and industrial applications is abundant. The present topic shows the interaction of solid particles (equiaxed crystals) and the melt flow. However, there is a lack of consistent data to support the numerous theories for flow-particle interaction that have been developed in recent years.[4–9]

Due to its transparency, the H_2O-NH_4Cl solution was used for many experimental studies in the past[1–3,6,10] as the perfect analog for metallic alloys solidification. Beckermann's group used hypereutectic alloys of H_2O-NH_4Cl to study the solidification and the convection phenomena.[11–13] The shadowgraph technique was used in this publication[11] for qualitative comparison between experimental measurements and numerical simulations. On the other hand, a carefully applied analysis of shadowgraph images could as well provide information about the distribution and sizes of grains in the liquid melt at least for small fractions of solid.

A brief introduction to the PIV technique is given elsewhere.[14–17] The current authors described in more detail the principals of the PIV technique in Part I of this paper.

If PIV recordings are evaluated in the conventional way, the resulting velocity value is affected by the signals from the two different phases. The results would probably be a sort of average of the two velocities. Therefore, the signal arising from the individual phases must be separated so that relative velocity can be determined. For the present paper, the relative velocities between melt and crystals have been extracted. Moreover, the influence on the liquid flow of the equiaxed crystals' movement was analyzed.

The technique used here for distinguishing between the two different signals employs fluorescent tracer particles.[18,19] The fluorescent tracers scatter the light at

ABDELLAH KHARICHA, Research Team Leader, MIHAELA STEFAN-KHARICHA, Ph.D. Student, ANDREAS LUDWIG, Professor, MENGHUAI WU, Associate Professor, are with the Department of Metallurgy, University of Leoben, Leoben, Austria. Contact e-mail: abdellah.Kharicha@notes.unileoben.ac.at

Manuscript submitted March 23, 2012.
Article published online September 19, 2012

a wavelength different from that scattered by the equiaxed crystals. The use of two cameras is necessary. The first camera mounted with a green filter (band pass filter of 532 nm) detects only the laser light scattered by the equiaxed crystals. The second camera uses an orange filter (570 nm) through which the light reemitted by the fluorescent dye (Rhodamine B) can be recorded. In the past, this technique was successfully applied to two-phase water-bubble flows with simultaneous separation and measurement of the different phases.

II. EXPERIMENTAL PROCEDURE

For our quantitative study of the interaction between melt flow and solidification, we have chosen the relatively thin rectangular cavity ($10 \times 10 \times 1$ cm^3), which was cooled from three sides with a predefined cooling rate. A hypereutectic H_2O-29.5 wt pct NH_4Cl solution was solidified under controlled conditions. The process was monitored with a two-camera PIV device, whereby a 1-mm-thick cross section in the middle of the test cell was illuminated from the top by Nd-YAG laser pulses.

The cell was made of brass with 1-mm-thick glass plates in the front and at the back. Inside the brass walls, cooling channels which follow a meandering path were designed to achieve a homogeneous temperature. The cooling was controlled by pumping water with a given temperature through the cooling channels.

The H_2O-NH_4Cl solution was prepared by mixing NH_4Cl powder with distillate water and heating to 318.15 K (45 °C) until the powder had completely dissolved. According to the H_2O-NH_4Cl phase diagram, the liquidus temperature of an alloy containing 29.57 wt pct NH_4Cl is 310.15 K (37 °C). Then, fluorescent tracer particles (polyamide particle colored with the Rhodamine B) were added, whereby the solution was intensively stirred. The average diameter of the particles was estimated to be around 10 μm and their material density was around 1.05 g/cm^3. The density of a H_2O-29.5 wt pct NH_4Cl solution at liquidus is about 1.078 g/cm^3 and that of a eutectic H_2O-NH_4Cl solution is 1.076 g/cm^3. Thus, particles and solution have a similar density (difference 2.7 pct for a 29.5 wt pct and 2.5 pct for the eutectic solution), and it is reasonable to assume that the particles follow correctly the flow of the solution. Even if we have a change in temperature during the process, we believe that the change in density is not major.

After having added the particles, the liquid H_2O-NH_4Cl solution is then poured into the preheated die casting cell at 317.15 K (44 °C). This was done slowly in order to prevent capturing air bubbles. Nevertheless, if air bubbles stacked to the cell walls, they were mechanically removed carefully. The filling height was kept at 8 cm. After filling, we waited typically for one hour to equilibrate the temperature field before we started cooling. In this time, the small, but continuous, heat loss through the front and back window resulted in a steady and symmetric thermal buoyancy flow which was used as a reproducible initial stage for the different experimental runs. Then, the brass cell walls were cooled by 1.2 K (1.2 °C)/min. The temperature of the brass walls and at the top middle position in the solution was recorded every 5 seconds with type k thermocouple (accuracy ± 0.1 K (± 0.1 °C). In order to avoid condensation of humidity on the glass plates, we stopped cooling when 278.15 K (5 °C) was reached. According to the H_2O-NH_4Cl phase diagram, this corresponds to a solid fraction of 30 pct. Thus, the solidification process terminated with a partly solidified cell.

The two-camera PIV system adopted in this study comprised a pulsed laser system for illumination, two CCD cameras for image acquisition, a synchronization unit, and a software packet for image and data processing. The laser was a double-pulsed solid-state Nd-YAG and had an output power of 120 mJ with a maximum pulse rate of 21 Hz. The images taken by the cameras were in the resolution of 1600×1186 pixels.

Perpendicular to the casting cell, the two CCD cameras were mounted in parallel. The PIV camera mount has a common housing with a shared observation window for the two cameras. This insures straightforward imaging of the same area of the flowing media, while allowing flexible camera positioning. To distinguish the flow from the moving crystals, a green filter was mounted on one CCD camera (band pass filter of 532 nm through which only laser light passes, which was scattered by the equiaxed crystals) and an orange filter on the other camera (high pass filter of 570 nm through which only the light passes, which was reemitted by the fluorescent dye (Rhodamine B)). In this way, the cameras captured images without ''interphase'' noise, which could then have been processed without any further treatment to obtain the two velocity fields. A set of 20 images was taken every 60 seconds and stored on a PC. The time separating two images was 0.25 seconds which was small enough to correctly catch the time variation of any motion.

III. RESULTS

In the Part I of the paper, different stages were described during the solidification process. The first regimes are only thermal: TH1 (when temperature is kept constant at 317.15 K (44 °C)), TH2 (just after start of cooling), and TH3 (at 8 minutes after the cooling started). The first and last thermal regimes are characterized by symmetric convection patterns, going up (TH1) or down (TH3) along the walls. The TH2 is an unstable transition stage. Once the solidification started, the regimes are driven by thermo-solutal convection. We distinguish then the perturbed thermal stage (PTH), the turbulent (TU) stage, the coherent chaotic (CC), and the meandering flow stage (MF). In this Part II of the paper, we will refer to these stages using the abbreviated forms, given above in brackets.

A. *Equiaxed Motion and Interaction with Melt Flow*

The interaction between the melt flow and the equiaxed crystals can be studied by comparing the horizontal and the vertical component of the crystals' velocity. Without any interaction with the flow, the

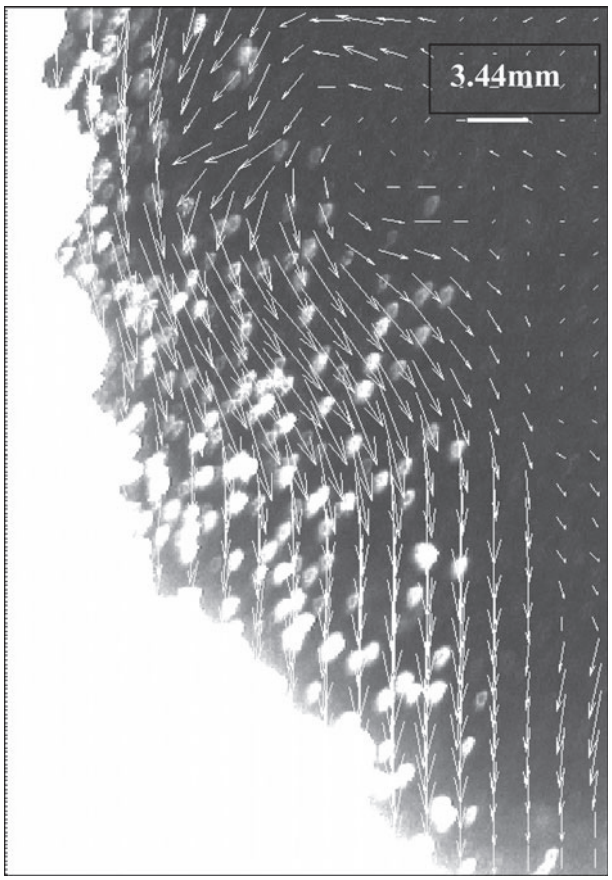

Fig. 1—Equiaxed crystal velocity field near the left solidification front at $t = 20$ min. The velocity vectors are scaled between $v_{min} = 0.28$ mm/s and $v_{max} = 3.76$ mm/s.

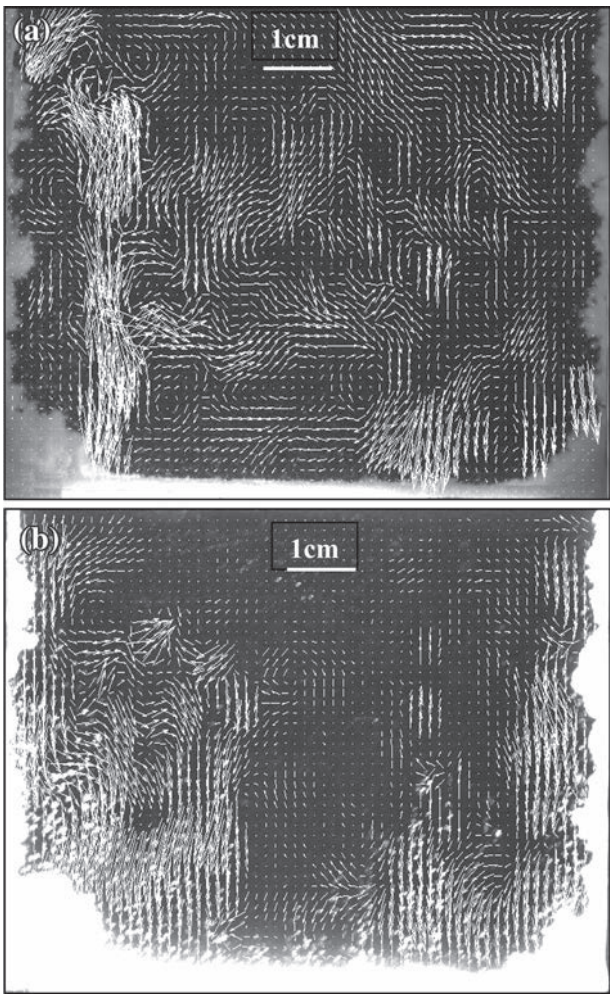

Fig. 2—Examples showing the melt velocities (*a*) and the equiaxed crystal velocities (*b*) for the so-called coherent chaotic regime (CC). The two-camera PIV measurement was done at $t = 15$ min. The velocity vectors are scaled between $v_{min} = 0.111$ mm/s and $v_{max} = 1.56$ mm/s for the liquid (a) and between $v_{min} = 0.278$ mm/s and $v_{max} = 3.87$ mm/s for the equiaxed crystals (b).

crystals would simply sink down. Therefore, the presence of a horizontal crystal movement is a direct indication of the interaction with the melt. The first observation is that even large crystals possess a horizontal velocity of typically 10 to 50 pct of the vertical velocity (Figure 1). In the upper part of the domain, where crystals are smaller than in the lower part, sometimes an upward motion was observed (Figures 2b and 3b). The quantification of the interaction between the melt flow and the equiaxed crystals is difficult,[20] but using the described two-camera PIV system, it is quite straightforward. We just estimated the vertical velocity difference between measured crystal velocity, $U_y^{crystal}$, and flow velocity, U_y^{flow}. To obtain accurate crystal velocities, it is necessary to choose an area where the number of crystals is large enough for the PIV correlation. In Figure 4, the vertical relative velocity at $t = 25$ minutes is plotted along three vertical lines, two located near the left and right solidification front and one near the center. It is obvious that the vertical relative velocity turns out to be irregular. The velocity difference is neither constant, nor increase linearly with the distance from the top surface. However, a power law or an exponential tendency can be noticed. This tendency is similar to that found by B. Appolaire et al.[21] for a single crystal falling in an undercooled liquid. It can be attributed to the increase in size of the crystal while falling. The equiaxed crystals surrounded by the undercooled liquid will grow,[21–23] while those which meet low concentrated liquid could experience melting.

The crystals' volume fraction increases during sedimentation. At the vicinity of the mushy zone, the numbers of crystals is high enough that an increase in inter-phase drag can be expected. The decrease of the typical crystal–crystal distance generates frictions so that the crystals and the liquid tend to equalize their velocities. In Figure 4, ΔU_y decreases over a distance of about 15 mm from the bottom solidification front. This phenomenon can be attributed to a change in drag regime, probably from a Stokes' to a porous kind of permeability law.[24] This explains the uniformity of the equiaxed crystals' flow field in all high crystal concentration areas, especially present in the vicinity of the solidification front (Figures 1, 2, 3). The same remark can be given in the stratified regime (MF) where the high density number of equiaxed forces the flow to reorient

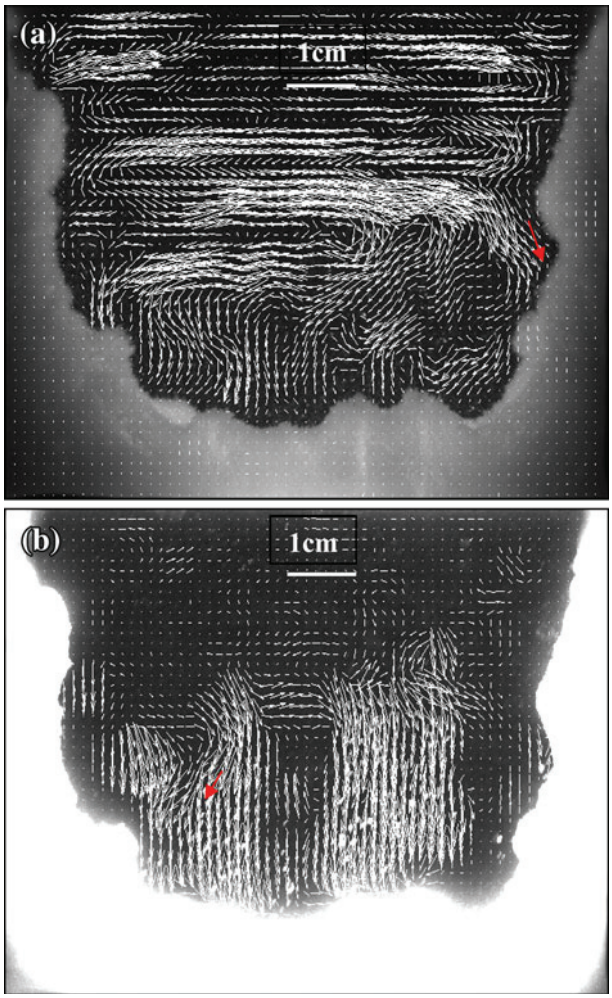

Fig. 3—Examples showing the melt velocities (*a*) and the equiaxed crystal velocities (*b*) for the meandering flow regime (MF). The two-camera PIV measurement was done at $t = 30$ min. The velocity vectors are scaled between $v_{min} = 0.067$ mm/s and $v_{max} = 0.466$ mm/s for the liquid (a) and between $v_{min} = 0.155$ mm/s and $v_{max} = 2.17$ mm/s for the equiaxed crystals (b).

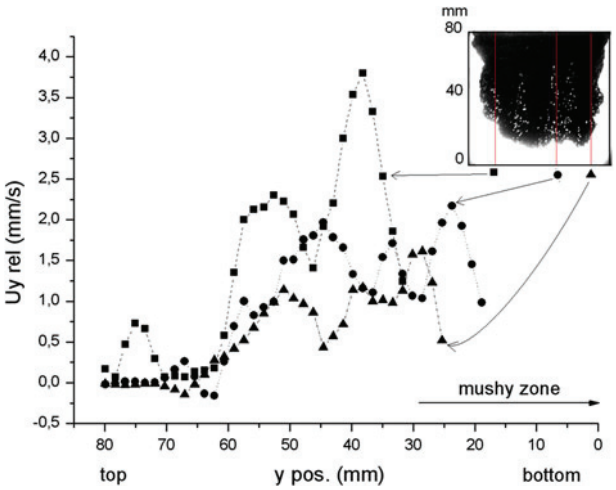

Fig. 4—Measured *Y*-component of the relative velocity along three vertical lines at $t = 25$ min (MF regime).

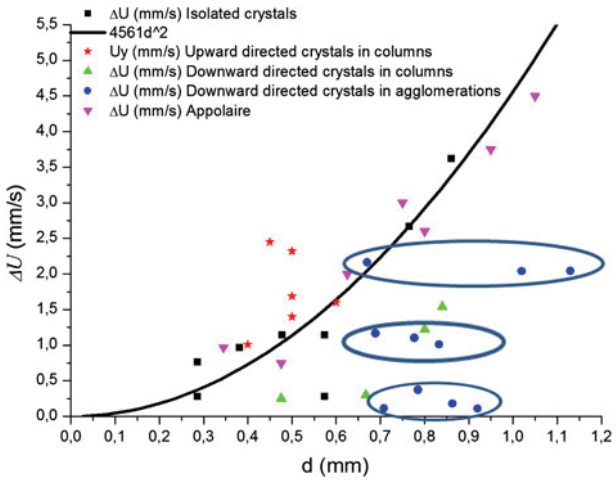

Fig. 5—Relative velocity for single crystals *vs* the crystal size (diameter), and a comparison between rising (red) and falling (green) velocity magnitude in chimneys (Color figure online).

and to finish its path in the downward direction through the mush.

The fundamental aspect is the relation between the relative velocity and the crystal size. Such a relation exists for a spherical particle and is known as Stokes' law. To check its validity for equiaxed crystals, it is necessary to extract the relative velocity for isolated crystals not in crystal agglomeration. In this case, as already mentioned, the use of picture correlation was not possible; so, the velocities were extracted by the particle tracking method.

To obtain precise results, it is better to choose a regime where the flow does not have a strong unsteady nature, and therefore we chose the regime MF for the following evaluation. At this regime, we can eliminate the influence of a strong time and space variation of the liquid velocity on the particle motion. In order to estimate the size of a single crystal, we simply counted the bright pixels representing the crystal. Here, it has to be mentioned that due to the light overexposure (necessary for acceptable PIV correlations) and the diffraction by the crystals, no morphological details of the equiaxed crystal were visible; the apparent size might be larger than the real size. In Figure 5, we have plotted the calculated relative velocity of a single crystal as a function of the measured size.

The results for the isolated crystals show an increase of the relative velocity with the measured size. The magnitudes of the relative velocities found for the corresponding sizes are very similar to those reported by Appolaire.[1,2] The correlation follows a clear power tendency. Based on the Stokes' law, the relative velocity of a compact sphere can be calculated by:

$$\Delta U = \alpha \cdot d^2, \qquad [1]$$

where α gathers the materials' properties (ρ_A the density of the sphere, ρ_W the density of the surrounding fluid, g the gravity constant, μ the dynamic viscosity of the fluid, and d is the diameter of the sphere) in one single factor.

Table I. Different Drag Coefficient Values Calculated for Measured Diameter Sizes and Relative Velocities

d (m)	ΔU (m/s)	Re	24/Re	C_D (Eq. [2])
3.82e−04	9.66e−04	4.34e−01	55.4	2.232e+03
2.86e−04	7.61e−04	2.56e−01	93.9	2.692e+03
4.78e−04	1.14e−03	6.42e−01	37.4	1.991e+03
7.648e−04	2.67e−03	2.40	10.0	5.85e+02
5.736e−04	2.79e−04	1.88e−01	128	4.0181e+04
2.86e−04	2.8e−04	9.41e−02	255	1.9891e+04
8.6e−04	3.62e−03	3.66	6.56	3.57e+02
5.736e−04	1.14e−03	7.69e−01	31.2	2.402e+03

Using the measured sizes and velocities, the particle Reynolds number $Re_P = \frac{\rho_A \Delta U_y d}{\mu}$ is always smaller than 4 allowing the use of Eq. [1]. We have just used Eq. [1] to fit the experimental data of Figure 5. With the materials' properties given in Table I in the Part I of this paper, the value of α can be calculated to be 188402.3. However, the fit to the measuring points from Figure 5 gives $\alpha = 4561$. Thus, the computed relative velocity for spheres (0.01 m/s for $d = 0.75$ mm) is almost 41 times larger than the measured ones.

Due to the fact that the equiaxed crystals are not spherical, and due to their rough fractal surface, this was expected. This is the reason why in the past, numerical simulation was performed by means of modified drag laws to account for the equiaxed shapes.[25–29] These drag laws predict systematically larger drag coefficients C_D than for spheres. In our case, we calculated the drag coefficient C_D using the equation below:

$$C_D = \frac{4}{3}\frac{d\Delta\rho g}{\rho_W \Delta U^2}, \qquad [2]$$

The different drag coefficients calculated for the measured sizes and relative velocities for the single equiaxed crystals are presented in Table I. For Reynolds numbers between 10^{-1} and 10^{-2}, the results obtained for C_D cover a large range between 10^2 and 10^4. These values are very similar to those calculated by Tang[30] for particles having fractal surfaces.

Based on the experimental correction of Eq. [1], the equiaxed relaxation time is estimated to be:

$$\tau_e = \alpha \frac{\rho_A - \rho_W}{\rho_A} d^2 \leq 10^{-4}\text{s}, \qquad [3]$$

Compared to the measurement frequency (250 ms), it is very small. It can be assumed that the crystals instantaneously reach their terminal relative velocity. Thus, the polynomial increase of ΔU_y observed in Figure 4 can be directly related to the growth of volume during the crystal fall. A linear or quadratic growth of the crystal diameter with time, as observed by Appolaire,[21,22] could easily reproduce the measured acceleration along the vertical direction (Figure 4).

The local maximum equiaxed volume fraction was estimated by the ratio of the volume of the crystals to the total volume. It was found smaller than 10 pct. Nevertheless, in this area of higher crystal number density, columns, and agglomerations, no clear correlation can be extracted; the results are very dispersed, see blue points in Figure 5. Smaller crystals can have higher relative velocities than larger ones. It can be observed that the same relative velocity can be reached by different crystal sizes. The blue points (crystals in agglomeration) are arranged along three lines where the crystals have different sizes, but approximately the same relative velocity. The crystals are slowed down by the presence of neighboring crystals; a higher solid fraction is known to increase the apparent viscosity. This situation occurs within the large and dense crystal clouds near the solidification front (agglomerations) or even in the bulk flow (columns or chimneys). The mechanism of momentum exchanges between the two phases might be controlled by some intermediate drag laws between the free particle regime and the packed bed regime where the crystals are almost not moving.

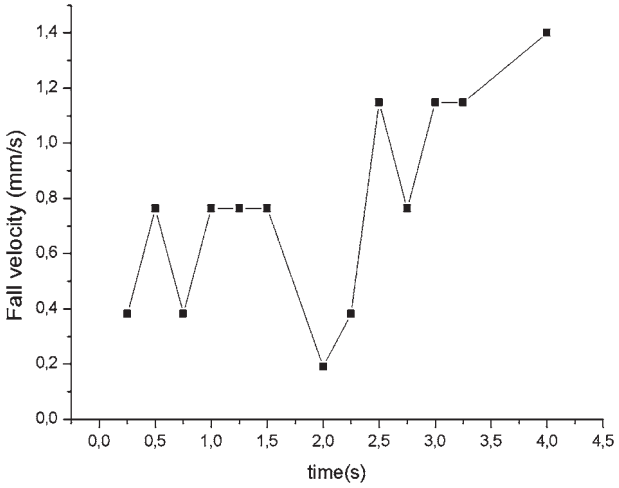

Fig. 6—Time evolution of the falling velocity of a single crystal ($d \sim 0.3$ mm) within a chimney at $t = 20$ min.

By comparing Figures 2(a) and (b), we can notice that variations of the liquid velocities are smoother in areas where a large number of equiaxed crystals exist. This phenomenon is particularly visible if we compare the flow coherence in the bulk with the high equiaxed number density regions. The flow in these regions is well structured in clear streamlines or in large eddies. Obviously, the presence of crystals' motion through drag interaction damps the turbulence eddies. We can suppose that due to the extension of the area of falling crystals and the decrease in magnitude of ΔC, a laminarization of the entire domain occurs, leading to a transition to the laminar chaotic regime (Figure 2).

B. *Equiaxed Motion in Solutal Flow Chimneys*

During the turbulent and chaotic regimes, equiaxed crystals are constantly accelerating or decelerating. In Figure 6, the falling velocity of a single crystal, in a chimney, at $t = 20$ min is plotted along the time until it hits the mushy zone. During this time, its appearing size was almost constant (it increased from 0.3 mm to 0.34 mm). This unstable behavior leads to the idea that

under such conditions, even for an isolated crystal, other forces might act on the crystal. The nonisotropic shape of the small crystals can generate rotation, and can cause a non-negligible lift action in regions with strong velocity gradients. It is also possible that eddies smaller than interrogation area sizes (0.16 mm), thus not fully caught in the flow map, act on the crystals in a quasi-random manner. If it exists, this phenomenon is believed to happen only during the turbulent regime, and near the solute jet in flow chimneys.

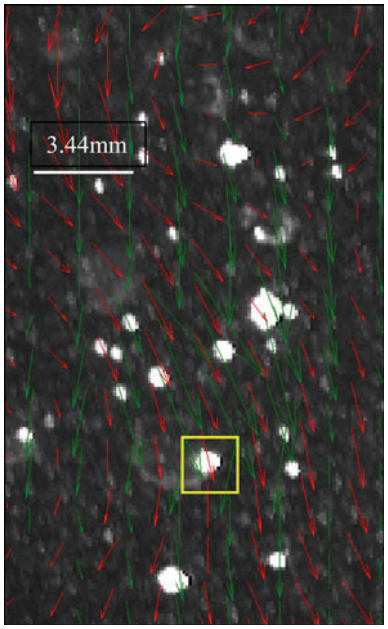

Fig. 7—Crystals and liquid velocities map within a chimney obtained by an adaptive-correlation technique at t = 23 min. Notice that the adaptive-correlation technique shows only downward vectors, although a rising crystal (marked by yellow square) is present. The velocity vectors are scaled between v_{min} = 0.04 mm/s and v_{max} = 0.16 mm/s for the liquid (red vectors) and between v_{min} = 0.525 mm/s and v_{max} = 2.27 mm/s for the equiaxed crystals (green vectors) (Color figure online).

These flow chimneys visible in Figures 7, 8, and 9 are the results of solute jets generated in the mushy zone, also called flow chimneys or columns. Most of the visible crystals fall downward, but some are rising upward at a higher speed (Figures 7 and 8). On one hand, the cross correlation method cannot catch this upward movement since this motion concerns only few crystals. On the other hand, due to the too short distance between the crystals, the particle tracking method can hardly be used to follow each moving crystal. The rising velocities' magnitudes reported in Figure 5 were directly calculated by measuring the displacement of the chosen crystal on the images. Owing to the presence of a strong solutal jet, the upward velocities are typically larger than the measured downward velocities (Figure 5). Unfortunately, the thin solute jet is not visible on the liquid velocity map. The 16 × 16 pixels resolution corresponding to a 2D 0.08-mm resolution is believed to be accurate enough to resolve the jet. In some experiments, no rising crystals were observed within the chimney, meaning that the jet was not illuminated by the laser light. However, even if a jet is localized within the 1-mm-thick laser plane, the volume of surrounding downward velocities (flow and crystal) will have a higher impact on the results of the correlation. The jet will be invisible from the flow velocity and crystal velocity map (Figure 7).

In the opposite to the lower parts of the chimneys, where the flow and the crystals' velocities are almost collinear, in the higher parts, the relative velocity can be very large. Sometimes, the measured liquid flow is almost perpendicular to the crystal flow. In Figure 9, the crystal

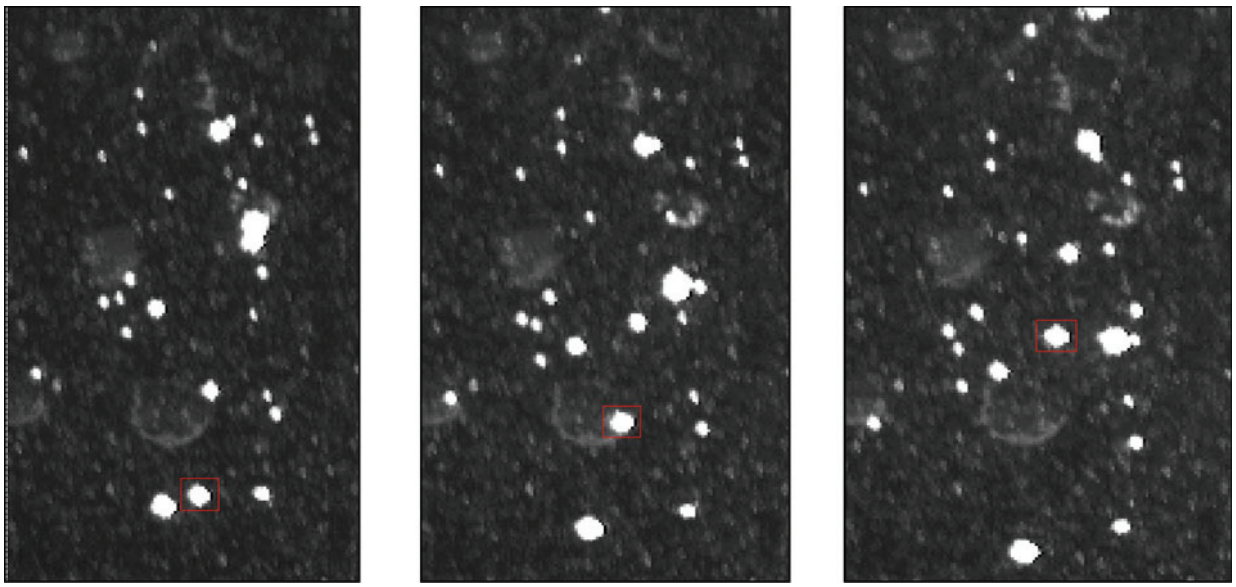

Fig. 8—Movement of an upward moving crystal surrounded by falling crystals at t = 23 min. The pictures show a zoom-in area of 12 × 20 mm^2.

moving within a chimney acts almost as a porous wall. It is clear that the two phases behave differently from what could be predicted by means of simple Stokes' drag law. By following the flow path, we can observe that a part of the liquid goes through and another part of the liquid flow is clearly reflected. If a chimney is interrupted at a certain height, the liquid will choose to flow through this interruption.

A collision between rising and falling crystals occurs (Figure 10). After the collision, the two crystals can coalesce in one single crystal and fall down. By considering the speed and the size of the two objects, the collision does not seem to respect the simple form of the momentum conservation law. Perhaps the kinetic energy has been absorbed by some viscous, thermodynamically or porosity-related phenomena. However, these collisions are relatively rare and surprisingly more frequent in diluted regions and never observed in high concentrated regions.

C. *Meandering Flow*

Due to its opacity, the flow through the mushy media is invisible. Nevertheless, in Figure 3a, the meandering flow starting from the top vanishes at the bottom mushy zone. The question is how the flow closes its streamlines. It is also possible that the closure is made along the front and the back glasses. At the end of the process, when the liquid reaches about 285.15 K (12 °C), the external room temperature 297.15 K (24 °C) can promote buoyant upward flow at these two walls. However, the flow map and the mass conservation suggest that this meandering flow closes its path through the mushy zone.

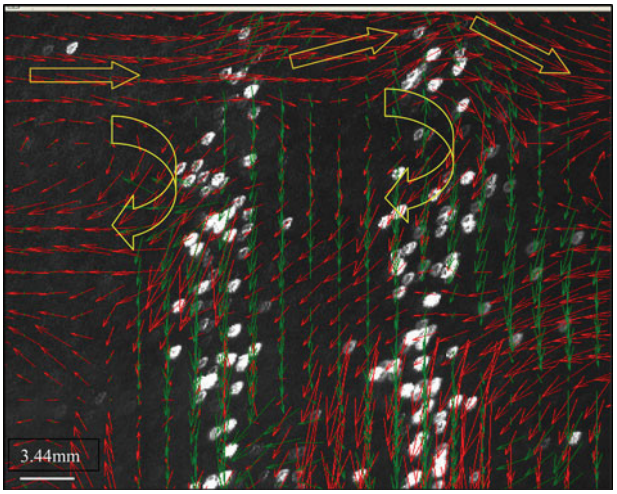

Fig. 9—Superimposition of the liquid melt flow and equiaxed crystals' motion filled in top chimneys at t = 20 min. The velocity vectors are scaled between v_{min} = 0.178 mm/s and v_{max} = 2.49 mm/s for the liquid (red vectors) and between v_{min} = 0.782 mm/s and v_{max} = 3.387 mm/s for the equiaxed crystals (green vectors) (Color figure online).

At the end of the experiment, the mushy zone represents 28 pct of the cell volume. According to the phase diagram, only 8 pct of the NH_4Cl mass will solidify. If the entire concentration solidifies in a packed form, it can fill only 6 pct of the cell volume. A simple calculation gives that in average, the mushy zone contains about 25 pct of solid and 75 pct of liquid. However, this is only an average value, the real solid fraction might be much higher at the vicinity of the cold wall and much lower near the solidification front. While the flow enters openly within the bottom mushy zone, it is deviated and curved by the solidification front surface. The vertical mushy regions act almost as nonpermeable media. Perhaps the fact that the vertical mushy regions are built with a succession of equiaxed and columnar layers might explain the difference with the bottom mushy layer. In addition, the sizes of equiaxed crystals that participate in the growth of the vertical walls are smaller than the ones reaching the bottom regions. Using a similarity between packed crystals and packed spheres, the Black-Kozeny law[24,25,31] predicts that the permeability increases with the crystals' size. These considerations, together with the flow observation, confirm that a strong variation in effective permeability (and porosity) might exist specially all over the surface of the solidification front.

IV. CONCLUSIONS

A special particle image velocimetry technique was used to measure the velocity field during a columnar/equiaxed solidification process. The single-phase measurement technique developed for PIV has been extended to cope with liquid-equiaxed flows. It was applied to H_2O-NH_4Cl solidification in a die cast cell of 10 × 10 × 1 cm^3 in which both the liquid velocity and the crystals' velocity maps could be extracted. The separation between the two velocity fields could be

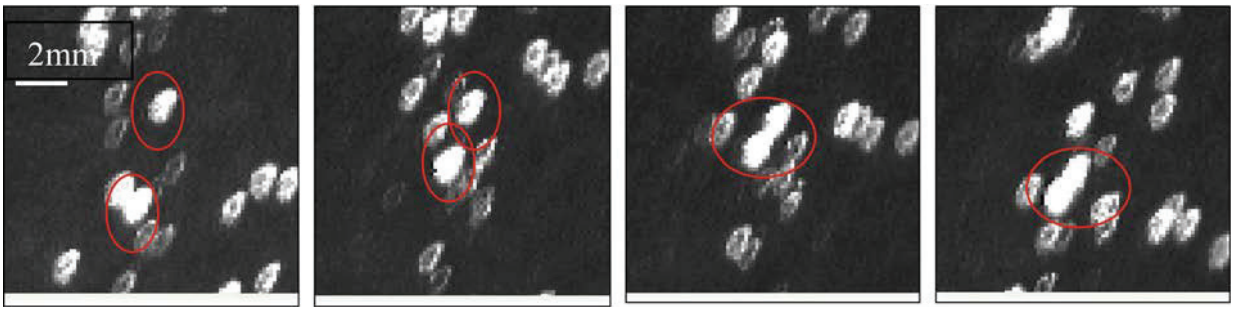

Fig. 10—Collision and coalescence of two crystals. Initial distance between the two crystals ~2 mm, t = 24 min.

obtained with the use of fluorescent particles' tracers that emit different waves when excited with the laser wavelength. Two images were taken simultaneously with two different cameras; the first one recorded only the laser light through a green filter, while the second one used an orange filter to record only waves emitted by the fluorescent particles. Thus, the first camera could follow only the trajectories of crystals, while the second camera recorded the liquid velocity field.

In general, no clear relation was found between the size and the settling velocities of the crystal. However, isolated crystals were found to fall 41 times slower than spheres of equivalent apparent sizes. In agreement to what is generally believed, only a drag coefficient larger than one can explain such velocities. Perhaps the origin of this phenomenon could be found in the fractal shape of the crystal.

The coupling between the fluid flow and the equiaxed crystal was found to be important in the area of high crystal number density; the two phases have often collinear velocity fields. In these regions, the liquid flow has shown smoother velocity variations than in the chaotic or the turbulent bulk. This observation is proof that equiaxed crystals tend to damp a part of the turbulence. Simultaneously, the velocities in the bulk flow were found to accelerate during the period of strong crystal fall near the vertical walls. When the region of equiaxed rain shifted to the bulk flow, the velocity magnitudes dropped strongly. This experience leads to the idea that the equiaxed motion has not only a stabilizing effect, but also can be a source of momentum acceleration. Perhaps in larger systems as in industrial scale, a generation of turbulence could be observed. This indicates that very complex behaviors can be expected from the interaction between flow and solidification in larger systems.

ACKNOWLEDGMENTS

We kindly acknowledge the FWF (Austrian Science Fund, grant number P17619-N02 and P22614-N22) which paid the PhD scholarship for Mrs. Stefan-Kharicha who performed the experiences, measurements, and calculations.

REFERENCES

1. C. Beckermann and R. Viskanta: *Appl. Mech. Rev.*, 1993, vol. 46, pp. 1–27.
2. C. Beckermann:, in *International Conference on Modeling of Casting, Welding and Advanced Solidification Processes VI*, T.S. Piwonka, V. Voller, and L. Kategerman, eds., TMS, Pennsylvania, Warrendale, 1993, pp. 181–192.
3. M. Rappaz: *Int. Mater. Rev.*, 1989, vol. 34, pp. 93–123.
4. R.A. Gore and C.T. Crowe: *J. Fluid Eng. T. ASME*, 1991, vol. 113, pp. 304–07.
5. G. Hetsroni: *Int. J. Multiph. Flow*, 1989, vol. 15, pp. 735–46.
6. D.A. Kalitov and E.K. Longmire: *Exp. Fluids*, 2002, vol. 32, pp. 252–68.
7. A. Kitagawa, Y. Hagiwara, and T. Kouda: *Exp. Fluids*, 2007, vol. 42, pp. 871–80.
8. G. Montante and F. Magelli: *Ind. Eng. Chem. Res.*, 2007, vol. 46, pp. 2885–91.
9. T. Virdung and A. Rasmuson: *Proceedings of the 11th European Conference on Mixing*, VDI-GVC, Bamberg, Germany, 2003, pp. 129–136.
10. FLUENT 6.3: *User's Guide*, Fluent Inc., Lebanon, NH, 2006.
11. C. Beckermann and C.Y. Wang: *Metall. Mater. Trans. A*, 1996, vol. 27A, pp. 2784–95.
12. C.Y. Wang and C. Beckermann: *Metall. Mater. Trans. A*, 1996, vol. 27A, pp. 2754–64.
13. C.Y. Wang and C. Beckermann: *Metall. Mater. Trans. A*, 1996, vol. 27A, pp. 2765–83.
14. R.J. Adrian: *Ann. Rev. Fluid Mech.*, 1991, vol. 23, pp. 261–304.
15. Z.-C. Liu, C.C. Landreth, R.J. Adrian, and T.J. Hanratty: *Exp. Fluids*, 1991, vol. 10, pp. 301–12.
16. C. Willert, B. Stasicki, M. Raffel, and J. Kompenhans: *SPIE Proc.*, 1995, vols. 2546–2519, pp. 32–39.
17. K. Okamoto and M. Oki: *International Conference on Advanced Optical Diagnostics in Fluids, Solids and Combustion*, Tokyo, Japan, 2004, pp. 1–5.
18. Y.A. Hassan, W.D. Schmidl, and J. Ortiz-Villafuerte: *J. Vis.*, 1998, vol. 1, pp. 291–301.
19. Y.M.C. Delauré, V.S.S. Chan, and D.B. Murray: *Exp. Therm. Fluid Sci.*, 2003, vol. 27, pp. 911–26.
20. C. Beckermann, C. Fan, and J. Mihailovic: *Int. Video J. Eng. Res.*, 1991, vol. 1, pp. 71–82.
21. B. Appolaire, V. Albert, H. Combeau, and G. Lesoult: *ISIJ Int.*, 1999, vol. 39, pp. 263–270.
22. B. Appolaire, Ph.D., INPL, 1999.
23. C. Bizon, J. Werne, A.A. Predtechensky, K. Julien, W.D. McCormick, J.B. Swift, and H.L. Swinney: *Chaos*, 1997, vol. 7, pp. 107–24.
24. C.Y. Wang, S. Ahula, C. Beckermann, and H.C. de Groh III: *Metall. Mater. Trans. B*, 1995, vol. 26B, pp. 111–19.
25. A. Badillo, D. Ceynar, and C. Beckermann: *J. Cryst. Growth*, 2007, vol. 309, pp. 197–215.
26. A. Badillo, D. Ceynar, and C. Beckermann: *J. Cryst. Growth*, 2007, vol. 309, pp. 216–24.
27. B. Appolaire, H. Combeau, and G. Lesoult: *Mater. Sci. Eng., A*, 2008, vol. 487, pp. 33–45.
28. M. Wu and A. Ludwig: *Acta Mater.*, 2009, vol. 57, pp. 5621–31.
29. M. Wu and A. Ludwig: *Acta Mater.*, 2009, vol. 57, pp. 5632–44.
30. P. Tang, H.-K. Chan, and J.A. Raper: *Powder Technol.*, 2004, vol. 147, pp. 64–78.
31. N. Zabaras and D. Samanta: *Int. J. Num. Methods Eng.*, 2004, vol. 60, pp. 1103–1138.

IOP Publishing | The Japan Society of Fluid Mechanics Fluid *Dynamics* Research

Fluid Dyn. Res. **46** (2014) 041424 (21pp) doi:10.1088/0169-5983/46/4/041424

Observation of flow regimes and transitions during a columnar solidification experiment

M Stefan-Kharicha, A Kharicha, M Wu and A Ludwig

Montanuniversity Leoben, Department of Metallurgy, Chair for Simulation and Modelling of Metallurgical Processes, Austria

E-mail: abdellah.kharicha@unileoben.ac.at

Received 14 November 2013
Accepted for publication 24 April 2014
Published 17 July 2014

Communicated by A D Gilbert and A Gelfgat

Abstract

Experimental data for the validation of numerical models coupling solidification and hydrodynamics are very rare. Many experiments made in the field of solidifications are performed with pure metals or alloys (Al-Cu, Pb-Sn, etc) which are opaque and do not allow direct observation of the hydrodynamic. Only the results related to solidification such as grain size and orientation, or macro-segregation are usually used for the validation. The present paper is dedicated to the description of well-controlled experiments where both solidification and fluid dynamic can be simultaneously observed. The important point is the almost purely columnar nature of the solidified mushy region. To our knowledge this is the very first reported macro-scale experiment with almost purely columnar solidification where the flow was measured with a PIV technique. The experiments consist in studying the hydrodynamics during the columnar solidification of a H_2O-NH_4Cl hypereutectic alloy in a die cast cell. Particle image velocimetry was employed to measure the flow velocity in the liquid bulk. Different flow regimes generated by complex thermo-solutal double diffusive convection were observed. In the beginning of the solidification the solutal buoyancy generates a turbulent flow, which is progressively replaced by the development of stratification from the top of the cell. Later, the stratification leads to the development of a long lasting meandering flow, which filled almost all the liquid region. The kinetic energy of the flow was calculated and it was found out that it decreased with time. The solidification front was smooth and no freckles appeared in the mushy zone. The evolution of the thickness of the mushy zone was measured. As this experiment showed a good reproducibility it represents an excellent benchmark for validation of the numerical models that target the simultaneous prediction of flow dynamics and solidification.

(Some figures may appear in colour only in the online journal)

1. Introduction

Solidification is a very complex process. Many parameters can influence the development of the solid, and thus the type of solidification. Columnar, equiaxed or mixed columnar/equiaxed solidification may occur. The cooling rate, the undercooling (temperature below the liquidus temperature without occurrence of solidification), the superheat (melt pouring temperature above liquidus), are important factors, which determine the occurrence of a certain type of solidification. A rapid cooling and a large undercooling will increase the number of nuclei, thus decrease the size of the resulting crystals. The final product will have a fine structure with small grains. Several phenomena take place during solidification: heat and solute transport, diffusion, convection due to temperature or concentration gradient, etc All of these processes are strongly coupled.

Solutal and thermal buoyancy cause double diffusive convection and the melt flow changes accordingly. The transport of heat and solute can be enhanced by the flow. The quality of the final solid product depends on the type of solidification, which is significantly influenced by the melt dynamic. Double diffusive convection is a very important phenomenon which influences solidification, so its impact on melt flow and solidification will be the focus of this paper.

Lesoult *et al* (1993) conducted some experimental and numerical work to study the influence of natural or forced flow on solidification. It was shown that the melt flow may change the heat transfer conditions, the grain distribution and the segregation. The effect of the melt stirring on the formation of equiaxed zone was definitely established.

During dendritic solidification instabilities in the mushy zone may lead to channel formation. Though those channels lighter interdendritic melt may rise so that a 'chimney'-type plume transports segregated melt into the bulk, where it may effects the motion and solidification of equiaxed crystals. At the end of solidification these channels are filled with descending equiaxed crystals. Such elongated regions of equiaxed crystals in columnar solidified areas are called freckles. They can be as long as the entire casting and represent a severe form of macrosegregation (Flemings 1974). Many ways were tested to suppress the occurrence of freckles: inclination of the mould, rotation, vibration, lid-driven flow, microgravity, low temperature gradient.

A large number of experimental and numerical work was dedicated to study casting defects (macrosegregation, A-segregated channels, freckles etc), their occurrence and prevention. On the experimental side different methods, such as shadowgraphy, computer tomography (CT), die injection, and particle image velocimetry (PIV) were used for visualisation of the phenomena which happens during solidification.

Chen and Chen (1991) presented an overview on channel and freckle formation concentrating on directional solidification of ammonium chloride. They studied the occurrence of plumes in the fluid region just above the mushy zone when the temperature gradient is large. They estimated the porosity across the mushy zone (using CT), the solute Rayleigh number, the inner diameter of the channel, the average size of the dendrites and the average flow velocity deep down in the mushy zone.

Channel formation and their prevention were already studied in the 1980s by Sample and Hellawell (1982, 1984) and so, implicitly the double diffusive convection during the solidification. They tried to understand the mechanism of formation and propagation of channels,

using a stationary mould, vertical, or inclined (between 20 and 30 deg.) or rotating at <5 rpm up to 10 rpm.

By means of shadowgraph and die techniques Magirl and Incropera (1992) studied unidirectional solidification and solidification from both sides and the bottom. In the last case, equiaxed grains formed (as consequence of columnar dendrites fragmentation), and enhanced the motion in the double diffusive convection cells, which impeded the motion of plumes.

A more recent work to understand double-diffusive convection during solidification in hypereutectic NH_4Cl-H_2O alloys was done by Shih and Tu (2009). By means of PIV they measured flow fields and for two concentrations (25 wt.% and 28 wt.%) they reported several flow circulation rolls near the mushy zone and in the melt. Shih *et al* (2013) experimented with lid-driven flow in order to suppress freckles. They also measured the temperature and the concentration during solidification and observed that reducing the temperature and concentration gradient reduced the number of freckles. The experimental results showed that increasing the slider speed supressed the development of double-diffusive convection effectively.

Tan (2005) tried mechanical vibration of the test cell to eliminate freckle formation. He varied initial concentration, temperature of the base plate and inclination. Experiments showed that for all hypereutectic alloys channels formed. The concentration increase will diminish the number of channels but will make them more pronounced. Decreasing the temperature of the base plate will decrease the number of channels. Also the amplitude and frequency of vibrations influence the formation of channels.

Saffie *et al* (2013) observed what they called 'snowing' phenomenon in a couple of experimental studies. Some were performed with unidirectional solidification, where equiaxed crystals formed near the bottom and were then carried up by thermo-convective flows and finally fell down similar to real snow in winter. The results showed that increasing the solute concentration will decrease the onset of 'snowing', but increase the size of equiaxed crystals. Varying the temperature does not affect the onset of 'snowing' but lengthens the period of the phenomenon.

Neilson and Incropera (1991, 1993) and Christenson *et al* (1989) worked on the unidirectional solidification of transparent binary NH_4Cl-H_2O alloys. Experiments and simulations of the impact of induced and rotated fluid motion on the development of the channel formation were performed. It was established that freckles originate from flow channels that nucleate in the mush. Another significant factor that influences channel formation turned out to be the mushy zone permeability. Their experimental study showed that radially induced flow by rotation and tilting of the mould could inhibit channel formation.

Aggregations and channel formation (Solomon *et al* 1999) during the solidification of ammonium chloride were investigated in a thin Hele-Shaw cell, with the cell being heated from below and cooled from above or vice versa. In the former case a lot of equiaxed crystals occurred and deposited so that aggregations formed. In the second case when the cell is cooled from below and heated from above no deposition of crystals was observed and a compact mushy zone formed. Somehow, if the environment was cool comparing to the liquidus temperature of the solution, some ballistic deposition occurred and the mushy layer, which formed now as mixture of dendrites and ballistic deposition, was found to be more permeable. In this case the formation of channels and plumes was enhanced. The ballistic deposition was also increased in the case when the cell was tilted. However, artificially induced flow in the liquid and in the mushy layer did not enhance the channel formation. These experimental data were supported with some numerical simulations which showed the same phenomena.

Chen (1997) performed experimental and numerical work on the double-diffusive layer during the directional solidification of a 28 wt% NH_4Cl-water, and measured the position of the melt/mush interface, the height of the eutectic solid, the number of plumes, the height of convective fingers and the position of each interface between the double diffusive layers. The growth of the mush was manipulated by the temperature of the bottom plate T_B. It was shown that the time to reach the maximum plumes number depends on the value of T_B; the time is shorter for lower T_B. The time for an onset of double-diffusive layering was also found to be shorter for lower T_B because double-diffusive layering occurred when the maximum number of plumes has established. However, the thickness of the layers did not depend on the T_B.

Beckermann and Viskanta (1988, 1989) studied numerically and experimentally the double-diffusive convection occurring during solidification. Remelting of columnar dendrites was found to be a possible condition for channel formation.

Experimental data performed by Stefan-Kharicha *et al* (2009) was used in a first attempt to model the columnar growth of ammonium chloride alloy in a die-cast cell (Könözsy *et al* 2009). A direct comparison of the distribution of the columnar growth at the end of their solidification experiment showed a qualitatively good agreement between experimental and numerical results.

Kharicha *et al* (2012) developed a cellular automaton 2D model to study double-diffusive convection during binary alloy solidification. Different flow regimes were reported and the existence of a turbulent regime was related to the generation of individual plumes at each columnar dendrite.

Ahmadein *et al* (2014) employed a 5-phase model (Wu *et al* 2010a, 2010b) to simulate the experimental data presented here. The 5 phases in the model represented the solid equiaxed crystal, the solid columnar dendrite, the extradendritic liquid melt, the intradendritic melt inside the equiaxed crystal and the intradendritic melt inside the columnar mushy zone. Different flow patterns were observed and the evolution of the solid front was calculated. Qualitative results were obtained but more efforts should be put for further quantitative comparison.

Experiments reporting both the flow hydrodynamics and the solidification are very scarce. In the present paper experiments with the transparent alloy NH_4Cl-H_2O and almost pure columnar solidification, where the mushy zone grows with a macroscopic flat envelope, are presented. The geometry and the experimental conditions are similar to the experiments previously performed by Kharicha *et al* (2013a, 2013b). Here, we report only the experimental data where no freckles develoed and where equiaxed crystals were rare. However, we have to admit that for us the reasons why sometimes freckles and equiaxed crystals appear and sometimes not are still unclear. Nevertheless, we postulate the existence of a kind of bifurcation where a small smooth change of a parameter might induce a totally different behaviour of the hydrodynamic-solidification system. It is known that the equiaxed crystals are formed by (a) nucleation, (b) fragmentation of secondary arms by re-melting or (c) fragmentation of secondary arms by mechanical breaking. All three mechanisms may be effected by hydrodynamics.

The reproduction of experiments with heavy equiaxed crystal falling represents still a challenge for numerical simulations. Correlations for the momentum transfer between the liquid phase and the falling crystals are only known for the limit of very diluted equiaxed fraction. For larger volume fractions the effective viscosity and the drag coefficients are unknown. In comparison the permeability of static columnar dendrites are much better known. This is why an experiment with almost pure columnar dendrites constitutes an excellent data set for the validation of numerical simulations. From the experiments presented

in this paper we have extracted the following parameters: thickness and growth of the mushy zone, flow behaviour (in terms of flow regimes) and kinetic flow energy (KE).

2. Experimental setup

The transparent 29.57 wt.% ammonium chloride-water alloy was chosen for the solidification experiments. The Particle Image Velocimetry (PIV) set-up consists of a source light (in our case a Nd-YAG double pulsed laser) and two CCD cameras. First CCD camera was used to record the flow movement and the second to record the equiaxed crystals movement. To measure the velocity of the flow a tracer particle is needed. To distinguish between the flow and the crystals movement a special tracer particle (polyamide particle coloured with Rhodamine B) was used. Each CCD camera was equipped with a specific filter. For the CCD camera which recorded the flow movement, an orange filter of 570 nm and for the second CCD camera, which was employed to measure equiaxed crystals velocities, a green filter of 532 nm were used. The commercial software, FlowManager[1], was used for recording and analysing of the images.

The dimensions of the test cell (Kharicha *et al* 2013a, 2013b) were 10*10*1 cm^3. It's laterals and bottom walls were made of brass. The front and back walls were made of commercial transparent glass. The top of the cell was left open. The temperature of the brass walls was controlled via a circulation bath by applying a linear cooling rate of 1.2 K min^{-1}. The room temperature for the experiments was maintained between 19 °C and 21 °C. The position of the test cell was horizontally adjusted.

The experimental procedure followed always the same steps. First the alloy was prepared. The necessary amount of NH_4Cl powder was weighted and mixed with distilled water. The mixture was heated up until the powder was completely dissolved. The solution was then poured into the test cell, which was previously heated to the same temperature. The height of the liquid in the cell was set to 8 cm. The system (test cell with solution) was left untouched for 30 min with keeping cell walls at the initial pouring temperature. In this way a quasi steady-state situation, avoiding the residual hydrodynamic turbulence, was achieved before the solidification experiment started. The time when the cooling bath was switched to the predefine cooling temperature of 5 °C is the starting point of our experiment, t_0. In all our experiments we have measured a constant cooling rate in the brass walls until the bath reached around 5 °C (Kharicha *et al* 2013a). Due to the meander-shaped cooling channel in the brass parts and the high flow rate of the cooling water we measured a uniform temperature in the brass walls. Note that with 29.57 wt.% NH_4Cl as solute, the NH_4Cl-H_2O solution will not completely solidify when being cold down to 5 °C. According to the phase diagram the remaining liquid may have reduced its NH_4Cl content to around 24 wt.%. That's a difference of $\Delta C = 6$ wt.%.

According to the NH_4Cl-H_2O phase diagram the liquidus temperature for a 29.57 wt.% NH_4Cl alloy is 37 °C. We decided to make several experiments with different starting temperatures: 5 °C, 10 °C, 15 °C and 20 °C above liquidus. For each superheat we performed two experiments with identical experimental conditions. The superheat is known to control the type of solidification: equiaxed or columnar. If ahead of the columnar front an undercooled liquid and a sufficient large number of equiaxed exist then columnar dendrites will be stopped by the equiaxed crystals and a so-called Columnar-to-Equiaxed Transition, CET, occurs. For the purpose of this paper the authors have chosen only experiments which revealed an

[1] FlowManager is a trademarked software from Dantec Dynamics, DK (http://www.dantecdynamics.com/).

extremely small number of equiaxed crystals during almost pure columnar growth. None of the experiments in this paper showed the presence of any channels, chimneys, or plumes during the whole solidification process.

3. Results and discussion

3.1. Flow visualisation and regimes

The cooling from the walls and the occurrence of solidification generate various and complex phenomena. Regardless of the superheat which was employed, each experiment followed similar flow regimes as described in the previous analysis of Kharicha *et al* (Kharicha et al 2013a, 2013b), where however massive equiaxed crystals were present. Only the time when a regime changes into the next depends on the superheat. In this section, the experiment with 5 °C superheat will be described first. The other experiments with different superheats (10 °C, 15 °C and 20 °C) will be detailed in section 3.2. In table 1 the values related to the onset time of the different flow regimes are gathered for the different experiments.

3.1.1. Thermal symmetrical regime (TH). Before starting the cooling, the solution was untouched for 30 min and a stable flow pattern with ascending flow along the vertical walls and a descending flow in the centre established (not shown). When the cooling bath was switched on this stable flow pattern was disturbed. However, after a few minutes two symmetrical rolls with descending flow along the vertical walls and ascending flow in the centre caused by thermal buoyancy appeared (figure 1). This laminar stable flow constituted the first regime which we call TH regime (thermal symmetrical). The time to reach this stable flow regime was, for the case of 5 °C superheat, around 7 min and it lasted for around 7 min.

When the cell walls reached the necessary undercooling for heterogeneous nucleation, dendritic crystals appeared at the brass walls. They grew first in form of very small islands, which developed and finally covered the whole wall surface (side and bottom wall simultaneously) with a very fine layer of dendritic crystals. In the case of the 5 °C superheat, solidification occurred around 12 min after the cooling was started. Although visible solidification at the cell walls happened the flow pattern stayed almost unchanged for 1–2 min.

3.1.2. Perturbed thermal regime (PTH). At around 13–14 min, perturbation of the symmetrical flow appeared by small eddies around the fine solid layer which formed at the side walls. These small perturbation of the flow pattern concerned only the vicinity of the solid, the bulk flow kept the same symmetrical convection rolls (figure 2). We call this regime PTH (perturbed thermal). It is the shortest regime as it lasted only around 2 min.

3.1.3. Turbulent regime (TU). Then, 16 min after starting cooling, small plumes started to rise from the bottom mush. They are originated by the rejection of lighter solute during solidification of the mushy zone and thus transport solute enriched melt into the bulk. So solutal buoyancy started to play an important role on the development of the flow. Now, the symmetry of the flow pattern became completely destroyed (figure 3). This regime we call TU as it is turbulent as we will show later. The TU regime lasted approximately 8 min. The simulation work of Kharicha *et al* (2012) suggested that the above mentioned solutal plumes are the origin of the TU regime. As shown later (figures 7 and 10), the strongest solidification rate occur during the TU regime, where strong interaction between plumes and perhaps inverse cascade of eddies takes place (Bizon *et al* 1997).

Table 1. Points in time when the different flow regimes occurred during the solidification process for different superheats between 5 °C and 20 °C.

Experiment	Initial temp. (Superheat)	Room temp.	TH Thermal stable regime	Time for first solidification	PTH Perturbed thermal regime	TU Turbulent regime	Occurring of equiaxed crystals	TU—ST Turbulent-stratified regime	MF Meandering flow regime
A	42 °C (+5 °C)	21 °C	7 min.	12 min.	14 min.	16 min.	22 min.	24 min.	32 min.
B	42 °C (+5°C)	20 °C	7 min.	12 min.	13 min.	15 min.	22 to 29 min.	23 min.	32 min.
C	47 °C (+10 °C)	20 °C	7 min.	15 min.	17 min.	18 min.	23 to 32 min.	24 min.	34 min.
D	47 °C (+10 °C)	20 °C	9 min.	15 min.	17 min.	18 min.	24 to 32 min.	25 min.	37 min.
E	52 °C (+15 °C)	19 °C	7 min.	16 min.	18 min.	19 min.	23 to 33 min.	29 min.	38 min.
F	52 °C (+15 °C)	20 °C	7 min.	18 min.	19 min.	21 min.	25 to 34 min.	27 min.	36 min.
G	57 °C (+20 °C)	20 °C	7 min.	20 min.	21 min.	23 min.	24 to 37 min.	32 min.	36 min.
H	57 °C (+20 °C)	19 °C	8 min.	19 min.	20 min.	23 min.	26 to 37 min.	30 min.	36 min.

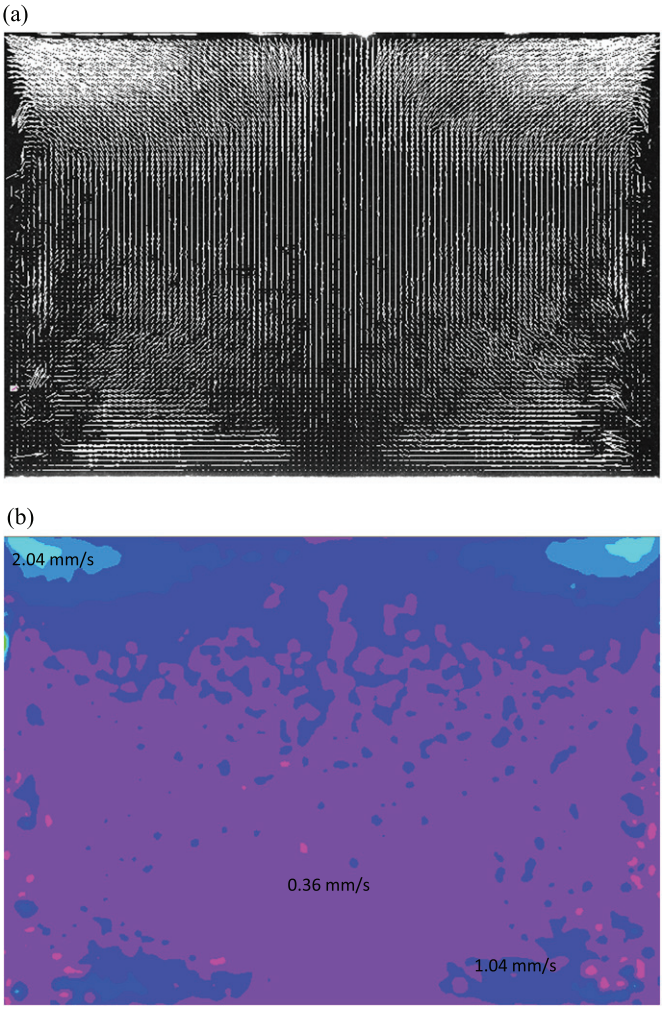

Figure 1. Thermal symmetric (TH) flow regime during the solidification of 29.57 wt.% NH_4Cl alloy for an initial superheat of 5 °C. (a) Measured flow field at $t = 10$ min and (b) measured velocity magnitude of the flow at $t = 10$ min.; v_{min}(purple) = 0.36 mms^{-1}; v_{max}(turquoise) = 2.04 mm s^{-1}.

The occurrence of turbulence can be estimated by considering the thermal and the solutal Rayleigh number. For a vertical wall the critical Rayleigh number for the occurrence of turbulence is $Ra = 10^9$ (Bejan 1993). Previous analysis performed by Kharicha *et al* 2013b has shown that the thermal Rayleigh number is too small ($\sim 10^8$) to induce a transition from lamellar to turbulence. The solutal Rayleigh number can be estimated by considering the difference between the initial and final NH_4Cl-concentration given by the phase diagram. Using known material properties, Kharicha *et al* 2013a showed that $Ra = 2.2*10^9*\Delta C$ (ΔC in wt.%) yields for NH_4Cl as solute in H_2O. As stated above we have a difference between the initial and the final solute content of $\Delta C = 6$ wt.%, which would lead to $Ra = 1.32 \cdot 10^{10}$, so far greater than the critic Rayleigh number. Thus, the onset of turbulence can easily be reached since a concentration difference of only $\Delta C = 4.5$ wt.% is enough to obtain 10^9. When

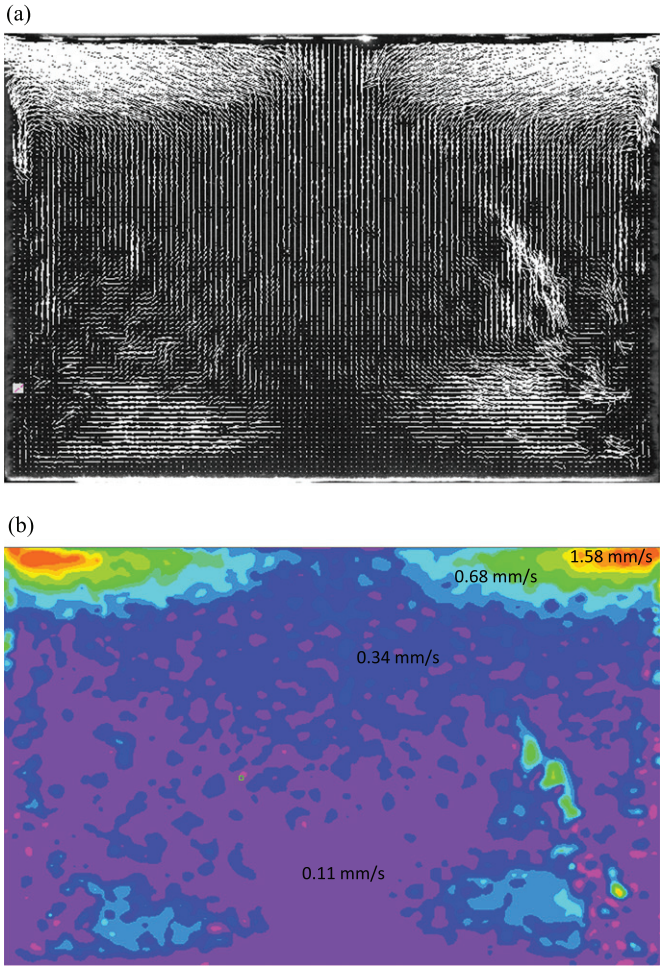

Figure 2. Perturbed thermal flow regime (PTH) during the solidification of 29.57 wt.% NH_4Cl alloy for an initial superheat of 5 °C. (a) Measured flow field at $t = 13$ min and (b) measured velocity magnitude of the flow at $t = 13$ min.; v_{min}(purple) = 0.11 mm s^{-1}; v_{max}(orange) = 1.58 s^{-1}.

the turbulent regime is effectively observed the solutal Rayleigh number exceeds probably 10^{10}.

However the situation is more complex since thermal buoyancy and inertia effects are simultaneously acting, whereby, thermal is acting in the opposite direction as solutal buoyancy. When a parcel of liquid cools at the vicinity of a wall its density increase because of the thermal buoyancy but decreases because of solidification (rejected solute contains more water and so it is lighter). This is why despite the high magnitude of the solutal Rayleigh number, most of the flow regimes observed could be qualified as laminar with (i) very large and coherent structures, and (ii) quasi divergence free 2D velocity fields. In opposite, the 'turbulent' regime shows the existence of a 3D highly transient and incoherent eddies of different scales.

The presence of the columnar mushy region can also explain the low level of turbulence observed. A flow convection exist also within this porous media, but it is not measurable

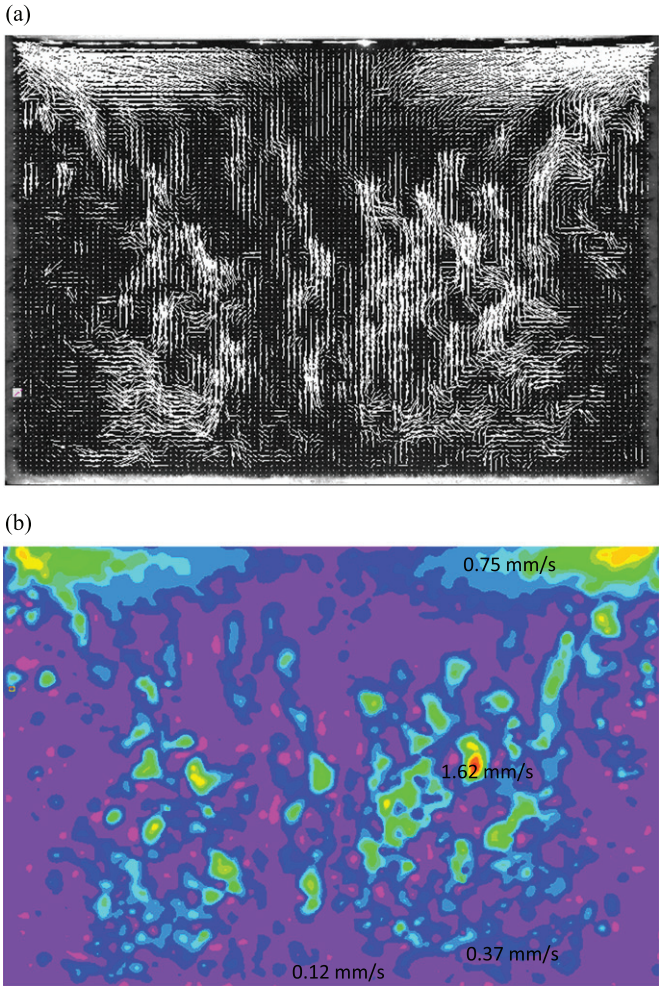

Figure 3. Turbulent flow regime (TU) during the solidification of 29.57 wt.% NH_4Cl alloy for an initial superheat of 5 °C. (a) measured flow field at $t = 15$ min and (b) measured velocity magnitude of the flow at $t = 15$ min. v_{min}(purple) = 0.12 mm s^{-1}; v_{max}(orange) = 1.62 mm s^{-1}.

experimentally with the present PIV method. By damping the turbulence (high Rayleigh number), the mushy region contribute probably to the 'laminarization' of the flow in this experiment.

3.1.4. Turbulent—stratified flow regime (TU-ST). At about 23–24 min after start cooling, the eddies present in the bulk had still a turbulent nature (figure 4). At the top of the cell the start of a flow stratification could be observed; already two symmetric layers are visible. This lasted for about 6 min for the case with 5 °C superheat. This regime was labelled the TU-ST (turbulent-stratified). In previous publication of the authors (Kharicha *et al* 2013a, 2013b) a coherent chaotic regime developed at this point in time; the eddies became large and coherent. Now, the lack of equiaxed crystals in the bulk may be at the origin of the missed coherent chaotic regime.

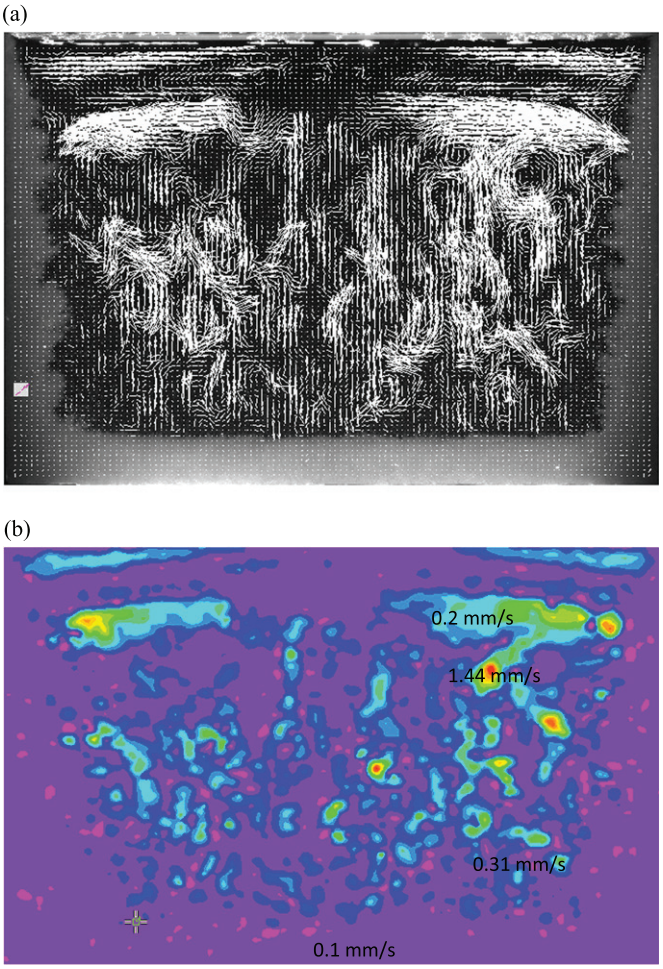

Figure 4. Turbulent stratified flow regime (TU-ST) during the solidification of 29.57 wt.% NH_4Cl alloy for an initial superheat of 5 °C. (a) Measured flow field at $t = 23$ min and (b) measured velocity magnitude of the flow at $t = 23$ min.; v_{min}(purple) = 0.1 mm s^{-1}; v_{max}(orange) = 1.44 mm s^{-1}.

Until 22 min after start cooling, solidification occurred only in a columnar form. The growth was very uniform and smooth along the whole length of the walls. No channels formed in the mushy zone, nor chimneys with the release of equiaxed crystals, as in previous publications (Kharicha 2013a, 2013b). However, at 22 min some equiaxed grains formed very close to the lateral walls. Mainly those grains flowed down, along the borders of the lateral solid front, until they reached the bottom, but some were captured in the lateral columnar zone and continue to grow. This rain of equiaxed crystals lasted 9 min, mainly during the turbulent-stratified flow regime.

3.1.5. Meandering flow regime (MF). After around 32 min the stratification of the flow, from the top to the bottom, became clearly visible (figure 5). The melt flow was organized horizontally in several layers from one side to the other side of the lateral columnar mushy zone. The protrusion of the vertical mushy front topography in interaction with the thermo-solutal convection may result in such a meandering flow. Approaching the bottom mushy

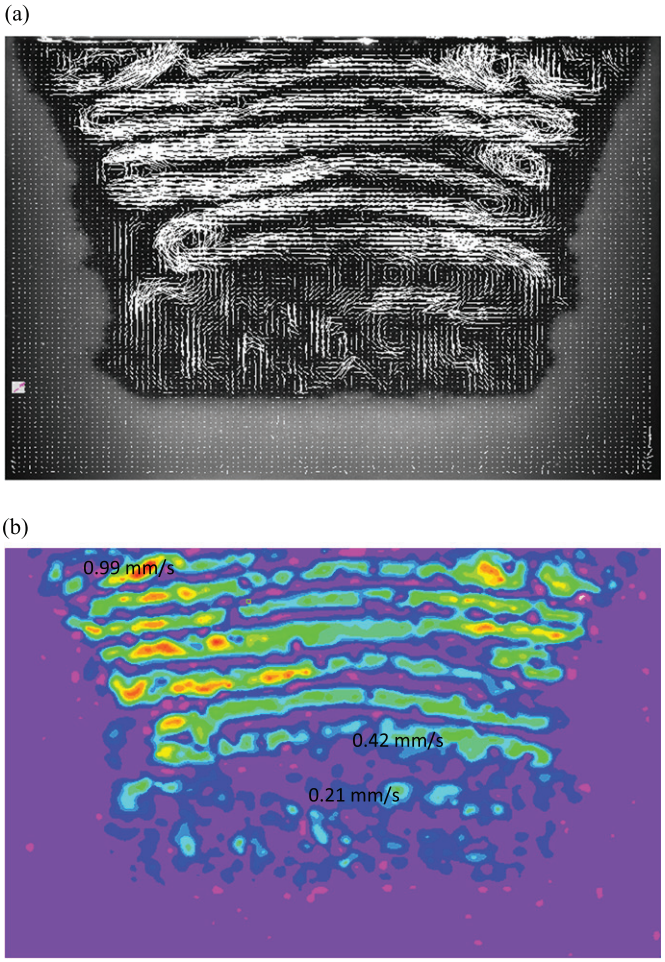

Figure 5. Meandering flow regime (MF) during the solidification of 29.57 wt.% NH_4Cl alloy for an initial superheat of 5 °C. (a) Measured flow field at $t = 32$ min and (b) measured velocity magnitude of the flow at $t = 32$ min.; v_{min}(dark blue) = 0.21 mm s^{-1}; v_{max}(orange) = 0.99 mm s^{-1}.

front the melt flows into the mushy zone at some locations and flows out of the mush at other locations. This stage is called the Meandering Flow regime (MF) and is the longest of all flow regimes. It lasted more than 20 min. The mechanism at the origin of this snaky flow is still unclear. When no visible growth of the columnar mushy zone took place, the solidification experiment was considered as finished. This happened about 50 min after start cooling.

3.2. Reproducibility of experiments with different superheats

Four sets, two experiments each, with 5 °C up to 20 °C superheats were performed. It turned out that the solidification regimes were similar, only the points in time when these regimes appeared were different. In table 1 the corresponding data are gathered.

Analysing the data in table 1 it become obvious that the first flow regime TH is not influenced by the superheat employed. Regardless the amount of superheat it always took

around 7 min to reach the corresponding natural convective flow pattern. Regime TH lasts always 1–2 min after first solidification occurs. The beginning of solidification is very important for the evolution of the flow pattern, as it initializes solutal buoyancy and with that double-diffusive convection. Visible solidification first appeared along the walls 15 to 20 min after the cooling was switched on. The exact point in time at which visible solidification occurred depends clearly on the initial temperature. The larger the superheat the longer it takes to reach the necessary undercooling for heterogeneous nucleation.

As reported above the PTH regime described the transition between the TH and the TU regime. Independent of superheat it lasted only 1–2 min.

Between 18 to 23 min, due to the thermo-solutal buoyancy, plumes developed in the bulk liquid. Large variations in flow velocities magnitude could be observed in the melt. This is characteristic for the turbulent flow regime.

Between 23 to 26 min a new phenomenon occurred, equiaxed crystals started to appear along the lateral mushy zone which developed on the side walls. For all experiments presented in this paper, the equiaxed crystals concentrated only next to the lateral mush, phenomenon which we call 'rain crystals'. The rain crystals occurred only between 8 and 13 min. It could be observed that for the smallest superheat the length of this phenomenon was the shortest (7 min), and for the highest superheat the rain crystals lasted the longest time (13 min).

A few minutes after the onset of the rain crystals, stratification began in the TU regime. At the top of the cell the flow started to stratify and two symmetrical layers developed (TU-ST). The flow stratification continued until the MF regime, when it was covering the whole cell from top to bottom.

In the meander flow regime (MF), the solutal buoyancy and the thermal buoyancy (the two main forces) equilibrated and gave an organized structure to the flow. The flow organized horizontally in 4 to 7 parallel layers. This flow stratification occurred 32 min after cooling was stared, but was perfect at 36 to 38 min. Not only the time when solidification started was different for the different superheats, but also the wall temperature at which the first crystals were visible along the walls. For lower superheat of 5 °C and 10 °C this wall temperature was around 28 °C, for the medium superheat of 15 °C we got 29.3 °C and 28 °C, and for the largest superheat of 20 °C we got 31 °C. Obviously, the larger the superheat employed, the higher the wall temperature when first crystals occur at the wall.

3.3. Start of a new flow regime

Accounting for the start of a new flow regime was difficult, because in many cases a transition stage between regimes existed. Once solidification has started the flow behaviour changed clearly, but to distinguish between PTH and TU regimes is very difficult. In fact, the PTH can be considered only as a transition between TH and TU, when turbulence is observed only locally. For this reason the onset of the TU regime can be considered 1 or 2 min before the given time in the table 1.

3.4. Total kinetic flow energy

The kinetic energy was calculated for each experiment from the beginning of cooling till no further solid formed (approximately 40 min). Of course, only the total kinetic energy contained in the visible liquid was considered, as the portion present within the mushy region remained invisible. The total flow kinetic energy was calculated with the following equation

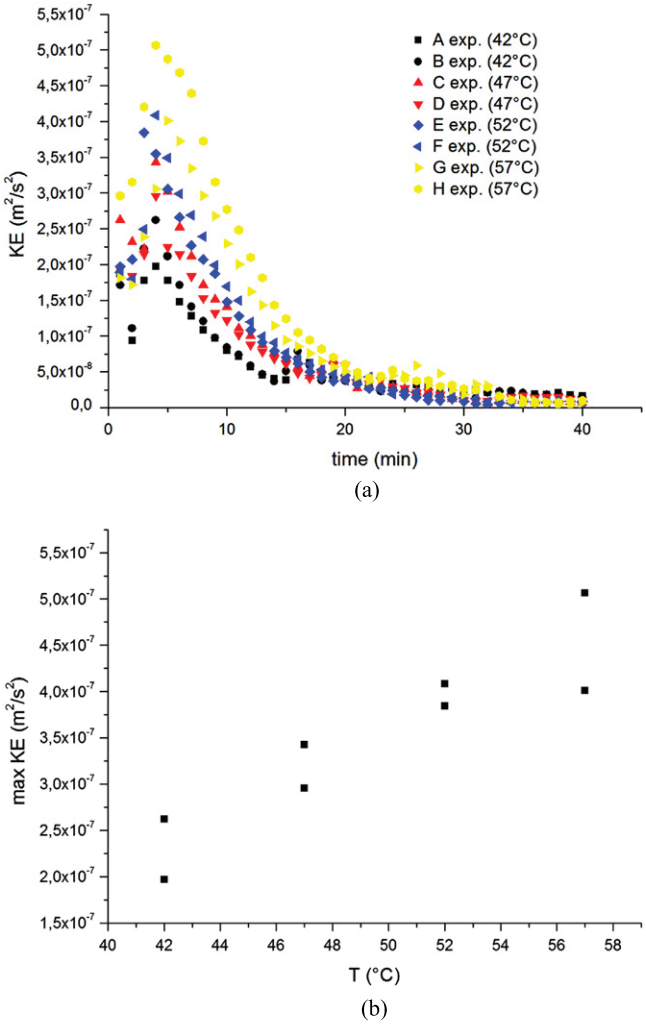

Figure 6. (a) General evolution of the flow kinetic energy during solidification for different superheats; (b) linear variation of the maximum flow kinetic energy with superheat.

$$KE = \rho^* S^* \varepsilon^* \sum_{i=1}^{N} \frac{1}{2} U_i^2 / N \tag{1}$$

where N is the total number of velocity vectors obtained by the PIV measurement. ρ is the density of the liquid, S the total vertical surface of the liquid in the cell at the beginning of the experiment and ε the thickness of the cell. Although there is a change in density with temperature and concentration, the difference doesn't exceed 1% between the beginning and the end of the experiment. Therefore the density is considered as constant.

As shown in figure 6(a), the flow kinetic energy decreases continuously with time except for a short time during the turbulent regime.

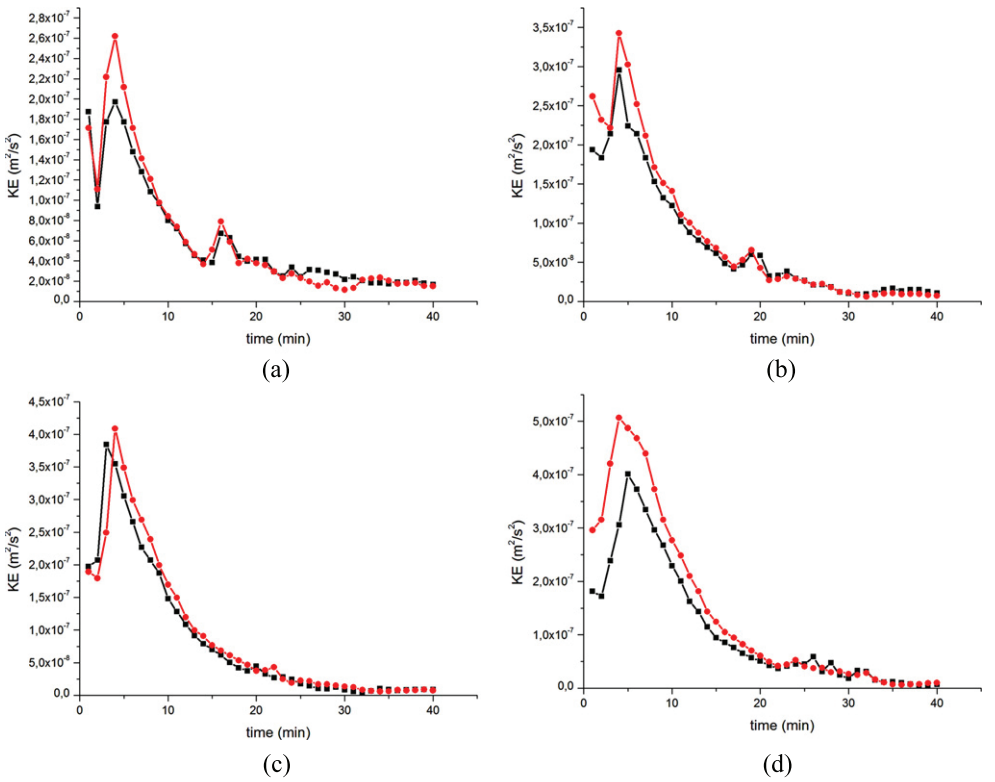

Figure 7. Evolution of the flow KE during solidification for different starting temperatures: (a) 42 °C (experiments A and B); (b) 47 °C (experiments C and D); (c) 52 °C (experiments E and F); (d) 57 °C (experiments G and H).

3.5. Reproducibility of experiments in terms of kinetic energy (KE)

The flow kinetic energy evolution follows the same decreasing tendency for all experiments regardless the superheat (figure 6(a)). The maximum value is reached 3 to 5 min after the start of the cooling bath. In this short period the flow kinetic energy follows a down-up fluctuation. From this point the flow kinetic energy continues to decrease exponentially. Until around 20 min the decrease is very strong, between 20 and 30 min the decrease is extremely slow but weak variations can appear, and after 30 min it is almost constant. A small elevation of the flow kinetic energy was always observed during the TU regime.

It can be seen in figure 6(a) that even though the global tendency is the same, some differences exist. At the beginning of the cooling, along the lateral walls a strong downwards flow occurs. The boundary layer of this downwards flow is very thin. Even though clearly visible with the naked eye, the software (Flow Manager) cannot resolve it correctly. For this reason the flow kinetic energy at the beginning of the experiment presents some differences (the error can be large), sometimes between experiments with the same superheat.

Straightforward is that the larger the superheat, the larger is the maximum values for the flow kinetic energy. In figure 6(b) it can be seen that the maximum value for the flow kinetic energy varies linearly with the starting temperature.

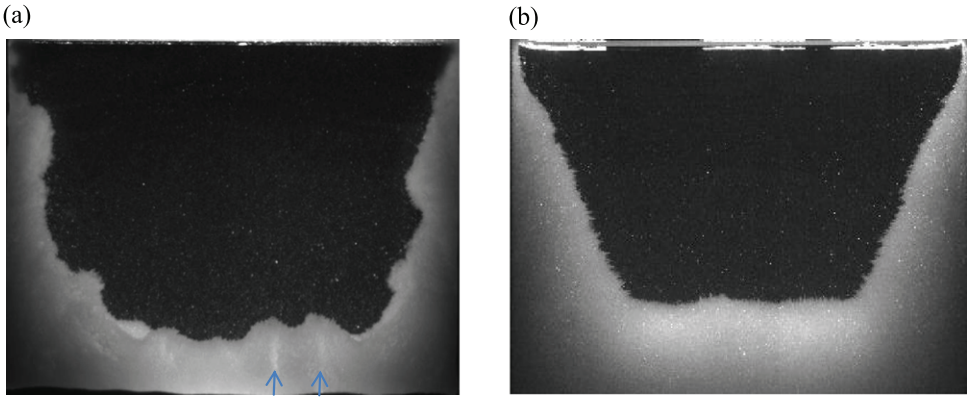

Figure 8. Comparison of mushy zone shape. (a) Solidification process which is dominated by equiaxed crystals. Note the freckle formation in the mush, taken from (Kharicha, 2013). (b) Solidification process where the presence of equiaxed crystals can be neglected and practically pure columnar solidification happens.

Figure 7 shows the flow kinetic energy for different experiments with different superheats. Each experiment was done two times. It can be observed that the reproducibility is very good. In figures 7(b) and (d) small differences can be seen at the starting point for the two experiments. This is due to the fact that the upwards flow along the laterals walls at the very beginning of the cooling is very difficult to catch, as the boundary layers are extremely thin. After a very short decrease (∼3 min) the flow kinetic energy increases shortly (2–3 min) until it reaches the maximum value. Then the flow kinetic energy decreases continuously. With a larger starting temperature the TH regime becomes longer, as the TH regime lasts as long as no solidification occurs and this depends on the applied superheat (section 3.2). Even though the global evolution of the flow kinetic energy decreases, very weak variations subsist and these small peaks are related to the onset of the TU regime (figure 7). As previously explained the start of the TU regime is very difficult to determine. For this reason, it seems that the TU starts one minute after the peak in figure 7(a), directly at the maximum peak value in figure 7(b) and before the peak in figures 7(c) and (d). Also one might think that the superheat has an influence on the TU-ST regime, as it is shorter for 15 °C and 20 °C superheat compared to 5 °C and 10 °C superheat. These are vague observations which depend on the subjective assessment of the different regimes.

3.6. Solidification rate and columnar thickness

During our columnar solidification experiments, where dendrites grew from all walls, sides and bottom, the mushy zone thickness along the bottom wall was very uniform and the boundary between the mushy zone and the liquid appeared smooth (figure 8(b)). However, sometimes quite a severe amount of equiaxed crystal occur, which can stick to the mould wall, grow together with the columnar front or settle down and form a sediment of crystals. Figure 8 shows the mushy zone for an experiment where a huge amount of equiaxed crystals were present (a) and for an experiment where practically the amount of equiaxed can be neglected (b).

In case of practically pure columnar solidification, the advance of the boundary between the mushy zone and the bulk liquid can be accurately measured. In figure 9(a) the measured

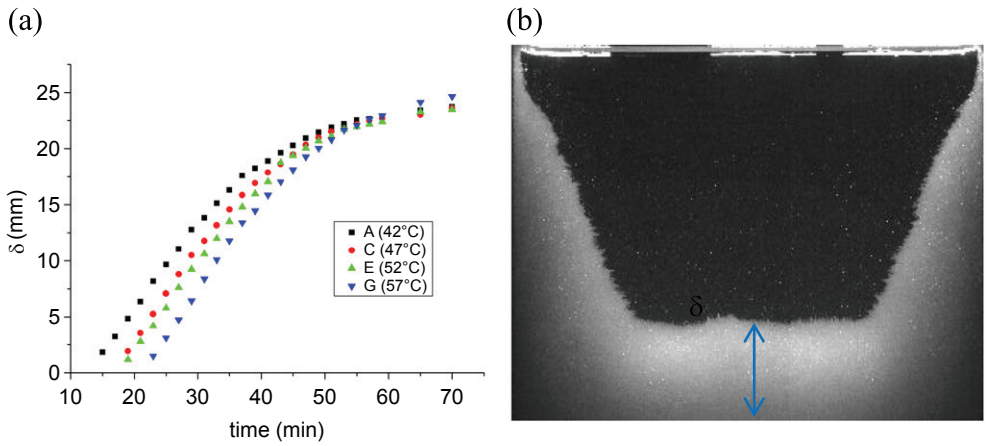

Figure 9. (a) Measured mushy zone thickness along the centre line (blue arrow) shown in (b).

evolution of the columnar mushy zone thickness is plotted with time. The thickness of the columnar zone was measured along the vertical centre line shown in figure 9(b). Obviously, the thickness of the mushy zone grows linearly at first and then the growth saturates. Note that these results are reproducible and thus the second experiment with a similar superheat gives the same result.

The solidification started at different times after the cooling was switched on namely 12 min for the experiments starting at 42 °C and 20 min for the ones starting at 57 °C (see table 1). Because the starting temperatures were different, the time where solidification started was different (section 3.2). Initially, the growth of the columnar mushy zone was linear in time with a slope independent of superheat. In this linear growth regime the dendrite tip velocity is obviously constant. The linear regime lasts between 35 min for the smallest superheat and 40 min for the largest superheat. After one hour, the bottom wall thickness for all experiments reached a plateau at around 25 mm.

The linear growth of the dendrite tip is related to the concentration difference between the bulk concentration and the equilibrium concentration at the dendrite tip. For the first few minutes the bulk concentration does not change as the solidification does not reject enough water-enriched liquid into the bulk. The temperature difference is constant and the growth as well. After 35 to 40 min the evolution of the columnar mushy zone enters a saturated growth.

Another way to quantify the solidification rate was to calculate the total mushy fraction in the cast cell. With a small in-house code this was done using the images taken during the experiment. The results show again the same trend: linear and saturated. In figure 10 the total solid fraction calculated from different experiments is plotted as function of time.

The first solid appeared between 12 min, for the experiment with the starting temperature of 42 °C and respectively 19 to 20 min, for the experiment with the starting temperature of 57 °C. The time to reach the solidification temperature is different because the starting temperature is different (section 3.2). The interesting phenomenon is that the solidification temperature is not fixed (conforming to the phase diagram), it depends as well on the starting temperature. For the 42 °C starting temperature experiment the solidification occurred at

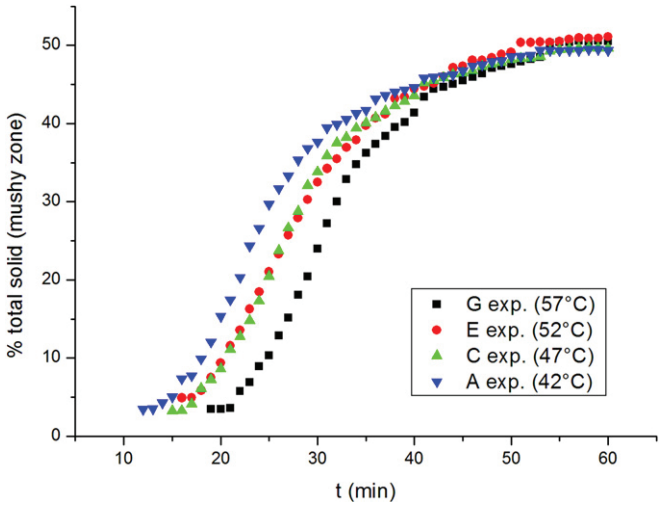

Figure 10 Total solid fraction calculated from the pictured taken during the solidification experiments.

2746 °C and for the 57 °C starting temperature experiment the solidification temperature is higher 3398 °C. The temperature is measured in the cell's walls. The walls temperature decreases linearly until approximately 6 °C then it is quasi-constant.

At the beginning the growth is linear and the duration of this linear regime is independent of the superheat employed! From the time when the first solid occurred until the end of the linear growth the time is approximately equal for all experiments: 15 to 16 min. Regardless of the different starting temperatures the linear growth always ends around 35% fraction mush in the cell (figure 11). The linear growth stops 3 to 11 min before the wall temperature becomes constant. The total solid fraction, after one hour of cooling, is independent of the starting temperature and always equal to 50% for all cases (figure 11).

4. Conclusions

A solidification experiment with an hypereutectic ammonium chloride-water alloy of 29.57 wt.% NH_4Cl was performed in a rectangular die-cast cell of 10*10*1 cm^3. Cooling was uniform for the two walls and the bottom and practically only columnar dendritic growth was observed. The amount of equiaxed crystals was negligible. This is a major difference with the previous observations done under similar experimental conditions (Kharicha *et al* 2013a, 2013b) where intense equiaxed crystals occur and freckle formation was observed. Images were recorded every minute and from the direct visualisation (PIV) and a special image treatment we could extract the thickness of the mushy zone, the total mushy fraction and the flow velocity as function of time.

Different flow regimes were observed and the importance of double-diffusive convection for the flow behaviour was addressed. The results were used to define different flow regimes with the corresponding measured typical velocity pattern. The flow kinetic energy for the entire cell was calculated and the occurrence of a maximum and a subsequent continuous decrease was discussed. For the solidification experiments presented in this paper, the mushy zone developed smoothly and its thickness grew linearly till it followed a saturated law.

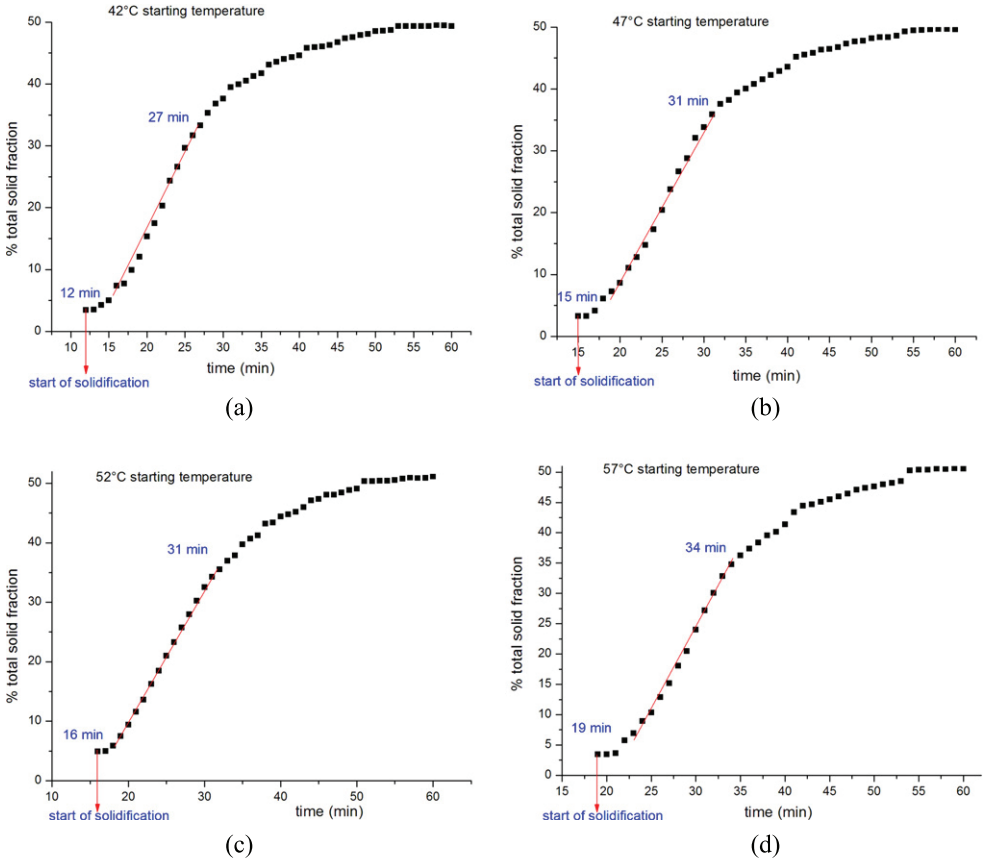

Figure 11. Total solid fraction calculated for different experiments with different starting temperatures; (a) 42 °C; (b) 47 °C; (c) 52 °C; (d) 57 °C.

Independent of superheat, the mushy fraction at the end of the linear regime was around 35% and the mushy fraction at the end of the experiment was around 50%.

Note that the primary aim of this descriptive paper is to give an experimental benchmark for the scientific community focusing on the interaction between solidification and hydrodynamics. At present, numerical models are under development worldwide. Therefore, there is an urgent need for experimental data with both flow and solidification measurements in order to valid these numerical models. In future, such validated simulations might shed a light on the parameter which actually controls the bifurcation between purely columnar and mixed columnar equiaxed solidification.

Acknowledgement

This work was supported by FWF Austrian Science Foundation (P 22614-N22) for which the authors kindly acknowledge.

References

Ahmadein M, Wu M, Stefan-Kharicha M, Kharicha A and Ludwig A 2014 A numerical study of the influence of pouring technique on the as-cast structure of Al-Cu ingots *Mater. Sci. Forum* in press

Beckermann C and Viskanta R 1988 Double-diffusive convection due to melting *Int. J. Heat Mass. Transfer* **31** 2077–89

Beckermann C and Viskanta R 1989 An experimental study of solidification of binary mixtures with double-diffusive convection in the liquid *Chem. Eng. Comm.* **85** 135–56

Bejan A 1993 *Heat Transfer* (New York: Wiley)

Bizon C, Werne J, Predtechensky A A, Julien K, McCormick W D, Swift J B and Swinney H L 1997 Plume dynamics in quasi 2D turbulent convection *Chaos* **7** 107–24

Chen F 1997 Formation of double-diffusive layers in the directional solidification of binary solution *J. Cryst. Growth* **179** 277–86

Chen C F and Chen F 1991 Experimental study of directional solidification of aqueous ammonium chloride solution *J. Fluid Mech.* **227** 567–86

Christenson M S, Bennon W D and Incropera F P 1989 Solidification of an aqueous ammonium chloride solution in a rectangular cavity-II. comparison of predicted and measured results *Int. J. Heat Mass Transf.* **32** 69–79

Flemings M C 1974 *Solidification Processing* (New York: McGraw-Hill)

Kharicha A, Stefan-Kharicha M, Wu M and Ludwig A 2012 Exploration of a double diffusive convection during dendritic solidification with a combined volume-averaging and cellular automata model *IOP Conf. Series: Mater. Sci. Eng.* **33** 012115

Kharicha A, Stefan-Kharicha M, Ludwig A and Wu M 2013a Simultaneous observation of melt flow and motion of equiaxed crystals during solidification using a dual phase particle image velocimetry technique. Part 2: relative velocities *Metall. Mater. Trans.* A **44** 650–60

Kharicha A, Stefan-Kharicha M, Ludwig A and Wu M 2013b Simultaneous observation of melt flow and motion of equiaxed crystals during solidification using a dual phase particle image velocimetry technique. Part 1: stages characterization of melt flow and equiaxed crystals motion *Metall. Mater. Trans.* A **44** 661–8

Könözsy L, Eck S, Stefan-Kharicha M, Wu M and Ludwig A 2009 Experimental and numerical investigations of NH4Cl solidification in a mould. Part 2: numerical results *Int. J. Cast Metals Res.* **22** 172–4

Lesoult G, Combeau H and Moukassi M 1993 Interactions between solidification and fluid flow. Effects on cast structures and segregations *J. Phys. IV France* **3** 813–22

Magirl C S and Incropera F P 1992 Flow and morphological conditions associated with unidirectional solidification of aqueous ammonium chloride *J. Heat Transfer* **115** 1036–43

Neilson D G and Incropera F P 1991 Unidirectional solidification of a binary alloy and the effects of induced fluid motion *Int. J. Heat Mass Transf.* **34** 1717–32

Neilson D G and Incropera F P 1993 Effect of rotation on fluid motion and channel formation during unidirectional solidification of binary alloy *Int. J. Heat Mass Transf.* **36** 489–505

Saffie M G M, Tan F L and Tso C P 2013 A study on the snowing phenomenon in binary alloy solidification *Applied Thermal Engineering* **50** 562–71

Sample A and Hellawell A 1982 The effect of mold precession on channel and macro-segregation in ammonium chloride- water analog castings *Met. Trans.* B **13** 495–501

Sample A and Hellawell A 1984 The mechanism of formation and prevention of channel segregation during alloy solidification *Met. Trans.* A **15** 2163–73

Shih Y-C and Tu S-M 2009 PIV study on the development of double-diffusive convection during the solidification effected by lateral cooling for a super-eutectic binary solution *Appl. Therm. Eng.* **29** 2773–82

Shih Y-C, Tu S-M and Chiu C-C 2013 Supressing freckles during solidification due to periodic motion of top liquid layer *Appl. Therm. Eng.* **50** 1055–69

Solomon T H, Hartley R R and Lee A T 1999 Aggregation and chimney formation during the solidification of ammonium chloride *Phys. Rev.* E **60** 3063–71

Stefan-Kharicha M, Eck S, Könozsy L, Kharicha A and Ludwig A 2009 Experimental and numerical investigations of NH4Cl solidification in a mould. Part 1: experimental results *Int. J. of Cast Metal Res.* **22** 168–71

Tan F L 2005 An experimental study on channels formation during solidification of aqueous ammonium chloride *Appl. Therm. Eng.* **25** 2169–92

Wu M, Ludwig A and Fjeld A 2010a Modeling mixed columnar-equiaxed solidification with melt convection and grain sedimentation-part 1: model description *Comp. Mater. Sci.* **50** 32–42

Wu M, Ludwig A and Fjeld A 2010b Modeling mixed columnar-equiaxed solidification with melt convection and grain sedimentation-part 2: illustrative modeling results and parameter studies *Comp. Mater. Sci.* **50** 43–58

On the Coupling Mechanism of Equiaxed Crystal Generation with the Liquid Flow Driven by Natural Convection During Solidification

MIHAELA STEFAN-KHARICHA, ABDELLAH KHARICHA, MENGHUAI WU, and ANDREAS LUDWIG

The influence of the melt flow on the solidification structure is bilateral. The flow plays an important role in the solidification pattern, *via* the heat transfer, grain distribution, and segregations. On the other hand, the crystal structure, columnar or equiaxed, impacts the flow, *via* the thermosolutal convection, the drag force applied by the crystals on the melt flow, *etc*. As the aim of this research was to further explore the solidification–flow interaction, experiments were conducted in a cast cell (95 * 95 * 30 mm^3), in which an ammonium chloride–water solution (between 27 and 31 wt pct NH_4Cl) was observed as it solidified. The kinetic energy (KE) of the flow and the average flow velocity were calculated throughout the process. Measurements of the volume extension of the mush in the cell and the velocity of the solid front were also taken during the solidification experiment. During the mainly columnar experiments (8 cm liquid height) the flow KE continuously decreased over time. However, during the later series of experiments at higher liquid height (9.5 cm), the flow KE evolution presented a strong peak shortly after the start of solidification. This increase in the total flow KE correlated with the presence of falling equiaxed crystals. Generally, a clear correlation between the strength of the flow and the occurrence of equiaxed crystals was evident. The analysis of the results strongly suggests a fragmentation origin of equiaxed crystals appearing in the melt. The transition from purely columnar growth to a strongly equiaxed rain (CET) was found to be triggered by (a) the magnitude of the coupling between the flow intensity driven by the equiaxed crystals, and (b) the release and transport of the fragments by the same flow recirculating within the mushy zone.

Graphical Abstract

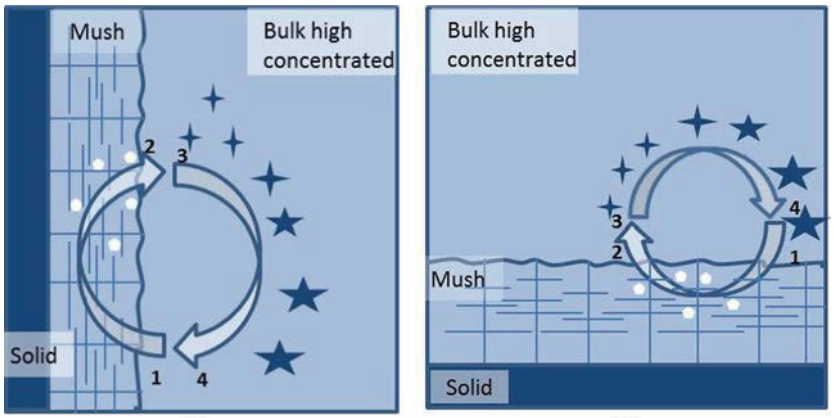

MIHAELA STEFAN-KHARICHA, ABDELLAH KHARICHA, MENGHUAI WU, and ANDREAS LUDWIG are with the Department of Metallurgy, Montanuniversitaet Leoben, Franz-Josef-Str. 18, 8700 Leoben, Austria. Contact e-mail: mihaela.stefan-kharicha@unileoben.ac.at

Manuscript submitted February 3, 2017.
Article published online February 14, 2018

Coupling mechanism at the origin of CET: 1-2 strong flow running through the mush transporting out dendrite fragments (white dots); 3-4 equiaxed growth and drag of the downward flow. If the vortex is sufficiently stable, the horizontal configuration can lead to freckle appearing; a) vertical solidification front; b) horizontal solidification front.

https://doi.org/10.1007/s11661-018-4489-3

I. INTRODUCTION

THE mechanism of how equiaxed grains originate can be explained by two theories: heterogeneous nucleation or fragmentation. The nucleation consists primarily in the creation of nuclei, and secondly, their growth. When the temperature falls below the melting temperature, low enough that an interface between solid and liquid can be created, a nucleus is formed. Most nucleation models postulate that nucleation is a thermally activated process.[1] Once the nucleus reaches the critical size R_c, it can continue to grow. The decreasing atoms' mobility at reduced temperatures contributes to the nucleation rate *via* the atomic variation frequency and the probability of capturing a new atom. The nucleation rate increases rapidly with rising undercooling. In the nucleation mechanism of equiaxed crystal formation, the flow plays an important role during the crystal growth, but is of no significance in nuclei creation phase. Through its interaction with the thermosolutal field, the flow impacts the size of the undercooled region, which needs to be sufficiently large to allow equiaxed crystal growth. In addition, flow also controls the transport of the nuclei.

The generation of equiaxed crystals by fragmentation inside the mushy zone entails the fulfillment of three conditions. First the production of dendrite's fragments in the mushy zone should take place. Secondly, a flow strong enough to penetrate the mush and carry these dendrite fragments in the bulk. The transformation of the fragments into equiaxed crystals is the last condition, *i.e.*, the existence of a sufficiently large undercooled region ahead of the columnar front.

Dendrite fragmentation could occur for different reasons and in many circumstances. Paradies *et al.*[2] performed experiments under forced flow convection (around 10 cm s^{-1}) in superheated SCN—acetone melt, under different system parameters (cooling rate, temperature difference between the chill walls, melt flow rate). The fragmentation rate (number of fragments counted per mm^2 and per second) correlated with a higher velocity melt near the mushy zone. Small fragments less than 0.2 mm were used to measure the velocity melt near the mushy region (0.2 mm beyond the longest dendrite and 0.4 mm into the mushy region). The increase in fragmentation rate correlated with the direction of the flow near the mushy zone, and observations showed that downward flow induced less of an increase than the upward flow near the mushy region. However, it was not possible to deduce a clear relation between the observed fragmentation rate and the controlling parameters of the system. The mechanism at the origin of fragmentation was unclear, but assumedly it was rather due to remelting or capillary pinching than mechanical shear, even if hydrodynamic shear could not be totally excluded.

Remelting of high-order (secondary and tertiary) trunk dendrites originates at the root branches, where the curvature comparing with the tip is larger. Undercooling is a pre-requisite in order to achieve solidification. The dendrite tip curvature during solidification drops as the undercooling rises, thus the greater the extent of undercooling, the faster solid growth occurs. Local changes in the solute concentration in the columnar mush can cause remelting of secondary or tertiary dendrite arms. Pileup of solute in the mush, caused by melt flow or variations in the grow velocity of the columnar front, are possible sources of interdendritic solute variations. Recalescence due to interdendritic melt solidification will raise the temperature and remelt dendrite branches. Jackson *et al.*[3] was the first to suggest that remelting was the mechanism of dendrite detachment due to local undercooling and solute concentration variations in the mushy zone. Equally, the forced convection due to electromagnetic stirring can cause dendrite fragmentation as found by Campanella *et al.*[4] in copper-base alloys. The fragmentation rate was found to be higher if the magnetic field is stronger, if the distance between the coil and the liquid–solid interface is shorter (the induced flow vortices are close to the dendrite tips and able to enter the mushy zone), and if the alloy is more permeable. In addition, a simple fragmentation criterion was found, based on Fleming's analysis of mushy zone remelting.[5] This indicates that a distance equal to $8\lambda_2$ (λ_2 being the final secondary dendrite arm spacing) is necessary to render fragmentation; otherwise only dendrite remelting takes place. Experiments in a modified Bridgman furnace (with an induced coil) on two copper-base alloys confirmed the numerical model based on the fragmentation criterion. A higher concentration alloy is more permeable and leads to finer grains.

Dragnevski *et al.*[6] presented a numerical flow model for dendritic solidification of strongly undercooled melt (50 K to 100 K), when both conditions for dendrite bending, high flow velocities and very fine dendrites, exist. They use a more realistic geometrical model than the analytical model of Pilling and Hellawell,[7] where the dendrites were modeled as cylinders. The results obtained with the two models, for the bending moment function of the flow Reynolds number, are in good

agreement. It was also proved experimentally that mechanical deformation can take place when the dendrite tip radius reaches a local minimum.

The scale of the scenery, where these fragmentation phenomena take place, is microscopic, hence it is difficult to distinguish between them. *In situ* observations were performed with X-ray microscopy[8] on the crystal fragmentation in an Al-Cu alloy. Experimental observations demonstrate that detachment always occurs on the tertiary branches first and sometimes a secondary-arm fragmentation can happen as a consequence of initial fragmentation. They prove that high-order side-branch remelting is prone to producing dendrite fragmentation as opposed to coarser parent branches. In conclusion, fragmentation rate depends on the degree of network branching.

Dendrite fragmentation can occur as a result of coarsening mechanisms or recalescence.[3] However, these phenomena occur deep in the mush and the transport and survival chance of detached dendrites through the low permeable mush is unpredictable. Remelting of tertiary branches at the root to the parent dendrite remains a better pathway for dendrite detachment. Previous to the dendrite fragmentation by remelting, a minor deceleration[9] of the columnar front velocity is noticeable. Ruvalcaba *et al*. hypothesized that this deceleration would induce enhancement of solute at the columnar front and subsequently the solute-rich liquid will settle into the mush and initiate dendrite detachment. The time it takes for a dendrite to detach was measured to be in the range of a few seconds.

Beckermann[10] presents a summary of experimental and numerical works on the convective transport of a single equiaxed crystal at the large scale of a casting. It is crucial to estimate the relative velocity between the settling crystal and the melt flow in convection cases. In this order, the drag force between the equiaxed grain and the melt plays a highly significant role. If the equiaxed grain is globular, Stoke's law applies, and if the grain has a dendritic structure Darcy's law is used to calculate the drag force. The dendrite tip speed can be one order of magnitude higher in the presence of convective flow than in the diffusion case. The solid phase transport is expected to reduce the macrosegregation in this system.

Kumar and Dutta[11] also took into account that dendrite fragmentation may occur as a consequence of local dendrite remelting near the dendrite stem. They tried to quantify a Rayleigh number based on a dendrite fragmentation criterion. The fragmentation criterion merely depends on the concentration difference, liquid fraction, permeability of the mush, grow rate of the mushy zone, and thermophysical parameters. A critical Rayleigh number equal to 1 was found to be necessary in order to induce remelting and subsequent fragmentation. For the same concentration difference, a more permeable mush is more likely to produce remelting and fragmentation. There is a lower probability for remelting and fragmentation in the mush with a faster solidification rate for a given concentration difference.

Montgomery and Incropera[12] studied experimentally the direct solidification of hypereutectic ammonium chloride alloys cooled by bellows (vertical direct solidification, VDS) or by the side wall (horizontal direct solidification, HDS). The fragments produced were counted in a delimited area. The number was found to increase with an increase of initial NH_4Cl concentration in the case of VDS. In contrast, the number rose with a decreasing initial ammonium chloride concentration, in the case of HDS. Moreover, the temperature of the chill plate was varied and the number and size of fragments increased in both cases with decreasing chill wall temperature. In both cases (VDS and HDS), several stages are presumed to exist in the fragment's production. The most important are: (a) remelting, due to latent heat release or drop of liquidus temperature (because of the water-rich interdendritic liquid) and (b) fragmentation in channels, due to strong flow or remelting in the upper region (where water-rich cells developed).

In order to better understand CET, Gandin[13] developed a one-dimensional model based on the interaction of the heat flow at the dendritic interface and the columnar front. When the maximum columnar front velocity was reached and the thermal gradient ahead in the liquid became negative, CET took place. Consequently, fragmentation by dendrite arm remelting and destabilization of the columnar dendritic interface are considered as a hypothesis for the CET. Comparison of simulation results with Al-Si solidification experiments showed good agreement.

The model for the columnar-to-equiaxed transition (CET) proposed by Martorano *et al*.[14] is based on the strong interactions of solutal undercooling and respectively solutal buoyancy, between the columnar front and the equiaxed crystals. Solutally driven flow is crucial in alloys where the rejected solute is lighter (as in hypereutectic ammonium chloride alloys). It was noticed that an increase in the columnar front velocity stimulated equiaxed solidification. The assumption that the CET is the result of the fragmentation of dendrites was emitted.

Hunt[15] considered the growth of equiaxed crystals ahead of a columnar front in his model. In his analysis, he used a simple relation between the velocity columnar front and the square of undercooling and took into account the solute rejection at the dendrite tip. Browne,[16] in his approach of columnar growth, considered the same expression developed by Hunt and he suggested that equiaxed solidification is more probable in alloys with high solute concentrations and where the heat transfer is low.

A great deal of work was conducted by Sivarupan *et al*.[17] on different Al-Si-Cu-Mg-Fe/Mn alloys. For a given composition a relationship between the cooling rate and the SDAS (secondary dendrite arm spacing) was found, in the form of $\lambda_2 = aR^{-n}$, where a and n are alloy-dependent constants, which vary with composition and cooling rate and R is the relation between the average cooling rate and the solidification time.

For peritectic directional solidification, a model was developed[18] in order to evaluate the secondary-arm spacing after coarsening. The model proposes three stages for the thin arm dissolution (thick-arm coarsening). The calculations show that $\lambda_2 V^m$ is constant for a

given alloy composition, where V is the growth tip velocity and m is a factor ranging from 1/3 to 1/2.

Hansen, Hellawell *et al.*[19] developed a six-step physical model in order to explain equiaxed crystal formation, and consequently, columnar-to-equiaxed transition (CET). The model considered remelting as a source for the equiaxed grains and the thermosolutal convection an essential transport mechanism in the mushy zone and in the open bulk. The model was compared with experimental investigations on the transparent system NH_4Cl-H_2O. Observations demonstrate that ripening and fragmentation by remelting take place constantly and depend on the permeability of the mush, which varies along its depth.

In previous works,[20–22] the authors have presented in detail the flow behavior and characteristics during a mainly columnar solidification of an NH_4Cl alloy in a thin (1 cm thickness) cast cell at liquid height of 8 cm. However, few equiaxed crystals occurred during the turbulent flow regime, in the region closed to the lateral mushy zone. This paper verifies the hypothesis that a higher liquid height in the cast cell (thus stronger buoyant melt flow) will enhance the columnar-to-equiaxed transition (CET).

II. EXPERIMENTAL PROCEDURE

For the experiments undertaken for this paper, a cell of 3 cm thick and 10 cm width was chosen and the height of the liquid in the cell was 9.5 cm. With this height we expect to increase the Rayleigh number, which should result in a stronger buoyant flow. The concentration of the ammonium chloride for the NH_4Cl-H_2O solution was varied between 27 and 31 wt pct. The solution was prepared as follows: the respective amount of NH_4Cl was weighted then distillate water was added to obtain the respective concentration. The above mixture was heated up while stirring until 315.15 K (or 318.15 K). In the meantime, the cast cell's walls were heated until 315.15 K (or 318.15 K) by use of a bath.

When the desired temperature was reached, the liquid solution was poured into the cell and left idle for approximately 15 minutes. After this time the thermal bath was set to 278.15 K, thus the cooling started. In order to measure the temperature evolution in time, several thermocouples were inserted in the cell's wall and one thermocouple in the bulk in the middle of the cell. During the solidification experiment with ammonium chloride, a thermocouple inserted into the bulk melt would have disturbed the solidification. Thus thermal measurements of the bulk temperature evolution were performed using pure water. The cooling was found to be uniform for the three walls, only a minute temperature difference of smaller than 0.1 K was recorded between them. The temperature difference between the middle of the bulk and the wall is reported in Figure 1 for the cases of 9.5 cm liquid height and 8 cm liquid height, respectively. The cooling rate applied by the thermal bath was the same in the two cases.

During the solidification process, pictures were taken simultaneously with two CCD cameras. One camera (green filter) was used to catch the ammonium chloride solid growth and the other camera (orange filter) to follow the liquid melt, *via* the Rhodamine-coated polyamide seeding particles. The images were recorded using the commercial software *Dynamic Studio*, generally every minute one set of 10 images. The time between each image in one set is 250 ms. The data treatment (PIV correlations) was also processed with the *Dynamic Studio* software. More details on the PIV technique can be found in previous works.[20–22] Once the velocities are extracted, the flow kinetic energy (KE) can be calculated as follows:

$$\mathrm{KE} = \sum_{\mathrm{IA}} \frac{1}{2} U^2 \times \mathrm{Vol} \times \rho / \mathrm{IA}, \qquad [1]$$

where IA is the total number of PIV interrogation areas (in the mushy zone the velocity vectors are zero), Vol is the volume occupied by the liquid in the cell, and $\rho = 1078$ is the liquid ammonium chloride density.

III. RESULTS

A. *The Problematic*

For the sake of providing greater clarity, the present section aims to illustrate the topic of the present publication with a single comparison. More results and a deeper analysis follow in the next sections.

1. *Flow kinetic energy*

Figure 2 presents two plots of the flow kinetic energy extracted, one during a equiaxed solidification experiment (red curve) and second during a columnar solidification experiment (black curve).

2. *Flow regimes during solidification*

A detailed description of the different flow regimes encountered during columnar solidification of ammonium chloride can be found in previous papers.[20,22] However, to gain a better understanding, a short overview of flow regimes found in currents experiments is in Figure 3. The flow vector maps corresponding to these regimes for a typical equiaxed experiment (shown in Figure 2, red curve), performed at 29.6 wt pct NH_4Cl in the 3-cm-thick cell at a liquid height of 9.5 cm, are presented: (a) thermal symmetric (TH) flow regime, when only the thermal convection plays a role; (b) turbulent solutal flow (TU) regime; (c) equiaxed-driven flow (EQ) regime when a lot of equiaxed occurred (this flow regime does not exist during experiment with mainly columnar solidification); and (d) a meandering flow (MF) regime when the double diffusion becomes the main event. Generally the flow regimes are the same as in the columnar solidification, the only major difference is the presence of the equiaxed-driven flow regime characterized by the intense sedimentation of equiaxed crystals. The melt flow during this regime is laminar due to the laminarization triggered by the

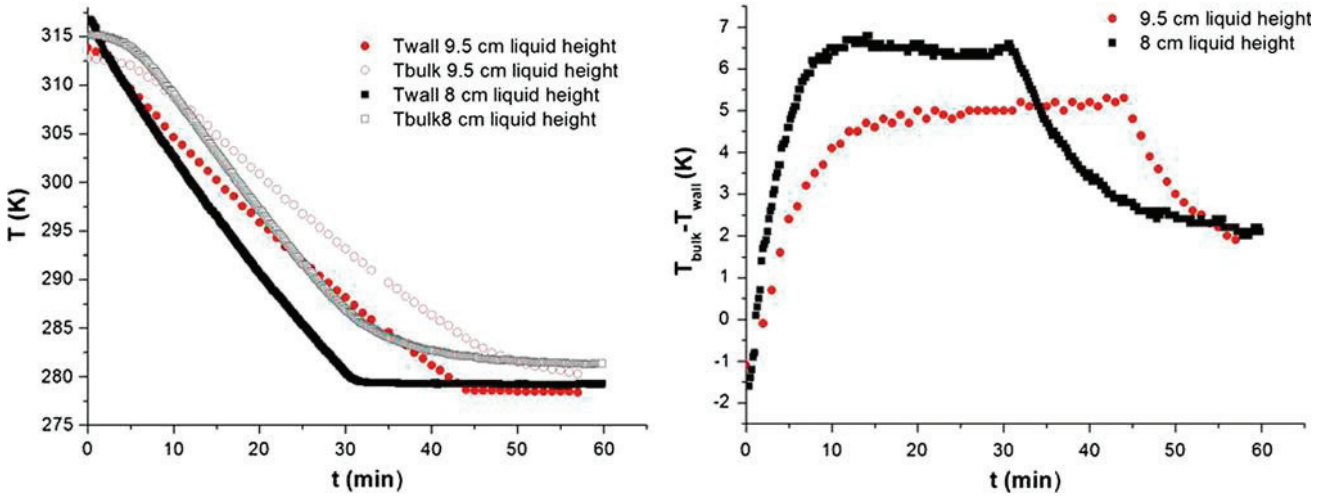

Fig. 1—Temperature evolution in the 3-cm-thick cell at 8 cm (lower cell) and 9.5 cm (higher cell) liquid height.

higher effective viscosity of the liquid-equiaxed mixture. This phenomenon of laminarization was locally observed in regions of high equiaxed crystal density, meanwhile the bulk liquid remained turbulent.[21]

3. *Relationships between flow kinetic energy and equiaxed crystals occurrence*

By relating the graph of Figure 2 with the observations of Figure 3, a correlation between the flow kinetic energy (KE) and the occurrence or not of the equiaxed crystals can be clearly asserted. The present paper aims to answer the following questions: (1) From the heterogeneous nucleation and fragmentation which can explain the best of the equiaxed occurrence? (2) How is the equiaxed crystal occurrence and the flow hydrodynamics related? (3) Is one or two way coupling?

The following presents the results of additional experiments with the 9.5 cm high cell. The average melt velocity and the solid front velocity will be extracted from the experimental data and the relationship between the two will be investigated. The experiments are divided into two series: a lower ammonium chloride concentration group with 27, 27.58, and 28 wt pct NH_4Cl and the higher concentration group with 29.6 and 31 wt pct NH_4Cl. The analysis focuses on the results from the nucleation and fragmentation perspective, and on their relationship with the melt flow magnitude.

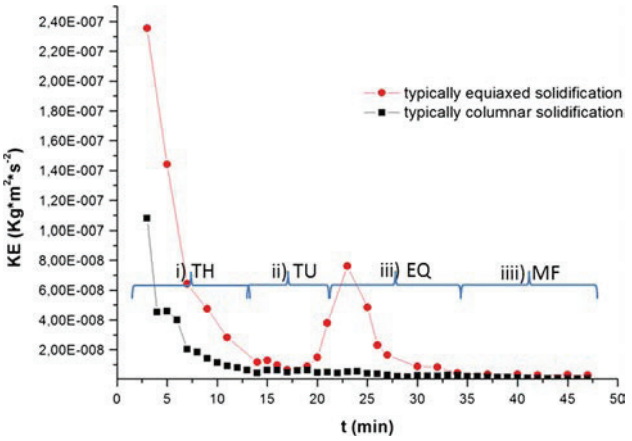

Fig. 2—Flow kinetic energy extracted during a typical equiaxed (9.5 cm high) and a typical columnar (8 cm high) solidification experiment. The time extension of the different flow regimes for the typically equiaxed solidification experiment: (TH) thermal buoyancy, (TU) turbulent-plume flow regime, (EQ) equiaxed-driven flow, (MF) meandering flow regime (Color figure online).

B. *Lower Concentration Group*

1. *Flow and solidification stages*

For the lower concentration group (27, 27.58, and 28 wt pct), solidification started around 25 minutes after cooling from 315.15 K was initiated. The solid appeared along the lateral walls first, under small islands, which developed further until they completely covered the 3 cell's walls (side and bottom walls). At 32, 33, and respectively 38 minutes, equiaxed crystal formation occurred next to the lateral mushy zone. Shortly after, 2 to 3 chimneys emerged from the bottom mush. A large number of equiaxed crystals appeared around these chimneys. After 45, 54, and 50 minutes, respectively, from the inception of cooling, the manifestation of equiaxed crystals stopped, but solidification continued in the form of columnar dendrites. Generally, the equiaxed event lasted about 13 minutes (21 minutes for the 27.58 wt pct experiment, red on Figures 4 and 5).

2. *Mush growth*

The mushy zone growth during the solidification process, was extracted from the pictures. We then estimated the 2D surface occupied by the mushy region; the percentage is named "percentage of apparent mush" in the cell. These results are plotted in Figure 4, where it is evident that the final amount (in pct) of apparent mush is situated around 52 to 55 pct of the cell, except for one experiment (black 28 wt pct on Figure 4) where the final mush is much greater, 71 pct.

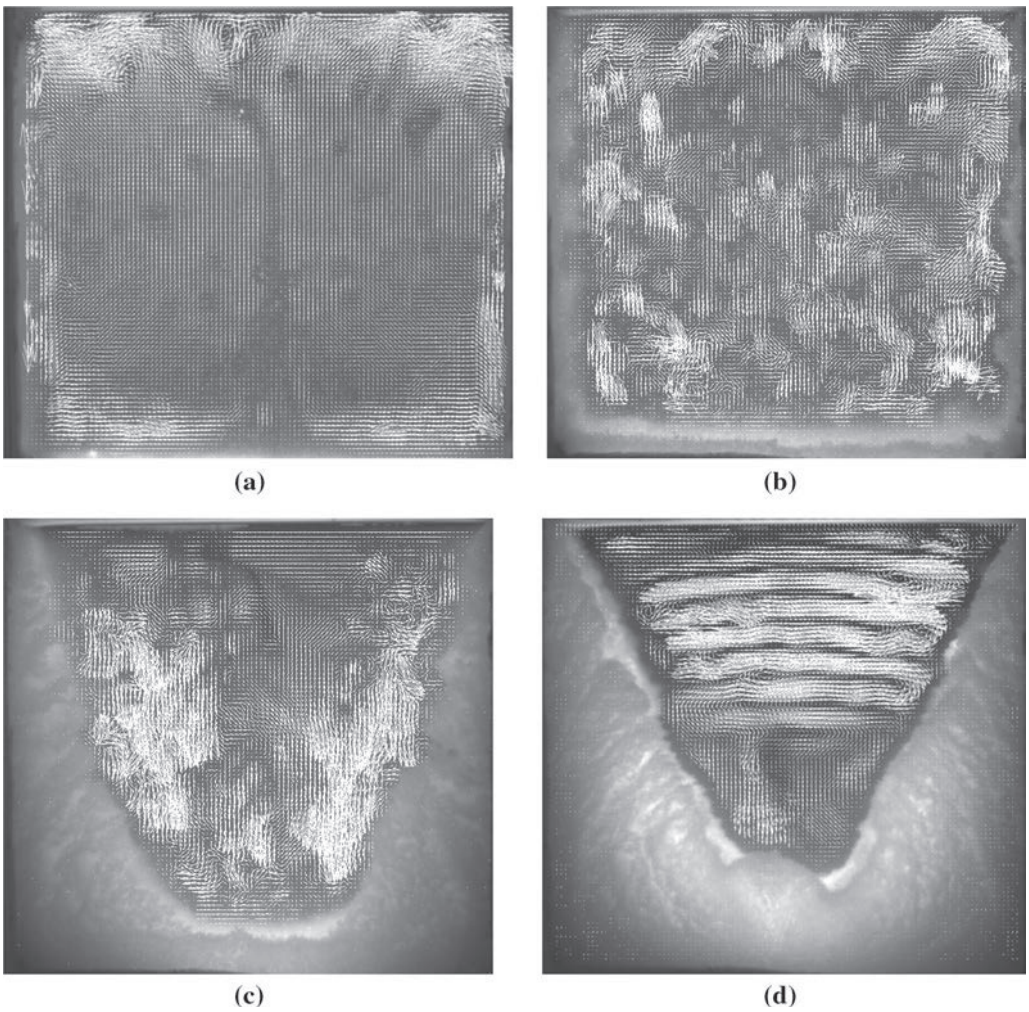

Fig. 3—Flow vector maps at different times corresponding to different flow regimes during the equiaxed solidification of 29.6 wt pct NH_4Cl performed in the 3-cm-thick cell at a liquid height of 9.5 cm: (*a*) Thermal Buoyancy (TU) at 14 min; (*b*) Solutal turbulence (TU) at 20 min; (*c*) Equiaxed-driven flows (EQ) at 25 min. with a lot of equiaxed crystals; (*d*) Meandering flow (MF) at 45 min.

3. *Flow kinetic energy*

The evolution of the liquid phase KE over time was calculated (Eq. [1]) using the measured velocity magnitude U, obtained by adaptive PIV correlation, applied on the pictures where only liquid phase velocity was measured (not the equiaxed grains). The results for 27, 27.58, and 28 wt pct ammonium chloride respectively are displayed in Figure 5. The KE values calculated with Eq. [1] are actually an average flow KE over the volume of the cell.

Although experiments started under identical initial conditions, we could expect the magnitude of the flow KE at the very beginning to be equal for all experiments. The system seems to be very sensitive to minor temperature variation and the initial flow KE values were found to be different between all of the cases. Generally, at the beginning of the cooling process, the flow is at its most powerful, driven by thermal buoyancy. Along the vertical walls, the strong, descending jets are difficult to resolve with the present PIV system, thus these velocities are missing in the calculation of the flow KE. The error

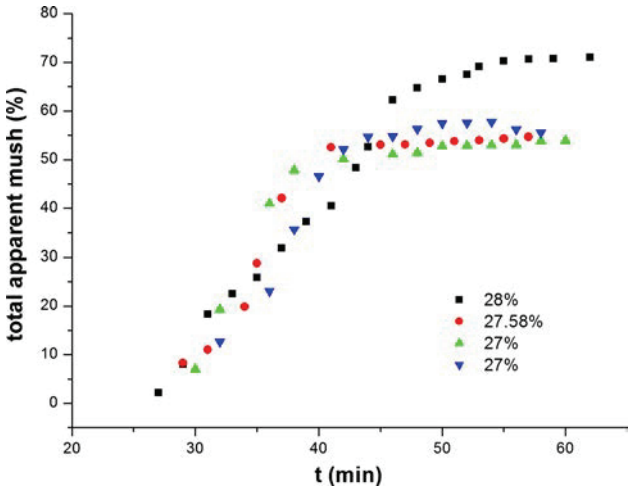

Fig. 4—Percentages of apparent mush in the cell during the solidification of 27 to 28 wt pct NH_4Cl alloys.

concerns only the first minutes when the jets are very thin. Later these jets thicken and then disappear especially once the solidification begins.

The decreasing trend is the same (except green curve on Figure 5). Before solidification occurs, only thermal buoyancy is present and as the temperature difference diminishes, the flow KE decreases. Despite the different hydrodynamic history after 15 minutes, the flow KE finally reaches a similar magnitude for all experiments.

Once the onset of equiaxed crystals begins (around 33 and 37 minutes, see Table I), an increase in the flow KE is clearly apparent (Figure 5). During the equiaxed grain event, 2 to 3 chimneys could be observed. A peak in the flow KE takes place after the commencement of the equiaxed crystal event. This peak can be correlated to the time when a maximum of equiaxed grain is created. The peak values are considerable and in the same order of magnitude for all experiments.

The equiaxed crystal rain was extinguished 45 to 54 minutes after cooling started. Later, only individual grains appeared locally intermittently. After the extinguishing, the flow KE falls down to minimal magnitude values, similarly to what was measured during purely columnar solidification experiments.[20]

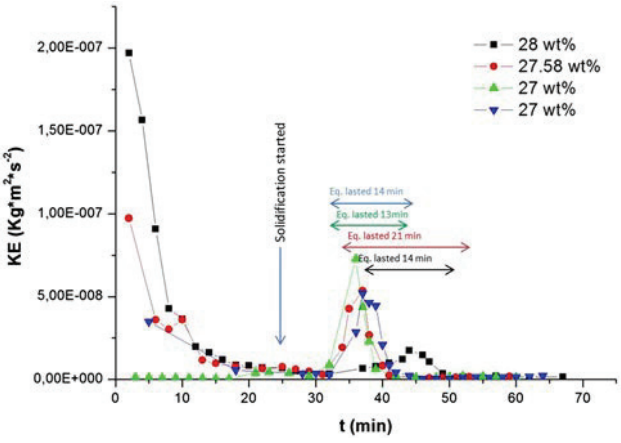

Fig. 5—Flow kinetic energy (KE) during the solidification of 27 to 28 wt pct NH_4Cl alloys (“Eq. lasted” stands for Equiaxed lasted for) (Color figure online).

C. *Higher Concentration Group*

1. *Flow and solidification stages*

For the higher concentration group (29.6 and 31 wt pct) study, the flow behavior, consequently the flow KE evolution, are similar to the example previously described for the lower concentration group. However, during the generation of equiaxed grains, no chimney phenomenon occurred. Therefore, the equiaxed rain event was much steadier and calmer compared to the low concentration group, where the chimneys produced equiaxed crystals in a far more chaotic and distorted manner. In Table I the times when the most important phenomena were visible during solidification (solidification start and equiaxed crystal occurrence) are documented for all series of experiments (low and high concentrations).

The cooling was initiated from 315.15 K (for the 29.6 wt pct experiment) and 318.15 K (for the 31 wt pct experiments), and solidification occurred at 14 minutes (29.6 wt pct), 9 and 6 minutes (31 wt pct) afterwards, respectively. At 17 minutes (29.6 wt pct), 10 and 8 minutes (31 wt pct) after the onset of the cooling, respectively, equiaxed crystals started to occur. The equiaxed grains were distributed throughout the bulk melt and their number was important.

2. *Mush growth*

The evolution of the apparent mush percentage was estimated and the final values reached 55 pct (29.6 wt pct), 66 pct, and 73 pct (31 wt pct) (Figure 6).

3. *Flow kinetic energy*

The evolution of the flow KE (Figure 7) follows the same decreasing tendency until the occurrence of the first equiaxed crystals at 17 minutes (29.6 wt pct), 10 and 8 minutes (31 wt pct). Beginning with these times, an increase in the flow KE can be observed and a peak was witnessed several minutes afterwards. This applies less to the green curve (31 wt pct) on Figure 7. For the 29.6 wt pct experiment (black curve on Figure 7) a clear peak can be observed at 23 minutes. This peak followed the occurrence of a large amount of equiaxed crystals at 19 minutes. However, the maximum of equiaxed crystals was achieved around 25 minutes. At this time the flow

Table I. Times When Most Important Phenomena (Start of Solidification, Equiaxed Crystals) Occurred During Solidification Experiments

NH_4Cl Concentration	Initial T of the Bath When Cooling Started (t_0)	T_{wall} When Cooling Started	t_{solid} (Time When Solid Occurred After t_0)	Time When Flow KE Peak Occurred	Equiaxed Crystals (Start)	Equiaxed Crystals (Maximum)	Equiaxed Crystals (End)
28 wt pct	315.15 K	313.05 K	25 min	44 min	37 min	44 min	51 min
27.58 wt pct	315.15 K	313.95 K	25 min	37 min	33 min	38 min	54 min
27 wt pct	308 K	306.55 K	25 min	36 min	32 min	36 min	45 min
27 wt pct	315.15 K	313.35 K	28 min	37 min	32 min	40 min	46 min
29.6 wt pct	315.15 K (42 °C)	315.35 K (42.2 °C)	14 min	23 min	17 min	25 min	46 min
31 wt pct	318.15 K (45 °C)	315.75 K (42.6 °C)	9 min	19 min 27 min	10 min	19 min 26 min	37 min
31 wt pct	318.15 K (45 °C)	315.35 K (42.2 °C)	6 min	16 min 24 min	8 min	12 min	32 min

kinetic energy started to decrease. For the green experiment (31 wt pct) in Figure 7 the very first equiaxed grains occurred 8 minutes after the cooling started and the event took place for 24 minutes. The increase in the flow KE is lower, and practically no peak can be observed. However, the maximum value was reached at 16 minutes and the maximum of equiaxed crystal was at 12 minutes. For the other experiment at 31 wt pct (red curve on Figure 7) two peaks are visible and each can be linked with an equiaxed event. The first peak at 19 minutes takes place simultaneously with many equiaxed grains. The second peak at 27 minutes follows the occurrence of a large amount of equiaxed crystals at 26 minutes. In this case, the equiaxed crystals lasted for 27 minutes.

Here again, as in the lower concentration group, a clear correlation was evident between the onset of the equiaxed crystals and the flow magnitude and behavior. In the flow kinetic energy evolution over time, an increase is immediately observed after the equiaxed crystals are produced and a peak takes place simultaneously (31 wt pct red) or very short before (29.6 wt pct black) or after (31 wt pct green) the maximum amount of equiaxed grains is reached.

In Figure 8 the total flow kinetic energies for all experiments performed in the thick cell at 9.5 cm liquid height are reported but all the times were set to zero at the start of solidification. It is remarkable that all the KE peaks superpose except for the 28 wt pct experiment (dark blue curve). Very important to notice is that the peaks occur at a certain time after the solidification started and this time seems to be the same for almost all experiments. The maximum values are all in the same order of magnitude 2 to 8 $\times$ 10^{-8} kg m^{-2} s^{-2}.

D. *Average Melt Velocity Related to Solid Front Growth*

From the calculated flow kinetic energy (KE), we extracted the average flow velocity using the following relation $\overline{U} = \sqrt{2\mathrm{KE}/\mathrm{Vol} \times \rho}$, where Vol represents the volume occupied by the liquid melt and ρ is the ammonium chloride density. Using the PIV pictures as those presented in Figure 3, the average solid bottom front velocity was also extracted: $V_{\mathrm{front}} = (\mathrm{d}S/\mathrm{d}t)/L$, where S is the apparent surface occupied by the mush and L is the length of the solidification front.

Figure 9 presents the velocity growth of the bottom solid front *vs* the average melt flow velocity. Generally, at small front velocity values correspond small average flow velocities and at large front velocities are associated with high melt velocity values. The kaki points represent the values where equiaxed crystals are not present (late time in solidification). At small velocity growth (0.2 mm s^{-1}), generally no equiaxed crystals are present. Nevertheless, some values corresponding to equiaxed crystal occurrence are present in this corner of small solid front velocity growth and small average flow velocity. In these cases, even if the average flow velocity is low, it does not mean that it will be low everywhere. Locally, high velocities can exist with the presence of equiaxed crystals.

Figure 9 illustrates the fact that the intense melt flows are more likely associated with the presence of equiaxed crystals. This goes in the direction that large flow velocities enhance the occurrence of equiaxed crystals, but the reciprocal might also be true. In the Discussion chapter the flow melt influence will be analyzed and a mechanism will be proposed for the equiaxed crystal creation.

IV. DISCUSSION AND ANALYSIS

In this chapter the analysis will cover the following steps: first the comparison between a mainly columnar and mainly equiaxed experiment, second the analysis of nucleation and fragmentation as origin for the equiaxed grains, and last the mechanism proposed to explain the CET and the important role played by the melt flow.

A. *Comparison Between a Typically Columnar and Equiaxed Solidification Experiments*

In Figure 10, the flow kinetic energy for a mainly columnar experiment, performed in the 3-cm-thick cell

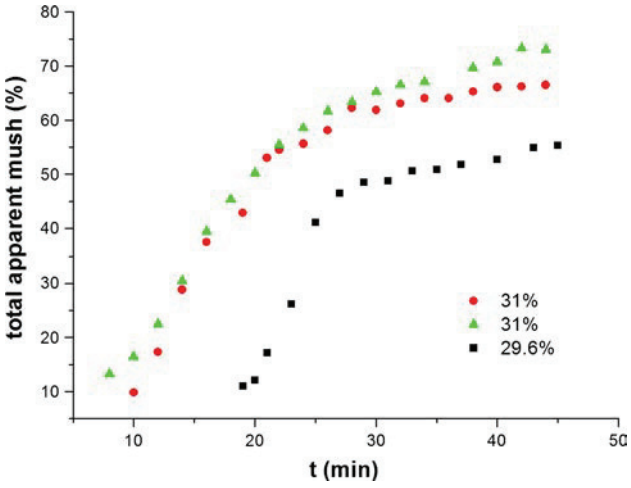

Fig. 6—Percentages of apparent mush in the cell during solidification of 29.6 and 31 wt pct NH_4Cl alloys.

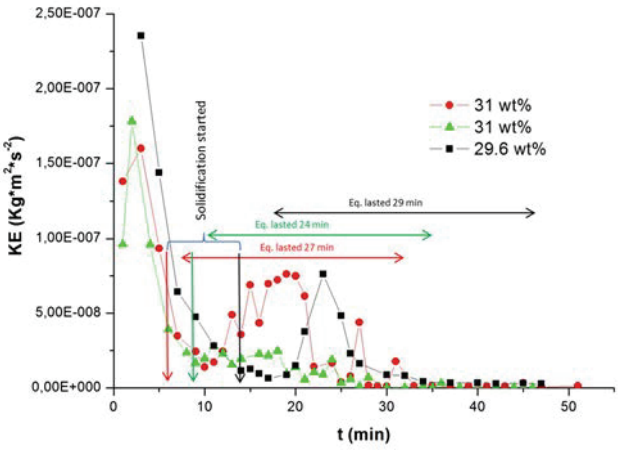

Fig. 7—Flow kinetic energy (KE) during solidification of 29.6 and 31 wt pct NH_4Cl alloys (Color figure online).

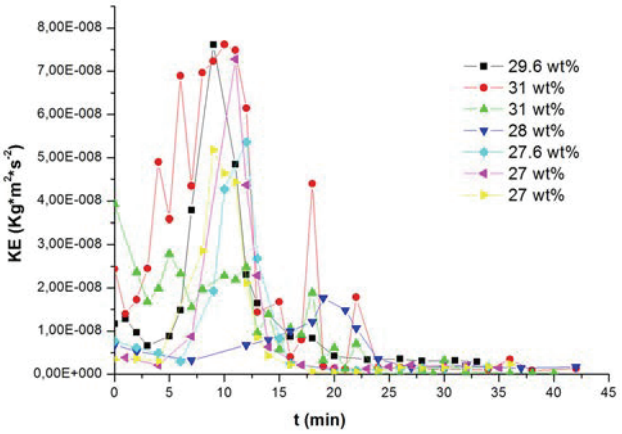

Fig. 8—Comparison of flow KE starting from the time when solidification occurred in the 9.5 cm high cell during the solidification of different ammonium chloride concentrations from 27 to 31 wt pct (Color figure online).

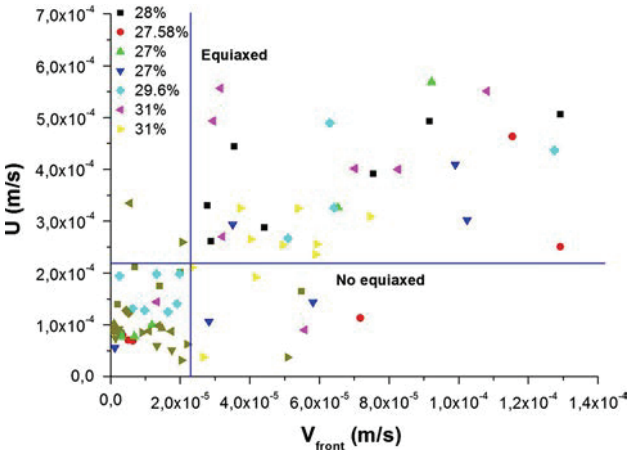

Fig. 9—Average velocity flow *vs* velocity front for different NH_4Cl alloy concentrations during solidification at 9.5 cm liquid height. Colored points stand for presence of equiaxed. The kaki points report situations when no equiaxed crystals occurred anymore (Color figure online).

at 8 cm liquid height (lower cell), is compared with flow KE for a mainly equiaxed experiment, performed in the present investigation with a 9.5 cm height cell. The ammonium chloride concentration used in the two cases is strictly the same (29.6 wt pct). The starting wall's temperature for both experiments was fixed at 315.15 K at the thermal bath, and the cooling rate was homogeneous (Figure 1).

The flow KE starting values are lower for the mainly columnar experiment (8 cm liquid height) than for the equiaxed experiment (9.5 cm liquid height) but in the same order of magnitude. This can be explained by the difference in the Rayleigh number. It is very clear that the global trend of the flow kinetic energy evolution with time (Figure 10), which expresses the flow behavior, is dramatically different in the case of a columnar solidification experiment, compared with an equiaxed solidification experiment. In the case of the mainly columnar experiment, the flow kinetic energy decreases

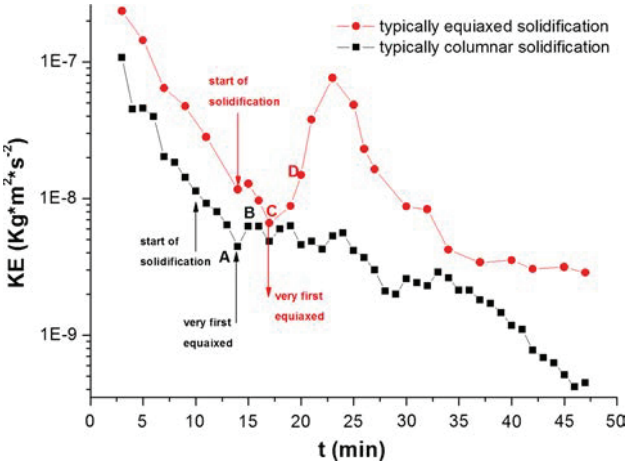

Fig. 10—Flow KE comparison at 8 cm liquid height (mainly columnar solidification) and 9.5 cm liquid height cell (equiaxed solidification) in logarithmic scale (Color figure online).

continuously and exponentially, and the values are usually smaller than in the case of the mainly equiaxed solidification experiment.

For the equiaxed solidification case (9.5 cm liquid height), the flow kinetic energy decreases until the start of equiaxed crystal apparition and then a significant increase in the flow kinetic energy takes place. In Figure 10, note that in the typical columnar solidification (black curve), the flow KE decreases continuously until the point A. The point A (14 minutes after cooling was started) marks the beginning of a very small increase in the flow KE and corresponds to the time when the solutal natural convection starts to become significant. This increase continues until point B, but then the flow KE decreases back with some oscillations. These small KE oscillations are believed to be induced by the solutal buoyancy, which creates a turbulent non-coherent flow regime.

The flow velocity map corresponding to point B (Figure 10) is shown in Figure 11(a). This flow doesn't have a stable structure neither in time nor space (Figure 11(a)). The flow will rise at some points and then come down following a sinusoidal wave from right to left (Figure 11(a)). The magnitudes of the flow in the bulk area are tiny (0.01 mm s^{-1}) with some maxima of 0.3 to 0.5 mm s^{-1} in the green areas. In the mush the flow cannot be visualized, it can only be observed where it enters the mush and where it comes out. At the right bottom corner (Figure 11(a)) the flow falls down with high velocity and immediately near it goes up (follow the big white arrow Figure 11(a)). In this same area only few equiaxed crystals were noticed.

Concerning the mainly equiaxed solidification experiment (red curve on Figure 10), the situation is completely different. At point C the very first equiaxed crystals were present and immediately the flow KE increases. The increase from point C to point D is similar to the increase observed for the black curve from point A to B, the only difference is that the corresponding flow is stronger at point C than at point A.

Moreover, for the mainly equiaxed solidification the increase continues after the point D and the occurrence of equiaxed crystals is massive. The magnitude of the flow at point D (see flow velocity map on Figure 11(b)) indeed shows maximum values are larger than at point B (see flow velocity map on Figure 11(a)) and these maximum values are spread all over the length of the mushy zone. Of course the flow in the mush is not visible, but one can assume that if the flow is high in the vicinity on the mush, it enters the mushy zone and can transport many dendrite fragments. The bulk is particularly patterned, presenting many areas with relatively large velocity ~ 0.6 mm s^{-1} (green zones on Figure 11(b)). The flow is strong and its impact is marked on the temperature and concentration distribution, creating local undercooled zones even far in the bulk and thus the possibility of equiaxed dendrite growth. In Figure 11(b), the zone delimitated by the red oval already contains many equiaxed crystals distributed everywhere (evident in Figure 11(c)). The flow present at point D is strong enough to have carried out many dendrite fragments and these fragments will have grown into equiaxed fragments in the bulk.

When equiaxed crystals form in the bulk, they grow and then fall down and accelerate the melt flow with their fall. This can be seen in Figure 11(b) inside the region delimitated by the red oval, the flow is downward in many places, which is the mark of falling equiaxed

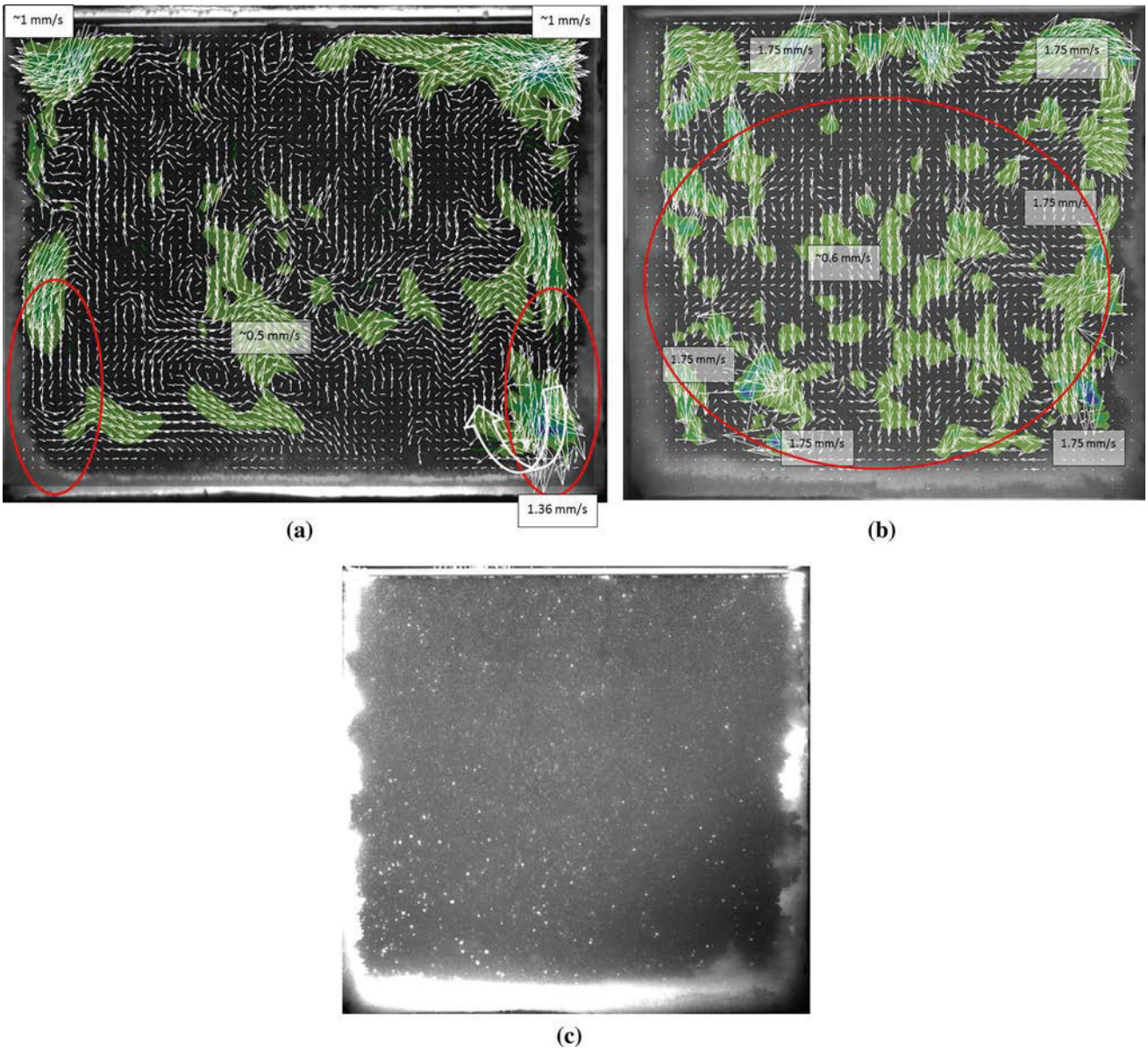

Fig. 11—(*a*) Flow velocity map at 16 min (point B on Fig. 10) after cooling started during the mainly columnar solidification experiment (maximum flow velocity values at top corners ~ 1 mm s^{-1} and right bottom corner ~ 1.36 mm s^{-1} and equiaxed crystals only present next to the lateral mush inside the 2 red ovals left and right); (*b*) Flow velocity map at 20 min (point D on Fig. 10) after cooling started during the mainly equiaxed solidification (large velocity values all along the length of the mushy zone and at the top ~ 1.75 mm s^{-1} and equiaxed grains are present everywhere in the zone delimited by the red oval); (*c*) Equiaxed crystals in the bulk at the same time as the flow map shown in Fig. 11(b)) (Color figure online).

crystals driving the flow. The melt flow will thus penetrate the bottom or lateral mushy zone. When leaving the mushy zone, this flow will bring into the bulk liquid a certain number of dendrite fragments. These fragments arriving in the undercooled melt will eventually grow and drag the flow in their fall. This phenomenon can sustain and intensify itself as long as the concentration and temperature in the bulk are adequate to enable the dendrite fragments to grow into equiaxed crystals.

An evaluation of the peak height in the flow KE time evolution was performed. The ratio between the maximum peak value and the base value (before the increase of the flow KE) was calculated (as shown in Figure 12(a)). These ratios were compared and a net tendency arises: In the case of mainly columnar experiments (data taken in Reference 20) the ratio situates in-between 1 and 2, for the present experiments with strong presence of equiaxed crystals the values set from 11 to 33. For the example showed in Figure 12(a) the ratio is equal to 11.51. Figure 12(b) presents the picture of the equiaxed crystals and mush at 2 minutes after the peak. Many equiaxed crystals are visible, they seem to come out from the lateral mush and fall down at the corners. Figure 12(b) can be correlated to Figure 12(c) where the flow map velocity is shown for the same time (2 minutes after the peak) and consequently it can be imagined that the flow comes out from the lateral mushy zone (drawn big arrows) where the equiaxed crystals occurred but also re-enter the mush where equiaxed crystals descend.

Comparing the percentage of the cell filled with mush over time, clear differences can be witnessed between a typically columnar and a typically equiaxed solidification experiment (Figure 13(a)). The solidification started at 10 minutes in the 8 cm liquid height cell, and at 14 minutes in the 9.5 cm liquid height cell (temperature gradient in the 9.5 cm cell is lower than in the 8 cm cell (Figure 1), thus the time to reach the solidification temperature was longer. However, until 23 minutes, the solid front growth is equivalent for the two cases (typically columnar and typically equiaxed). At 21 minutes an acceleration of the solidification front speed can be observed for the equiaxed case (Figure 13(a), red curve). This acceleration is related to the equiaxed event which started already at around $t = 17$ minutes after the cooling started, but the maximum strength was reached at $t = 25$ minutes. By the end of the solidification process (~ 1 hours after the cooling started) the final amount of apparent mush is 5 pct larger in the case of the experiment with equiaxed crystals than in the columnar case. This can be explained by the fact that columnar mush has a regular structure, with lower permeability. In opposite, the occurrence of equiaxed crystals in front of the columnar zone increases the permeability and consequently the volume occupied is larger. The final shape of the mushy zone is also different for the two cases (Figures 13(b) and (c)). For the typically columnar case the final shape is fine and regular with a flat bottom mush. For the typically equiaxed case, the final shape of the mush is irregular, forming a V profile. Such differences in shape and growth speed have been verified for all present and past experiments.[20–22]

B. *Interpretation Based on the Assumption that Equiaxed Crystals are Created by Nucleation*

The heterogeneous nucleation implies the existence of a substrate (mold or foreign particles), which can be simply impurities or refining particles. Oldfield[23] has demonstrated experimentally that the grain's density N is related with the maximum undercooling (attained at recalescence):

$$N \propto A\Delta T_u^2 \qquad [2]$$

In this case nucleation is instantaneous and the nucleation sites have different activation potentials at characteristic temperatures. The size distribution of the foreign particles is essential in the activation of nucleation as the undercooling increases.

Once the creation of the first nuclei has taken place, the second growth phase can commence. As the nucleation increases, the growth rate, V will also rise, since the nucleation will provide sites on which to grow. As ΔT_u increases, the growth rate V will approach that of uniform growth, $V \sim$ const. ΔT_u, as the nuclei already created provide sufficient spots to grow.

In addition, to grow nuclei it need to spend time in the undercooled region. Hence larger is the undercooled zone better are the conditions for growth.

Based on the above consideration, Hunt[24] proposed a model for the transition from columnar to equiaxed growth. Two characteristic length can be considered: first the undercooled length in front of the columnar zone, $L_C = \Delta T_C/G$ and second the space between the nuclei forming the equiaxed zone, L_N. The latter is related to the density of nuclei, $L_N = N^{-1/3}$. Remark that larger N permits the equiaxed zone to grow more rapidly and larger ΔT_C increases the columnar front undercooling and thus the length over which the equiaxed grains can grow. It can be resumed that the equiaxed zone is favored at low temperature gradient and/or high undercooling. A correlation between the columnar front growth and the equiaxed crystal occurrence is also considered in this model and the relation is shown in Eq. [3]:

$$V = A \cdot T_C^2, \qquad [3]$$

where A is a factor which cumulates the solute rejection at the dendrite tip. It is shown that the undercooling is connected with the columnar velocity front, higher undercooling corresponds to larger growth velocity.

During current solidification experiments the temperatures were measured for the 8 cm liquid height case and 9.5 cm liquid height case (Figure 1). The temperature difference between the bulk and the wall is larger in the case of 8 cm liquid height, thus the temperature gradient is higher in this case. With the following equation:

$$L_C = \frac{\Delta T_C}{G} = \frac{\Delta T_C * \Delta x}{\Delta T}, \qquad [4]$$

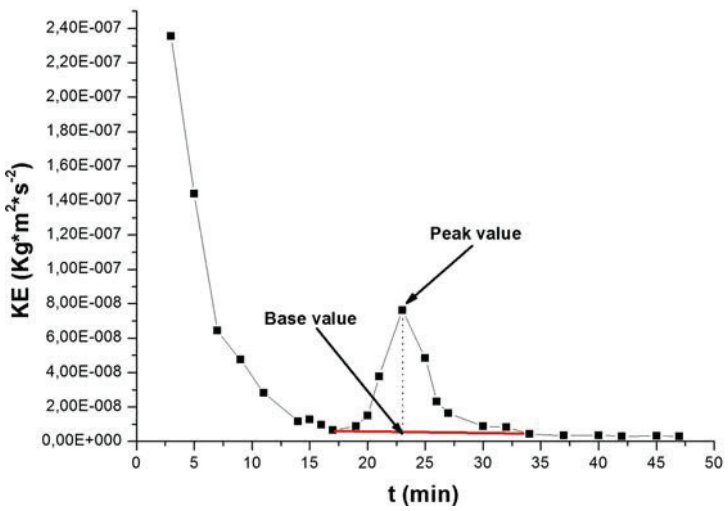

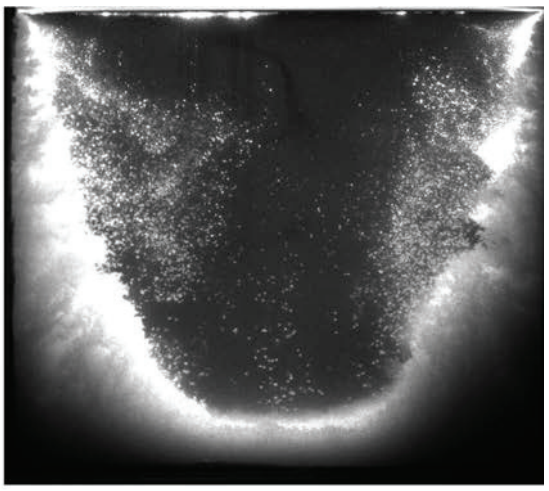

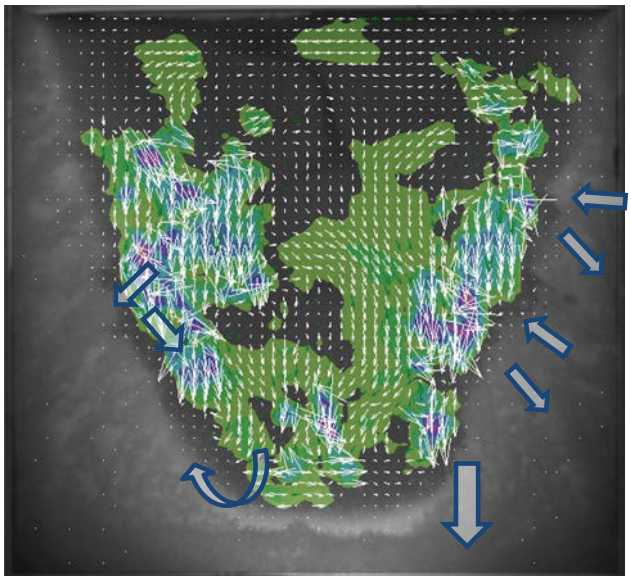

Fig. 12—(*a*) Schema of the baseline value and peak value in the case of equiaxed solidification; (*b*) Picture of experiment with mushy zone and equiaxed crystals fall at about 2 min after the peak; (*c*) Liquid phase flow velocity map at 2 min after the peak. Large vectors represent the probable direction of the liquid flow out or into the mushy region. These vectors are emanating from the mushy zone in areas where equiaxed crystals suddenly appeared and re-entering the mushy zone where equiaxed crystals fall down.

the length of the undercooled region δ can be estimated for a given global temperature gradient $G \cong \frac{\Delta T}{\Delta x}$ (where $\Delta T = T_{\text{bulk}} - T_{\text{wall}}, \Delta x$ is the distance between the wall and the middle of the bulk) and a certain undercooling $\Delta T_C = T_l - T_C$, (where T_l is the liquidus temperature corresponding to the initial alloy concentration, and T_C is the temperature of the columnar front). In the case of the 8 cm liquid height, the undercooled region's length is smaller than for the 9.5 cm liquid height case. Due to the greater length of the undercooled region in the higher cell, the chances of obtaining a nucleation of equiaxed crystals are larger than in the lower cell.

Introducing relations given in Eqs. [4] into [3], the front velocity growth can be correlated with the length of the undercooled region, $V \propto L_C^2$. In Figure 9 it can be observed that for front velocity larger than 3 μm s^{-1}, hence large undercooled zone, equiaxed crystals occurred (colored points). For lower columnar front growth velocity, thus small undercooled zone, no equiaxed crystals happen (kaki points). These observations support relations from Eqs. [3] and [4]. On the other hand, the kaki points (when no equiaxed occurred) are located late after the cooling has started, when thermal and solutal forces diminish. Equiaxed crystals (colored points on Figure 9) occur when the themosolutal forces are intense. Considering only the nucleation theory, no clear correlation can be made between the flow strength and the equiaxed crystal creation, because the flow exerts no direct influence on nucleation. However, the correlation between high V

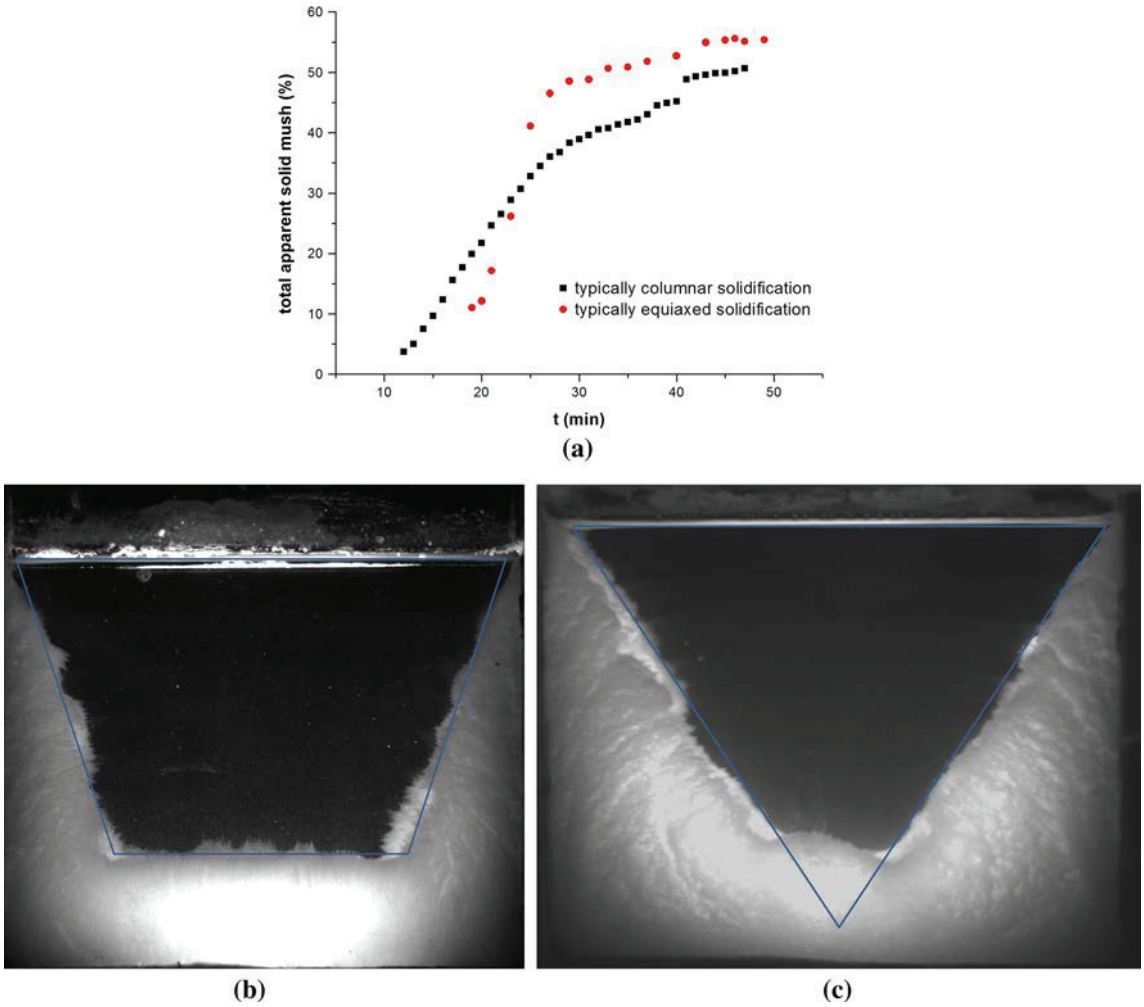

Fig. 13—(*a*) Evolution of the percentage of apparent mush in the cell in the 8 and 9.5 cm height cell during the solidification of 29.6 wt pct ammonium chloride; (*b*) Final shape of the mush in the 8 cm height cell, typical columnar solidification; (*c*) Final shape of the mush in the 9.5 cm height cell, typical equiaxed solidification (Color figure online).

and large melt flow velocity can be understood by the enhancement of solutal buoyancy when the front velocity increases, as lighter solute is rejected at the solidification front. In addition, the falling equiaxed crystals drive the flow due to drag interaction and will result in flow acceleration. It has been seen in experimental investigations that in areas with a large number of equiaxed crystals, high melt flow velocities are generated. In summary, there is a one-way coupling: nucleation rate can directly influence the flow, but the flow cannot directly influence the nucleation rate. In next section, a much stronger coupling will be shown if we assume equiaxed crystal growth from fragments expelling from mushy zone.

C. *Interpretation of the Results Based on the Fragmentation Phenomena*

Ideally, in order to estimate the potential strength of equiaxed creation by fragmentation, it is necessary to quantify the number of fragments leaving the mushy zone. Inside the mushy zone, the number of available dendrite fragments is directly correlated to the number density of primary, secondary, and tertiary arms. These arms are mainly controlled by the temperature gradient G and the front velocity V.

Two theories were developed by Hunt,[24] Kurz, and Fisher,[25] who proposed a power law correlating the primary λ_1 arm spacing and the columnar front velocity V, the gradient G, and the initial alloy concentration C_0. In the two models, only the constant K is different and the respective relation is shown in Eq. [5]:

$$\lambda_1 = KC_0^{0.25}G^{-0.5}V^{-0.25} \qquad [5]$$

where K is connected with: the Gibbs–Thomson coefficient, the liquidus line slope, the solute partition coefficient, and D the liquid solute diffusivity.

Considering this relation, we can conclude that the larger the velocity growth, smaller the dendrite arm spacing λ_1 and λ_2, thus more branching occurs.

Experimental observations on Succinonitrile (SCN)–carbon tetrabromide (CTB) alloy solidification[26] have been made for different CTB concentrations, constant temperature gradient (7.5 K mm^{-1}), and

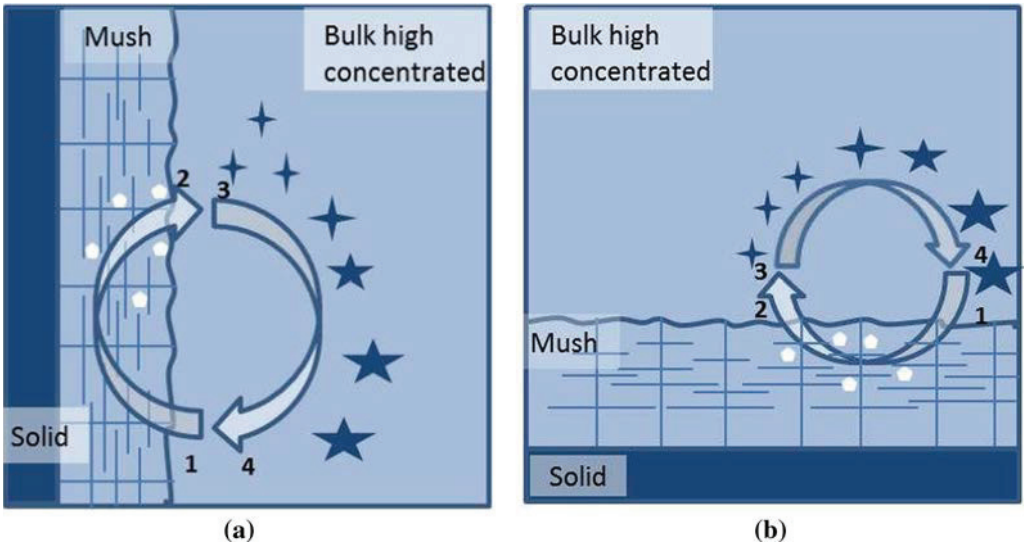

Fig. 14—Coupling mechanism at the origin of CET: 1-2 strong flow running through the mush transporting out dendrite fragments (white dots); 3-4 equiaxed growth and drag of the downward flow. If the vortex is sufficiently stable, the horizontal configuration can lead to freckle appearing; (*a*) vertical solidification front; (*b*) horizontal solidification front.

different growth rates. Results indeed indicate that the values of λ_1 and λ_2 decrease as the growth rate V increases, for a given concentration. Eqs. [6] and [7] present the relationship found for SCN-5 wt pct CTB, where k_1 and k_2 are constants:

$$\lambda_1 = k_1 V^{-0.25}, \quad [6]$$

$$\lambda_2 = k_2 V^{-0.46}. \quad [7]$$

These exponent values demonstrate that the dependency of the secondary dendrite arm spacing on the growth rate is stronger than the primary dendrite arm spacing, for the same concentration alloy.

Assuming a small cubic volume element Δx^3, the number of columnar primary arms (supposing they are uniformly distributed in the element) is $N_{d1} = \Delta x^2/\lambda_1^2$. The number of secondary arms F_2 growing perpendicularly to a single primary arm is equal to $4\Delta x/\lambda_2$. If we neglect the tertiary arms, the total number of dendrite arms $N_d = N_{d1} + N_{d2}$ existing in this volume element can be expressed by the following relation:

$$N_d \propto \Delta x^3 \left(\frac{1}{\lambda_1^2} \cdot \frac{4}{\lambda_2} \right). \quad [8]$$

By considering $\lambda_1 = 10^{-3}$ and $\lambda_2 = 10^{-6}$, which are common values for ammonium chloride, Eq. [8] gives a number density in the order of 10^{12} arms per m^3. As mentioned in Eqs. [5] through [7], λ_1 and λ_2 are closely related with G and V, therefore N_d can be related with G and V and the relation is shown in Eq. [9]:

$$N_d \propto G^{3/2} V \quad [9]$$

Using the relations from Eqs. [3] and [4], N_d is found to increase with the 7/2 power of the columnar front undercooling:

$$N_d \propto \Delta T_C^{7/2} \quad [10]$$

This equation expresses the fact that an increase in the velocity growth or undercooling will induce a huge increase of the number of dendrite arms, which theoretically can be broken and become dendrite's fragments susceptible to grow into equiaxed grains later. It can be noticed that N_d increases much faster with undercooling than the nucleation rate based on N (Eq. [2]), this because of the power 7/2 larger than 2, but also because $\Delta T_u \leq \Delta T_C$. Thus the fragmentation hypothesis presents a higher potential for the creation of equiaxed crystals (even neglecting tertiary dendrite arms) than the nucleation hypothesis where only a limited number of inoculants might exist.

Experiments demonstrate that fragmentation/detachment of secondary dendrites is more frequent in concentrated alloys under high growth rate.[27] The large velocity growth will provide a large tip undercooling and creates thinner secondary arms with finer arm neck, consequently these structures are more prone to remelt, than a coarser arm neck. Higher growth rate will also create larger number of secondary arms, thus the condition to enable detachment is increased.

Remelting, which can be at the origin of dendrite fragments is favored by the increase of the solid front velocity. When the solidification rate increases, the solutal buoyancy increases, due to more solute being rejected, this will bring about an intensification of the melt flow. This strong convection enhances the heat and mass transfer, brings more solute locally in the mushy

zone and induces remelting.

The formation of dendrite fragments in the mushy zone is only the beginning of the creation of equiaxed grains. Those fragments should be transported out of the mush into an undercooled zone. In this case, a strong flow would be beneficial. The stronger is the melt flow, the more likely the fragments will be transported out of the mushy zone.

Via a calculation of the Rayleigh (*Ra*) number, the association of the liquid height in the cell and flow magnitude can be accomplished.[21] For a higher liquid height a larger *Ra* number is obtained, respectively a more important flow is encountered. The flow KE evolution during the solidification, confirms that in the higher cell, the flow is stronger than in the lower cell (Figure 10). Thus the likelihood of importing a fragment from the mush out in the undercooled zone is much greater in the case of the higher cell. Figure 9 shows a good correlation with this theory. It can be seen that for large melt velocity equiaxed crystals always occurred (colorful points) and for small flow velocity equiaxed crystals are not present (kaki points). Considering the fragmentation theory, the strength of the melt flow can be correlated with the creation of equiaxed crystals as was experimentally observed by Paradies *et al.*[2] in their investigation on the convection influence on the fragmentation. It showed an increase of the fragmentation rate with the increase of the melt flow next to the mushy region.

D. *Final Assessment: Nucleation or Fragmentation as Source for equiaxed Grains and Mechanism of Creation of Equiaxed Grains*

Concerning the heterogeneous nucleation the seeding flow particle (20 μm polyamide particles coated with Rhodamine) can be considered as substrate. Solidification experiments with and without the seeding flow particles (Rhodamine-coated polyamide particle) were performed. A large amount of equiaxed crystals was noticed in both experiments without and with seeding particles. We did not count the number of equiaxed grains, we only evaluated area size covered by equiaxed crystals. If heterogeneous nucleation occurred on seeding particles, then much less equiaxed would have been observed during the experiments without seeding particles. This situation confirms in the balance that fragmentation is at the origin of equiaxed crystals, because fragmentation occurs independently of seeding particles.

The fact that the equiaxed crystals always appeared after a layer of columnar mush occurred at the cell's walls, and never prior to that, is another strong argument for the fragmentation theory. This assertion was also published by Montgomery and Incropera in their study of directional solidification of ammonium chloride.[12] They observed a maximum of dendrite's fragments at 2.5 mm mushy region growing at the lateral wall. The presence of columnar region seems to be a necessary condition for the creation of the first equiaxed crystals. Equiaxed crystals appear a few minutes after the start of columnar region at cell's walls. The equiaxed crystals were observed in both cases low cell and high cell, but their number, distribution in space and time was very different. This difference resulted in the final solidification type, mainly columnar in former case and predominantly equiaxed for the second.

Based on our experimental results and analysis, we propose a mechanism that couples the naturally driven flow with the equiaxed grain dynamics. This mechanism depicted schematically in Figure 14, can trigger a transition from a purely columnar to an equiaxed solidification (CET). Solutal convection cells are present along the mushy zone. At point 1, an ammonium chloride-rich flow penetrates the mushy zone and the columnar front continues to solidify. As the solidification takes place the liquid flowing through the mush becomes lighter. Due to this local change in the interdendritic composition, the liquidus temperature increases and remelting occurs. Consequently, dendrite fragments form in the mush. The flow will exit the mushy zone at point 2 carrying out dendrite's fragments. These fragments arriving in the undercooled and high concentrated bulk liquid will grow into equiaxed dendrites (Figure 14 point 3). Once they reach a certain size, the equiaxed crystals will descend (Figure 14 point 4). Due to the drag interaction the flow will be accelerated by the falling equiaxed crystals (Figure 14 point 3 to 4). In this manner, the full convection cell is strengthened, and the flow which renters the mush is now able to transport even more fragments out of the mushy zone. As follows, a coupling between the strength of flow and production equiaxed grains takes place. By this mechanism, the flow is accelerated as long as fragments are produced in the mushy region and as the concentration in the liquid bulk stays high enough. However, the acceleration of the flow is constrained by the mush permeability, and perhaps by a limited possible number of fragments created in the mush during solidification. As explained in Section IV–C, the fragmentation theory is constrained by the number of dendrite arms, which is indisputably extremely high but decreases with time as solid fraction increases in the mush.

This coupling mechanism can also explain the observations made by Montgomery and Incropera.[12] In the present experiments, a eutectic reaction does not take place, so the latent heat release cannot be at the origin of the first dendrite fragments. Nevertheless, local concentration changes in the interdendritic liquid take place and may cause remelting. Even if all stages for the creation of dendrite's fragments cannot be accounted for in current investigations, the fact that the number of equiaxed crystals starts to increase once the solutal convection becomes strong is a good indication that the coupling mechanism strongly correlates with flow behavior. In Reference 12 during vertical direct solidification (VDS) it was also observed that fragments reached a peak during transition from solutal fingers to channels, which means that the presence of strong solutal flow was beneficial in the formation of dendrite fragments. For horizontal direct solidification (HDS) the influence of the flow was more obvious as the thermal convection was the first source of fragments, but later, the water-rich interdendritic liquid was again

at the origin of the fragment production *via* salt fingering and channels. In our present investigations, the number of equiaxed crystals was indeed more important at the horizontally growing mush and always occurred initially along the horizontally growing mush. However, when channels occurred at the vertically growing mush, then the amount of equiaxed crystal reached a peak.

From the experimental observations it seems that the coupling mechanism occurs easier at the lateral mush (first equiaxed grains are always observed there), but the same mechanism can also occur at the bottom mush (Figure 14(b)). Along the lateral mush, the convection cells are relatively more stable and for this reason the coupling mechanism occurs with greater ease. It is necessary that the convection cell is relatively stable so that the flow enters and exits the mushy zone in the same region for a certain time until enough dendrite fragments are transported out of the mush. The strength of the flow at the mushy zone entry (point 1 in Figure 14) is a capital factor in the occurrence of this mechanism as it depends on how many fragments are transported out of the mush. The results shown in Figure 10 confirm this assertion and as for the predominantly equiaxed solidification (red curve) the point C has a higher flow velocity than point A on the black curve (mainly columnar solidification). This mechanism is fully verified, considering the fact that in the case of the higher cell, the flow was stronger than in the case of the lower cell at the moment when the very first equiaxed crystals occurred. If the vortex is sufficiently stable (points 3 to 4 in Figure 14), the equiaxed crystal falls can considerably strengthen the solutal convection. Remelting and/or low velocity front solidification can occur at the vicinity of point 2 (Figure 14(b)), giving rise to a freckle with its associated strong liquid jet driving away fragments far into the liquid bulk.

V. CONCLUSIONS

For the current experiments (9.5 cm liquid height) equiaxed crystals were generated in all cases for all concentrations from 27 to 31 wt pct.

1. The phenomena took place throughout the bulk melt and lasted for a long time (between 30 and 54 minutes). For the lower concentration group (27 to 28 wt pct), even chimneys appeared and the amount of equiaxed grains was enormous.
2. The flow kinetic energy showed a clear correlation between the occurrence of the equiaxed crystals and the flow; the onset of equiaxed crystals is always accompanied by an increase of the flow kinetic energy.
3. A coupling mechanism between the flow and the creation of equiaxed crystals was proposed in order to explain the occurrence of CET. The strength of the naturally driven flow at the mushy zone entrance is an important factor in the coupling mechanism and has been confirmed by the present results. In this mechanism, the number of equiaxed crystals is increased by the number of fragments driven out of the mushy region by the interdendritic flow. The solutal, convective flow is strengthened by the falling equiaxed crystals dragging in the liquid bulk. A coupling can occur if the bulk flow and the interdendritic flow are part of a single circulation cell. This mechanism can thus generate freckles at horizontal solidification fronts, and trigger a CET transition.

ACKNOWLEDGEMENTS

Open access funding provided by Montanuniversity Leoben.

REFERENCES

1. J.A. Dantzig, M. Rappaz, *Solidification*, EPFL Press, 2009.
2. C.J. Paradies, R.N. Smith, and M.E. Glicksmann: *Metall. Mater. Trans. A*, 1997, vol. 28A, pp. 875–83.
3. K.A. Jackson, J.D. Hunt, D.H. Uhlmann, and T.P. Seward: *Trans. TMS-AIME*, 1966, vol. 236, pp. 149–58.
4. T. Campanella, C. Carbon, and M. Rapaz: *Metall. Mater. Trans. A*, 2004, vol. 35A, pp. 3201–10.
5. M.C. Flemings: *Solidification Processing*, 1974.
6. K. Dragnevski, A.M. Mullis, D.J. Walker, and R.F. Cochrane: *Acta Mater.*, 2002, vol. 50, pp. 3743–55.
7. J. Pilling and A. Hellawell: *Metall. Mater. Trans. A*, 1996, vol. 27A, p. 229.
8. R.H. Mathiesen, L. Arberg, P. Bleuet, and A. Somogyi: *Metall. Mater. Trans. A*, 2006, vol. 37A, pp. 2515–24.
9. D. Ruvalcaba, R.H. Mathiesen, D.G. Eskin, L. Arnberg, and L. Katgerman: *Metall. Mater. Trans. B*, 2009, vol. 40B, pp. 312–16.
10. C. Beckermann: *JOM*, 1997, vol. 49, pp. 13–17.
11. A. Kumar and P. Dutta: *J. Phys D*, 2008, vol. 41, pp. 1–9.
12. W.C. Mongomery and F.P. Incropera: *Exp. Heat Transf.*, 1998, vol. 11, pp. 59–86.
13. Ch.A. Gandin: *Acta Mater.*, 2000, vol. 48, pp. 2483–2501.
14. M.A. Martorano, C. Beckermann, and Ch.A. Gandin: *Metall. Mater. Trans. A*, 2003, vol. 34A, pp. 1657–74.
15. J.D. Hunt: *Mater. Sci. Eng.*, 1984, vol. 65, pp. 75–83.
16. D.J. Browne: *ISIJ Int.*, 2005, vol. 45, pp. 37–44.
17. T. Sivarupan, C. H. Caceres, and J. A. Taylor: *Metall. Mater. Trans. A,* 2013 on line.
18. D. Ma, W. Xu, S.C. Ng, and Y. Li: *Mat. Sci. Eng. A*, 2005, vol. 390, pp. 52–62.
19. G. Hansen, A. Hellawell, S.Z. Lu, and R.S. Steube: *Metall. Mater. Trans. A*, 1996, vol. 27A, pp. 569–81.
20. M. Stefan-Kharicha, A. Kharicha, M. Wu, and A. Ludwig: *Fluid Dyn. Res.*, 2014, vol. 46, pp. 1–21.
21. A. Kharicha, M. Stefan-Kharicha, A. Ludwig, and M. Wu: *Metall. Mater. Trans. A*, 2013, vol. 44A, pp. 650–60.
22. A. Kharicha, M. Stefan-Kharicha, A. Ludwig, and M. Wu: *Metall. Mater. Trans. A*, 2013, vol. 44A, pp. 661–68.

23. W. Oldfield: *Trans. ASM*, 1966, vol. 59, pp. 945–61.
24. J. D. Hunt: *Solidification and Casting of Metals,* Metals Society London, 1979, pp. 1-3.
25. W. Kurz and J.D. Fisher: *Acta Metall.*, 1981, vol. 29, pp. 11–20.
26. H. Kaya, E. Cadirli, K. Keslioglu, and N. Marasli: *J. Cryst. Growth*, 2005, vol. 276, pp. 583–93.
27. T. Sato, W. Kurz, and K. Ikawa: *Trans. Jpn. Inst. Metals*, 1987, vol. 28, pp. 1012–21.

Massive Formation of Equiaxed Crystals by Avalanches of Mushy Zone Segments

A. LUDWIG, M. STEFAN-KHARICHA, A. KHARICHA, and M. WU

It is well known that the growth and motion of equiaxed crystals govern important microstructural features, especially in larger castings such as heavy ingots. To determine the origin of the equiaxed crystals, heterogeneous nucleation, and/or fragmentation of dendrite arms from columnar regions are often discussed. In the present study, we demonstrate that under certain conditions relatively large areas of mushy regions slide downward and form spectacular crystal avalanches. These avalanches crumble into thousands of dendritic fragments, whereby the larger fragments immediately sediment and the smaller proceed to behave as equiaxed crystals. Traces of such crystal avalanches can be seen by conspicuous equiaxed layers in the lower part of the casting. From the arguments in the discussion, it is believed that such a phenomenon may occur in alloys which reveal an upward solutal buoyancy in the interdendritic mush. This would include certain steels and other alloys such as Cu-Al, Pb-Sn, or Ni-Al-alloys. Moreover, the occurrence of crystal avalanches contribute to the formation of V-segregations.

DOI: 10.1007/s11661-017-4008-y

I. INTRODUCTION

MANY common alloys solidify by forming an outer equiaxed zone, followed by a columnar zone and a more-or-less extended inner equiaxed zone.[1,2] The grains of the outer equiaxed zone form in contact with the mold wall by heterogeneous nucleation, and with the columnar dendritic zone by growth competition from the outer equiaxed zone.[3] In the interior of the casting, equiaxed crystals form by either heterogeneous nucleation[4] or fragmentation of dendrites from the columnar zone.[5–7] However, both mechanisms reveal same uncertainties. For instance, the origin of a heterogeneous site that reduces the energy barrier for nucleation is often unknown, especially for non-inoculated alloys. Conversely, the proposed criteria for the occurrence of fragmentation of dendrite arms[5,7] can hardly be applied due to the complex overall interdendritic flow caused by forced or natural convection or deformation of the dendrite skeleton.

In the present study, observations are reported which show that relatively large areas of vertical columnar zones—especially at the upper part of the casting mold—may slide downward and form crystal avalanches. These avalanches consist of thousands of dendritic fragments from which equiaxed crystals grow. In the framework described above, this can be seen as substantial fragmentation and thus massive formation of equiaxed crystals.

A. LUDWIG, M. STEFAN-KHARICHA, A. KHARICHA, and M. WU are with the Montanuniversitaet Leoben, Department of Metallurgy, Chair for Simulation and Modelling of Metallurgical Processes, 8700 Leoben, Austria. Contact e-mail: ludwig@unileoben.ac.at
Manuscript submitted August 12, 2016.
Article published online March 16, 2017

II. EXPERIMENTAL PROCEDURE

A relatively large container (0.6 m tall, 0.4 m wide and 0.06 m thick) was filled with a 29.6 wt pct ammonium chloride—water solution. The given measures are internal dimensions. The lateral walls are made of brass, the bottom plate is made of aluminum, and the front and back walls are made of commercial PMMA (Polymethylmethacrylat) plates. The top of the cell was left open. The temperature of the brass walls was controlled via a circulation bath by applying an exponential cooling curve as $T(t) = T_\alpha \exp(-\alpha t) + T_{\text{inf.}}$ with $T_\alpha = 47$ K, $\alpha = 0.033$, and $T_{\text{inf.}} = 279$ K (6 °C). For the experiment reported in this work, we started with an alloy at a temperature of $T_0 = 325$ K (52 °C), which was then cooled down to $T_{\text{inf.}} = 279$ K (6 °C) via the side walls. Note that the interdendritic eutectic in the ammonium-water system forms at around 253 K (−15 °C). Thus, even by reaching the minimal cooling temperature some interdendritic melt in the mushy zone remains liquid.

The ammonium chloride—water solution was prepared directly in the container by mixing ammonium chloride powder with distilled water at 325 K (52 °C). After the well-stirred alloying, we waited typically 1 hour to equilibrate the temperature field before cooling. During this time, the small, but continuous, heat loss through the front and back window resulted in a steady and symmetric thermal buoyancy flow which was used as the reproducible initial stage for the different experimental runs.[8] After the equilibration time, cooling of the lateral and bottom walls was initiated.

III. RESULTS

In the experiments, solidification started by heterogeneous nucleation along the lateral and the bottom walls.

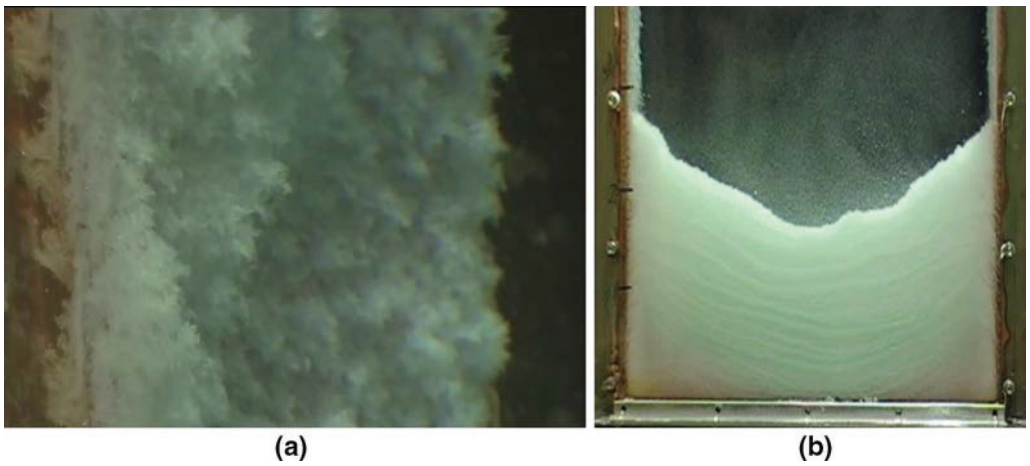

Fig. 1—(*a*) Mushy zone growing from the brass wall into the bulk melt. Note that the picture shows an inclined view of the 0.06-m-thick left brass wall. (*b*) Sedimented equiaxed crystals at the bottom of the 0.4-m-wide containment with around 15 traces of massive equiaxed formation due to repetitive occurrence of avalanches.

From those first crystals, visible dendritic structures grew more or less perpendicularly to the walls forming the columnar zone. Figure 1(a) shows the lateral brass wall covered with a mushy zone sticking to the brass mold surface. A clear influence of gravity on the dendrites' morphology and growth direction could not be observed. Additionally to the formation of the columnar dendrites, small equiaxed crystals exist in the bulk melt. As they grow in size, these crystals descend and sediment toward the bottom.

After the columnar zone has reached a certain thickness of 0.01 to 0.02 m occasionally parts of the columnar mushy zone, especially from the upper part of the containment, began to slide downwards. Within seconds the columnar mush disappeared, leaving behind a segment of the brass mold surface with only a thin layer of crystals. From this thin layer, columnar solidification started again, until eventually a new sliding event occurred. Fig. 2 shows a sequence of pictures taken with the time interval of $\Delta t = 0.9$ seconds. In order to illustrate the sliding motion, we have marked two segments. The whole sliding process takes only a few seconds. Figure 3 shows the consequence: Crumbling of the sliding columnar area results in an avalanche of dendritic fragments whereby larger fragments immediately sediment and smaller proceed to behave as equiaxed crystals.

The sliding down parts of the mushy zone and the occurrence of such an avalanche of fragments is not a singular event. Rather in our experiments it happened repeatedly. Figure 1(b) shows corresponding traces of around 50 of such avalanches in the sedimented equiaxed bed. The first avalanche happened around 31 minutes after initial cooling, where the wall had a temperature of about 296 K (23 °C). From then on, avalanches occurred again and again from both side walls leading to a sedimentation trace of relative large dendritic fragments at the bottom of the container. However, every 5 to 6 minutes the avalanche activity diminished for a while, and descending of smaller equiaxed crystals from the bulk changed the appearance sedimentation traces. In Figure 1(b), recurring stages of lower avalanche activity leads to 15 sedimentation traces of finer equiaxed crystals. The avalanche presented in Figure 2 occurred around 92 minutes after initial cooling. At that time, the wall had nearly reached it minimal temperature of 279 K (6 °C).

IV. DISCUSSION

The ammonium chloride-water system forms a eutectic phase diagram[9] with a eutectic concentration at $C_E = 19.7$ wt pct NH_4Cl. Thus, the ammonium chloride—water solution used for the reported experiments [29.57 wt pct NH_4Cl with $T_L = 310$ K (37 °C)] is a hyper-eutectic alloy, where ammonium crystals form on cooling. In consequence, the interdendritic liquid enriches in water and so its density decreases compared to the unsegregated bulk melt. This leads to a rising solutal interdendritic buoyancy flow as already observed and discussed in References 10 through 13.

For similar experiments in a smaller container ($0.1 \times 0.1 \times 0.01$ m^3), the present authors reported the occurrence of different flow regimes.[8,14,15] Before solidification starts thermal buoyancy results in a downward flow along the cold lateral walls and a rising flow at the cell center. Such a flow pattern is also expected to occur in the present larger containment ($0.6 \times 0.4 \times 0.06$ m^3). When solidification starts along the lateral and the bottom walls, solutal buoyancy leads first locally to a reversing of the flow. In References 8 and 15 this stage was called "perturbed thermal stage." The next stages following are the "turbulent flow stage" and the "coherent chaotic flow stage." In both stages, the main flow characteristics in the bulk melt were observed as being turbulent/chaotic but downward, so that in conclusion it can be stated that the interdendritic flow in the columnar mushy zone along the vertical walls was upwards.[8,15]

In contrast to the geometrical constrains for the small containment used in References 8 and 15 the present

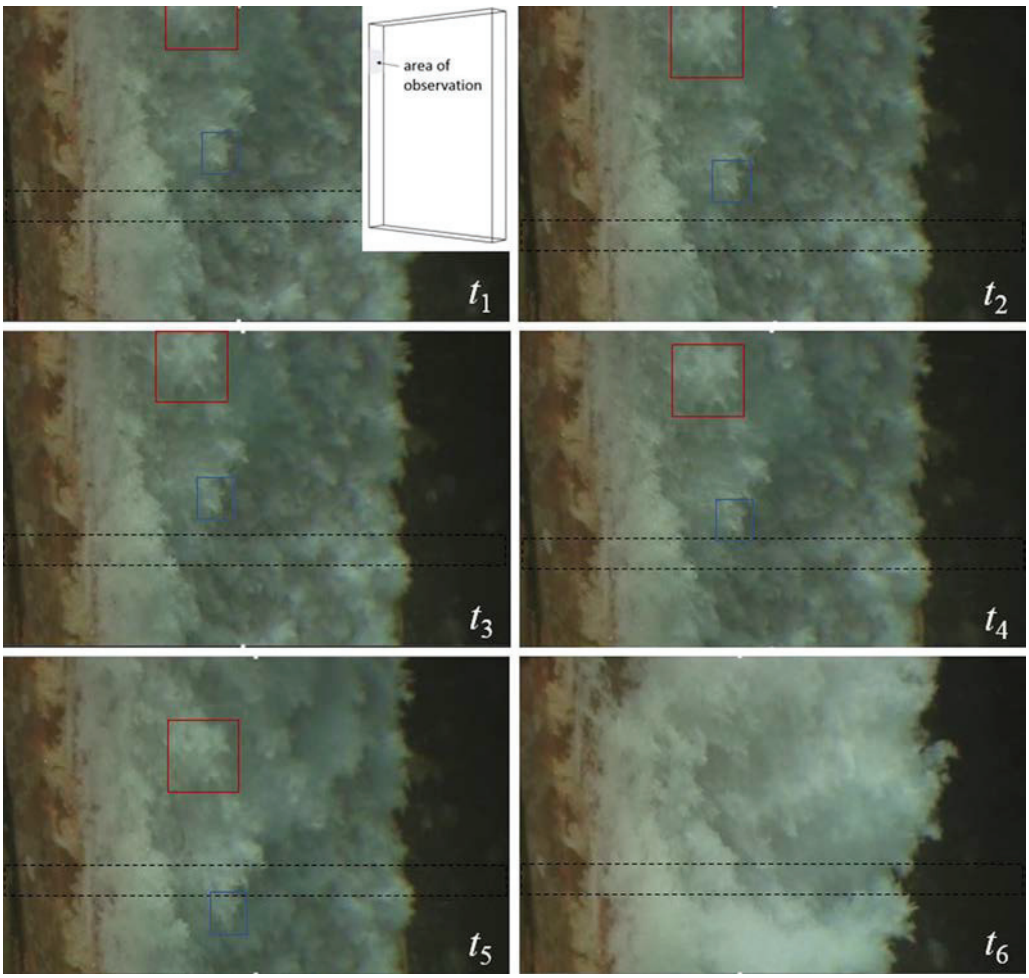

Fig. 2—Sliding of a mushy zone segment. Pictures are taken at constant time interval of $\Delta t = 0.9$ s. For improved visibility, two segments have been marked so that the motion can be followed. Note that the sliding started extremely slowly, so that pictures t_1 to t_3 look quite similar.

larger containment allows a relatively free development of solutal buoyancy flow—especially for the segregated interdendritic melt rising along the lateral walls. It is believed that this interdendritic flow results in an increase of the local microsegregation level in the upper part of the containment. Hence, there is melting of dendrite stems within the mushy zone and the overall mechanical stability diminishes. Obviously, the acting gravitational force due to the larger solid density compared to the liquid density exceeds the drag force from the upward flowing liquid, and so the whole mushy zone segment breaks and slips off.

A flow perpendicular to a horizontally solidifying dendritic mush would in principle not change the interdendritic microsegregation profiles. However, if the rising flow along the lateral walls has a horizontal component (as near the surface of the liquid where the global vortex turns away from the wall), slightly higher segregated melts is moving into areas of lower segregated melts. Due to the fact that for alloys, the thermal Prandtl number is much smaller than the solutal Prandtl number, the local temperature can be assumed to be approximately unaffected by the flow and thus solutal melting occurs.

It is also worth mentioning that the fact that the avalanche activity from time to time diminished reveals a certain unsteadiness of the flow. As reported in References 8 and 15 the overall flow pattern in such a solidification situation is generally turbulent even without avalanches. However, a detailed analysis of the corresponding flow pattern including a description of interdendritic melt flow and alteration of local microsegregation that leads to a local remelting is beyond the scope of the present report. However, from the discussion above, we can gather the following conditions for the appearance of such avalanches:

- The solid density must be sufficiently larger than the density of the melt.
- Interdendritic segregation must lead to a rising solutal buoyancy in vertical columnar mushy zone regions which should be stronger than any downwards thermal buoyancy flows.
- Global or even local vortices must deviate the rising solutal buoyancy flow to a horizontal direction.
- A relative broad mushy zone, which typically appear with small temperature gradients, must exist along the vertical wall.

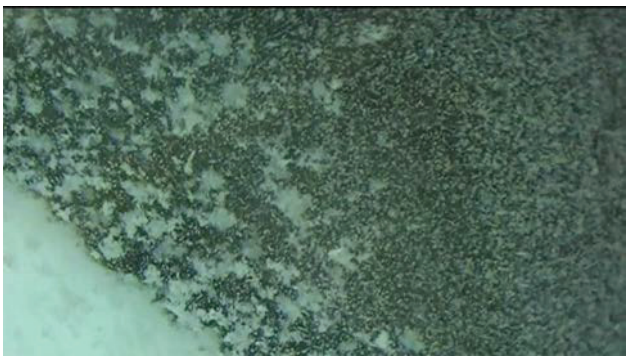

Fig. 3—Massive amount of crystal fragments that has formed only 16 s after a sliding down of a columnar area has started. Note that beside the larger fragments, the smaller fragments resemble the pre-existing equiaxed crystals and can thus not be distinguished.

- The solidifying volume must be sufficiently large.

How relevant the described observation of crystal avalanches really is, cannot be answered easily. Especially during solidification of large steel ingots, the appearing microstructure is partly explained by the so-called ''grain rain'' phenomenon.[2] Hereby, the grains are though to originate by hot-topping compound particle, nonmetallic inclusions, or dendrite fragmentations in such an amount that they form the well-known sedimentary cone at the bottom of the ingot. Furthermore, Kohn[16] reported about an autoradiographic study of solidification on axial sections of killed steel ingots weighing from 1 to 30 tons. He stated on the formation of V-segregation: ''It can be assumed that periodically the mound collapses and the crystals roll down to the bottom of the funnel, thus forming the alternating structure described above.'' Although in our experiment, the recurring V-shaped sedimentation traces extend over the whole width of the mold, it is conceivable that avalanches of mushy zone segments are also contributing to the occurrence of V-segregation in center regions of big steel ingots.

Finally, we would like to notice that although much progress had been made in modeling of ingot solidification[2,17] (nowadays the motion and growth of equiaxed crystals in the presence of columnar solidifying dendrites can even be modeled together with the formation of shrinkage cavities[18–22]), the presented phenomena is still far too complex for recent simulation models.

V. CONCLUSIONS

Parts sliding down from the vertically growing columnar mushy zone—especially from the upper part of the containment—lead to avalanches of dendritic fragments appearing. These fragments further behave similarly to equiaxed crystals. We thus think that the observed phenomena, especially as it happened repeatedly, may significantly contribute to the formation of the inner equiaxed zone in castings. We have discussed solutal melting of columnar dendrite stems, initiated by solutal buoyancy flow, as the likely origin of these sliding down of columnar arrays. Therefore, we expect such avalanches to appear for certain steels, Cu-Al, Pb-Sn, or Ni-Al-alloys, where it is known that rising interdendritic solute buoyancy flow exists. Especially, with the so-called 'hot topping,' often applied during ingot casting, relatively large columnar segments in the upper part of the casting may slide downward as the low temperature gradient results in relatively long columnar dendrites and obviously inward-turning vortices exit there. It is also possible that the described phenomenon contributed to the formation of V-segregation in big steel ingots. The present report is a good example showing that solutal melting is quite important for the dynamic of solidification processes.

ACKNOWLEDGMENT

Open access funding provided by Montanuniversität Leoben. We kindly acknowledge the FWF (Austrian Science Fund, Grant Number P17619-N02 and P22614-N22) which paid the Ph.D. scholarship for Mrs. Stefan-Kharicha.

OPEN ACCESS

REFERENCES

1. W. Kurz and D.J. Fisher: *Fundamental of Solidification*, 4th ed., Trans Tech Publications, Aedermansdorf, 1998.
2. W. Wołczyński: in *The Encyclopedia of Iron, Steel, and Their Alloys*, Taylor & Francis Group, New York, 2016, pp. 1910–24.
3. Ch.-A. Gandin and M. Rappaz: *Acta Metall.*, 1994, vol. 42, pp. 1133–46.
4. P. Thevoz, J.L. Desbiolles, and M. Rappaz: *Metall. Trans. A*, 1989, vol. 20, pp. 311–22.
5. T. Campanella, C. Charbon, and M. Rappaz: *Metall. Mater. Trans. A*, 2004, vol. 35A, pp. 3201–10.
6. R.H. Mathiesen, L. Arnberg, P. Bleuet, and A. Somogyi: *Metall. Mater. Trans. A*, 2006, vol. 37A, pp. 15–20.
7. A. Kumar and R. Dutta: *J. Phys. D*, 2008, vol. 41, pp. 155501–10.
8. A. Kharicha, M. Stefan-Kharicha, A. Ludwig, and M. Wu: *Metall. Mater. Trans. A*, 2013, vol. 44A, pp. 631–60.
9. T. Nishimura, T. Imoto, and H. Miyashita: *Int. J. Heat Mass Transf.*, 1994, vol. 37, pp. 1455–64.
10. C. Beckermann and R. Viskanta: *Int. J. Heat Mass Transf.*, 1988, vol. 31, pp. 2077–89.
11. C. Beckermann and R. Viskanta: *Chem. Eng. Commun.*, 1989, vol. 85, pp. 135–56.
12. D.G. Neilson and F.P. Incropera: *Int. J. Heat Mass Transf.*, 1991, vol. 34, pp. 1717–32.
13. D.G. Neilson and F.P. Incropera: *Int. J. Heat Mass Transf.*, 1993, vol. 36, pp. 489–505.

14. A. Kharicha, M. Stefan-Kharicha, M. Wu, and A. Ludwig: *IOP Conf. Ser. Mater. Sci. Eng.*, 2012, vol. 33, p. 12115.
15. M. Stefan-Kharicha, A. Kharicha, M. Wu, and A. Ludwig: *Fluid Dyn. Res.*, 2014, vol. 46, p. 41424.
16. A. Kohn: in *Int. Conf. Solidif. Cast. 1. London Inst. Met.*, 1977, pp. 356–62.
17. A. Ludwig, M. Wu, and A. Kharicha: *JOM*, 2016, vol. 68, pp. 2191–97.
18. M. Wu and A. Ludwig: *Acta Mater.*, 2009, vol. 57, pp. 5621–31.
19. M. Wu and A. Ludwig: *Acta Mater.*, 2009, vol. 57, pp. 5632–44.
20. M. Wu, A. Fjeld, and A. Ludwig: *Comput. Mater. Sci.*, 2010, vol. 50, pp. 32–42.
21. M. Wu, A. Ludwig, and A. Fjeld: *Comput. Mater. Sci.*, 2010, vol. 50, pp. 43–58.
22. M. Ahmadein, M. Wu, J.H.H. Li, P. Schumacher, and A. Ludwig: *Metall. Mater. Trans. A*, 2013, vol. 44A, pp. 2895–2903.

Journal of chemical & engineering data

Review

Cite This: J. Chem. Eng. Data 2018, 63, 3170−3183

pubs.acs.org/jced

Review of Ammonium Chloride−Water Solution Properties

Mihaela Stefan-Kharicha, Abdellah Kharicha,* Johann Mogeritsch, Menghuai Wu, and Andreas Ludwig

Chair for Simulation and Modelling of Metallurgical Processes, Department of Metallurgy, Montanuniversitaet Leoben, Franz-Josef-Straße 18, 8700 Leoben, Austria

ABSTRACT: Ammonium chloride is commonly used as a buffer solution to control pH levels in a wide variety of chemical and medical applications and is also used as a fertilizer because it acts as a sufficient source of nitrogen for the soil. More recently it is used to create an experimental benchmark, useful to model/simulate metal solidification. In electronics and metallurgy it is also used for cleaning, to prevent the formation of oxides during welding or smelting of metals. In the literature different values are available for the thermo-physical parameters and in the current paper an overview of measured or calculated values of the most important properties is presented. For an ammonium chloride−water solution different phase diagrams are accessible, and the calculation of the liquidus and solidus line is completed. A comparison of calculated heat capacity values for ammonium chloride is made with the literature values. Measured data for the ammonium chloride density are available in the literature, and the values for different temperatures and concentrations are presented here. Thermal conductivity values are gathered in the present work. The viscosity can be estimated in between 283 and 333 K and for mass fraction up to 0.324 kg·kg^{-1}, with a model for the calculation of the aqueous solutions viscosity, based on the viscosity of solute and water. The variation curve of diffusivity values with the concentration, exists only for 293 and 298 K. For this reason an approximation with NH_3 diffusivity values, which are measured for different temperatures and concentrations, can be recommended. Additional analysis of two experimental measurements, performed in order to estimate the ammonium chloride diffusivity in water and further extract the Gibbs−Thomson coefficient, is done.

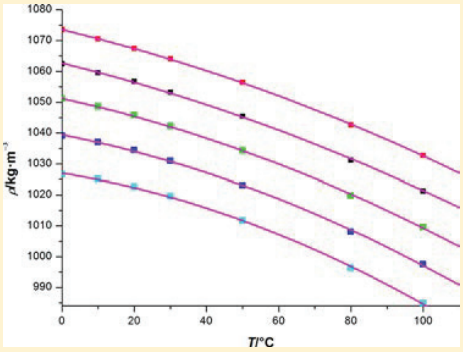

1. INTRODUCTION

Good knowledge of physical properties of a substance is very important to understand its behavior during phase change. In the course of metal's solidification it is not possible to see either the solid structure or the liquid melt behavior because metals are opaque. Ammonium chloride was used extensively in modeling metal solidification because it solidifies like metals, and the liquid melt has the advantage of being transparent.[1−3] Its melting temperature range is considerably lower that metal's melting temperature, making the operating conditions much easier for experimental studies in the laboratory. Other metal analogue alloys were used in modeling solidification, such as SCN (succinonitrile),[4−11] NPG-TRIS,[12−16] or NaCl.[17,18]

Besides experimental work, numerical simulation became an important tool to understand solidification. The two domains developed in parallel in order to obtain a better understanding of the solidification process. Moreover experimental studies on ammonium chloride solidification were used to validate such numerical models. For accurate numerical simulations it is crucial to have precise physical data.

Solidification is a temperature-dependent process and the main parameters in this field such as diffusivity, viscosity, and density are concentration and temperature related. A nonexhaustive list of values found in literature for these physical parameters, concerning the ammonium chloride, will be given in this paper.

Recently a series of experiments were performed on the solidification of a hypereutectic ammonium chloride alloy[19−23] in a cast cell cooled homogeneously from the three walls. Heterogeneous solidification occurred simultaneously along verticals and horizontal walls where a columnar mushy zone developed. The occurrence of equiaxed crystals was sometimes observed, and a mechanism was proposed to explain the equiaxed crystal's origin and growth in an undercooled melt for which convection is important.[23] With the PIV (particle image velocimetry) technique the investigation of the flow was possible in the same time as the NH_4Cl columnar/equiaxed growth. Such experimental work constitutes a valuable benchmark for validating numerical models.

One of the phenomena occurring during solidification is the double-diffusive convection due to thermal and solutal buoyancy forces. To estimate the thermos-solutal buoyancy, parameters such as density, thermal and solutal expansion coefficient, and viscosity are very important to know precisely. Experimental studies on the double-diffusive convection during ammonium chloride solidification were performed by Ghenai et al.,[24] Nishimura and Imoto,[25] McCay et al.,[26] and Skudarnov et al.[27]

Received: December 11, 2017
Accepted: May 29, 2018
Published: June 6, 2018

DOI: 10.1021/acs.jced.7b01062
J. Chem. Eng. Data 2018, 63, 3170−3183

The influence of the initial ammonium chloride alloy concentration on the solidification was considered in many studies. Skudarnov et al.[27] considered concentrations from hypo- to hypereutectic and qualitatively quantified the influence on the convection pattern. Once more density, thermal/solutal expansion coefficients, viscosity, and liquid diffusivity are playing an important role. The variation of these parameters with both temperature and concentration is at the origin of the double-diffusive convection, and thus their temperature evolution needs to be well-known.

Steady state ammonium chloride solidification with mushy zone development was considered by Pepin et al.[28] in a Hele-Shaw cell. Measurement of undercooling and height of the mushy region was performed, and a relation with the velocity growth was extracted. Morphological transitions were observed and a diagram considering initial solution concentration and pulling velocity in the occurrence of different growth regimes was described. Convection in the mushy layer seems to be at the origin of chimneys, and a key parameter to evaluate the convection force is the Rayleigh number. For the calculation of the Rayleigh number the density and viscosity are some of the data needed.

C. F. Chen[29] performed experiments on the effect of viscosity on ammonium chloride direct solidification in a Hele-Shaw cell. Viscosity is another parameter playing an important role in solidification. The melt viscosity changes with temperature and concentration, its influence should be taken into account in the Rayleigh number calculation, which represents a significant parameter in the evaluation of the melt flow.

C. Beckermann and colleagues[30−34] realized a significant work in both experimental and numerical investigations on ammonium chloride solidification. For numerical simulation having thermos-physical property data at desired temperatures and concentrations is required. Approximation or interpolation by linear or polynomial functions is in some cases necessary. Experimental and numerical insight on the solidification of ammonium chloride was also given by Kumar et al.[35]

Beside physical parameters, the phase diagram is fundamental for understanding liquid−solid phase transformation. The phase diagram is characterized by the liquidus and solidus lines and the eutectic point in the case of an alloy (two components melt). The liquidus and solidus lines provide us information about the concentration corresponding to a given temperature at the equilibrium. The liquidus lines are usually approximated with a line but they are actually curved. The slope which can be extracted from the phase diagram is very useful in calculation of liquid concentration at the solid liquid interface or far in the bulk melt. But if the liquidus line is very curved the effect on the slope is dramatic. In this case the liquidus slope is not constant anymore; it is changing with the temperature.

The eutectic point, defined by the C_{eut} and T_{eut}, represents the fact that the three phases (liquid and two solid components for a binary alloy) are in thermodynamical equilibrium. When a eutectic alloy will solidify, eutectic growth will occur, which means that the two phases will grow simultaneously. The near eutectic compositions present good casting properties for alloys, almost as pure metals and also excellent final product qualities. For this reason a lot of casting alloys are solidified around eutectic concentration; thus having a well-defined eutectic point is valuable.

Some of the above numerated parameters and examples of ammonium chloride phase diagram will be presented in this paper.

2. PHASE DIAGRAM, LIQUIDUS/SOLIDUS LINE, EUTECTIC POINT

In literature two phase diagrams for ammonium chloride are available. One phase diagram (Figure 1) presents only a part of

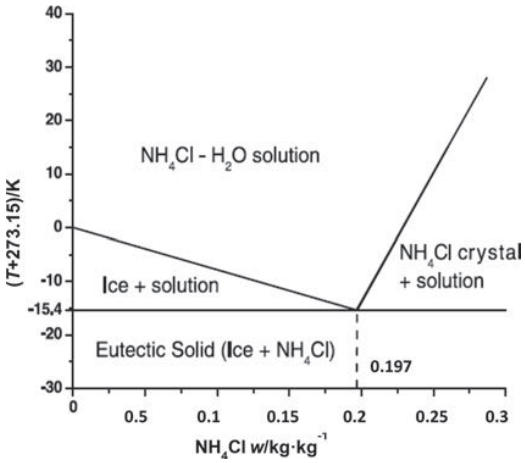

Figure 1. Ammonium chloride phase diagram. Figure reprinted with permission from ref 27. Copyright 2002 Elsevier.

the alloy concentration, where just the liquidus line is shown; the solidus line is supposed to be a vertical line at 100% ammonium chloride.[27,36] All through the paper the solvent for ammonium chloride solution is water. From the liquidus line we can calculate the liquidus line slope m_l and use eq 1 to calculate the liquidus temperature for any given concentration. The liquidus slope m_l calculated from the phase diagram in Figure 1 is 534 (K·kg·kg^{-1}).

$$T_l = m_l \cdot (C_l - C_{eut}) + T_{eut} \quad (1)$$

The second phase diagram found in the literature is complete (Figure 2) showing a liquidus line and a solidus line.[37,38]

It can be noticed that the liquidus line slope is steeper in the second (Figure 2) than that in the first phase diagram (Figure1). The liquidus slope calculated from the phase diagram in Figure 2 is 476.19 (K·kg·kg^{-1}). With eq 1 and

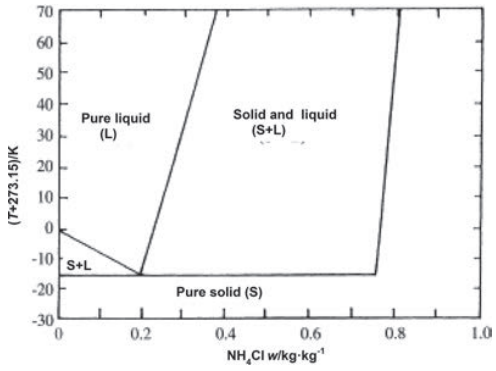

Figure 2. Ammonium chloride complete phase diagram. Figure adapted from refs 37 and 38. Copyright 1998 and 1989 Elsevier.

DOI: 10.1021/acs.jced.7b01062
J. Chem. Eng. Data 2018, 63, 3170−3183

Table 1. Different Values for Some Physical Parameters (Eutectic Concentration C_{eut}, Eutectic Temperature T_{eut}, Liquidus Line m_l, Diffusivity D, Gibbs-Thomsom Coefficient Γ) Used in Literature

authors	T_{eut} (K)	C_{eut} (kg·kg^{-1})	m_l (K·kg·kg^{-1})	D (m^2·s^{-1})	Γ (K·m)
Beckermann and Wang,[31] Kumar et al.[35]	259.2	0.197	461	4.8×10^{-9}	5×10^{-8}
Ramani and Beckermann[30]			480	2×10^{-9}	0.5 to 4×10^{-8}
Pepin et al.[28]	257.25	0.197	490		
Rady and Nada[37]	257.75	0.197		4.8×10^{-9}	
Appolaire et al.[40]			480	2.3×10^{-9}	3.54×10^{-7}
Tanaka and Sano[41]				2.6×10^{-9}	5.09×10^{-7}
Liu et al.[42]				5×10^{-10}	6.6×10^{-8}
FactSage[39] software	266.361	0.157			

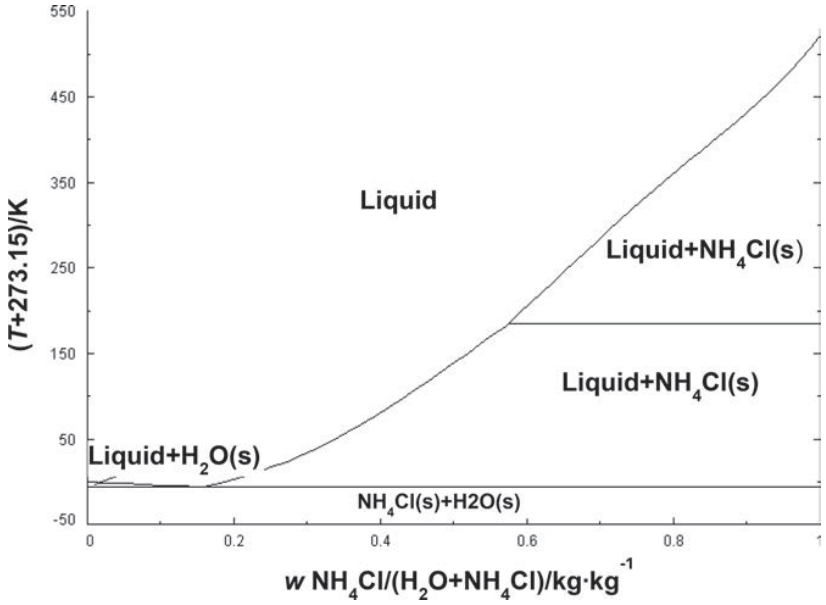

Figure 3. Ammonium chloride phase diagram calculated with the FactSage[39] software.

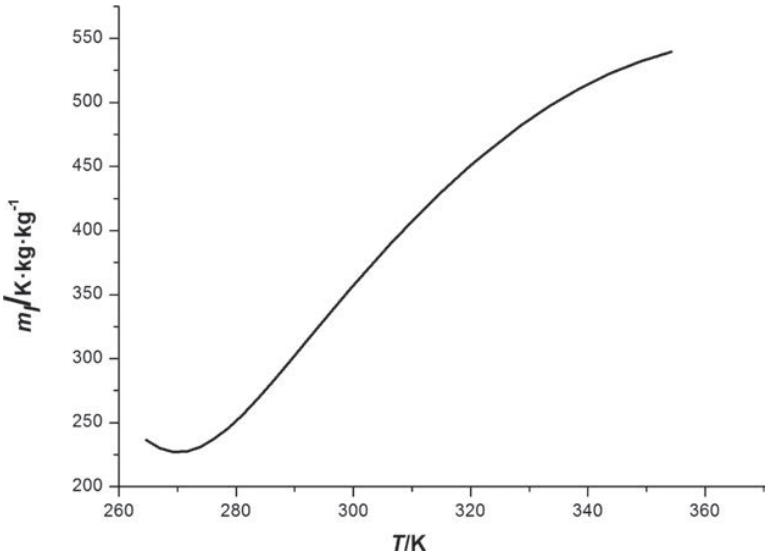

Figure 4. Evolution of the ammonium chloride liquidus slope.

using m_l, T_l can be calculated again. For mass fraction 0.3 NH_4Cl, the liquidus temperature T_l can be 312 K, if m_l is extracted from first phase diagram, or 303 K, if the second phase diagram is used. These 9 K represent a large difference and can change much in the simulation of the solidification process.

In Table 1 some values for m_l, used in the literature are gathered. The minimum value found is 461 (K·kg·kg^{-1})

DOI: 10.1021/acs.jced.7b01062
J. Chem. Eng. Data 2018, 63, 3170−3183

Table 2. Experimental Values of the Ammonium Chloride Density ρ, Measured at Different Mass Fractions and Temperatures[43]

w/kg·kg^{-1}	273.15 K	283.15 K	293.15 K	303.15 K	323.15 K	353.15 K	373.15 K
0.01	1003.3	1002.9	1001.3	998.7	991.0	974.9	961.7
0.02	1006.7	1006.2	1004.5	1001.8	994.0	978.0	965.1
0.04	1013.5	1012.6	1010.7	1007.7	999.9	984.2	971.8
0.08	1026.6	1025.1	1022.7	1019.5	1011.6	996.3	984.9
0.12	1039.1	1037.0	1034.4	1031.0	1023.1	1008.1	997.5
0.16	1051.0	1048.5	1045.7	1042.2	1034.3	1019.8	1009.6
0.20	1062.5	1059.6	1056.7	1053.2	1045.4	1031.2	1021.3
0.24	1073.6	1070.5	1067.4	1064.1	1056.4	1042.6	1032.7

(Beckermann and Wang[31] in their paper from 1996) and the maximum value is 490 (K·kg·kg^{-1}) (Worster et al.[28]).

For further comparison concerning T_l and m_l we used FactSage,[39] a software designed for thermodynamic calculations. The phase diagram calculated with FactSage[39] is presented in Figure 3. The T_l calculated with FactSage[39] for a mass fraction of 0.3 NH_4Cl is 306.58 K. Anyway the solidification temperature observed during our experimental studies is lower and respectively 300.95 K for this alloy concentration (w = 0.3 kg·kg^{-1}).

It is very important to note that the "liquidus line" is not a straight line in the phase diagram given by FactSage.[39] This can explain the existence in the literature of different liquidus slopes, as for a different temperature a different liquidus slope will be obtained. The eutectic temperature and concentration are 266.361 K and 0.157 NH_4Cl/H_2O + NH_4Cl (kg·kg^{-1}). The liquidus line between the eutectic point and 0.40 NH_4Cl/H_2O + NH_4Cl (kg·kg^{-1}) was approximated by the polynomial function shown in eq 2:

$$T_l = -79.15 + 915.47C - 4593.379C^2 + 12444.29C^3 - 10448.116C^4 \quad (2)$$

where C is the mass fraction NH_4Cl/H_2O + NH_4Cl (kg·kg^{-1}) (C = 1 for 100% NH_4Cl).

Using the derivative of eq 2 we can calculate the slope of the liquidus line, and its evolution versus the temperature is plotted in Figure 4.

From Figure 4 it can be noticed that the slope is strongly changing with temperature, from a value of 230 (K·kg·kg^{-1}) to a value of 530 (K·kg·kg^{-1}).

The phase diagram shown in Figure 1 supposes that the solidus line is a vertical line at 1 mass fraction NH_4Cl, which gives C_s = 1. The second phase diagram presented in Figure 2 gives a solidus line which is almost a vertical line at approximately 0.8 mass fraction NH_4Cl, which means that the solid formed does not contain 100% NH_4Cl but a mixture of water and ammonium chloride of a concentration C_s defined by the solidus line m_s. The solidus line slope is m_s = 1386.38 (K· kg·kg^{-1}). In literature papers most of the numerical simulations consider C_s (solid concentration) to be equal to 1, except Rady and Nada[37] and Christerson and Incropera.[38] The FactSage[39] software calculations give also C_s = 1.

Other important information that we can extract from the phase diagram are the temperature and the concentration of the eutectic point. For the C_{eut} and T_{eut}, the values found in literature are C_{eut} = 0.197 kg·kg^{-1} and T_{eut} = 257.75 K, but other values can be found too (see Table 1).

3. DENSITY

The ammonium chloride density was measured for different temperatures and concentrations. The density is not a constant; it varies with temperature and concentration. The experimental values found in the literature[43] are presented in Table 2.

The plot of the density versus concentration, at different temperatures, is shown in Figure 5.

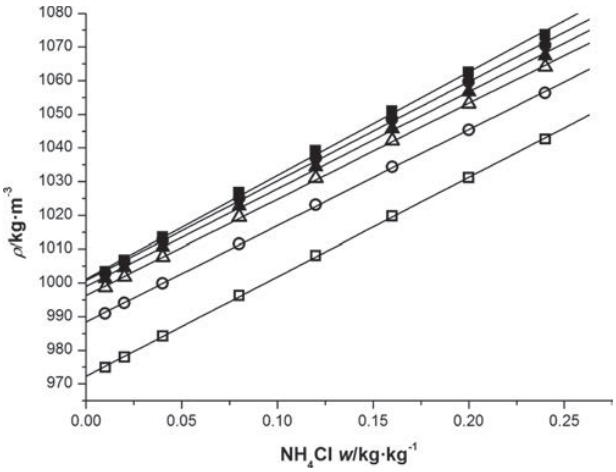

Figure 5. Evolution of the ammonium chloride density vs concentration, measured at different temperatures[43] (■) 273.15 K, (●) 283.15 K, (▲) 293.15 K, (△) 303.15 K, (○) 323.15 K, (□) 353.15 K). The lines represent the linear fit to the experimental data.

For each temperature the density varies linearly with the concentration. Thus, each set of data (dots of same shape) corresponding to a certain temperature, were fitted with a linear equation (strait line).

$$\rho = \rho_T + \beta_C(T)\cdot\rho_{ref}\cdot C \quad (3)$$

where ρ_T and β_C (solutal expansion coefficient) are depending on the temperature. The reference density ρ_{ref} is taken constant and equal to 1000 (kg·m^{-3}). From the linear eq 3 we extracted the values of ρ_T and β_C. Their evolution with the temperature is reported in Figure 6, and values are given in Table 3.

To fit the extracted values for $\rho_T(T)$ and respectively $\beta_C(T)$ the following polynomial functions presented in eq 4 and correspondingly eq 5 were employed:

DOI: 10.1021/acs.jced.7b01062
J. Chem. Eng. Data 2018, 63, 3170−3183

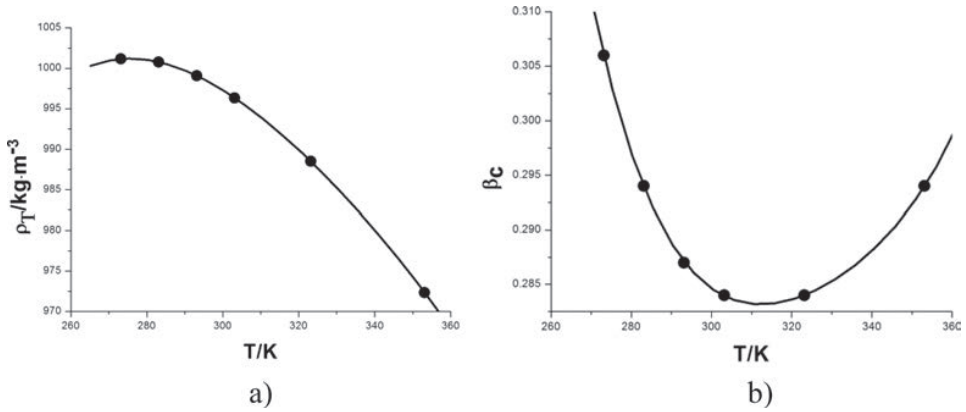

Figure 6. (a) ρ_T and (b) solutal expansion coefficient β_C values (dots), extracted from the linear fit of density with concentration, at different temperatures and their fitted polynomial functions (line).

Table 3. ρ_T and Solutal Expansion Coefficient β_C Values Extracted from the Linear Fit of Density with Concentration, at Different Temperatures

temp	ρ_T (T)	β_C (T)
273.15 K	1001.16	0.306
283.15 K	1000.76	0.294
293.15 K	999.095	0.287
303.15 K	996.315	0.284
323.15 K	988.503	0.284
353.15 K	972.35	0.294

$$\rho_T(T) = 1001.15503 + 0.03854\cdot(T - 273.15) - 0.00824\cdot(T - 273.15)^2 + 6.06948\cdot10^{-5}\cdot(T - 273.15)^3 - 2.48971\cdot10^{-7}\cdot(T - 273.15)^4 \quad (4)$$

$$\beta_C(T) = 0.30602 - 0.0154\cdot(T - 273.15) + 3.63497\cdot10^{-5}\cdot(T - 273.15)^2 - 3.72741\cdot10^{-7}\cdot(T - 273.15)^3 + 1.68757\cdot10^{-9}\cdot(T - 273.15)^4 \quad (5)$$

4. HEAT CAPACITY AND THERMAL CONDUCTIVITY

The ammonium chloride heat capacity c_p was extracted from the FactSage[39] software calculations. In Figure 7 a plot of the NH_4Cl heat capacity for three concentrations at different temperatures is presented. It can be observed that in the solid state only small differences exist for a given concentration versus the temperature (average value $c_{p\ (solid)}$ = 1861 (J·kg^{-1}·K^{-1})). In the liquid state values are more spread. For 0.15 mass fraction NH_4Cl hypoeutectic aqueous solution the heat capacity is almost constant after the eutectic point (T_{eut} = 266.361 K) with an average value of $c_{p\ (liquid)}$ = 3925 (J·kg^{-1}·K^{-1}). For the case of 0.30 mass fraction ammonium chloride (hypereutectic alloy the heat capacity values in the liquid are slowly descending until T = 306.55 K when the phase change (liquid−solid) takes

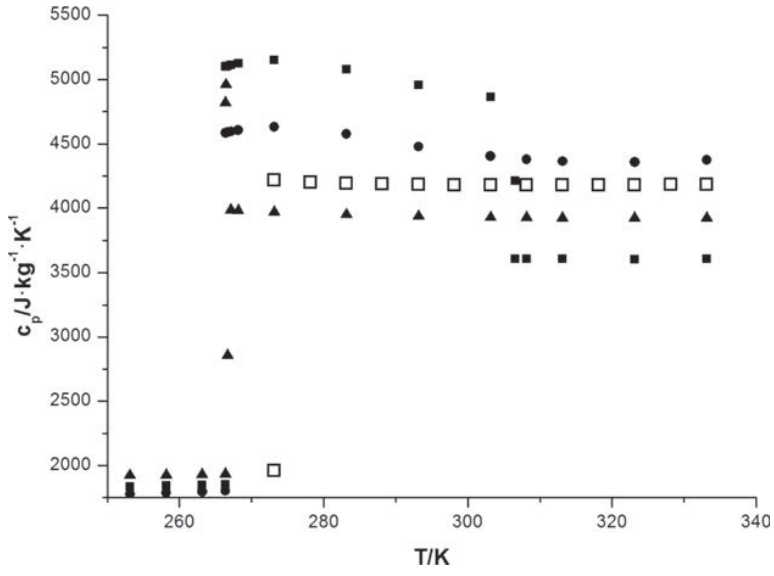

Figure 7. FactSage[39] calculations for ammonium chloride heat capacity at different mass fractions: (▲) 0.15, (■) 0.30, (●) 0.40, and comparison with water heat capacity (□ H_2O).

DOI: 10.1021/acs.jced.7b01062
J. Chem. Eng. Data 2018, 63, 3170−3183

Table 4. Specific Heat Capacity c_p and Thermal Conductivity k_s, k_l Values Gathered from Literature

authors	$c_{p\ (solid)}$ ($J \cdot kg^{1-} \cdot K^{-1}$)	$c_{p\ (liquid)}$ ($J \cdot kg^{1-} \cdot K^{-1}$)	k_s ($W \cdot m^{-1} \cdot K^{-1}$)	k_l ($W \cdot m^{-1} \cdot K^{-1}$)
Zabaras and Samanta[45]	1870	3249	0.393	0.468
Sanyal et al.[46]	1870	3249	0.393	0.468
Beckermann and Wang[31]	1827	3249	2.7	0.468
Pepin et al.[28]	2.28×10^6 ($J \cdot m^{-3} \cdot K^{-1}$)	3.68×10^6 ($J \cdot m^{-3} \cdot K^{-1}$)	2.2	0.54

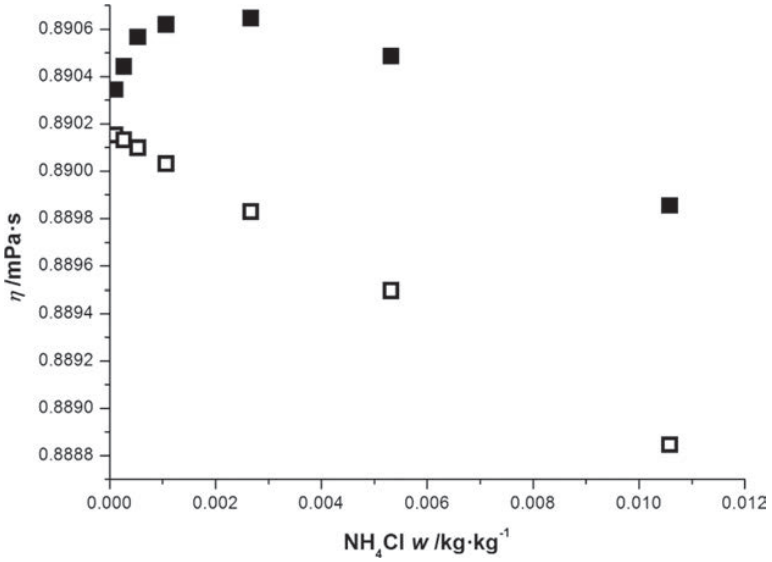

Figure 8. Viscosity measured (■) for diluted ammonium chloride solution[47] and comparison with calculation (□) at 298.15 K.

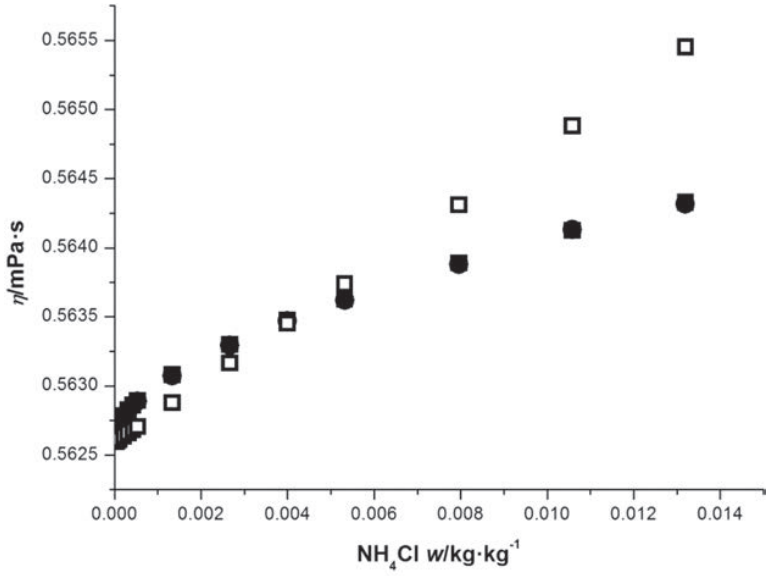

Figure 9. Viscosity−concentration curve for dilute solution of ammonium chloride at 308.15 K: (■) measurement,[48] (●) calculation,[48] (□) calculation[57]).

place with release of latent heat and the heat capacity decreases drastically. After the complete solid change took place, the heat capacity has a constant value ($c_{p\ (solid)}$ = 3600 ($J \cdot kg^{1-} \cdot K^{-1}$)). For 0.4 mass fraction NH_4Cl, the $\mathbf{c}_{p\ (liquid)}$ values descend slowly until complete phase change (liquid−solid) will take place ($\sim T$ = 354.15 K not shown here). Water's heat capacity values are also plotted in Figure 7, and its values are almost constant in between 273.15 K (liquid phase) and 333.15 K (the average value for $c_{p\ (liquid)}$ is 4186 ($J \cdot kg^{-1} \cdot K^{-1}$)).

The National Institute of Standard and Technology (NIST) makes accessible a data plot for the heat capacity of ammonium chloride.[44] In some papers treating the numerical simulation of ammonium chloride, two values for the heat capacity are given, one for solid state 1870 ($J \cdot kg^{-1} \cdot K^{-1}$), and one for liquid state, 3249 ($J \cdot kg^{-1} \cdot K^{-1}$).[45,46] Beckermann and Wang[31] used the same

DOI: 10.1021/acs.jced.7b01062
J. Chem. Eng. Data 2018, 63, 3170−3183

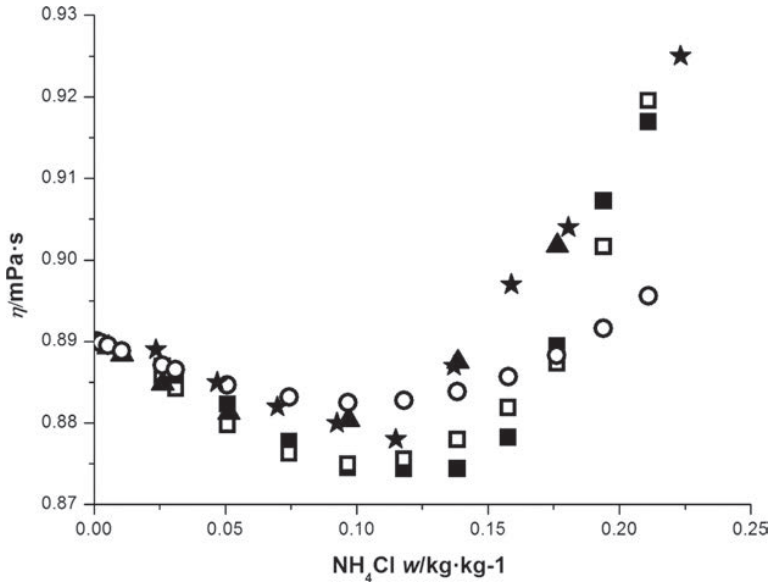

Figure 10. Ammonium chloride viscosity measured: (■) Sahu and Behera,[49] (▲) Monica et al.,[50] (★) Getman.[51] Comparison with calculation: (□) Sahu and Behera,[49] (○) Laliberte [57], at 298.15 K.

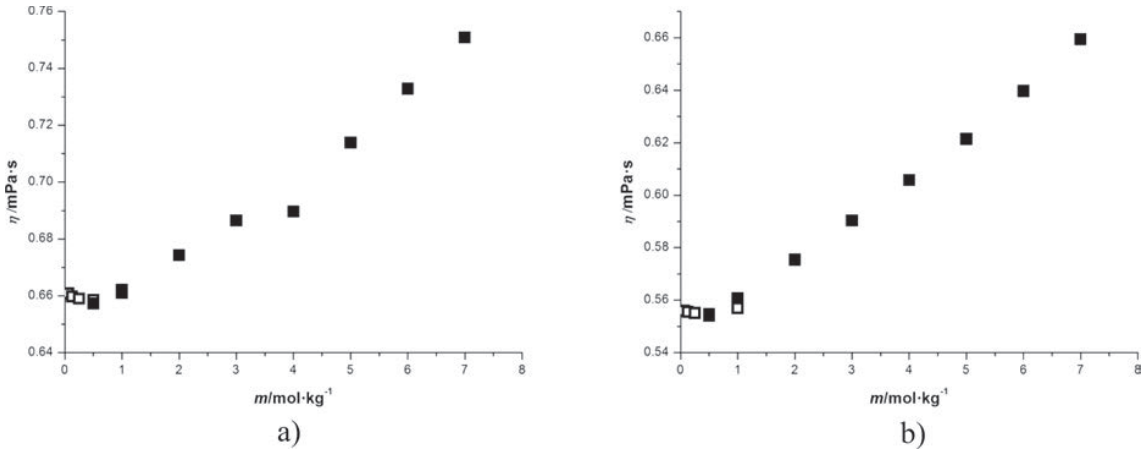

Figure 11. Absolute ammonium chloride viscosity−concentration curves, measurements at: (a) 313.15 K and (b) 323.15 K: (□) Motin,[52] (■) Goldsack and Franchetto.[53]

value for the liquid specific heat 3249 ($J \cdot kg^{-1} \cdot K^{-1}$) but 1827 ($J \cdot kg^{-1} \cdot K^{-1}$) for the solid specific heat. In Table 4 the values found in the literature for the specific heat capacity and the thermal conductivity are gathered.

The effective thermal conductivity was calculated by Pepin et al.[28] and values for the ammonium chloride solution, 0.54 ($W \cdot m^{-1} \cdot K^{-1}$) and pure ammonium chloride solid, 2.22 ($W \cdot m^{-1} \cdot K^{-1}$), are found. Ramani and Beckermann[30] used also two values: one for the thermal conductivity of the liquid phase of 0.468 ($W \cdot m^{-1} \cdot K^{-1}$) and one for the solid phase of 2.7 ($W \cdot m^{-1} \cdot K^{-1}$). Beckermann and Viskanta[32] used a thermal conductivity ratio $k^* = k_s/k_l$ (between the solid and liquid) of 4.68 ($W \cdot m^{-1} \cdot K^{-1}$). Zabaras and Samanta[45] and Sanyal et al.[46] used 0.393 ($W \cdot m^{-1} \cdot K^{-1}$) for solid ammonium chloride thermal conductivity, and 0.468 ($W \cdot m^{-1} \cdot K^{-1}$) for liquid ammonium chloride thermal conductivity.

5. VISCOSITY

Einstein in 1911 derived from the principle of hydrodynamics a linear equation between viscosity of aqueous solution and solute concentration. Finkelstein in 1930 extended this assessment and concluded that viscosity should increase proportionally to the concentration. However, for salts the deviation from linear law becomes evident and even more pronounced at low concentration.

Jones and Talley[47] measured the relative viscosity (the viscosity of solution with respect to the solvent) at 298.15 K for different diluted salts. They used a new method for the automatic measurement of the flow-time in a new Oswald-type quartz viscometer. Their results proved that even salts which decrease the viscosity of water at moderate concentration will increase it at sufficiently low concentration (0.05 $mol \cdot L^{-1}$). The results for the corresponding viscosity values extracted from his measurements for ammonium chloride are shown in Figure 8.

Das[48] in 1954, using two Oswald viscometers, performed measurements of relative viscosity for diluted solution of

DOI: 10.1021/acs.jced.7b01062
J. Chem. Eng. Data 2018, 63, 3170−3183

ammonium chloride at 308.15 K. He compared the experimental results with calculation obtained using Jones and Dole's equation.[48] Figure 9 presents the corresponding viscosity values extracted from his measurements and the computed values.

Comparison between viscosity for concentrated aqueous solutions, extracted from conductance measurements performed at 298.15 K by Sahu and Behera,[49] M della Monica,[50] and Getman[51] and calculations using a modified Einstein limiting equation for aqueous solutions of 1:1 electrolytes[49] is shown in Figure 10.

Absolute viscosity measurements for ammonium chloride solution were performed at different temperatures but only for low concentrations by Motin.[52] Goldsack and Franchetto[53] present measurements of absolute viscosity for a larger scale of concentrations and a large scale of temperatures (283.15 to 333.15 K). Comparison of their results[52,53] at 313.15 and 323.15 K is shown in Figure 11.

Good agreement between the viscosity values measured by Getman[51] in 1908 and Goldsack and Franchetto[53] in 1978 can be seen in Figure 12.

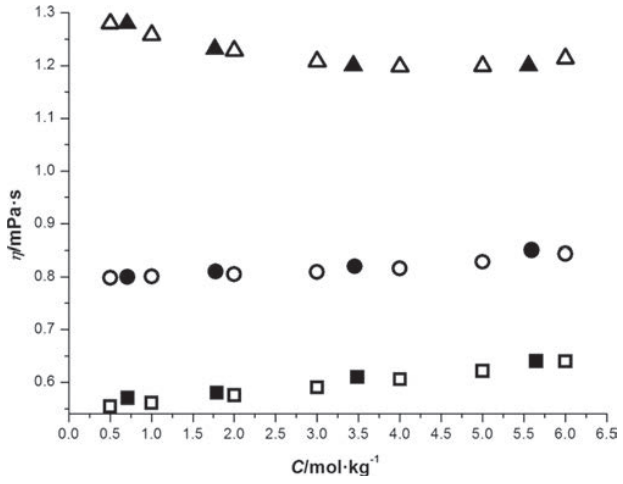

Figure 12. Viscosity−concentration curves, measurements at 283.15 K, 303.15 K, and 323.15 K (plain symbols (▲,●, ■) Getman[51] and empty symbols (△, ○, □) Goldsack and Franchetto[53]).

The variation of the relative viscosity of supersaturated solutions of ammonium chloride with temperature was measured by Chatterji and Gopal,[54] and their results are shown in Figure 13.

The viscosity of the ammonium chloride solution[55,56] versus the concentration was measured at 393.15 K and the results are presented in Figure 14.

An analysis of all the data presented from Figure 8 to Figure 14 shows that the ammonium chloride viscosity varies with the temperature and with the concentration. Moreover it can be observed that the evolution with the concentration presents a minimum (except for diluted solutions).

Moreover a model for calculating the viscosity of aqueous solution was developed by M. Laliberte.[57] For ammonium chloride the model is based on several experimental data, some were presented before (Figure 8 to Figure 14), and is valid for solute concentration up to 0.324 mass fraction and temperatures in between 383.15 and 346.15 K.

Figure 15a displays the evolution of calculated ammonium chloride viscosity[57] for different temperatures versus the concentration. Equation 6 presents the formula used to describe the NH_4Cl viscosity:[57]

$$\eta_m = \eta_i^{w_i} \cdot \eta_w^{w_w} \tag{6}$$

where η_m is the ammonium chloride solution viscosity, η_i is the solute viscosity, η_w is the water viscosity, and w_i and w_w are solute and water mass fraction, respectively.

The viscosity of the solute and water are expressed as follows:

$$\eta_i = \exp\left(\frac{\nu_1(1 - w_i)^{\nu_2} + \nu_3}{(\nu_4 T(°C) + 1)(\nu_5(1 - w_w)^{\nu_6} + 1)}\right) \tag{7}$$

$$\eta_w = \frac{T(°C) + 246}{(0.05594T(°C) + 5.2842)T(°C) + 137.37} \tag{8}$$

The factors ν_1 to ν_6 are given in Table 5.

The values measured at 283.15, 303.15, and 323.15 K, by Goldsack and Franchetto[53] are presented in Figure 15b, and good agreement is found with the values calculated by Laliberte.[57] In Figure 15c the values measured at 313.15 and 323.15 K, by Motin[52] are compared with Laliberte's calculation[57] and for concentrations up to 0.02 mass fraction (diluted solution) some deviation is observed, but for more concentrated solution good agreement can be seen.

Figures 10 and 14 show also good agreement between measured and calculated[57] values at 298.15 and 293.15 K. However, for a diluted solution, deviation from experimental data can be observed (Figures 8 and 9).

6. DIFFUSIVITY

6.1. Available Experimental Data. Other physical data very important in solidification are the diffusion coefficient D and the Gibbs−Thomson coefficient Γ. The range for these data values used in numerical simulations is large, between 10^{-9} and 10^{-10} for the diffusion coefficient and between 10^{-7} and 10^{-9} (2 orders of magnitude) for the Gibbs−Thomson coefficient (Table 1). As a first approximation, because for ammonium chloride there is not sufficient experimental data available, it is possible to assume that the ammonium chloride diffusivity is close to the NH_3 diffusivity. The advantage is that NH_3 diffusivity in water was measured[58] for a large range of temperatures and concentrations (Figure 16). It can be observed that the diffusivity is concentration and temperature dependent, and the dependence is not linear. The Arrhenius relation, shown in eq 9 was employed to model the temperature variation of the diffusion coefficients, and it is the best correlation seen.

$$D = AT e^{-E_a/K_B T} \tag{9}$$

where T is the absolute temperature (in Kelvins), A is a constant pre-exponential factor, K_B is the Bolzmann constant, and E_a is the activation energy (in Joules molecule^{-1}).

For ammonium chloride, measurements of differential diffusivity have been done only at 293.15 and 298.15 K. Two ammonium chloride solutions of different concentrations very nearly equal, were put in contact, and the diffusivity measured is equal to the differential diffusivity at the mean concentration.[59,60] Figure 17 presents these experimental results, and respectively the calculated integral diffusivity,[59] which cover the

DOI: 10.1021/acs.jced.7b01062
J. Chem. Eng. Data 2018, 63, 3170−3183

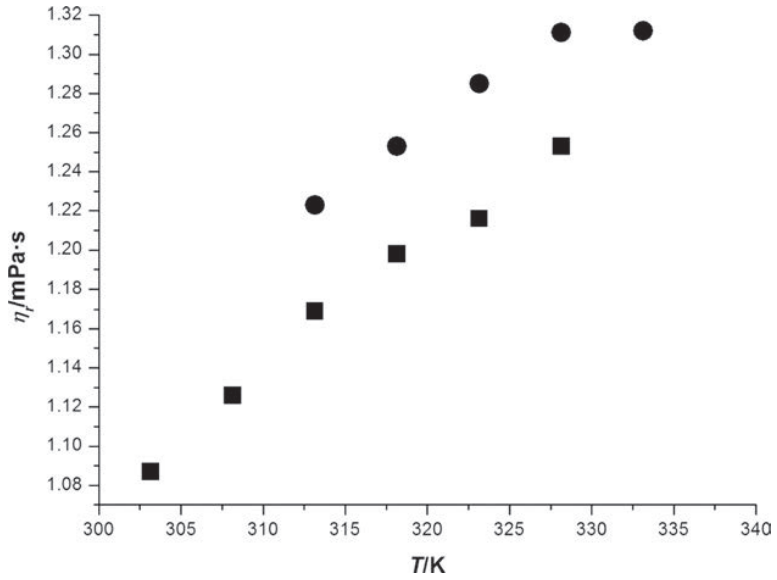

Figure 13. Relative viscosity versus temperature for supersaturated solution of ammonium chloride: (■) 0.295 mass fraction NH_4Cl, (●) 0.324 mass fraction NH_4Cl.[54]

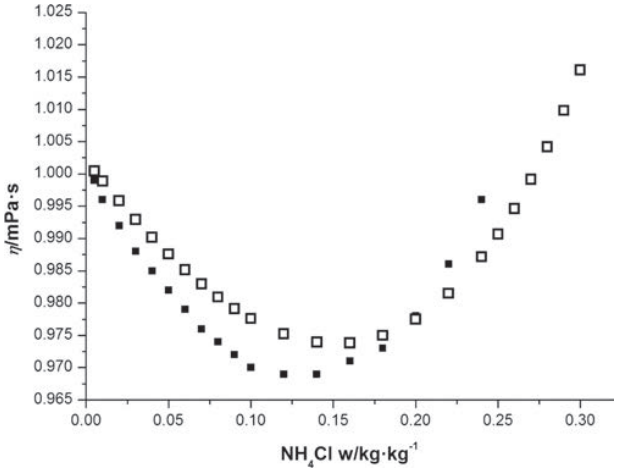

Figure 14. Ammonium chloride viscosity versus concentration measured (■, Wolf,[55] Söhnel and Novotny[56]) and calculated (□, Laliberte[57]) at 293.15 K.

range of concentration from equilibrium until the bulk solution and are the relevant diffusivity in the case of solidification.

6.2. Calculation of Diffusivity with Einstein–Stock Relation. The ammonium chloride dissociates in water and forms an ion of NH_4^+ and an ion of Cl^-. The size of the ion is very important and also the hydration of the ion (how many water molecules are around). The size of the single NH_4^+ ion is similar to that of the single Cl^- ion (Table 6).

The Stokes–Einstein formula to calculate the mass diffusivity of a molecule in aqueous solution is given in eq 10.

$$D = \frac{K_B T}{6\pi\eta r} \tag{10}$$

where K_B is the Bolzmann constant, η is the water dynamic viscosity, and r is the ion radius.

Using this relation we can calculate the diffusivity of ammonia NH_4^+ and chlorine Cl^-, in water. A comparison of theoretical values obtained using eq 10 (for NH_4^+ and Cl^-) and NH_3 experimental values, can be done, and the results are presented in Table 6. The measured diffusion coefficient[61] for a Cl^- ion in water varies from 1.38×10^{-9} ($m^2 \cdot s^{-1}$) at 298.15 K to 3.11×10^{-9} ($m^2 \cdot s^{-1}$) at 333.15 K, being values that are very close to the corresponding calculated values with the relation given in eq 10 (Table 6). It should be kept in mind that the Stokes–Einstein equation overpredicts the diffusivity as it considers only one ion unhydrated, but in reality all ions are hydrated (up to four molecules of water can exist around an ammonia ion). Moreover the diffusion coefficient calculated at 298.15 and 333.15 K for one ion of ammonia is proximate to the measured[58] diffusion coefficient of 0 mol NH_3 at these temperatures.

The measured diffusion coefficient D_{Cl-} presents the lowest values for all three temperatures 293.15, 298.15, and 333.15 K, and the diffusion coefficient D_{NH_3} values are the highest measured at 293.15 and 298.15 K, but at 333.15 K these values are lower than the diffusion coefficient $D_{NH_4^+}$. The diffusion coefficients $D_{NH_4^+}$ at 293.15 and 298.15 K are situated in between the D_{Cl-} and D_{NH_3} values. The existent measurement values are not easily compared because we do not dispose of values for different concentrations and different temperatures, for each ion (Cl^-, NH_4^+). However, we believe that the NH_3 diffusivity, th values of which are better known, can be used as a good approximation for the NH_4Cl diffusivity, when other measurements or calculations are not available.

6.3. Estimation of the Diffusivity and the Gibbs–Thomson Coefficient from the Experiments of Melt[40]/Solidification.[62] In this section two experiments of measurement of the capillary length of the ammonium chloride, used to extract the diffusivity and the Gibbs–Thomson coefficient, from Dougherty and Nunnally[62] and from Tanaka and Sano,[40] are reported and discussed. The approach to fit their results is presented, and comparison between these estimations is performed.

Dougherty and Nunnally[62] performed solidification experiments with an aqueous solution of ammonium chloride (0.38

DOI: 10.1021/acs.jced.7b01062
J. Chem. Eng. Data 2018, 63, 3170–3183

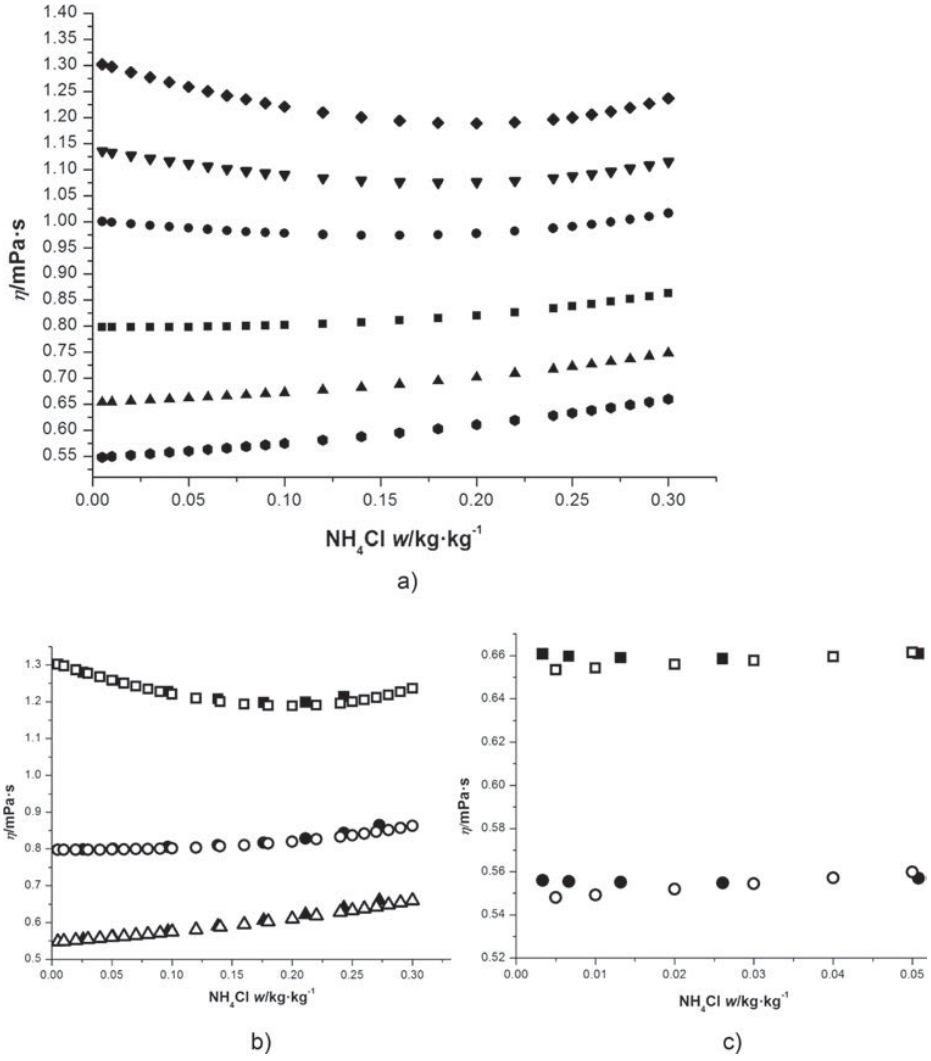

Figure 15. (a) Evolution of calculated NH_4Cl viscosity[57] with the concentration at different temperatures (♦, 283.15 K; ▼, 288.15 K; ●, 293.15 K; ■, 303.15 K; ▲, 313.15 K; ⬣, 323.15 K. (b) Comparison of measured[53] (■, 283.15 K; ●, 303.15 K; ▲, 323.15 K) and calculated (□, 283.15 K; ○, 303.15 K; △, 323.15 K) viscosity.[57] (c) Comparison of measured[52] (■, 313.15 K; ●, 323.15 K) and calculated (□, 313.15 K; ○, 323.15 K) viscosity.[57]

Table 5. Factors[57] ν_1 to ν_6 Used for the Calculations of NH_4Cl Viscosity

factor ν	
ν_1	12.396
ν_2	1.5039
ν_3	−1.7756
ν_4	0.23471
ν_5	−2.7591
ν_6	2.8408

mass fraction NH_4Cl) at a saturation temperature of 344.15 K. The solution was first heated to dissolve the ammonium chloride, then kept constant for 500 s and at last cooled down (1 K/600 s) to initiate the growth. The investigation was complete in a quasi-2D glass cell (40 × 10 × 2 mm^3). At the beginning the seed was growing spherically until instabilities appeared and dendrite started to grow. To model the initial stages of growth of a sphere, eq 11 was used:

$$\frac{dR}{dT} = \frac{D\chi}{R}\left(\Delta - \frac{2d_0}{R}\right) \tag{11}$$

where D is the diffusion coefficient for NH_4Cl in aqueous solution, χ is a geometric factor (χ = 1 for a growth in all direction), R is the radius of the spherical seed, Δ is the dimensionless supersaturation, and d_0 is the capillary length, and the estimated value for D, extrapolated from experiments,[60,63] was 2.5 × 10^{-9} ($m^2 \cdot s^{-1}$). Somehow Dougherty and Nunnally considered for their transient growth dendrite an effective diffusion constant equal to 0.71D (χ = 0.71), because the crystal rests on the bottom plate of the cell. The supersaturation was approximated via eq 12:

$$\Delta = \frac{d\Delta}{dT}(T_{eq} - T) = C_T \Delta T \tag{12}$$

where C_T is estimated to be constant (0.005/K) from the fit of eq 12. The value used for d_0 to fit eq 11 was 3 × 10^{-10} (m). The capillary length can be express with eq 13:

DOI: 10.1021/acs.jced.7b01062
J. Chem. Eng. Data 2018, 63, 3170−3183

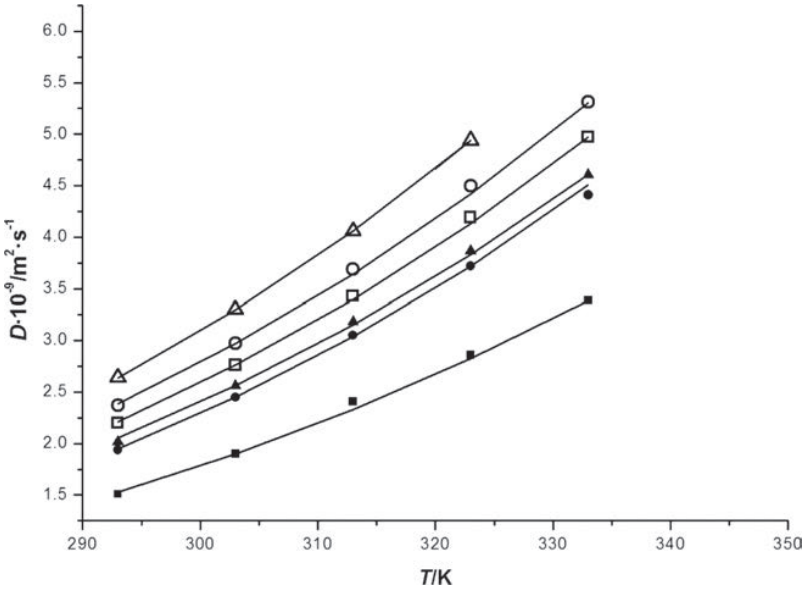

Figure 16. NH_3 measured diffusivity[58] versus temperature at different mol concentrations: (■) 0.0 mole fraction, (●) 0.053 mole fraction, (▲) 0.105 mole fraction, (□) 0.157 mole fraction, (○) 0.209 mole fraction, (△) 0.312 mole fraction). The strait lines correspond to the fit with the Arrhenius law.

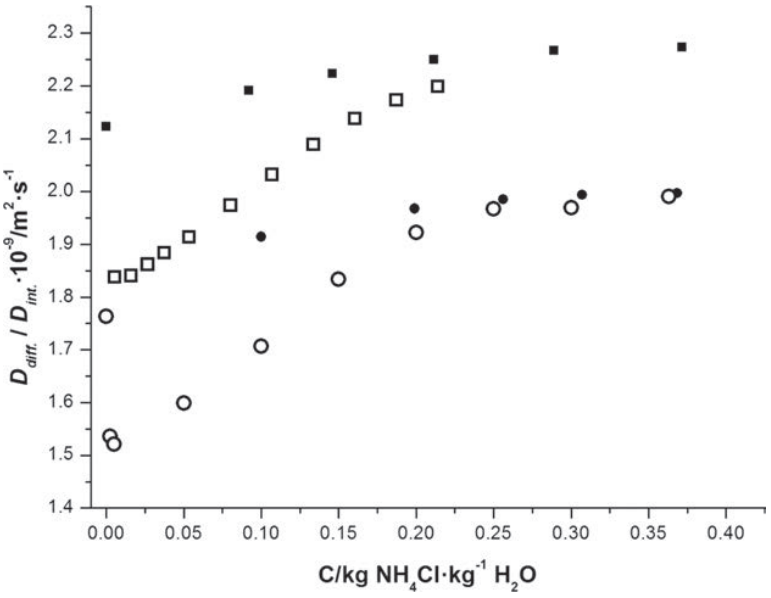

Figure 17. Measured differential diffusivity (○, 293.15 K; □, 298.15 K) and calculated integral diffusivity (●, 293.15 K; ■, 298.15 K).[59,60]

$$d_0 = \frac{\Gamma}{C_s - C_{eq}} \tag{13}$$

and consequently the value for The Gibbs−Thomson coefficient can be extracted, $\Gamma = 1.86 \times 10^{-10}$ (K·m).

Tanaka and Sano[40] performed practically the opposite experiment than Dougherty and Nunnally,[62] the dissolution of an ammonium chloride crystal of initial diameter $R = 53.2 \times 10^{-6}$ (m) (0.33 mass fraction NH_4Cl, saturation temperature 321.15 K) in a glass cell (26×50 mm^2) with a thickness of 0.5 mm on one side and 1 mm at the other side. From eq 11 we can notice that the larger is the radius of the crystal, the lower is the growth rate, thus the smaller is the crystal, the more precise are the measurements. The value for the diffusion coefficient, 2.6×10^{-9} (m^2·s^{-1}), was extrapolated from literature values,[64] but like Dougherty, Tanaka used a geometric factor of 0.71 to reduce it, because they believe a constraint growth will take place, as the crystal rested on the bottom of the cell. To fit eq 11 Tanaka used $d_0 = 1.59 \times 10^{-9}$ (m) and subsequently using eq 13, Γ was calculated to be equal to 1.06×10^{-9} (K·m).

To model the growth/dissolution measured by Dougherty and Tanaka in their experiments, eq 11 was modified by taking into account the density difference between the liquid and solid phase and calculating the supersaturation differently. Equation 14 shows this new relation:

DOI: 10.1021/acs.jced.7b01062
J. Chem. Eng. Data 2018, 63, 3170−3183

Table 6. Comparison between Different Diffusion Coefficients (D_{Cl-}, D_{NH_4+}, D_{NH_3}, D_{NH_4Cl}) Calculated with Stokes-Einstein Relation[a] (eq 10) and Experimental Measurements[58−61]

	T = 293.15 K	T = 298.15 K	T = 333.15 K
r_{Cl-} (m)	$1.64 \cdot 10^{-10}$	$1.64 \cdot 10^{-10}$	$1.64 \cdot 10^{-10}$
r_{NH_4+} (m)	$1.48 \cdot 10^{-10}$	$1.48 \cdot 10^{-10}$	$1.48 \cdot 10^{-10}$
η_{H2O} (Pa·s)		$0.89 \cdot 10^{-3}$	$0.46 \cdot 10^{-3}$
D_{Cl-} (calculated) ($m^2 \cdot s^{-1}$)	$1.306 \cdot 10^{-9}$	$1.495 \cdot 10^{-9}$	$3.19 \cdot 10^{-9}$
D_{Cl-} (measurement)[61] ($m^2 \cdot s^{-1}$)		$1.38 \cdot 10^{-9}$	$3.11 \cdot 10^{-9}$
D_{NH_4+} (calculated) ($m^2 \cdot s^{-1}$)	$0.9 \cdot 10^{-9}$	$1.657 \cdot 10^{-9}$	$3.53 \cdot 10^{-9}$
D_{NH_3} (measurement)[58] ($m^2 \cdot s^{-1}$)	$1.5 \cdot 10^{-9}$	$1.70 \cdot 10^{-9}$	$3.39 \cdot 10^{-9}$
D_{NH_4Cl} (measurement)[59] ($m^2 \cdot s^{-1}$)	$1.54 \cdot 10^{-9}$		
D_{NH_4Cl} (measurement)[60] ($m^2 \cdot s^{-1}$)		$1.84 \cdot 10^{-9}$	

[a] r_{Cl-}, r_{NH_4+} represent the radius of the chloride ion and the ammonium ion respectively; η_{H_2O} is the water viscosity.

$$\frac{dR}{dT} = \frac{\rho_l}{\rho_s}\frac{D\chi}{R}\left(\Omega - \frac{2d_0}{R}\right) \quad (14)$$

with the supersaturation $\Omega = \frac{C_l - C_{eq} - \frac{2\Gamma}{R}}{C_s - C_{eq} - \frac{2\Gamma}{R}}$ and $\chi = 1$ (because its value is not known when the growth is restraint). The ratio $\frac{\rho_l}{\rho_s} = \frac{1078}{1527}$ gives exactly 0.7059, which is almost the value of the geometric factor that Dougherty and Tanaka used to reduce the diffusion coefficient extrapolated from literature values. To fit the experimental results from Dougherty (Figure 18a) and Tanaka (Figure 18b) a value of $d_0 = 0.5 \times 10^{-9}$ (m) was used, and the extracted diffusion coefficients are 4.5×10^{-9} ($m^2 \cdot s^{-1}$) and respectively 3×10^{-9} ($m^2 \cdot s^{-1}$) (instead of 2.5×10^{-9} and 2.6×10^{-9} ($m^2 \cdot s^{-1}$)). In the case of the Tanaka experiment, only the last values (from $R = 19.74 \times 10^{-6}$ (m)) were used for fitting, since the rate of dissolution increased with decreasing the radius and thus the measurements are more precise. The diffusivity values found by ourselves in order to fit the experimental results of Dougherty and Tanaka are obviously larger than their values, thus we believe the geometrical factor χ should have a value lower than 1.

The Γ values found by our approach (eq 14) are 3.1×10^{-10} (K·m) (~1.6 times the value found by Dougherty 1.86×10^{-10} (K·m)) and correspondingly 3.75×10^{-10} (K·m) (~2.8 times lower than the value of Tanaka 1.06×10^{-9} (K·m)).

In Figure 19 we plotted together with the NH_3 diffusivity values the only experimental values available for the ammonium chloride (from Figure 17). In Figure 17 it can be observed that the diffusivity is almost constant after 0.20 mass fraction NH_4Cl, thus we consider for all concentrations larger than 0.20 mass fraction NH_4Cl an average value (1.99×10^{-9} ($m^2 \cdot s^{-1}$) at 293.15 K and 2.26×10^{-9} ($m^2 \cdot s^{-1}$) at 298.15 K), which are plotted on Figure 19. Using these two values we extrapolated the diffusivity using the Arrhenius relation (eq 9 with $A = 4.87$ and $E_a = 1926.89$ (J·molecule^{-1})) to the two temperatures of

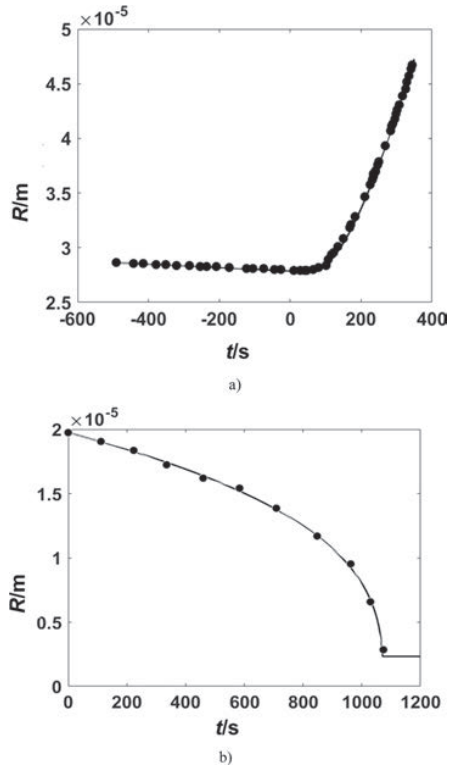

Figure 18. Experimental results (dots) for the seed radius: (a) Dougherty and Nunally;[62] (b) Tanaka and Sano[40] and fitted line using our approach (eq 14).

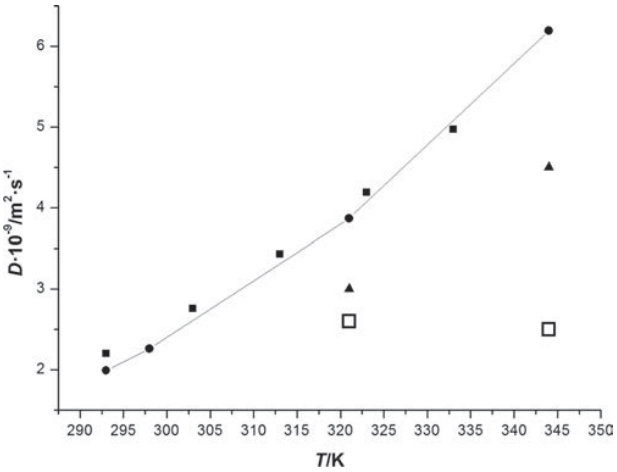

Figure 19. Diffusivity values extrapolated from measurements[59,60] (dots and line) for ammonium chloride concentration larger than 0.20 mass fraction NH_4Cl, compared with NH_3 measurements at 0.157 NH_3 mol fraction[58] (filled squares), measurements from Dougherty and Nunally,[62] and Tanaka and Sano[40] (empty squares), and calculated values using eq 14 (triangles).

DOI: 10.1021/acs.jced.7b01062
J. Chem. Eng. Data 2018, 63, 3170−3183

interest 321.15 and 344.15 K, corresponding to Tanaka and Dougherty experiments. Their diffusivity values are not fitting this plot, they correspond closely to the diffusivity measured at 298.15 K, but they are far from the values corresponding to 321.15 and 344.15 K. The diffusivity values calculated with our approach (eq 14) to fit these two experiments are not on this extrapolated curve. There exists a factor of 0.73 and respectively 0.77 between our values and the extrapolated plot, which should correspond to the geometrical factor χ. These factors are very close to the reduction factor 0.71 used by Tanaka and Dougherty in order to reduce the growth due to the flat bottom.

As a conclusion, ammonium chloride properties are very well-known including phase diagram, density, heat capacity, and viscosity. Concerning the thermal conductivity, the diffusivity, and the Gibbs–Thomson coefficient, little data are available.

AUTHOR INFORMATION

Corresponding Author

*E-mail: abdellah.kharicha@unileoben.ac.at.

ORCID

Mihaela Stefan-Kharicha: 0000-0002-5970-5182

Funding

The authors kindly acknowledge the FWF (Austrian Science Fund, Grant Nos. P17619-N02 and P22614-N22) for their support.

Notes

The authors declare no competing financial interest.

REFERENCES

(1) McDonald, R. J.; Hunt, J. D. Fluid motion through partially solid regions of a casting and its importance in understanding A type segregation. *Trans. Metall. Soc. AIME* **1969**, *245*, 1993–1997.

(2) McDonald, R. J.; Hunt, J. D. Convection fluid motion within the interdendritic liquid of casting. *Metall. Trans. A* **1970**, *1*, 1787–1788.

(3) Ohno, A. Compositional depression of undercooling and formation of segregation between columnar and equiaxed zones, Proceedings of 1st Solidification Processing Conference, Brighton, UK, 1967; The Solidification of Metals, The Iron and Steel Institute: London, 1968; p 349.

(4) Huang, S.-C.; Glicksman, M. E. Fundamentals of dendritic solidification—I. Steady-state tip growth. *Acta Metall.* **1981**, *29*, 701–715.

(5) Huang, S.-C.; Glicksman. Fundamentals of dendritic solidification—II. Development of side branch structure. *Acta Metall.* **1981**, *29*, 717–734.

(6) Somboonsuk, K.; Mason, J. T.; Trivedi, R. Interdendritic spacing. Part I: Experimental studies. *Metall. Mater. Trans. A* **1984**, *15 A*, 967–975.

(7) Kaya, H.; Cadirli, E.; Keslioglu, K.; Marasli, N. Dependency of the dendritic arm spacings and tip radius on the growth rate and composition in the directionally solidified succinonitrile–carbon tetrabromide alloys. *J. Cryst. Growth* **2005**, *276*, 583–593.

(8) Li, Q.; Beckermann, C. Modeling of Free Dendritic Growth of Succinonitrile-Acetone Alloys with Thermosolutal Melt Convection. *J. Cryst. Growth* **2002**, *236*, 482–498.

(9) Badillo, A.; Beckermann, C. Growth of Equiaxed Dendritic Crystals Settling in an Undercooled Melt, Proceedings of the 5th Decennial International Conference on Solidification Processing, Sheffield, UK, July 2007. Jones, H., Ed.; Dept. Engineering Materials, The University of Sheffield: Sheffield, UK, 2007; pp 176–180.

(10) Melendez Ramirez, A. J. Experimental Investigation of Free Dendritic Growth of Succinonitrile-Acetone Alloys. Ph.D. Thesis, University of Iowa, 2009.

(11) Üstün, E.; Cadirly, E.; Kaya, V. Dendritic solidification and characterization of a succinonitrile–acetone alloy. *J. Phys.: Condens. Matter* **2006**, *18*, 7825–7839.

(12) Mogeritsch, J.; Eck, S.; Grasser, M.; Ludwig, A. Situ Observation of Solidification in an Organic Peritectic Alloy System. *Mater. Sci. Forum* **2010**, *649*, 159–164.

(13) Mogeritsch, J.; Ludwig, A. In-situ observation of coupled growth morphologies in organic peritectics. *IOP Conf. Ser.: Mater. Sci. Eng.* **2011**, *27*, 012028.

(14) Ludwig, A.; Mogeritsch, J.; Kolbe, M.; Zimmermann, G.; Sturz, L.; Bergeon, N.; Billia, B.; Faivre, G.; Akamatsu, S.; Bottin-Rousseau, S.; Voss, D. Advanced Solidification Studies on Transparent Alloy Systems: A New European Solidification Insert for Material Science Glovebox on Board the International Space Station. *JOM* **2012**, *64*, 1097–1101.

(15) Ludwig, A.; Mogeritsch, J. Recurring instability of cellular growth in a near peritectic transparent NPG-TRIS alloy system. *Mater. Sci. Forum* **2014**, *790–791*, 317–322.

(16) Ludwig, A.; Mogeritsch, J. In-situ observation of the dynamic of peritectic coupled growth using the binary organic system TRIS-NPG. *IOP Conf. Ser.: Mater. Sci. Eng.* **2015**, *84*, 012055.

(17) Okada, M.; Gotoh, K.; Murakami, M. Solidification on an aqueous solution in a rectangular cell with hot and cold vertical walls. *Nippon Kikai Gakkai Ronbunshu, B-hen* **1990**, *56*, 1790–1795.

(18) Peppin, S. S. L.; Aussillous, P.; Huppert, H. E.; Worster, M. G. Steady-state mushy layers: experiments and theory. *J. Fluid Mech.* **2007**, *570*, 69–77.

(19) Stefan-Kharicha, M.; Kharicha, A.; Wu, M.; Ludwig, A. Observation of flow regimes and transitions during a columnar solidification experiment. *Fluid Dyn. Res.* **2014**, *46*, 1–21.

(20) Kharicha, A.; Stefan-Kharicha, M.; Ludwig, A.; Wu, M. Simultaneous observation of melt flow and motion of equiaxed crystals during solidification using a dual phase Particle Image Velocimetry technique. Part I: Stages characterization of melt flow and equiaxed crystals motion. *Metall. Mater. Trans. A* **2013**, *44*, 650–660.

(21) Kharicha, A.; Stefan-Kharicha, M.; Ludwig, A.; Wu, M. Simultaneous observation of melt flow and motion of equiaxed crystals during solidification using a dual phase Particle Image Velocimetry technique. Part II: Relative velocities. *Metall. Mater. Trans. A* **2013**, *44*, 661–668.

(22) Kharicha, A.; Stefan-Kharicha, M.; Wu, M.; Ludwig, A. Simultaneous observation of melt flow and motion of equiaxed crystals during solidification using a dual phase PIV technique. *IOP Conf. Ser.: Mater. Sci. Eng.* **2012**, *33*, 012042.

(23) Stefan-Kharicha, M.; Kharicha, A.; Wu, M.; Ludwig, A. On the Coupling Mechanism of Equiaxed Crystal Generation with the Liquid Flow Driven by Natural Convection During Solidification. *Metall. Mater. Trans. A* **2018**, *49*, 1708–1724.

(24) Ghenai, C.; Mudunuri, A.; Lin, C. X.; Ebadian, M. A. Double-diffusive convection during solidification of a metal analog system (NH_4Cl–H_2O) in a differentially heated cavity. *Exp. Therm. Fluid Sci.* **2003**, *28*, 23–35.

(25) Nishimura, T.; Imoto, T.; Miyashita, H. Occurrence and Development of Double-Diffusive Convection during Solidification of a Binary System. *Int. J. Heat Mass Transfer* **1994**, *37*, 1455–1464.

(26) McCay, M. H.; Hopkins, J. A.; McCay, T. D. J. Convective flow effects on diffusion layers during NH_4Cl–H_2O dendritic solidification. *J. Cryst. Growth* **1994**, *144*, 346–352.

(27) Skudarnov, P. V.; Lin, C. X.; Wang, M. H.; Pradeep, N.; Ebadian, M. A. Evolution of convection pattern during the solidification process of a binary mixture: effect of initial solutal concentration. *Int. J. Heat Mass Transfer* **2002**, *45*, 5191–5200.

(28) Peppin, S. S. L.; Huppert, H. E.; Worster, M. G. Steady-state solidification of aqueous ammonium chloride. *J. Fluid Mech.* **2008**, *599*, 465–476.

(29) Chen, C. F. Viscosity effects on the directional solidification of NH_4Cl solution in a Hele-Shaw cell. *Phys. Fluids A* **2003**, *34*.1879

DOI: 10.1021/acs.jced.7b01062
J. Chem. Eng. Data 2018, 63, 3170–3183

(30) Ramani, A.; Beckermann, C. Dendrite tip growth velocities of settling NH_4Cl equiaxed crystals. *Scr. Mater.* **1997**, *36*, 633−638.
(31) Beckermann, C.; Wang, C. Y. Equiaxed dendritic solidification with convection. 3. Comparisons with NH_4Cl-H_2O experiments. *Metall. Mater. Trans. A* **1996**, *27A*, 2784−2795.
(32) Beckermann, C.; Viskanta, R. Natural convection solid/liquid phase change in porous media. *Int. J. Heat Mass Transfer* **1988**, *31*, 2077−2089.
(33) Beckermann, C.; Fan, C.; Mihailovic, J. Numerical Simulations of Double-Diffusive Convection in a Hele-Shaw Cell. *Int. Video J. Eng. Res.* **1991**, *1*, 71−82.
(34) Wang, C. Y.; Beckermann, C. A unified solute diffusion model for columnar and equiaxed dendritic alloy solidification. *Mater. Sci. Eng., A* **1993**, *171A*, 199−211.
(35) Kumar, P.; Chakraborty, S.; Srinivasan, K.; Dutta, P. Studies on transport phenomena during directional solidification of a noneutectic binary solution cooled from the top. *Metall. Mater. Trans. B* **2003**, *34B*, 899−909.
(36) Nishimura, T.; Imoto, T.; Miyashita, H. Occurrence and development of double-diffusive convection during solidification of a binary system. *Int. J. Heat Mass Transfer* **1994**, *37*, 1455−1464.
(37) Rady, M. A.; Nada, S. A. Solidification of hypereutectic and hypoeutectic binary alloys with buoyancy and surface tension driven natural convection. *Heat Mass Transfer* **1998**, *34*, 337−347.
(38) Christerson, M. S.; Incropera, F. P. Solidification of an aqueous ammonium chloride solution in a rectangular cavity—I. Experimental study. *Int. J. Heat Mass Transfer* **1989**, *32*, 47−68.
(39) Collections of phase diagrams. http://www.crct.polymtl.ca/fact/phase_diagram.php?file=H2O-NH4Cl_no_gas.jpg&dir=FTfrtz (accessed April 13, 2018).
(40) Appolaire, B.; Albert, V.; Combeau, H.; Lesoult, G. Free Growth of Equiaxed. Crystals Settling in Undercooled NH4Cl-H2O Melts. *Acta Mater.* **1998**, *46*, 5851−5862.
(41) Tanaka, A.; Sano, M. Measurement of the kinetic effect on the concentration field of a growing dendrite. *J. Cryst. Growth* **1992**, *125*, 59−64.
(42) Liu, J.-M.; Liu, Z.-G.; Wu, Z.-C. In-Situ observations of dendritic growth of ammonium chloride crystals from an aqueous solution system. *Scr. Metall. Mater.* **1995**, *32*, 445−450.
(43) Perry, R. H.; Green, D. W.; Maloney, J. O. *Perry's Chemical Engineers' Handbook*; 7th ed.; The McGraw-Hill Companies: New York, 1999.
(44) Chase, M. W., Jr. *Journal of Physical and Chemical Reference Data, Monograph 9, NIST-JANAF Thermochemical Tables*, 4th ed.; American Chemical Society, American Institute of Physics for National Institute of Standards and Technology: Washington, DC, 1998.
(45) Zabaras, N.; Samanta, D. A stabilized volume-averaging finite element method for flow in porous media and binary alloy solidification processes. *Int. J. Numer. Meth. Eng.* **2004**, *60*, 1103−1138.
(46) Sanyal, D.; Ramachandra Rao, P.; Gupta, O. P. Modelling of free boundary problems for phase change with diffuse interfaces. *Math. Probl. Eng.* **2005**, *3*, 309−324.
(47) Jones, G.; Talley, S. K. The viscosity of aqueous solutions as a function of the concentration. *J. Am. Chem. Soc.* **1933**, *55*, 624−642.
(48) Das, P. K. Viscosity and apparent molal volume of aqueous solutions of ammonium chloride and ammonium bromide at 35 °C. *J. Indian Chem. Soc.* **1954**, *31*, 170−172.
(49) Sahu, B.; Behera, B. Viscosity of concentrated aqueous solutions of 1:1 electrolytes. *Indian J. Chem.* **1980**, *19A*, 1153−1157.
(50) Monica, M. D.; Ceglie, A.; Agostiano, A. A conductivity equation for concentrated aqueous solutions. *Electrochim. Acta* **1984**, *29*, 933−937.
(51) Getman, F. H. A study of the solutions of some salts exhibiting negative viscosity. *J. Am. Chem. Soc.* **1908**, *30*, 721−737.
(52) Motin, M. A. Temperature and concentration dependence of apparent molar volumes and viscosities of NaCl, NH_4Cl, $CuCl_2$, and $MgSO_4$ in pure water and water + urea mixtures. *J. Chem. Eng. Data* **2004**, *49*, 94−98.
(53) Goldsack, D. E.; Franchetto, R. C. The viscosity of concentrated electrolyte solutions. II. Temperature dependence. *Can. J. Chem.* **1978**, *56*, 1442−1450.
(54) Chatterji, A. C.; Gopal, R. The variation of relative viscosity with temperature. *J. Indian Soc.* **1947**, *24*, 455−460.
(55) Wolf, A. V. *Aqueous Solutions and Body Fluids: Their Concentrative Properties and Conversion Tables*; Harper & Row: New York and London, 1966.
(56) Söhnel, O.; Novotny, P. *Densities of Aqueous Solutions of Inorganic Substances*; Elsevier: Amsterdam, 1985.
(57) Laliberte, M. Model for calculating the viscosity of aqueous solutions. *J. Chem. Eng. Data* **2007**, *52*, 321−335.
(58) Frank, M. J. W.; Kuipers, J. A. M.; van Swaaij, W. P. M. Diffusion Coefficients and Viscosities of CO_2 + H_2O, CO_2 + CH_3OH, NH_3 + H_2O, and NH_3 + CH_3OH Liquid Mixtures. *J. Chem. Eng. Data* **1996**, *41*, 297−302.
(59) Nienow, W.; Unahabhokha, R.; Mullin, J. W. Diffusion of NH_4Cl and KCl in aqueous solution. *J. Appl. Chem.* **1968**, *18*, 154−156.
(60) Hall, J. R.; Wishaw, B. F.; Stokes, R. H. The diffusion coefficients of Calcium Chloride and Ammonium Chloride in concentrated aqueous solutions at 25°C. *J. Am. Chem. Soc.* **1953**, *75*, 1556−1560.
(61) Tang, A.; Sandall, O. C. Diffusion coefficient of chlorine in water at 25−60°C. *J. Chem. Eng. Data* **1985**, *30*, 189−191.
(62) Dougherty, A.; Nunnally, T. The Transient Growth of Ammonium Chloride Dendrites. *J. Cryst. Growth* **2006**, *300*, 0603636vl.
(63) Lutz, J. L.; Mendenhall, G. D. Diffusion coefficients by NMR-spin echo methods for the systems water−ammonium chloride, water−succinonitrile, and acetone−succinonitrile. *J. Cryst. Growth* **2000**, *217*, 183−188.
(64) Billings, B. H.; Gray, D. E. *American Institute of Physics Handbook*; McGraw-Hill: New York, 1972.

NOTE ADDED AFTER ASAP PUBLICATION

This article published June 6, 2018 with errors in figures, equations, and tables. The corrected article published August 1, 2018.

DOI: 10.1021/acs.jced.7b01062
J. Chem. Eng. Data 2018, 63, 3170−3183